RL-996

036065-1-F

Digital Topography From SAR Interferometry: Determination of and Correction for Vegetation Height

Kamal Sarabandi

September 1998

RL-996 = RL-996

RL-996

FINAL REPORT FOR NASA GRANT NAGW-4555/ NAG5-4939

DIGITAL TOPOGRAPHY FROM SAR INTERFEROMETRY: DETERMINATION OF AND CORRECTION FOR VEGETATION HEIGHT

Submitted to :
Office of Mission to Planet Earth
NASA Headquarters
300 E. Street SW
Washington D.C. 20546
Attention: Dr. Diane Wickland

Kamal Sarabandi ,

Radiation Laboratory
Department of Electrical Engineering and Computer Science
The University of Michigan
Ann Arbor, MI 48109-2122
Tel: (313) 764-0500, Fax: (313) 747-2106

Project Duration: March 15, 1995 to September 15, 1998

Contents

1 Background and Objectives 1

2 Summary of Accomplished Results 2

2.1 Theoretical Model Development 2

2.1.1 Δk Radar Equivalence of an INSAR 2

2.1.2 Statistical Analysis 3

2.1.3 Vegetation Model 3

2.2 Development of a Monte Carlo Coherent Scattering Model for Tree Canopies Based on Fractal Theory 4

2.3 INSAR Response to Short vegetation 9

2.4 INSAR Response to Trees 9

2.5 Inversion Algorithm Based on Multi-incidence Angle and/or Multi-frequency SAR/INSAR 10

2.6 Experimental Activities 12

3 Graduate Students 12

4 Publications 14

4.1 Journal Papers 14

4.2 Conference Papers 15

I Δk-Radar Equivalent of Interferometric SARs: A Theoretical Study for Determination of Vegetation Height I-1

II Electromagnetic Scattering Model for a Tree Trunk Above a Ground Plane II-1

III A Monte Carlo Coherent Scattering Model For Forest Canopies Using Fractal-Generated Trees III-1

IV Simulation of Interferometric SAR Response for Characterization of Scattering Phase Center Statistics of Forest Canopies IV-1

V Electromagnetic Scattering from Short Branching Vegetation V-1

VI Retrieval of Forest Parameters Using a Fractal-Based Coherent Scattering Model and a Genetic Algorithm VI-1

VII An Evaluation of JPL TOPSAR for Extracting Tree Heights VII-1

VIII GPS Measurements for SIR-C/X-SAR and TOPSAR Forest Test Stands at Raco, Michigan Site VIII-1

1 Background and Objectives

Accurate estimation of gross forest parameters such as total vegetation biomass, total leaf area index, and tree height on a regional to global scale has long been an important goal within the remote sensing community. Over the past two decades much effort has been devoted to the development of scattering models [1, 2, 3] for understanding of the interaction of electromagnetic waves with vegetation, and to the construction and development of advanced imaging radars for acquiring test data and examining the feasibility of the remote sensing problem [4]. In most practical situations the number of vegetation parameters influencing the radar response usually exceeds the number of radar observation parameters. For this reason the application of multi-frequency and multi-polarization radar systems was proposed and such a system was flown aboard the Shuttle Endeavor in April and October 1994 [4]. Preliminary results indicate that the classification and retrieval of vegetation biophysical parameters indeed require many simultaneous radar channels, however, free-flight of such systems is not practical due to the exorbitant power requirements.

Characterization of the spatial organization of particles in a vegetation canopy is of great importance for determining many ecosystem processes including energy and chemical exchanges. Traditional remote sensing instruments provide two-dimensional spatial information of the target which may contain, depending on the instrument, some information on the vertical particle arrangement in a convoluted fashion. Recent advancements in the field of radar interferometry have opened a new door on radar remote sensing of vegetation. In addition to the backscattering coefficient of a distributed target, radar interferometers provide two additional parameters that contain information about the target. These parameters are the correlation coefficient and the interferogram phase [5, 6]. To interpret these parameters and to characterize their dependence on the physical parameters of the target, a thorough understanding of the coherent interaction of electromagnetic waves with vegetation particles is required. The premise of this investigation with regard to retrieving vegetation parameters from INSAR is that the location of the scattering phase center of a target is a strong function of the target structure. For example the scattering phase centers of non-vegetated terrain are located at or slightly below the surface depending upon the wavelength and the dielectric properties of the surface media. Whereas for vegetated terrain, these scattering phase centers lie at or above the surface depending upon the wavelength of the SAR and the vegetation attributes. Another important feature of interferometric SARs with regard to estimation of forest parameters is its sensitivity to biomass. Radar backscattering coefficients are found to increase with increasing biomass until saturation at biomass values that depend on the radar frequency. For example, at L-band the backscattering coefficients reach a saturation level for above-ground biomass values around 100–150 tons/ha. Our preliminary investigations show that the scattering phase center height reaches a saturation level at biomass levels significantly higher than biomass values at which the backscattering coefficients reach their saturation levels. It also must be recognized that the vegetation cover in many interferometric SAR applications where the vegetation itself is not the primary target, such as geological field mapping or surface change monitoring, acts as interference. In these cases it is also important to identify and characterize the effect of vegetation on the topographic information obtained from the interferometric SAR. In order to utilize the information gathered by INSARs, forward and inverse models have to be developed and their accuracies be examined. Extensive modeling efforts were devoted to achieve reliable models. Using these models in conjunction with careful experimentations we were able

to demonstrate the applicability and importance of INSAR data in retrieval of tree parameters. This report gives a brief summary of our activities. The appendices are also provided here to give the detailed description of methodologies procedures for the interested readers.

2 Summary of Accomplished Results

In March, 1995, the University of Michigan, in collaboration with the Radar Science Group of Jet Propulsion Laboratory, was awarded a three-year grant by the Terrestrial Ecology Program at NASA Headquarters to characterize and quantify the role of vegetation attributes in determining the scattering phase centers as observed by interferometric SARs. The objectives of the study were to:

1. Quantify the role of vegetation attributes in determining the location of the scattering phase centers as measured by SAR interferometry using a coherent electromagnetic scattering model for vegetation.

2. Map vegetation height through the combined use of SAR interferometry in conjunction with available standard digital elevation data (derived largely from optical techniques).

3. Correct SAR interferometry for vegetation effects through use of an inversion algorithm based upon vegetation type and biomass. The end product is surface elevation.

4. Estimate crown layer vegetation attributes (such as thickness) using multifrequency SAR interferometry.

5. Integrate the products derived from SAR interferometry into ecophysiological classifications and forest biophysical parameter estimations.

For this purpose analytical, numerical, and experimental aspects of electromagnetic scattering from forest canopies have been under investigation. A summary of accomplishments realized to date is given next. The details are provided in the attached appendices.

2.1 Theoretical Model Development

2.1.1 Δk Radar Equivalence of an INSAR

A fundamental relationship between INSAR and Δk radar is established. This relationship is the cornerstone of analytical and numerical analysis of the problem at hand. Understanding the relationship between the tree height and the corresponding location of the scattering phase centers requires numerical simulations (Monte Carlo simulation of a fractal generated forest stand) or controlled experiments using scatterometers. The scattering phase center of a target can also be obtained using a Δk-radar assuming that the incidence angle is known. Evaluation of the scattering phase centers using frequency shift can easily be accomplished in a numerical simulation or in a controlled experiment using a wideband scatterometer. Basically, by requiring that the backscatter phase differences, one obtained from a small change in the aspect angle and

the other one obtained from a small change in the frequency of operation, be identical for both approaches we established that

$$\Delta f = f_0 \frac{B}{2r} \sin(\theta - \alpha_0) \tag{1}$$

where Δf is the frequency shift of the equivalent Δk radar, f_0 is the operating frequency, B and α_0 are, respectively, the baseline distance and angle, r is the slant range, and θ is the look angle. It is mathematically proven that this equivalence relationship is valid for multiple scattering among particles and the scattering interaction between particles and the ground plane. The details are reported in Appendix I [7].

2.1.2 Statistical Analysis

In estimating the height of the scattering phase center of a distributed target, random fluctuations of the calculated/measured phase due to fading was investigated. An analytical form for the p.d.f. of the interferogram phase was obtained in terms of two independent parameters: (1)ζ: mean phase and (2)α: degree of correlation, which is given by

$$f_\Phi(\phi) = \frac{1-\alpha^2}{2\pi\left[1-\alpha^2\cos^2(\phi-\zeta)\right]} \cdot \left\{1 + \frac{\alpha\cos(\phi-\zeta)}{\sqrt{1-\alpha^2\cos^2(\phi-\zeta)}}\left[\frac{\pi}{2} + \tan^{-1}\frac{\alpha\cos(\phi-\zeta)}{\sqrt{1-\alpha^2\cos^2(\phi-\zeta)}}\right]\right\} , \tag{2}$$

ζ is proportional to the mean scattering phase center height and α is inversely proportional to the uncertainty with which ζ can be estimated. It is shown that α is directly related to the frequency correlation function (FCF) of the distributed target given by

$$\alpha = \frac{|<E_1 E_2^*>|}{<|E_1|^2>} \tag{3}$$

Using this pdf the uncertainty in estimation of ζ, or equivalently the mean height, from a single pixel can be evaluated. Figure 1 shows the phase uncertainty range for 80% and 90% confidence criteria [7]. Statistical analysis shows that the uncertainty in the height estimation of a distributed target is a function of the equivalent frequency decorrelation bandwidth and is independent of the baseline distance.

2.1.3 Vegetation Model

Theoretical vegetation models capable of predicting backscattering coefficients and location of scattering phase center for simple canopy structures (homogeneous particle distribution) were developed [7, 8]. It is also shown that for a uniform closed canopy the extinction and the physical height of the canopy top can be estimated provided that the correlation coefficient (α) can be measured very accurately. For example for a dense canopy it is found that the extinction coefficient can be directly obtained from α. Also the location of the scattering phase center (from the canopy top) is given by the following simple relationship:

$$\Delta d = \frac{\cos\theta}{2\kappa}. \tag{4}$$

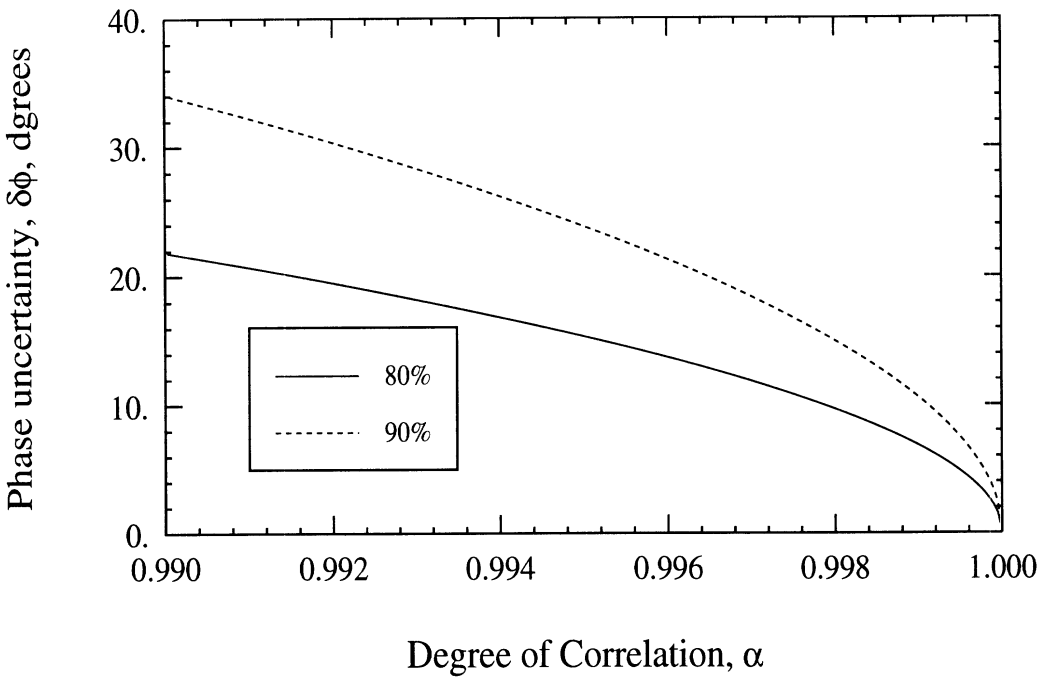

Figure 1: The interferogram phase uncertainty for 80% and 90% error probability criteria as a function of the Degree of Correlations, α. A high degree of correlation, near 1, gives a small error in the interferometric phase.

However, for finite canopies, estimation of extinction and scattering phase center is not straightforward.

Using the model developed in [8], the estimation of tree height and surface topography was attempted. It was shown that measurements of interferometric phase and amplitude were not enough to estimate the three relevant parameters, which are the tree height, ground-surface altitude, and extinction coefficient, if only volume scattering (from the leaf-branch-trunk canopy) is considered. The first demonstration was therefore supplemented with *in situ* extinction coefficient measurements and the dual-baseline estimates were based on INSAR data alone [11].

2.2 Development of a Monte Carlo Coherent Scattering Model for Tree Canopies Based on Fractal Theory

Although there are a number of EM scattering models for vegetation canopies [1, 2], they are of little use with regard to INSAR applications due to the their inability to predict the absolute phase of the scattered field. The absolute phase of the scattered field is the fundamental quantity from which the interferogram images are constructed. As mentioned earlier in order to simulate the response of an INSAR system a coherent scattering model capable of preserving the absolute phase of the scattered field is needed. Traditional scattering models for forest canopy such as radiative transfer and the distorted Born approximation are incapable of providing the phase of the backscatter and do not preserve the effect of coherence caused by the relative position of scatterers within a tree.

We have completed the task of [9, 10]. The details of these models can be obtained in Appendices II and III. In this model random generation of tree architectures is implemented by

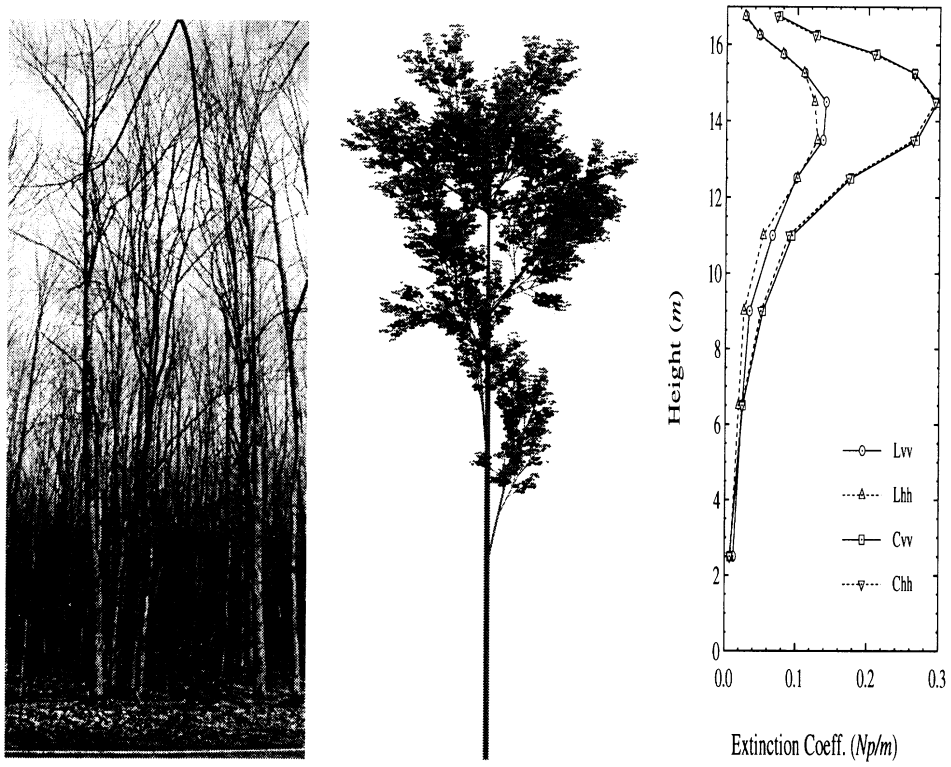

(a) Stand 31 (b) Fractal Tree (c) Extinction Profile

Figure 2: The generated fractal tree (b), based on forest Stand 31 (a), and the calculated extinction profile (c).

employing the Lindenmayer systems (L-systems). An L-system is a convenient tool for creating fractal patterns of botanical structures. After generating a tree structure, the electromagnetic scattering problem is then solved by invoking the single scattering theory. In this solution scattering from individual tree components when illuminated by the mean field is computed and then added coherently. This model was examined thoroughly and its validity was tested using SIR-C data. We used our test site (Hiawatha National Forest) in Michigan's Upper peninsula for which we collected extensive ground-truth data during the SIR-C overflight. Figure 2 shows a photo of a red maple stand, computer simulated tree structure of the same stand, and the exact extinction profile derived from the Monte Carlo simulation. Figures 3a and 3b show the comparison between the model prediction and SIR-C polarimetric backscattering coefficients at L- and C-band respectively. The three angular measurement points correspond to three different orbits of the October 94 mission. To our knowledge this model is the most accurate and sophisticated scattering model for forest canopies to date. The model preserves the exact structure of the trees, it can simulate a forest over a hilly terrain, it can simulate both coniferous and deciduous trees, it can also incorporate a radially inhomogeneous dielectric profile for the branches and the tree trunk. The details of this model and all related references are reported in [10].

We have also used the Monte Carlo coherent model in simulating the location of the scattering phase center of different forest stands [12]. As mentioned in the summary of the theoretical activities, the equivalence relationship can be invoked to find the location of the scattering phase

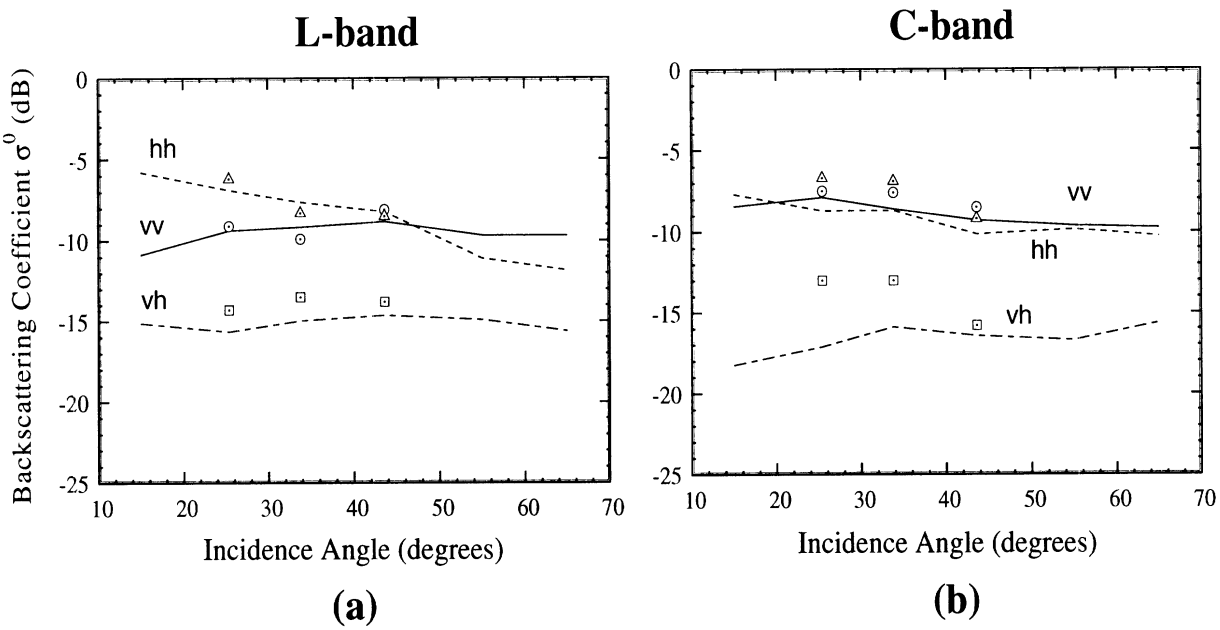

Figure 3: Comparison between the model predictions (lines) and SIR-C data (symbols) at (a) L-band and (b) C-band.

center of a tree. This is basically done by evaluating the backscatter from a forest stand at two slightly different frequencies and calculating the phase difference (for details see Appendix IV). The difference in frequency is directly proportional to the base-line distance and is also a function of the center frequency and the incidence angle. In April 1995 JPL TOPSAR flew over one of our test sites in the Michigan's Upper peninsula. For this site extensive ground truth data for vegetation including tree heights, type, number density, dielectric constant and for the ground surface including soil moisture and surface elevation were collected. Starting from a relatively poor TOPSAR data we were able to compare the result of our model with the actual measurement of TOPSAR at C-band after a calibration process (see the measurement section for more details). Figure 4 shows a photo of a red pine stand, and a computer generated red pine. Figures 5 and 6 respectively show the TOPSAR image of the test stand and the measured (at two incidence angles) and estimated height of the scattering phase centers of this stand. Finally Fig. 7 shows the measured and calculated backscattering coefficients. In Figs. 6 and 7 excellent agreements between the measured and calculated results are shown. The details of this simulation and some sensitivity analysis can be found in [12]. Figure 6 shows the measured (at two incidence angles) and estimated height of the scattering phase centers of this stand. Figure 6 show excellent agreement between the measured and calculated results. This shows that we can reliably estimate the height of a tree stand whose class we know using a simple model of the phase center height variation with local incidence angle. The estimated tree height is within 1 meter of the known 9 meter height. The details of this simulation and some sensitivity analysis can be found in [12].

(a) Stand 22 (b) Fractal Tree

Figure 4: The red pine forest stand (a), the generated fractal tree (b).

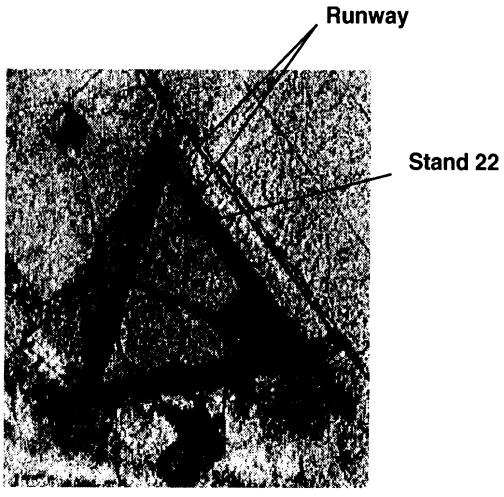

Figure 5: C-band image (σ^0_{vv}) of Stand 22 in Raco, Michigan.

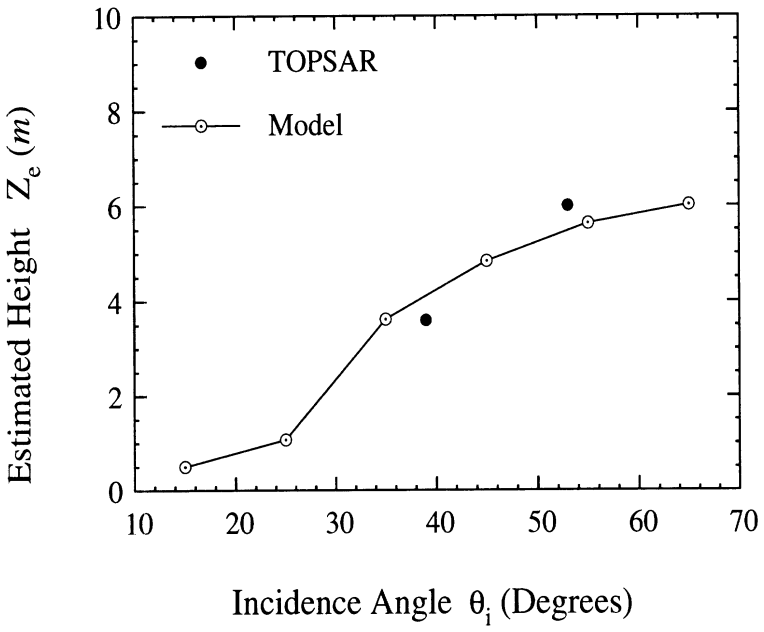

Figure 6: The estimated height of scattering phase center of Stand 22, compared with the interferometric data from JPL TOPSAR.

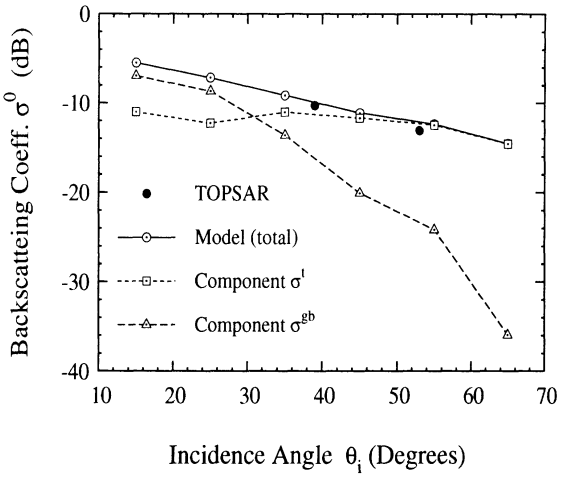

Figure 7: The simulated backscattering coefficient of Stand 22, compared with the measured data from JPL TOPSAR.

2.3 INSAR Response to Short vegetation

Classification of SAR images using C-band and higher frequency SAR faces a difficulty in separating short vegetation from tall trees. However, using INSAR the location of scattering phase center and correlation coefficient (coherence) can be used. We have conducted experiments with TOPSAR and the polarimetric wideband scatterometers at KBS site. We have also developed a very sophisticated and comprehensive scattering model for short vegetation [13]. This is the first complete second order scattering model for vegetation that accounts for multiple scattering in dense vegetation media. The result of this model was verified experimentally using polarimetric scatterometers and the JPL AIRSAR. This model was also successfully used to retrieve parameters of soybean fields. The details on this model can be found in Appendix V.

2.4 INSAR Response to Trees

Because the radar backscatter is well-known to saturate in response to high-biomass forests there is some concern that INSAR will suffer from the same trouble. Consequently, we performed simulations with the Monte-Carlo model for an increasingly taller red pine forest as shown in Fig. 8(a). The biomasses far exceeded those that saturate the radar power responses (which is about 200 tons/ha), yet the interferometric phase continued to track the increase in height. Figure 8(b) and (c) shows the simulated scattering coefficients and scattering phase center (SPC) at L band as a function of dry biomass and tree height, respectively. It is obvious that there is no saturation problem when using the interferometric phase even for relatively large values of biomass (600 tons/ha), and so this technique could be applied to old-growth forests, such as in the Amazon and other areas around the world.

The L-band interferometric phase is also sensitive to the tree density. In Figure 8 for a 12 meter red pine stand, the estimated phase center height is shown with increasing tree density. As expected, the denser the forest, the higher the phase center height, due to the progressively increasing importance of the branch scattering over the ground-trunk scattering.

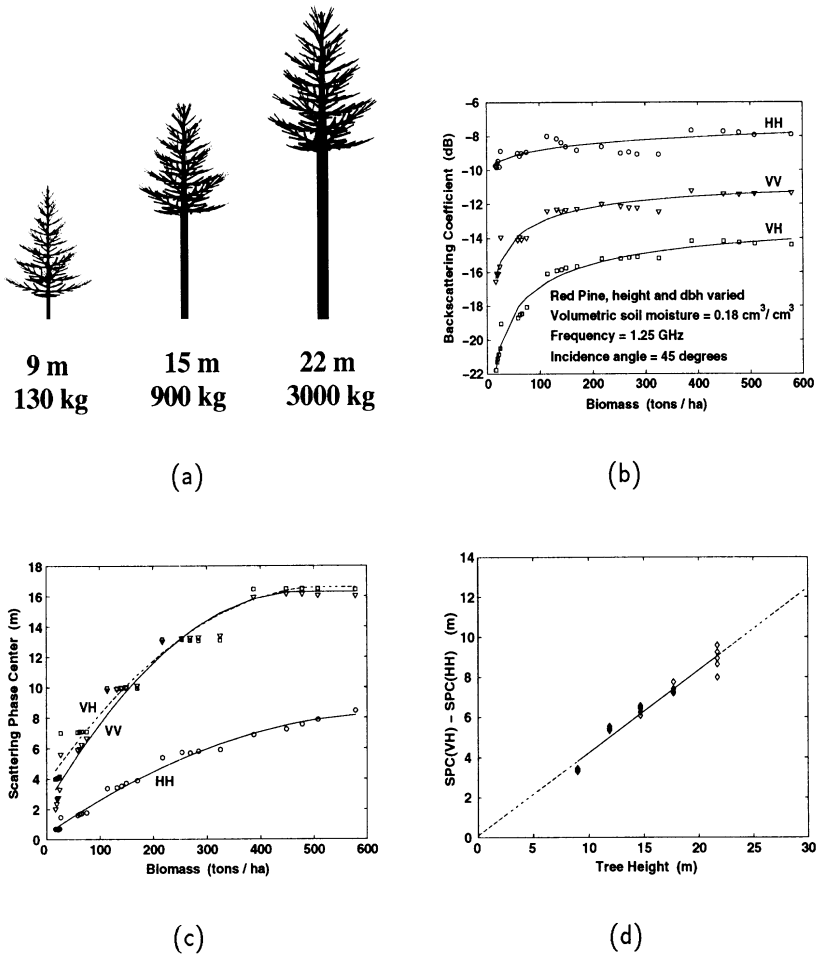

Figure 8: L-band SAR/INSAR simulation of red pine as a function of biomass. The progression of fractal trees used is shown in (a). The saturation of the backscattered powers is demonstrated in (b). The scattering phase center is shown in (c) where the HH-polarized term is still showing sensitivity out to about 500 tons/ha. The plot in (d) shows the difference in the scattering phase center between the hv-polarized and hh-polarized responses. The striking linearity of the response extends up to at least 25-meter-tall trees.

2.5 Inversion Algorithm Based on Multi-incidence Angle and/or Multi-frequency SAR/INSAR

An obtain canopy parameters from an available set of SAR and INSAR data, a robust and comprehensive inversion algorithm is needed so that any combination of multi-frequency, multi-incidence angle, and/or multi-polarization SAR and/or INSAR data set can be used as the input to the algorithm. A sensitivity analysis was carried out for determining the most influential canopy parameters on the SAR/INSAR responses using the Monte Carlo coherent model. The result of this analysis was used to identify the most sensitive SAR/INSAR channels to the changes in the canopy parameters. Since the Monte Carlo coherent model is computationally intensive, its direct application would cause the inversion process to be significantly slower. To rectify this deficiency while maintaining the high fidelity of the model, simple empirical models based on the

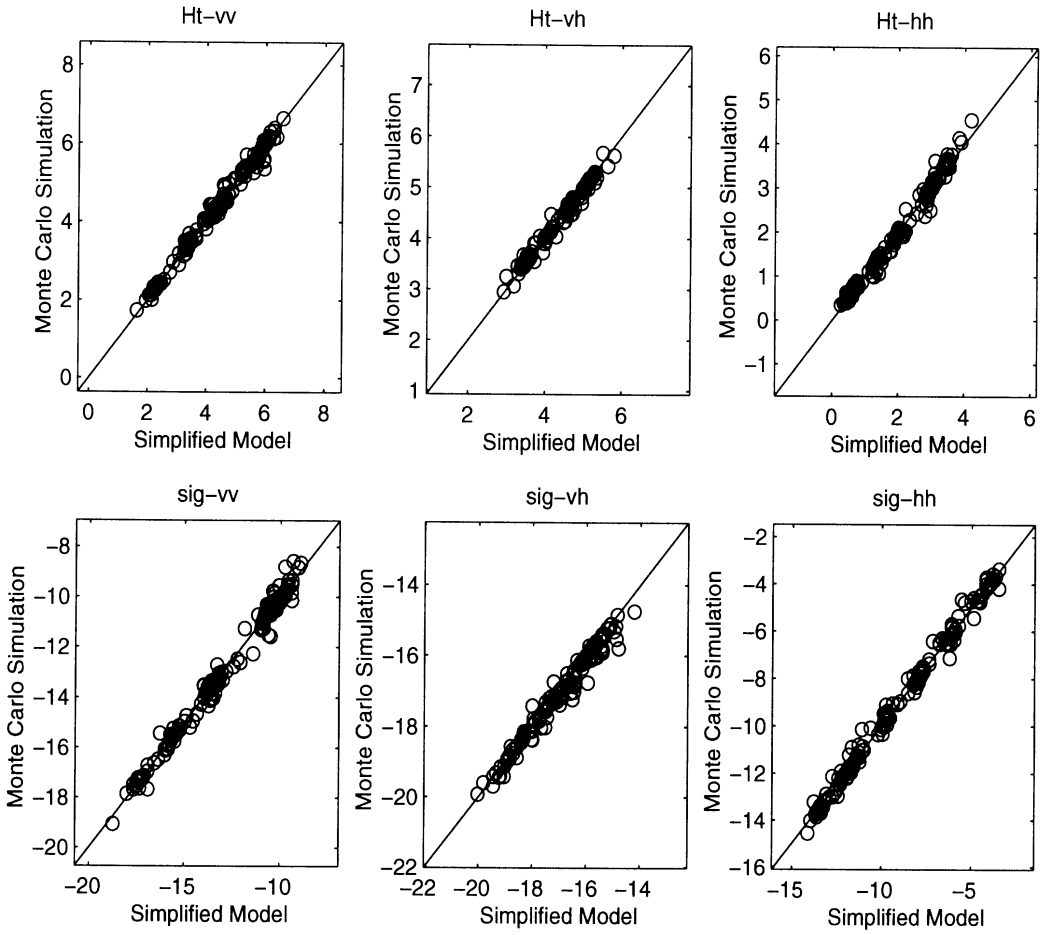

Figure 9: A comparison between an empirical scattering model and the Coherent Monte Carlo model for a red pine stand.

Monte Carlo model for different tree types was developed first. Since the quantities of interest are ensemble average quantities, such as backscattering coefficients and the location of the scattering phase center, it is expected that the dependence of these quantiles on the canopy parameters be very gentle. Therefore it is possible to obtain simple algebraic expressions for these quantities in terms of canopy parameters. For example for a given frequency and polarization, a Taylor series expansion can be used to relate radar measured quantities to the canopy parameters at a specific incidence angle. Then by repeating this process for many incidence angles, the Taylor expansion coefficients can be fit to an algebraic equation in terms of incidence angle.

This process was demonstrated successfully [20] and the details are provided in Appendix VI. For a red pine stand Figure 9 shows a comparison between the empirical model and the Monte Carlo model at C-band over a wide range of parameters including the incidence angle range $25^\circ - 70^\circ$, and 40% variation on trunk diameter (dbh), tree height, tree density, branch angle, branch moisture, and soil moisture. The top three graphs show the height of the scattering phase center at the three principal polarizations and the lower three graphs show the backscattering coefficients.

Once a comprehensive (multi-frequency and multi-polarization) easily-calculable scattering and interferometric models for all tree types of interest are developed, inversion for any available combination of INSAR and/or SAR data can be attempted by searching for an optimum set

of canopy parameters which would minimize the difference between the model prediction and measured quantities. It is expected that the objective function will be highly non-linear and complex containing many local minima. In these situations traditional gradient-based (TGB) optimization methods usually converge to a weak local minimum. Stochastic algorithms such as simulated annealing [17] and genetic algorithms [18, 19] offer an alternative for the traditional gradient-based optimization methods where the dimension of the parameter space is large and/or the objective function is non-differentiable. Applying this algorithm the parameters of Stand 22 was obtained from the JPL TOPSAR.

2.6 Experimental Activities

Our experimental activities were focused over two well-characterized sites: 1) Hiawatha National Forest (HNF) in Michigan's Upper peninsula, and 2) the Kellogg Biological Station (KBS) near Kalamazoo, Michigan. Nearly 25 different forest stands were chosen in the NHF test site which included varieties of tree types, tree height and density, and surface topography. For these stands, extensive ground truth data were collected. The ground truth for vegetation includes tree heights, type and structure, number density, and dielectric constant and for the ground surface includes soil moisture and surface elevation (see Appendix VIII for detailed experimental procedures and the data). In April 1995 JPL TOPSAR flew over this site and interferometric images were collected at two incidence angles. Figure 10 shows the map of HNF site and the location of some of the forest test stands. The grey level indicates the surface elevation as measured by TOPSAR at incidence angle $31°$. An important and most difficult-to-characterized ground truth parameter was the forest floor surface elevation data which is required to extract the scattering phase center height from INSAR images. To accomplish this, differential GPS was used to characterize the elevation map of the forest floor of each stand with a vertical resolution of the order of ± 5 cm (see Appendix VIII). Figure 11 shows a typical surface elevation map of a stand generated from the differential GPS measurements.

In using TOPSAR data we noticed problems in quality of the DEM data. After comparing sets of DEM obtained from the same area with USGS DEM, height discrepancies as high as 50 m were observed. Then we developed a correction model to correct for the aircraft residual roll angle error and multipath. The details of this procedure is given in Appendix VII.

We also conducted an experiment at the KBS site mainly to characterize the role of short vegetation on the phase and amplitude of interferograms. TOPSAR and polarimetric L- and C-band AIRSAR data were collected for this site. Different test fields with different vegetation type including wheat, alfalfa, corn, and native grass were considered. Ground truth data for each test field were also collected. We have also conducted an extensive polarimetric wideband backscatter measurements of these fields using The University of Michigan L- and C-band scatterometers. We used the KBS data to verify our short vegetation model and to demonstrate vegetation parameter estimation.

3 Graduate Students

This NASA contract supported the following Ph.D. and M.S. students.
Ph.D. Students:

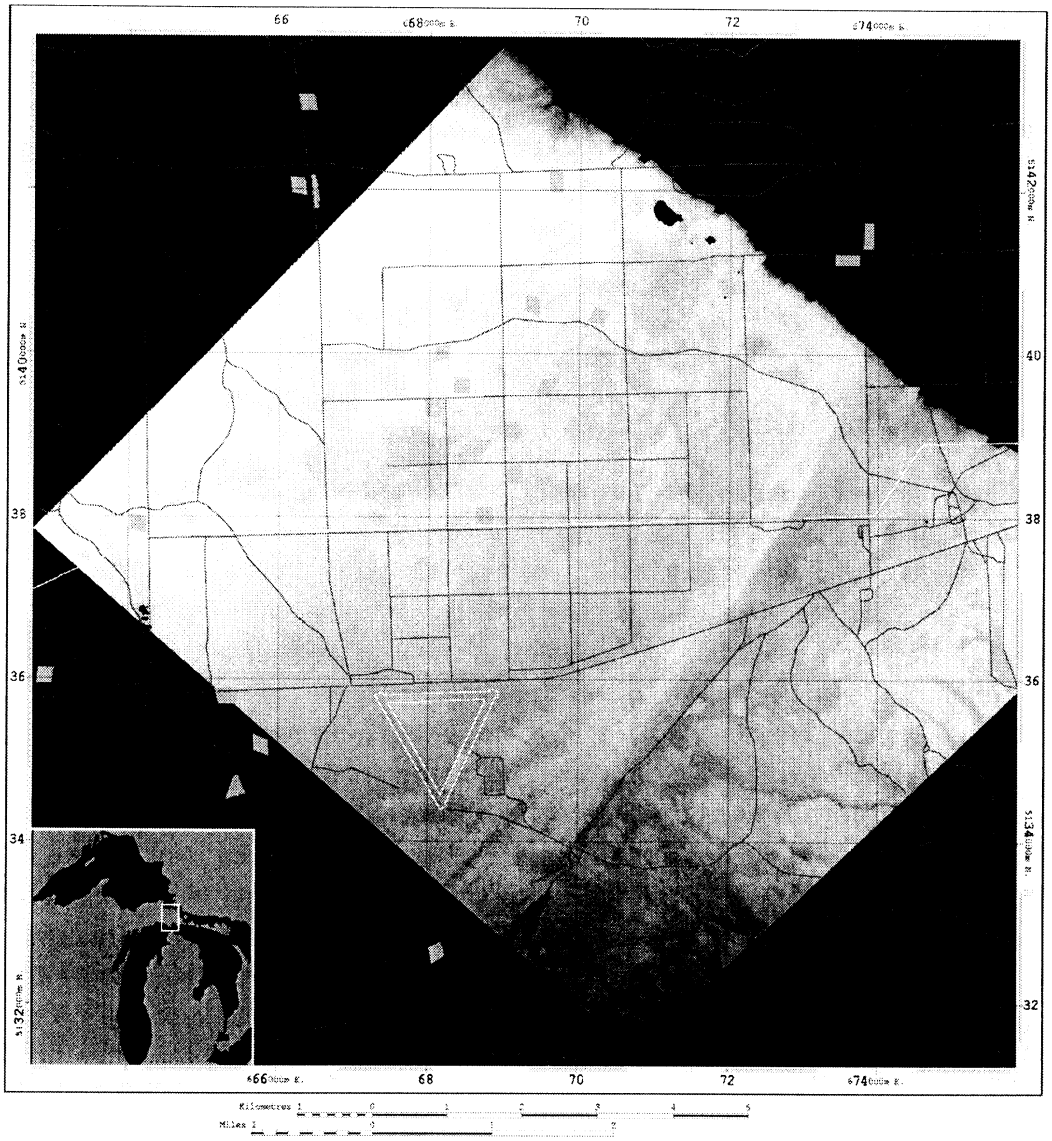

Figure 10: The surface elevation map (measured by TOPSAR) and road map of HNF site and the location of some of the forest test stands.

1. James M. Stiles, "A Coherent, Polarimetric Microwave Scattering Model for Grassland Structures and Canopies," The University of Michigan, 1996. (partially supported by this project)

2. Yi-Cheng Lin, "A Fractal-Based Coherent Scattering and Propagation Model for Forest Canopies," The University of Michigan, 1997. (fully supported by this project)

3. Tsen-Chieh Chiu, "Electromagnetic Scattering from Rough Surfaces Covered with Short Branching Vegetation," The University of Michigan, 1998. (partially supported by this project)

M.S. Students:

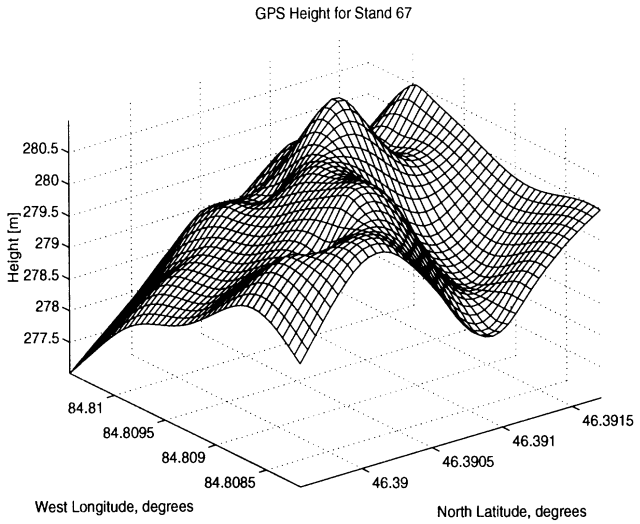

Figure 11: Surface elevation map of Stand 67 at HNF as measured by differential GPS.

1. Yutaka Koboyashi, "Assessment of TOSAR DEM Data Quality for Extracting Tree Heights," 1996-1998. (partially supported by this project)

2. Criag Wilsen, "Sensitivity of INSAR Response to Biomass Saturation," 1998- Present. (fully supported by this project)

4 Publications

A significant number of scientific papers were produced during the course of this project. The articles are grouped into reviewed articles which appeared in scientific journal and conference papers.

4.1 Journal Papers

1. Lin, Y.C., and K. Sarabandi, "Electromagnetic scattering model for a tree trunk above a ground plane," *IEEE Trans. Geosci. Remote Sensing.*, vol. 33, no. 4, pp. 1063-1070, July 1995.

2. Stiles, J.M., and K. Sarabandi, "A scattering model for thin dielectric cylinders of arbitrary cross-section and electrical length," *IEEE Trans. Antennas Propagat.*, vol. 44, no.2,260-266, Feb. 1996.

3. R. N. Treuhaft, J. J. van Zyl, and K. Sarabandi, "Extracting Vegetation and Surface Characteristics from Multibaseline Interferometric SAR," EOS Transactions, American Geophysical Union, 76, November 1995.

4. Sarabandi,K., "Δk-Radar equivalent of Interferometric SARs: A Theoretical Study for determination of vegetation height," *IEEE Trans. Geosci. Remote Sensing.*, vol. 35, no. 5, Sept. 1997.

5. Chiu, T.C., and K. Sarabandi, "Electromagnetic Scattering from Short Branching Vegetation," *IEEE Trans. Geosci. Remote Sensing.*, submitted for publication (Jan. 98).

6. Lin, Y.C., and K. Sarabandi, "A Monte Carlo Coherent Scattering Model For Forest Canopies Using Fractal-Generated Trees," *IEEE Trans. Geosci. Remote Sensing.*, vol. 37, no. 1, pp. 440-451, Jan. 1999.

7. Lin, Y.C., and K. Sarabandi, "'Retrieval of forest parameters using a fractal-based coherent scattering model and a genetic algorithm," *IEEE Trans. Geosci. Remote Sensing.*, accepted for publication .

8. Chiu, T.C., and K. Sarabandi, "Electromagnetic scattering interaction between a dielectric cylinder and a slightly rough surface," *IEEE Trans. Antennas Propagat.*, accepted for publication.

9. Sarabandi, K., and Y.C. Lin, "Simulation of Interferometric SAR Response for Characterization of Scattering Phase Center Statistics of Forest Canopies," *IEEE Trans. Geosci. Remote Sensing.*, accepted for publication (Jan. 99).

10. Y. Kobayashi, K. Sarabandi, L. Pierce, M.C. Dobson, "An Evaluation of JPL TOPSAR for Extracting Tree Heights," *IEEE Trans. Geosci. Remote Sensing*, accepted for publication, (Feb. 1999).

4.2 Conference Papers

1. R. N. Treuhaft, J. J. van Zyl, and K. Sarabandi, "Extracting Vegetation and Surface Characteristics from Multibaseline Interferometric SAR," EOS Transactions, American Geophysical Union, 76, November 1995.

2. Sarabandi, K., "Determination Of Vegetation Height From SAR Interferometry: A Theoretical Study," *Proc. IEEE Trans. Geosci. Remote Sensing Symp.*, Lincoln, Nebraska, May 1996.

3. Lin, Y.C., and K. Sarabandi, "A coherent scattering model for forest canopies based on monte carlo simulation of fractal generated trees," *Proc. IEEE Trans. Geosci. Remote Sensing Symp.*, Lincoln, Nebraska, May 1996.

4. Stiles, J.M., and K. Sarabandi, "Scattering from cultural grass canopies: a phase coherent model," *Proc. IEEE Trans. Geosci. Remote Sensing Symp.*, Lincoln, Nebraska, May 1996.

5. Treuhaft, R., M. Moghaddam, J. van Zyl, and K. Sarabandi, "Estimating vegetation and surface topographic parameters from multibaseline radar interferometry," *Proc. IEEE Trans. Geosci. Remote Sensing Symp.*, Lincoln, Nebraska, May 1996.

6. Sarabandi, K., "Characterization of canopy parameters using interferometric SARs," *American Geophysical Union,* Spring meeting, Baltimore, May 1996.

7. Sarabandi, K., and Y.C. Lin, "Characterization of Scattering Phase Center Statistics of Forest Canopies Using a Monte Carlo Coherent Scattering Model Based on Fractal Generated Trees," *URSI General Assembly*, Lille, France, August 1996 (invited).

8. Treuhaft, R.N., E. Rodriguez, M. Moghaddam, J.J. van Zyl, and K. Sarabandi, "Estimating vegetation and surface characteristics with multifrequency SAR interferometry," *URSI General Assembly*, Lille, France, August 1996 (invited).

9. Sarabandi, K., and Y.C. Lin, " Simulation of Interferometric SAR Response to Deciduous and Coniferous Forest Stands," *Proc. IEEE Trans. Geosci. Remote Sensing Symp.*, Singapore, 1997.

10. Chiu, T.C., and K. Sarabandi, "Electromagnetic scattering interaction between a dielectric cylinder and a slightly rough surface," *Proc. IEEE Trans. Geosci. Remote Sensing Symp.*, Singapore, 1997.

11. Y.C. Lin, and K. Sarabandi, "Coherent scattering and propagation model for coniferous and deciduous tree canopies," *Proc. IEEE Trans. Antennas Propagat.& URSI Symp.*, Montreal, Canada, July 1997.

12. Chiu, T.C., and K. Sarabandi, "Electromagnetic scattering from targets above rough surfaces," *Proc. IEEE Trans. Antennas Propagat.& URSI Symp.*, Montreal, Canada, July 1997.

13. Y.C. Lin, and K. Sarabandi, "Tree parameter estimation from interferometric radar responses," *Proc. IEEE Trans. Geosci. Remote Sensing Symp.*, Seattle, 1998.

14. T. Chiu and K. Sarabandi, "A coherent second-order scattering model for short vegetation," *Proc. IEEE Trans. Geosci. Remote Sensing Symp.*, Seattle, 1998.

15. C.B. Wilsen, K. Sarabandi, Y.C. Lin "The Effect of Tree Architecture on the Polarimetric and Interferometric Radar Responses," *Proc. IEEE Trans. Geosci. Remote Sensing Symp.*, Seattle, 1998.

16. Y. Kobayashi, K. Sarabandi, L. Pierce, M.C. Dobson, "Extracting Tree Heights using JPL TOPSAR DEM data," *Proc. IEEE Trans. Geosci. Remote Sensing Symp.*, Seattle, 1998.

17. Sarabandi, K., C.G. Brown, and L. Pierce, "Tree height estimation from the polarimetric and interferometric radar response," *Proc. IEEE Trans. Geosci. Remote Sensing Symp.*, Hamburg, Germany, 1999.

18. Wilsen, C.B., and K. Sarabandi, "Modeling of INSAR response to forest biomass variation," *Proc. IEEE Trans. Geosci. Remote Sensing Symp.*, Hamburg, Germany, 1999.

References

[1] F. T. Ulaby, K. Sarabandi, K. MacDonald, M. Whitt, and M. C. Dobson, " Michigan Microwave Canopy Scattering Model", *Int. J. Remote Sensing*, Vol. 11, No. 7, pp. 1223-1253, 1990.

[2] M. A. Karam, A. K. Fung, R. H. Lang, and N. H. Chauhan, " A microwave scattering model for layered vegetation," *IEEE Trans. Geosci. Remote Sensing.*, vol. 30, no. 4, pp. 767-784, July 1992.

[3] K. Sarabandi, *Electromagnetic Scattering from Vegetation Canopies*, Ph.D. Dissertation, University of Michigan, 1989.

[4] R. L. Jordan, B. L. Huneycutt, and M. Werner, "The SIR-C/X-SAR synthetic aperture radar system," *IEEE Trans. Geosci. Remote Sensing.*, vol. 33, pp. 829-839, July 1996.

[5] Zebker, H/A., S. N. Madsen, J. Martin, K. B. Wheeler, T. Miller, Y. Lou, G. Alberti, S. Vetrella, and A. Cucci, " The TOPSAR interferometric radar topographic mapping instrument," *IEEE Trans. Geosci. Remote Sensing.*, vol.30, No.5, pp.933-940, 1992.

[6] Rodriguez, E., and J.M. Martin, "Theory and design of interferometric synthetic aperture radars," *IEE Proceedings,* vol. F139, no. 2, pp. 147-159, 1992.

[7] Sarabandi,K., "Δk-Radar equivalent of Interferometric SARs: A Theoretical Study for determination of vegetation height," *IEEE Trans. Geosci. Remote Sensing.*, Vol. 35, No. 5, Sept. 1997.

[8] R. N. Treuhaft, M. Moghaddam, and J. J. van Zyl, "Inteferometric Remote Sensing of Vegetation and Surface Topography," Radio Science, vol. 31, pp. 1449-1485.

[9] Lin, Y.C., and K. Sarabandi, "Electromagnetic scattering model for a tree trunk above a tilted ground plane," *IEEE Trans. Geosci. Remote Sensing.*, vol. 33, no. 4, pp. 1063-1070, July 1995.

[10] Lin, Y.C., and K. Sarabandi, "A Monte Carlo Coherent Scattering Model For Forest Canopies Using Fractal Generated Trees," *IEEE Trans. Geosci. Remote Sensing.*, vol. 37, no. 1, pp. 440-451, Jan. 1999.

[11] Treuhaft, R.N., E. Rodriguez, M. Moghaddam, J.J. van Zyl, and K. Sarabandi, "Estimating vegetation and surface characteristics with multifrequency SAR interferometry," *URSI General Assembly*, Lille, France, August 1996 (invited).

[12] Sarabandi, K., and Y.C. Lin, "Simulation of Interferometric SAR Response for Characterization of Scattering Phase Center Statistics of Forest Canopies," *IEEE Trans. Geosci. Remote Sensing.*, accepted for publication.

[13] Chiu, T.C., and K. Sarabandi, "Electromagnetic scattering interaction between a dielectric cylinder and a slightly rough surface," *IEEE Trans. Antennas Propagat.*, submitted for publication (June 1997).

[14] Goldstein, R.M., H.A. Zebker, and C.L.Werner, "Satellite radar interferometry: Two-demensional phase unwrapping," *Radio Sci.*, vol.23, no.4, pp. 713-720, July-August 1988.

[15] Gens, R., and J.L. van Genderen, "Review article: SAR interferometry issues,techniques,applications," *Inter. J. of Remote Sensing,* vol. 17, no. 10,pp. 1803-1835, 1996.

[16] Zebker, H.A., C. L. Werner, P.A. Rosen, S. Hensley, "Accuracy of Topographic Maps Derived from ERS-1 Interferometric Radar," *IEEE Trans. Geosci. Remote Sensing.*, vol. 32,no.4, pp. 823-836, July 1994.

[17] Kirkpatrick, S., J.C.D. Gelatt, and M.P. Vecchi, "Optimization by simulated annealing," *Sci.,* vol. 220, pp. 671-680, 1983.

[18] Holland, J.H., "Genetic Algorithms," *Scientific American*, pp. 66-72, July 1992.

[19] DeJong, K.A.,"An Analysis of the behavior of a class of genetic adaptive systems," Ph.D. dissertation, The University of Michigan, Ann Arbor, 1975.

[20] Lin, Y.C., and K. Sarabandi, "'Retrieval of forest parameters using a fractal-based coherent scattering model and a genetic algorithm," *IEEE Trans. Geosci. Remote Sensing.*, accepted for publication .

Appendix I

Δk-Radar Equivalent of Interferometric SARs: A Theoretical Study for Determination of Vegetation Height

Δk-Radar Equivalent of Interferometric SARs: A Theoretical Study For Determination Of Vegetation Height

Kamal Sarabandi
Radiation Laboratory
Department of Electrical Engineering and Computer Science
The University of Michigan, Ann Arbor, MI 48109-2122
Tel :(313) 936-1575, Fax:(313) 747-2106
email: saraband@eecs.umich.edu

In this paper the theoretical aspects of estimating vegetation parameters from SAR interferometry is presented. In conventional applications of interferometric SAR (INSAR), the phase of the interferogram is used to retrieve the location of the scattering phase center of the target. Although the location of scattering phase center for point targets can be determined very accurately, for a distributed target such as a forest canopy this is not the case. For distributed targets the phase of the interferogram is a random variable which in general is a function of the system and target attributes. To relate the statistics of the interferogram phase to the target attributes, first an equivalence relationship between the two-antenna interferometer system and an equivalent Δk radar system is established. This equivalence relationship provides a general tool to related the frequency correlation function (FCF) of distributed targets, which can conveniently be obtained experimentally, analytically, or numerically, to the phase statistics of the interferogram. An analytical form for the p.d.f. of the interferogram phase is obtained in terms of two independent parameters: (1)ζ: mean phase and (2)α: degree of correlation. ζ is proportional to the scattering phase center and α is inversely proportional to the uncertainty with which ζ can be estimated. It is shown that α is directly related to the FCF of the distributed target which in turn is a function of scattering mechanisms and system parameters. It is also shown that for a uniform closed canopy the extinction and the physical height of the canopy top can be estimated very accurately. Some analytical and numerical simulations are demonstrated.

1 Introduction

Vegetation cover on the earth's surface is an important factor in the study of global changes. The total vegetation biomass is the most influential input to models for terrestrial ecosystems and atmospheric chemistry. Monitoring parameters such as

the total vegetation biomass, total leaf area index, and rate of deforestation is vital to keep our planet capable of supporting life. Microwave remote sensing techniques offer a unique opportunity to probe vegetation canopies at different depths. Since a forest stand is a very complicated random medium with many attributes that influence the forest radar response, accurate estimation of the forest physical parameters requires a large number of independent radar observations (multi-frequency and multi-polarization backscatter) in conjunction with some a priori information about the forest stand [1, 2, 3, 4]. The use of polarimetric synthetic aperture radars as active sensors to survey forested areas has reached a level of maturity. Despite considerable advancement in retrieving the canopy parameters from multi-polarization and multi-frequency backscatter data, an unsupervised reliable inversion algorithm has not yet been developed. With the recent advances in the development of interferometric SARs [5]-[10], another set of independent radar observation has become available for the estimation of vegetation biophysical parameters.

The interferometric technique relies on a coherent imaging process to find the range or distance to the scattering phase center of the scatterers in the radar image. Based on this principle, there are two standard approaches for extracting topographical information using synthetic aperture radars. In one approach, SAR systems equipped with two separate antennas mounted on the SAR platform are used to generate two complex co-registered images from two slightly different aspect angles. The phase difference calculated from the cross product of the two complex images, referred to as an interferogram [6], is processed to estimate the height information. In the second approach the interferogram is formed using two successive images taken by a single SAR with almost the same viewing geometry [7, 8]. It is shown that the phase of the interferogram is proportional to the wavelength, slant range, look angle, distance between the antennas (baseline distance), orientation of the antennas with respect to each other, and the height of the scattering phase center above a reference line [5, 9]. For non-vegetated terrain, the scattering phase centers are located at or slightly below the surface depending upon the wavelength of the SAR and the dielectric properties of the surface media. Whereas for vegetated terrain, these phase centers lie at or above the surface depending upon the wavelength of the SAR and the vegetation attributes. Although it is expected that for vegetated surfaces the temporal decorrelation would hamper repeat-pass interferometry from producing the location of scattering phase center, experimental investigations has shown that even after 18 days the correlation associated with forested area can be as high as 0.5 [11, 12].

The significant vegetation attributes are: (1) the type of vegetation, (2) the quantity or biomass of the vegetation and (3) the dielectric properties of the vegetation. As pertains to SAR interferometry, the type of vegetation refers to the structural attributes of vegetation elements and includes the shapes and sizes of foliage and woody stems relative to wavelength and their three-dimensional organizational structure. The biomass refers to attributes such as the height of the

vegetation, the thickness and density of the crown layer that contains foliage and stems, and the number of plants per unit area. The dielectric properties of the vegetation elements determine scattering and propagation through the media; these may vary with time due to seasonal changes in plant physiology and the phase of water (liquid or frozen) or due to the presence of water films resulting from intercepted precipitation or dew.

The main objective of this paper is to establish a thorough understanding of the relationship between the INSAR parameters and the vegetation attributes and the accuracy with which the vegetation scattering phase center can be measured. To accomplish these goals an equivalence between INSAR and Δk-radar techniques is established which facilitates numerical simulations and controlled experiments using scatterometers. Monte Carlo simulation of a forest canopy which preserves the absolute phase of the radar backscatter allows for quantifying the role of vegetation attributes in determining the location of the scattering phase centers as measured by SAR interferometry.

2 Δk-Radar Equivalent of an INSAR

In this section an equivalence relationship between an interferometric SAR and a Δk-radar is obtained. As will be shown later the statistics of the phase of the interferogram or equivalently the location of the scattering phase center and its statistics is a very strong function of the location and number density of the forest constituent particles and their dielectric and scattering properties. Understanding the relationship between the tree height and the corresponding location of the scattering phase centers requires numerical simulations (Monte Carlo simulation of a fractal generated forest stand) or controlled experiments using scatterometers. The scattering phase center of a target can also be obtained using a Δk-radar assuming that the incidence angle is known. Evaluation of the scattering phase centers using frequency shift can easily be accomplished in a numerical simulation or in a controlled experiment using a wideband scatterometer.

To demonstrate the equivalence between an INSAR and a Δk-radar consider a two-antenna interferometer as shown in Fig. 1. In this scheme one of the antennas is used as the transmitter and receiver and the other one is used only as the receiver, the phase of the interferogram (ϕ) is related to the difference in path lengths from the antennas to the scattering phase center (δ) by

$$\delta = \frac{\lambda_0}{2\pi}\phi \tag{1}$$

where $\lambda_0 = c/f_0$ is the wavelength (in repeat-pass interferometry the 2π factor in (1) must be replaced by 4π). Having calculated δ from (1) and knowing the baseline

distance B and baseline angle α, the look angle θ can be computed from

$$\sin(\theta - \alpha) \approx \frac{-\delta}{B} \tag{2}$$

Referring to Fig. 1 it can easily be shown that the height of the scattering phase center, with respect to an arbitrary reference level, is given by

$$h = H - r[\cos(\alpha)\cos(\theta - \alpha) - \sin(\alpha)\sin(\theta - \alpha)]. \tag{3}$$

The accuracy in height estimation using this method is directly proportional to the accuracy in the measurement of the interferogram phase. The uncertainty in phase measurements is caused by two factors: (1) systematic errors, and (2) indeterministic errors. The sources of systematic errors are image misregisteration and lack of maintaining the geometry of the interferometer. The source of indeterministic error is fading. Basically the backscatter signal from a distributed target including many scatterers decorrelates as the incidence angle changes.

Now let us consider a radar capable of measuring the backscatter at two slightly different frequencies $f_1 = f_0$ and $f_2 = f_0 + \Delta f$. Denoting the phase difference between the two backscatter measurements by ϕ, it can be shown that

$$\phi = 2\Delta k r = 4\pi \Delta f \; r/c \tag{4}$$

where c is the speed of light and r is the radar distance to the target scattering phase center. Comparing (4) with (1) and (2) the desired relationship between the Δk-radar and INSAR can be obtained. Basically by requiring the backscatter phase differences, once obtained from a small change in the aspect angle and the other one obtained from a small change in the frequency of operation, be identical for both approaches we have

$$\Delta f = f_0 \frac{B}{2r} \sin(\theta - \alpha) \tag{5}$$

Noting that $r = H/\cos(\theta)$, it can easily be shown that Δf is rather insensitive to variations in incidence angle over the angular range $30° - 60°$. For example, a C-band (5.3 GHz) interferometer with a horizontal baseline distance 2.4 m at an altitude 6 Km is equivalent to a C-band Δk-radar with $\Delta f = 530$KHz.

The equivalence relation given by (5) is derived based on a single target. In regard to this relationship there are two subtle issues that require clarification. In almost all practical situations the scatterers are located above a ground plane which give rise to three significant scattering terms besides the direct backscatter. These include the bistatic scattering from the target reflected from the ground plane, the bistatic scattering from the target when illuminated by the reflected wave, and the backscatter reflected by the ground plane when the target is illuminated by the reflected wave. The last term can be regarded as the direct backscatter of the incident wave from the image target and therefore the equivalent Δk-radar can

accurately predict the interferometric phase associated with this term. However, for the other two scattering terms (single-bounce terms), the validity of the equivalence relationship is not obvious. Suppose a two-antenna interferometer, as shown in Fig. 2, is illuminating a target at point C above the ground plane. For the equivalent Δk-radar located at A_1, the interferometric phases of the two single-bounce terms (ϕ_b) are identical and are given by:

$$\phi_b = \Delta k(A_1B_1 + B_1C + CA_1) = 2\Delta k A_1O \quad . \tag{6}$$

Equation (6) indicates that the location of the scattering phase center for the ground-bounce terms appears at the ground interface for the Δk-radar. The interferometric phase of the two single-bounce terms for the two-antenna system can be obtained from:

$$\phi_b' = \angle 2e^{ik(A_1C+CB_1+B_1A_1)} - \angle\left(e^{ik(A_1C+CB_2+B_2A_2)} + e^{ik(A_1B_1+B_1C+CA_2)}\right)$$

Noting that $B_1C = B_1C'$, $B_2C = B_2C'$, and after some simple algebraic manipulation, it can be shown that

$$\phi_b' = \frac{k}{2}[(A_1C + A_1C') - (A_2C + A_2C')].$$

Referring to Fig.2, it can easily be shown that $C'C'' = 2OO'$ and therefore $A_2C + A_2C' = 2A2O$. Similarly, it can be shown that $(A_1C + A_1C') = 2A_1O$, thus

$$\phi_b' = k(A_1O - A_2O).$$

which indicates that the location of scattering phase center for the two single-bounce terms is at O. Therefore the equivalence relation (5) guarantees that $\phi_b = \phi_b'$.

The second issue pertains to the validity of the equivalence relation in regard to multiple scattering terms. As mentioned earlier the equivalence relationship is derived based on a single target and therefore it would be valid for a random medium, if the overall backscatter is dominated by the first-order scattering mechanisms. To demonstrate that the equivalent Δk-radar provides the location of the scattering phase center accurately even in the presence of multiple scattering, consider two scatterers located at two arbitrary points C and D within a resolution cell. For an INSAR whose antennas are at points A_1 and A_2, the interferometric phase associated with the second order scattering terms is calculated from:

$$\phi_{INSAR}^{(2)} = \angle 2e^{ik(A_1C+CD+DA_1)} - \angle(e^{ik(A_1C+CD+DA_2)} + e^{ik(A_1D+CD+CA_2)})$$

In derivation of the above equation, the reciprocity theorem is used which indicates that the second-order scattering amplitude obtained from the interaction between particle C and particle D is equal to that obtained from the interaction between particle C and particle D. As before it can easily be shown that

$$\phi_{INSAR}^{(2)} = \frac{k}{2}[(A_1C + A_1D) - (A_2C + A_2D)]$$

Let us define M as point in the middle of CD line. Since the distance between the antennas and the scatterers are much larger than the distance between the scatterers, we have

$$\phi^{(2)}_{INSAR} = k(A_1M - A_2M)$$

which indicates that the phase center of the second order term apperas at the mid-point between the two scatterers. For a Δk-radar at A_1 the same second order phase term is given by:

$$\phi^{(2)}_{\Delta k} = \Delta k(A_1C + CD + DA_1)$$

Noting that $A_1C + A_1D \approx A_1M$ and $CD \ll A_1M$, the above expression reduces to

$$\phi^{(2)}_{\Delta k} = 2\Delta k \; A_1M \tag{7}$$

Equation (7) shows that the location of scattering phase center measured by a Δ-k radar is at M as well.

What remains to be shown is the algorithm by which the target height can be extracted from an equivalent Δk-radar. Let us consider a random collection of scatterers within a range and azimuth resolution cell illuminated by a plane wave as shown in Fig. 3. The height of the scattering phase center for this collection can be considered to be the algebraic sum of the physical height of the pixel center and a residual apparent height of the scatterers which is a complex function of particles and radar attributes. Suppose there are M scatterers within a resolution cell. Let s_n denote the scattering amplitude of the nth scattering component of the ensemble which can represent the direct backscattering from a particle, a multiple scattering term between a number of the scatterers in the ensemble, or a bistatic scattering term reflected from the ground plane. Without loss of generality let us assume that the phase reference is on the reference plane just below the pixel center (see Fig. 3). The total backscattered field is the coherent sum of all the scattering components which can be obtained from:

$$E^s = \frac{e^{ik_0r}}{r} \sum_{n=1}^{N} s_n e^{-i2k_0r_n} \tag{8}$$

where r is the distance from the origin to the observation point, r_n is the total round trip path length difference between a ray traveled to the origin and the ray corresponding to the nth scattering component. Note that a time convention of $e^{-i\omega t}$ has been assumed and suppressed. The equivalent problem is to replace the collection of the random particles and the underlying ground plane with an equivalent scatterer placed at the scattering phase center whose backscattering amplitude is denoted by $S_e = |S_e| \exp(i\Phi_e)$. In this case the backscattered field is given by

$$E^s = \frac{e^{ik_0r}}{r} S_e e^{-2ik_0h\cos(\theta)}$$

Computing the phase of the backscattered field (Φ^s) from (8) and noting that the phase calculation is modulo 2π, the height of the scattering phase center can be obtained from

$$-2k_0 h\cos(\theta) + \Phi_e = 2m\pi + \Phi^s \tag{9}$$

However, in computation of h from (9) two important parameters, namely m and Φ_e are missing. This problem could be rectified, if a radar measurement from the same collection of particles and the same viewing angle but at a slightly different frequency were available. Suppose the change in frequency is small enough so that the change in the phase of the scattering amplitudes is negligible. In this case the change in the phase of the scattered field ($\phi = \Phi_2^s - \Phi_1^s$) due to the change in the wavenumber ($\Delta k = k_2 - k_1$) is basically dominated by the path length differences and it can easily be shown that

$$h = \frac{-1}{2\cos(\theta)} \quad \frac{\phi}{\Delta k} \tag{10}$$

Equation (10) is the fundamental basis for extraction of height information from a two-frequency radar. It should be emphasized that in this process the incidence angle must be known which is the case in a numerical simulation or in a measurement using a narrow beam scatterometer system. Since the shift in frequency is very small (less than 0.1% of center frequency), the scattering amplitude terms s_n do not change when the frequency is changed from f_1 to f_2 and therefore they need not be computed twice in a numerical simulation. However, the phase terms associated with the path length differences must be modified by replacing k_0 with $k_0 + \Delta k$.

Expressing the measured phase in degrees, the difference in slant range ($\Delta r = h\cos(\theta)$) in meters, and the difference in frequency (Δf) in MHz, (8) can be rewritten as

$$\phi = 2.4\Delta r \Delta f \quad . \tag{11}$$

Therefore if the uncertainty in the phase calculation/measurement is 1° and a distance resolution of 1m is required, a minimum frequency shift of 416.66 KHz is needed assuming that the uncertainty in phase calculation/measurement is independent of frequency shift (a wrong assumption). Using this frequency shift the unambiguous range of 360m can be achieved noting that the phase is measured modulo 360°. The uncertainties in height estimation using a Δk-radar can easily be obtained as the relationship between h and θ is explicitly expressed by (10). It can easily be shown that the uncertainty in height due to the lack of accuracy in the knowledge of the incidence angle is given by:

$$\delta h = h\tan(\theta)\delta\theta$$

For uncertainties in incidence angle as high as 3°, the error in height is 5% of h at $\theta = 45°$.

Through the combination of two or more frequency shifts, an unambiguous height profile with fine resolution can be achieved. The resolution in height estimation using Δk-radar is characterized by the frequency correlation function of the target as will be discussed next. Equation (10) indicates that accuracy in the height measurement increases as the frequency shift increases. On the other hand as the frequency shift (baseline distance) increases the phase shift caused by the path length differences will change in a nonlinear and random fashion which causes an uncertainty in the measurement of distance (height). Hence there may exist a critical frequency shift for which the finest height resolution for a given distributed target can be achieved. This critical frequency shift is the counterpart of a critical baseline distance in an interferometer for which the finest height resolution for the same distributed target is achievable.

3 Statistical Analysis

In estimating the height of the scattering phase center of a distributed target using (11), random fluctuations of the calculated/measured phase as a function of frequency due to fading must be considered. In this section the effect of random position of the scatterers on the height estimation is studied. Also a procedure for calculation of the critical frequency shift (baseline distance) in terms the statistical properties of the distributed target is outlined. Phase statistics of polarimetric backscatter response of distributed targets for single- and multi-look can be found in literature [14, 15, 16]. The statistical analysis of interferometric phase given here parallels the method given in [14]. For a random collection of particles the scattered field given by (8) is a complex random variable. Since the location of the scatterers in the illuminated volume is random, the process describing the scattered field is a Wiener process [13]. If the number of scattering components M is large, the central limit theorem mandates that the process is Gaussian. Let us denote the scattered field at f_1 and f_2 by $E_1^s = X_1 + iX_2$ and $E_2^s = X_3 + iX_4$, respectively, where X_j denotes the real or imaginary part of the scattered fields. These quantities are jointly Gaussian and can be represented by a four-component random vector $\boldsymbol{X}$. The joint probability density function (pdf) of the random vector can be fully characterized from a 4×4 symmetric positive definite matrix known as the covariance matrix Λ whose entries are given by

$$\lambda_{ij} = \lambda_{ji} =< X_i X_j > \qquad i,j \in \{1,\cdots,4\} \quad .$$

It has been shown that the entries of the covariance matrix for the Wiener process satisfy the following conditions [14]:

$$\lambda_{11} = \lambda_{22} =< X_1^2 >=< X_2^2 > \quad , \tag{12}$$

$$\lambda_{12} =< X_1 X_2 >= 0 \quad , \tag{13}$$

$$\lambda_{33} = \lambda_{44} =< X_3^2 >=< X_4^2 > \quad , \tag{14}$$

$$\lambda_{34} =< X_3 X_4 >= 0 \quad , \tag{15}$$

$$\lambda_{13} = \lambda_{24} =< X_1 X_3 >=< X_2 X_4 > \quad , \tag{16}$$

$$\lambda_{14} = -\lambda_{23} =< X_1 X_4 >= - < X_2 X_3 > \quad . \tag{17}$$

In the same paper [14] it is also shown that the pdf for the difference between phases of E_2^s and E_1^s (for a single-look case) is related to the elements of the covariance matrix and is given by:

$$f_\Phi(\phi) = \frac{1-\alpha^2}{2\pi\left[1-\alpha^2\cos^2(\phi-\zeta)\right]} \cdot \left\{1 + \frac{\alpha\cos(\phi-\zeta)}{\sqrt{1-\alpha^2\cos^2(\phi-\zeta)}}\left[\frac{\pi}{2} + \tan^{-1}\frac{\alpha\cos(\phi-\zeta)}{\sqrt{1-\alpha^2\cos^2(\phi-\zeta)}}\right]\right\} \quad , \tag{18}$$

where

$$\alpha = \sqrt{\frac{\lambda_{13}^2 + \lambda_{14}^2}{\lambda_{11}\lambda_{33}}} \quad , \qquad \zeta = \tan^{-1}\frac{\lambda_{14}}{\lambda_{13}} \quad .$$

The parameter α is known as the degree of correlation and can vary from 0 to 1. When the scattered fields are completely correlated $\alpha = 1$ and the pdf of ϕ is a delta function. In this case the calculation of the height from (10) has no error in principle when the effect of thermal noise is ignored. The parameter ζ is known as the coherent phase difference and can vary from $-\pi$ to π. For $\phi = \zeta$ the pdf assumes its maximum and this point corresponds to the average height of the scattering phase center for a uniform distributed target over a flat ground plane.

In this analysis the objective is to establish a relationship between a desired height resolution and the corresponding required frequency shift for a given error probability criterion. The Wiener processes considered in this problem satisfy one more condition beyond those given by (12)-(17). This condition can be derived by noting that the required frequency shift for the height estimation is much smaller than the operating center frequency of the radar, therefore it is expected that backscattered power carried by the two processes be equal. This requirement renders the following condition:

$$\lambda_{11} = \lambda_{33} \quad . \tag{19}$$

Let us define the normalized correlation function of the process by

$$R(\Delta f) = \frac{|< E_1 E_2^* >|}{< |E_1|^2 >} \tag{20}$$

which is also known as the frequency correlation function [17]. Using (16), (17), and (19), it can easily be shown that

$$R(\Delta f) = \alpha \quad . \tag{21}$$

It is interesting to note that the maximum of the normalized frequency correlation function occurs at $\Delta f = 0$ ($\frac{\delta R}{\delta \Delta F}|_{\Delta f=0} = 0$), hence $\alpha = 1$ to the first order in Δf. In other words for small variation of frequency the pdf of the phase difference is very narrow which ensures accurate estimation of the height. As expected, when Δf increases, $\alpha = R(\Delta f)$ approaches zero which corresponds to a uniform distribution for the phase difference. In this case the probability of error in the height estimation is close to unity.

To quantify the accuracy of the height estimation for a given distributed target, let us assume that the normalized frequency correlation function of the target is known. In this case only the coherent phase difference (ζ) is missing to fully characterize the pdf of the phase difference. The objective is to estimate ζ from which the mean height can be obtained from

$$\bar{h} = \frac{-\zeta}{2.4\Delta f \cos(\theta)} \quad . \tag{22}$$

However, the difficulty in calculation of $\bar{h}$ is that only one measurement of the phase for each pixel is available. Suppose $\delta\phi = \phi - \zeta$ represents the deviation in the phase measurement which corresponds to an error in height measurement given by

$$\delta h = \frac{\delta\phi}{2.4\Delta f \cos\theta} \tag{23}$$

where δh is in meters, $\delta\phi$ is in degrees, and Δf is in MHz. The uncertainty in the estimation of height can be quantified according to a prescribed error probability criterion. For example, $\delta\phi$ can be chosen such that the probability of measuring the phase within the $\delta\phi$ neighborhood of the coherent phase difference to be 90%, that is

$$P(\phi \in [\zeta - \delta\phi, \zeta + \delta\phi]) = 0.9 \quad .$$

Hence, using this criterion the estimate of the height is

$$\tilde{h} = \bar{h} \pm \delta h$$

with a probability of 0.9.

The uncertainty in the height measurement defined by this criterion is a complex function of Δf noting that $\delta\phi$ is a function of α which is related to Δf through the correlation function. Referring to (23), it seems that the height uncertainty decreases when Δf is increased; however, it should also be noted that $\delta\phi$ increases when Δf is increased. This behavior suggests that there may exist a frequency shift Δf for which δh is minimized. This particular frequency shift will be referred to as the critical frequency shift. In order to investigate the possibility of finding the critical frequency shift, the relationship between the height uncertainty and the frequency shift must be obtained. The relationship between $\delta\phi$ and α can be directly obtained from the cumulative distribution function (cdf) of $\Delta\phi = \phi - \zeta$.

Unfortunately, a close form for the cdf of $\Delta\phi$ does not exist and the relationship between $\delta\phi$ and α must be obtained numerically. Figure 4 shows the cdf of $\Delta\phi$ for different values of α and the corresponding $\delta\phi$ for the 90% probability criterion. Note that for most practical cases $\alpha > 0.95$ (baseline distance or equivalently the frequency shift is rather small). The relationship between $\delta\phi$ and α is shown in Fig. 5 for the 80% and 90% probability criteria.

Assuming a Gaussian form for the normalized frequency correlation function the uncertainty in height estimation can easily be related to the frequency shift. Suppose the normalized frequency decorrelation function is given by

$$R(\Delta f) = e^{-(\Delta f/F_d)^2}$$

where F_d is the decorrelation bandwidth defined as the frequency shift for which $R(\Delta f) = e^{-1}$. Using (21) the frequency shift can be related to the degree of correlation through

$$\frac{\Delta f}{F_d} = \sqrt{-\ln(\alpha)} \quad .$$

For values of α close to unity the right-hand side of the above equation is approximately equal to $\sqrt{1-\alpha}$. Referring to Fig. 5, it can also be observed that

$$\delta\phi \approx C\sqrt{1-\alpha}$$

where C is a constant proportional to the probability criterion. Therefore $\delta\phi$is linearly proportional to Δf where upon substituting in (23) it can be shown that the height uncertainty is independent of the frequency shift and the critical frequency shift is not well defined. This result may be generalized to all frequency correlation functions because for small values frequency shift, the frequency correlation function of all targets can be approximated by

$$R(\Delta f) \approx 1 - (\Delta f/F_d)^2 \tag{24}$$

where F_d is a free parameter equal to the frequency decorrelation bandwidth of an equivalent Gaussian correlation function. Figure 6 shows the product of the height uncertainty and the equivalent decorrelation bandwidth versus frequency shift normalized to the decorrelation bandwidth for both the 80% and 90% criteria. Thus the uncertainty in height measurement for a distributed target with known equivalent decorrelation bandwidth is independent of frequency shift or equivalently the baseline distance. In other words, the frequency decorrelation bandwidth of the target is the determining factor in the height measurement error.

4 Frequency Correlation Function of Distributed Targets

As was shown in the previous section the frequency correlation function of a distributed target is the most important parameter in estimating its scattering phase

center height. The literature concerning the frequency correlation function of distributed targets is rather scarce. Analytical expressions for the frequency correlation function of simple targets such as uniform independent scatterers and rough surfaces using Kirchhoff approximation have been obtained for simple uniform plane wave illuminations [18, 19]. For the uniform distribution of scatterers illuminated by a uniform plane wave the frequency correlation function is given by

$$R(\Delta f) = \frac{\sin(\pi \rho_r \Delta f/150)}{\pi \rho_r \Delta f/150}$$

where ρ_r is the slant range in meters and Δf is in MHz. The corresponding Gaussian equivalent decorrelation bandwidth for this function is $F_d = 117/\rho_r$ MHz. Since product of δh and F_d is independent of $\Delta f/F_d$, the uncertainty in height measurement can be improved by decreasing the slant range resolution.

In a recent study [17] it was shown that the frequency correlation function, in general, depends on two sets of parameters: (1) radar parameters such as incidence angle, frequency, polarization, and footprint size, and (2) target parameters such as penetration depth and albedo. It is also shown that when the scattering is localized, that is, the field correlation distance in the random media is relatively small, the frequency correlation function can be expressed in terms of product of two expressions, one depending only on the radar parameters and the second one depending only on the target attributes. For example an expression for the frequency cross correlation of backscatter from a homogeneous layer of random particles such as leaves and stems above a smooth ground plane is found to be [17]

$$\begin{aligned} < E_{pp}(f_2) E^*_{pp}(f_2) > = & \left[\int\int \frac{e^{2i\Delta k r(x,y)}}{r^4(x,y)} |G(x,y)|^2 dxdy\right] \cdot \Big\{ 4d|R_p|^2 W^s_{pppp} e^{2(i\Delta k \cos\theta - \kappa \sec\theta)d} \\ & + W^b_{pppp}(1 + |R_p|^4 e^{2(i\Delta k \cos\theta - \kappa \sec\theta)d}) \frac{1 - e^{2(i\Delta k \cos\theta - \kappa \sec\theta)d}}{2(\kappa \sec\theta - i\Delta k \cos\theta)} \Big\} \end{aligned} \tag{25}$$

where θ is the incident angle, d is the layer thickness, and R_p is the Fresnel reflection coefficient for p-polarized incident wave ($p \in v, h$). The first term in (25) is the system dependent component in which G is the antenna gain or the SAR point-target response (ambiguity function), r is the radar distance, and the limits of the integrals represents the antenna footprint or the pixel area. The curly bracket in equation (25) represents the target dependent component in which κ denotes the layer extinction and W^b_{pppp} and W^s_{pppp} are the copolarized components of the phase matrix in the backscatter and specular (with respect to the vertical axis) directions which are defined by

$$W^{b,s}_{pppp} = \lim_{\Delta V \to 0} \frac{< (\Delta S^{b,s}_{pp})(\Delta S^{b,s}_{pp})^* >}{\Delta V}, \qquad p \in v, h$$

where ΔS_{pp} represents a scattering matrix element of a small volume ΔV of the random medium. In the expression given by (25) the reference phase plane is assumed

to be at the top of the layer, i.e., the ground plane is assumed to be at $z = -d$ as shown in Fig. 7.

The decorrelation caused by the system dependent component for an imaging radar is directly proportional to the system slant range resolution. Also for conventional radars the decorrelation caused by the system component is inversely proportional to antenna beamwidth and directly proportional to range and incidence angle. In most existing INSAR systems the measured decorrelation is dominated by the system component. As discussed before the uncertainty in height estimation increases as the correlation bandwidth increases. Fortunately the decorrelation caused by the system parameters can be calibrated out since its effect appears as a simple multiplicative factor. If the system ambiguity function or the antenna pattern is known, the system component of frequency correlation function can easily be computed and removed from the measured data. In cases where the ambiguity function or the antenna pattern is not well characterized the correlation over a rough surface (a distributed target with no vertical extent) approximately represents the system component of the decorrelation and can be used for calibration. Once the target dependent component of the correlation function is obtained, the equivalent frequency decorrelation bandwidth can be computed from which the uncertainty in height estimation can be evaluated. As shown in the simple model described by (25) the target decorrelation contains information about its physical parameters.

Figure 8 shows the frequency correlation function of a uniform random layer of flat leaves with average area $50cm^2$, thickness 1.3 mm, and dielectric constant $\epsilon_l = 19 + i6.3$ above a ground plane with dielectric constant $\epsilon_g = 15 + j2.0$ at 5.3 GHz and incidence angle $\theta = 30°$. In this simulation the layer thickness was chosen to be $d = 2$ m and leaf number density N_0 was varied as a parameter. It is shown that as the leaf number density, and as a direct result the extinction, increases the frequency decorrelation bandwidth increases. Scattering contributions from the ground bounce mechanisms are manifested in terms of oscillations on the frequency correlation function due to constructive and destructive interferences among the different scattering mechanisms. Existence of contribution from ground bounce scattering mechanisms significantly reduce the frequency decorrelation bandwidth. For interferometric SARs the equivalent frequency shift is rather small (< 1 MHz) and the approximate form of the frequency correlation function given by (24) seems to be adequate for all cases. Figure 9 shows F_d of the layer as a function of depth for different values of particle number density. As the vegetation depth decreases F_d should approach infinity and when the vegetation depth increases F_d reaches its asymptotic value for the corresponding to a semi-infinite medium.

The theoretical expression for the frequency cross correlation function given by (25) can be used to calculate the height of the scattering phase center above the ground plane. Substituting the phase of the target dependent term of (25) in (22), the mean height of the scattering phase center of the medium can be computed. Figures 10a and 10b show the height of the scattering phase center of the uniform

medium as a function of layer thickness and extinction for 30° and 60° incidence angles respectively. It is shown that depending on the layer thickness, extinction, and incidence angle the scattering phase center may appear below or above the ground plane, but always below the canopy top. Note that when the double-bounce scattering mechanism (ground-target-ground) is dominant, the scattering phase center appears below the ground plane. Other numerical simulations showed that particle orientation distribution can significantly influence the location of the scattering phase center as well. This is due to the fact that the relative contribution of the direct backscatter mechanism with respect to that of the double-bounce scattering mechanism is a function of particle orientation distribution.

To illustrate the ability of INSAR in retrieving vegetation parameters, let us consider a simple case of semi-infinite uniform medium. Vegetation canopy can be regarded as a semi-infinite medium, when canopy transmissivity is below 0.1. In this case an analytical expression for frequency correlation function and the phase of the frequency cross correlation (mean phase) can be obtained directly from (25) by setting $\kappa \sec(\theta) = \infty$. The expression for the frequency correlation function and the mean phase are, respectively, given by

$$R(\Delta f) = \frac{1}{\sqrt{1 + (\frac{2\pi\Delta f}{c\kappa})^2}} \approx 1 - (\frac{\pi\Delta f \cos^2\theta}{2c\kappa})^2, \tag{26}$$

$$\zeta = \tan^{-1}\frac{\Delta k \cos^2\theta}{\kappa} \approx \frac{\Delta k \cos^2\theta}{\kappa}. \tag{27}$$

Using (26) the extinction coefficient of a thick vegetation layer can be obtained as follows. For a system with a known baseline distance the equivalent Δf can be calculated from (5) which together with the measured decorrelation can be substituted in (26) to calculate κ. Having found κ, (27) can be substituted in (22) to calculate the location of the scattering phase center from the canopy top Δd which is given by

$$\Delta d = \frac{\cos\theta}{2\kappa}. \tag{28}$$

It should be noted that for forest stands where particle size orientation and distribution are highly non-uniform the simple uniform and homogeneous model described above may not provide satisfactory results. More accurate models that preserve the effect of tree structure are needed for this purpose. A coherent scattering model based on Monte Carlo simulation of fractal generated trees is under development which allows efficient and accurate computation of frequency cross correlation statistics.

5 Conclusions

In this paper theoretical and statistical relationships between the measured parameters obtained from an interferometric SAR, namely the phase and correlation

coefficient of interferogram, and target parameters are obtained. First an equivalent relationship between an INSAR and a Δk radar is established. It is shown that the knowledge of the frequency correlation behavior of radar backscatter is sufficient to derive the desired statistics of height estimation using an interferometric SAR. The equivalence relationship allows for conducting controlled experiments, using a scatterometer, to characterize the response of a distributed target when imaged by an INSAR. Similarly efficient numerical codes can be developed to simulate the results. Statistical analysis shows that the uncertainty in the height estimation of a distributed target is a function of equivalent frequency decorrelation bandwidth and is independent of the baseline distance. It was also shown that how the INSAR measured parameters can be used to evaluate the extinction, the physical height, and the height of the scattering phase center of a closed and uniform semi-infinite canopy.

References

[1] K., Sarabandi, "Electromagnetic Scattering From Vegetation Canopies," Ph.D. Thesis, The University of Michigan, 1989.

[2] F.T. Ulaby, K. Sarabandi, K. McDonald, M. Whitt, M.C. Dobson, "Michigan Microwave Canopy Scattering Model", *Int. J. Remote Sensing*, vol. 11,no. 7, 1223-1253, July 1990.

[3] M.C. Dobson, F.T. Ulaby, L.E. Pirece, T.L. Sharik, K.M. Bergen, J. Kellndorfer, J.R. Kendra, E. Li, Y.C. Lin, A. Nashashibi, K. Sarabandi, and P. Siqueira, "Estimation of Forest Biomass," *IEEE Trans. Geosci. Remote Sensing.*, vol. 33, no. 4, pp. 887-895, July 1995.

[4] K.J. Ranson, S. Saatchi, and G. Sun, "Boreal forest ecosystem characterization with SIR-C/X SAR," *IEEE Trans. Geosci. Remote Sensing.*, vol. 33, no. 4, pp. 867-876, July 1995.

[5] H.A. Zebker, S.N. Madsen, J. Martin, K.B. Wheeler, T. Miller, Y. Lou, G. Alberti, S. Vetrella, and A. Cucci, "The TOPSAR interferometric radar topographic mapping instrument," *IEEE Trans. Geosci. Remote Sensing,* vol. 30, no. 5, pp. 933-940, 1992.

[6] F.K. Li, and R.M. Goldstein, "Study of multibaseline spaceborne interferometric synthetic aperture radars," *IEEE Trans. Geosci. Remote Sensing,* vol. 28, no. 1, pp. 88-97, Jan. 1990.

[7] A.L. Gray and P.J. Farris-Manning, "Repeat-pass interferometry with airborne synthetic aperture radar,"*IEEE Trans. Geosci. Remote Sensing,* vol. 31, no. 1, pp. 180-191, Jan. 1993.

[8] A.K. Gabriel and R.M. Goldstein, "Crossed orbit interferometry: Theory and experimental results from SIR-B," *Int. J. Remote Sensing,* vol. 9, no. 5, pp. 857-872, 1988.

[9] S.N. Madsen, H.A. Zebker, and J. Martin, "Topographic mapping using radar interferometry: Processing techniques," *IEEE Trans. Geosci. Remote Sensing,* vol. 31, no. 1, pp. 246-256, Jan. 1993.

[10] E. Rodriguez and J.M. Martin, "Theory and design of interferometric synthetic aperture radars," *IEE Proceedings*, vol. F139, no. 2, pp.147-159, 1992.

[11] H.A. Zebker and J. Villasenor, "Decorrelation in Interferometric Radar Echoes," *IEEE Trans. Geosci. Remote Sensing,* vol. 30, no. 5, pp. 950-959, Sept. 1992.

[12] J.O. Hagberg, L.M.H. Ulander, and J. Askne, "Repeat-pass SAR interferometry over forested terrain," *IEEE Trans. Geosci. Remote Sensing,* vol. 33, no. 2, pp. 331-340, March 1995.

[13] W.B. Davenport, *Probability and random processes*, New York: McGraw-Hill, 1970.

[14] K. Sarabandi, "Derivation of phase statistics of distributed targets from the Mueller matrix," *Radio Sci.,* vol. 27, no. 5, pp 553-560, 1992.

[15] I.R. Joughin, D.P. Winebrenner, and D.B. Percival, "Probability density functions for multilook polarization signatures," *Trans. Geosci. Remote Sensing,* vol. 32, no. 3, pp. 562-574, May 1994.

[16] J. Lee, K.W. Hoppel, S.A. Mango, A.R. Miller, "Intensity and phase statistics of multilook polarimetric and interferometric SAR imagery," *Trans. Geosci. Remote Sensing,* vol. 32, no. 5, pp. 1017-1028, Sept. 1994.

[17] K. Sarabandi and A. Nashashibi, "Analysis and applications of backscattered frequency correlation function," *IEEE Trans. Geosci. Remote Sensing,* to be submitted for pulication.

[18] W.P. Brikemeier and N.D. Wallace, "Radar tracking accuracy improvement by means of pulse to pulse frequency modulation," *IEEE Trans. Commu. Electron.*, no. 1, pp. 571-575, Jan. 1963.

[19] A.A. Monakov, J. Vivekanandan, A.S. Stjernman, and A.K. Nystrom, " Spatial and frequency averaging techniques for a polarimetric scatterometer system," *Trans. Geosci. Remote Sensing,* vol. 32, no. 1, pp. 187-196, Jan. 1994.

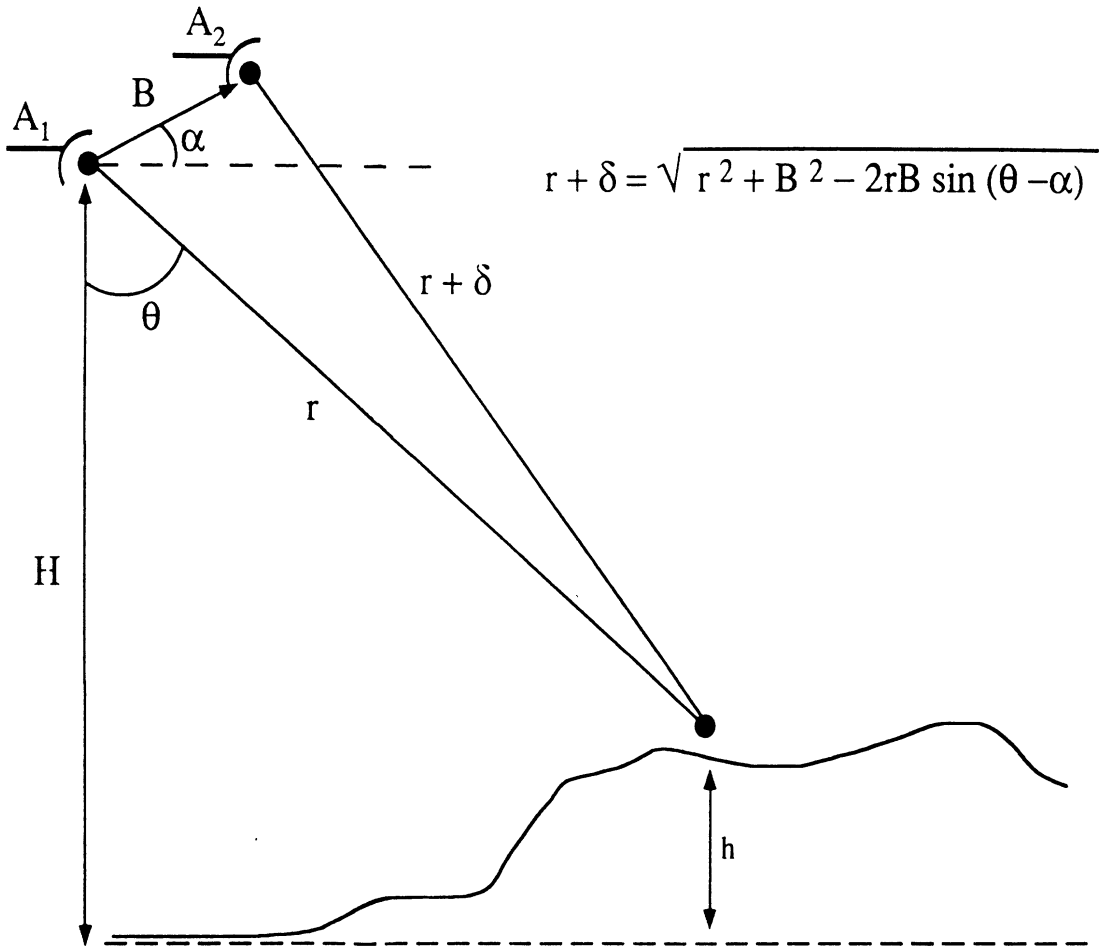

Figure 1: Geometry of a two-antenna interferometer.

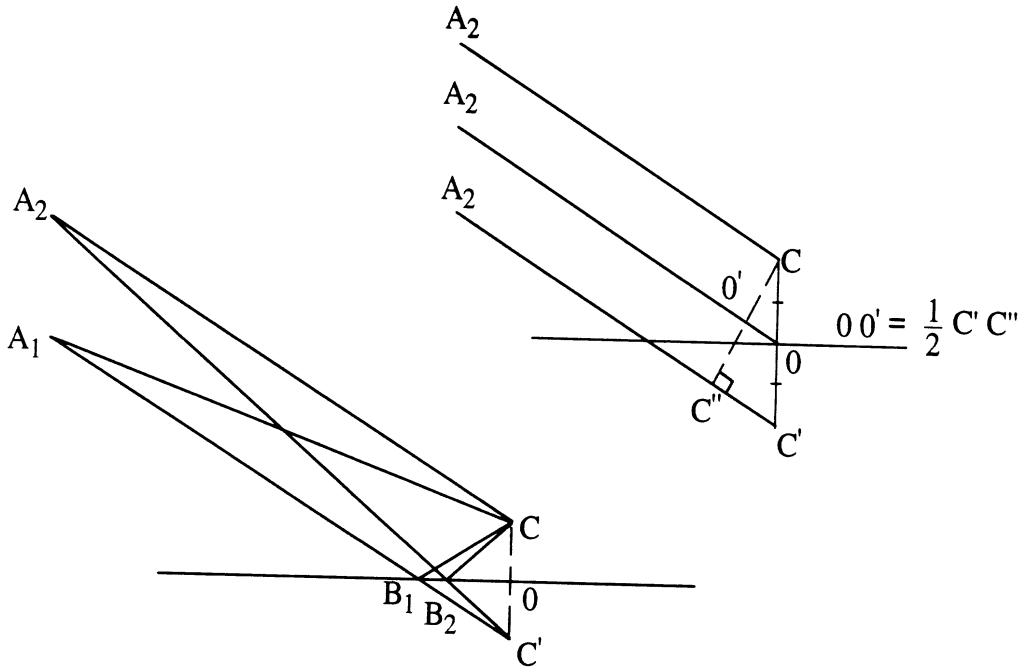

Figure 2: Ray path configuration of the single-bounce ground-target scattering mechanism for a two-antenna interferometer.

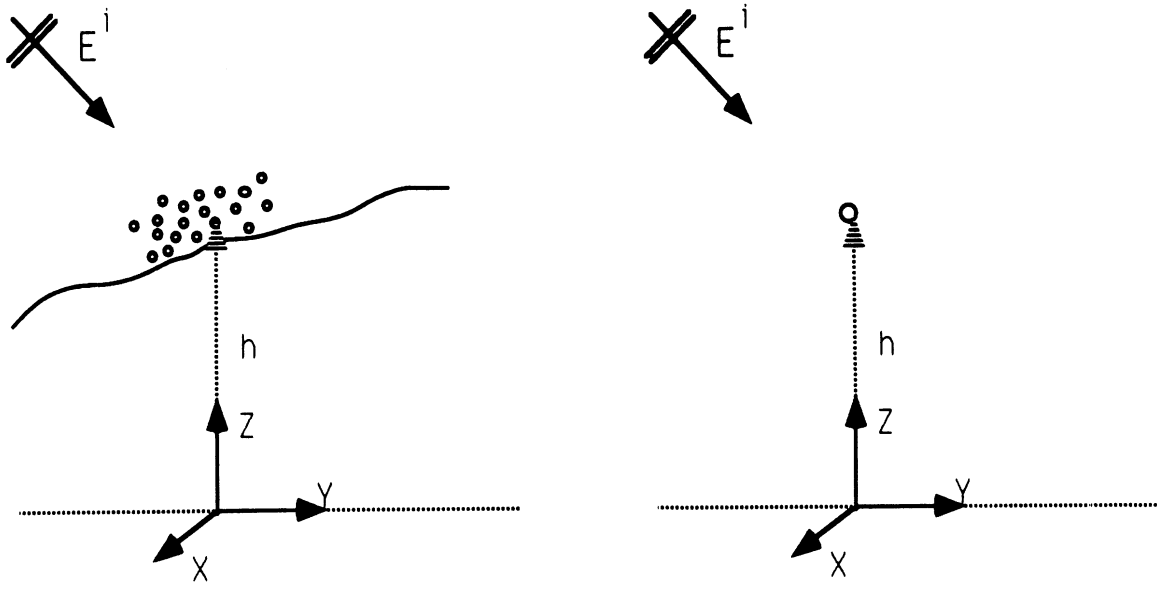

Figure 3: A random collection of M scatterers above a ground plane and its equivalent scatterer.

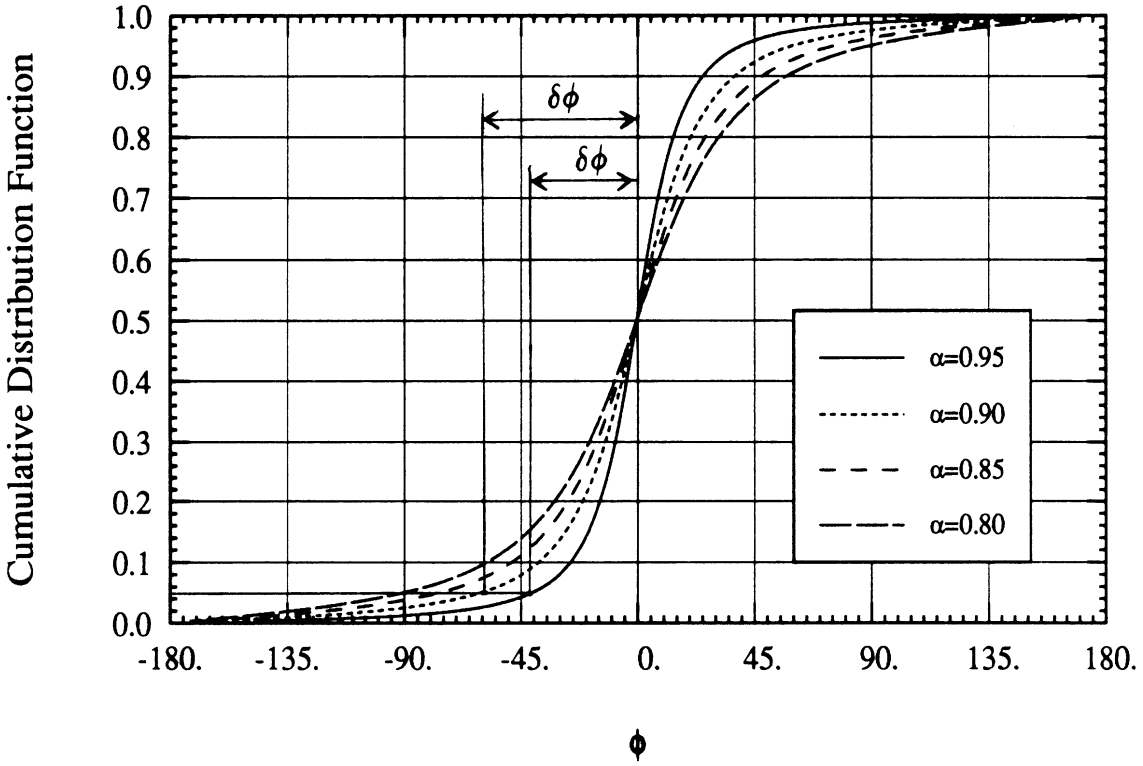

Figure 4: Cumulative distribution function of the phase error for different values of α.

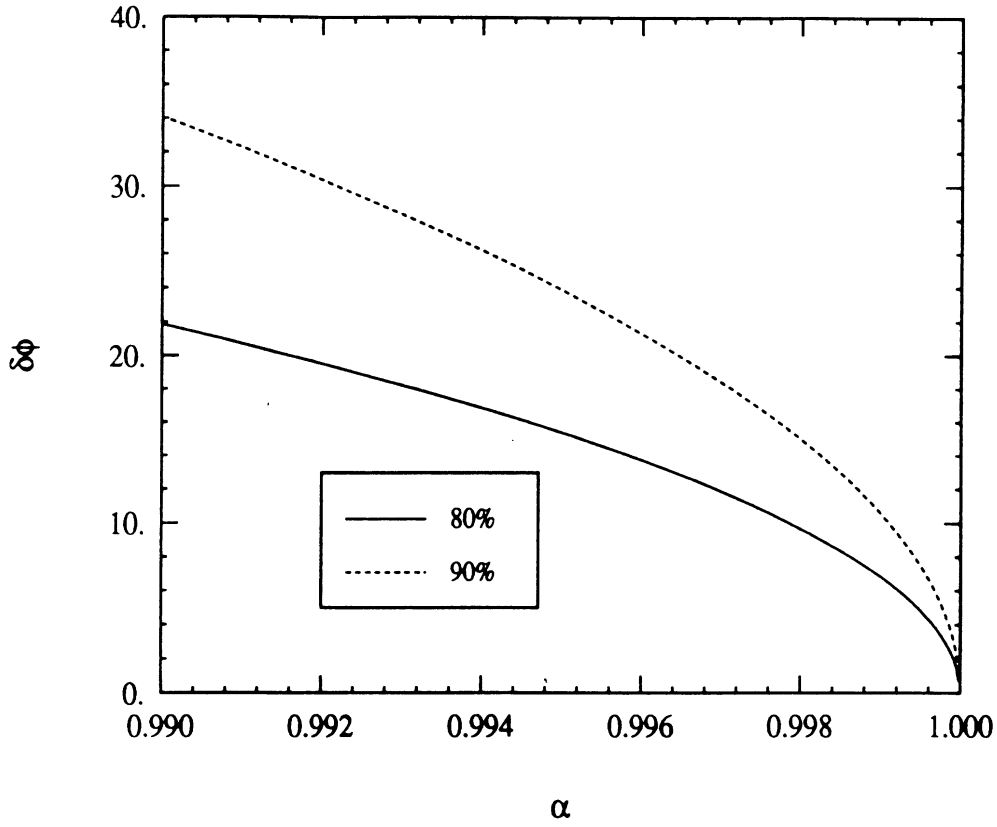

Figure 5: The phase uncertainty for 80% and 90% percent error probability criteria as a function of α.

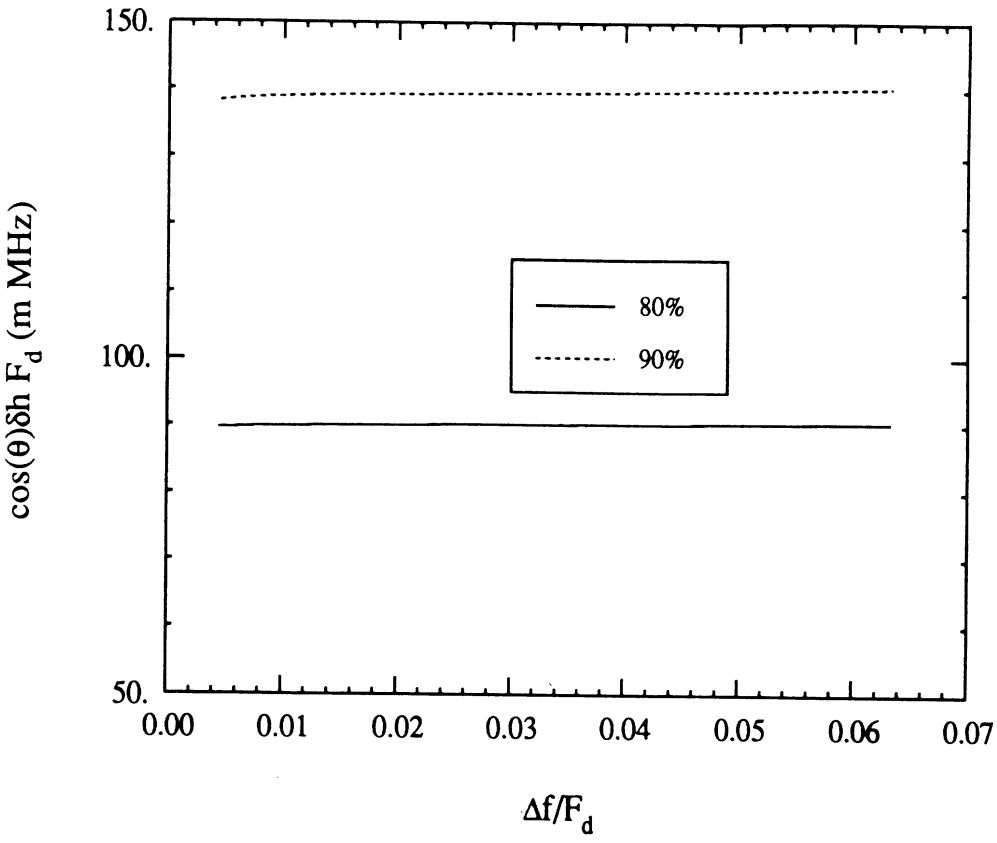

Figure 6: Product of the height uncertainty and decorrelation bandwidth versus frequency shift normalized to the decorrelation bandwidth for a Gaussian correlation function.

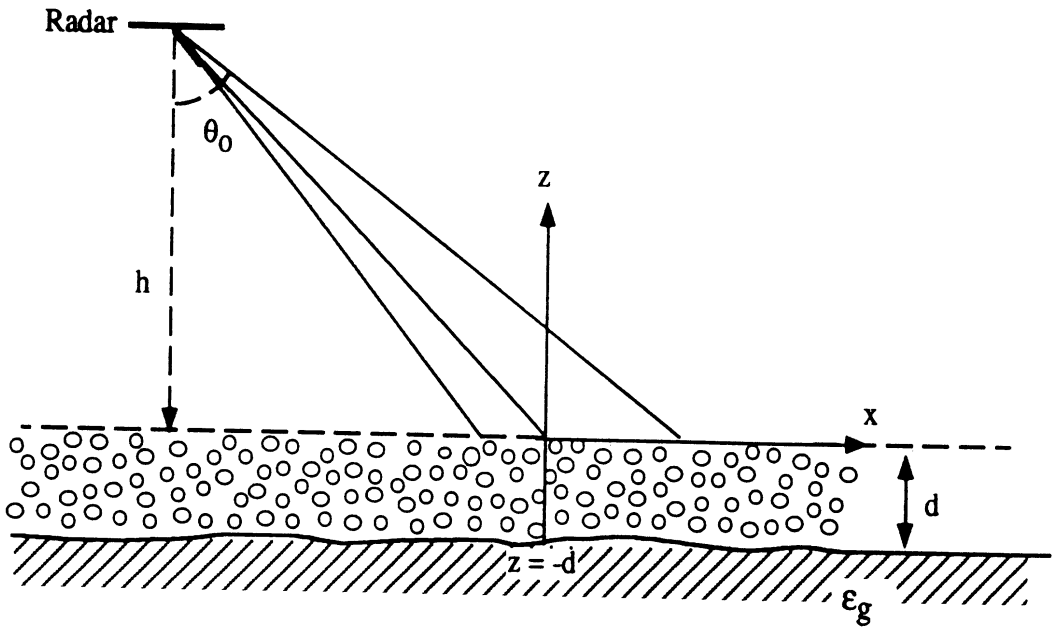

Figure 7: Geometry of a homogeneous layer of random particles above a ground plane.

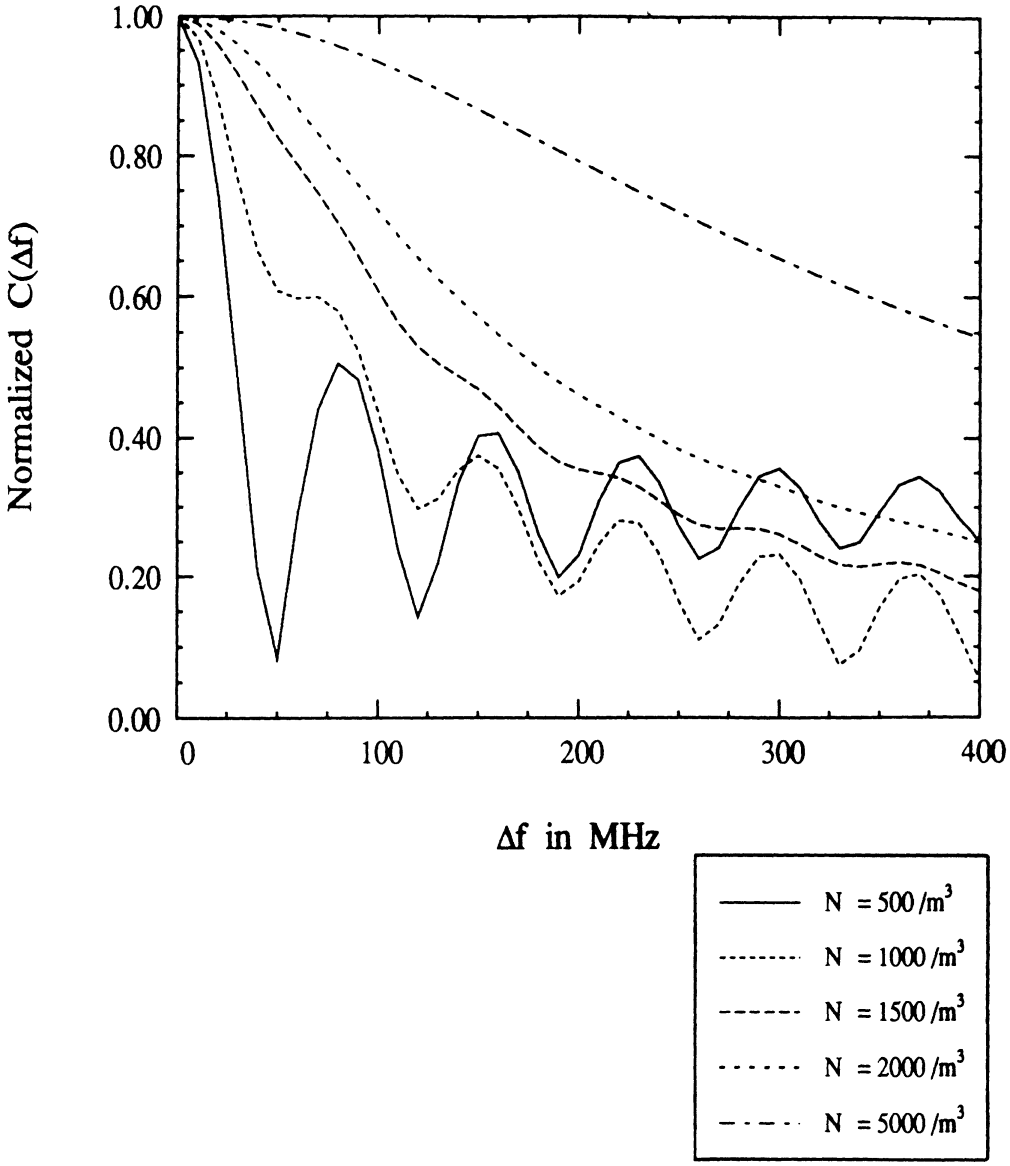

Figure 8: Frequency correlation function of a 2m-thick random layer of flat leaves with average area $50cm^2$, thickness 1.3 mm, and dielectric constant $\epsilon_l = 19 + i6.3$ above a ground plane with $\epsilon_g = 15 + j2$ at 5.3 GHz and $\theta = 30°$ (note for INSAR case $\Delta f < 1$MHz).

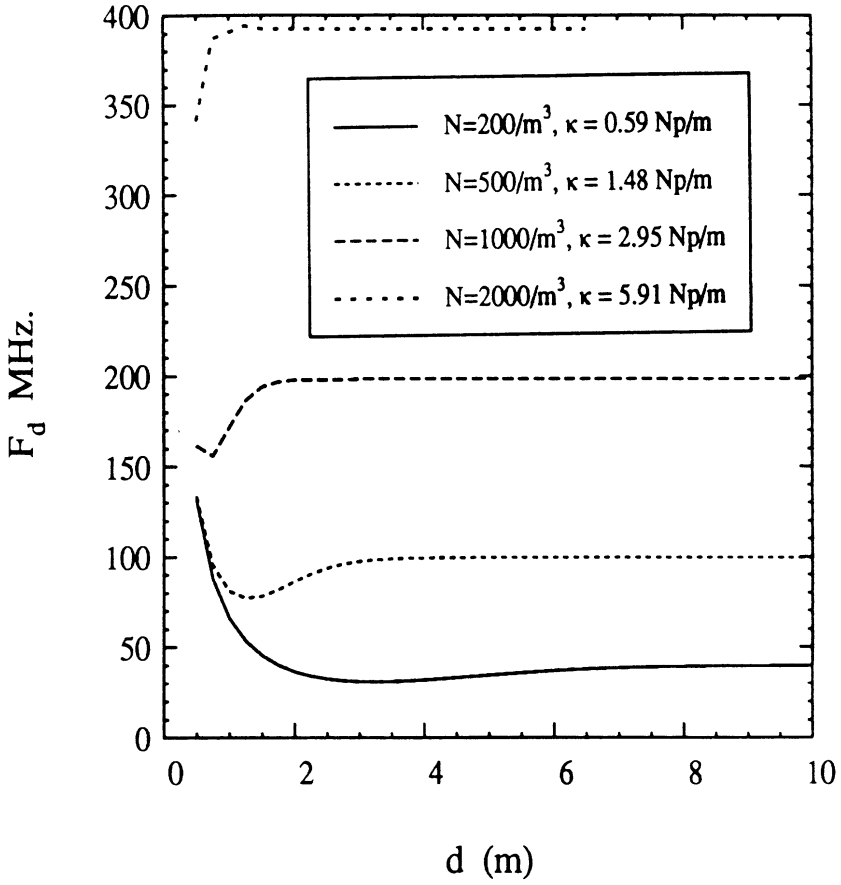

Figure 9: Gaussian equivalent decorrelation bandwidth of the layer as a function of depth for different values of particle number density at $f = 5.3$GHz and $\theta = 30°$.

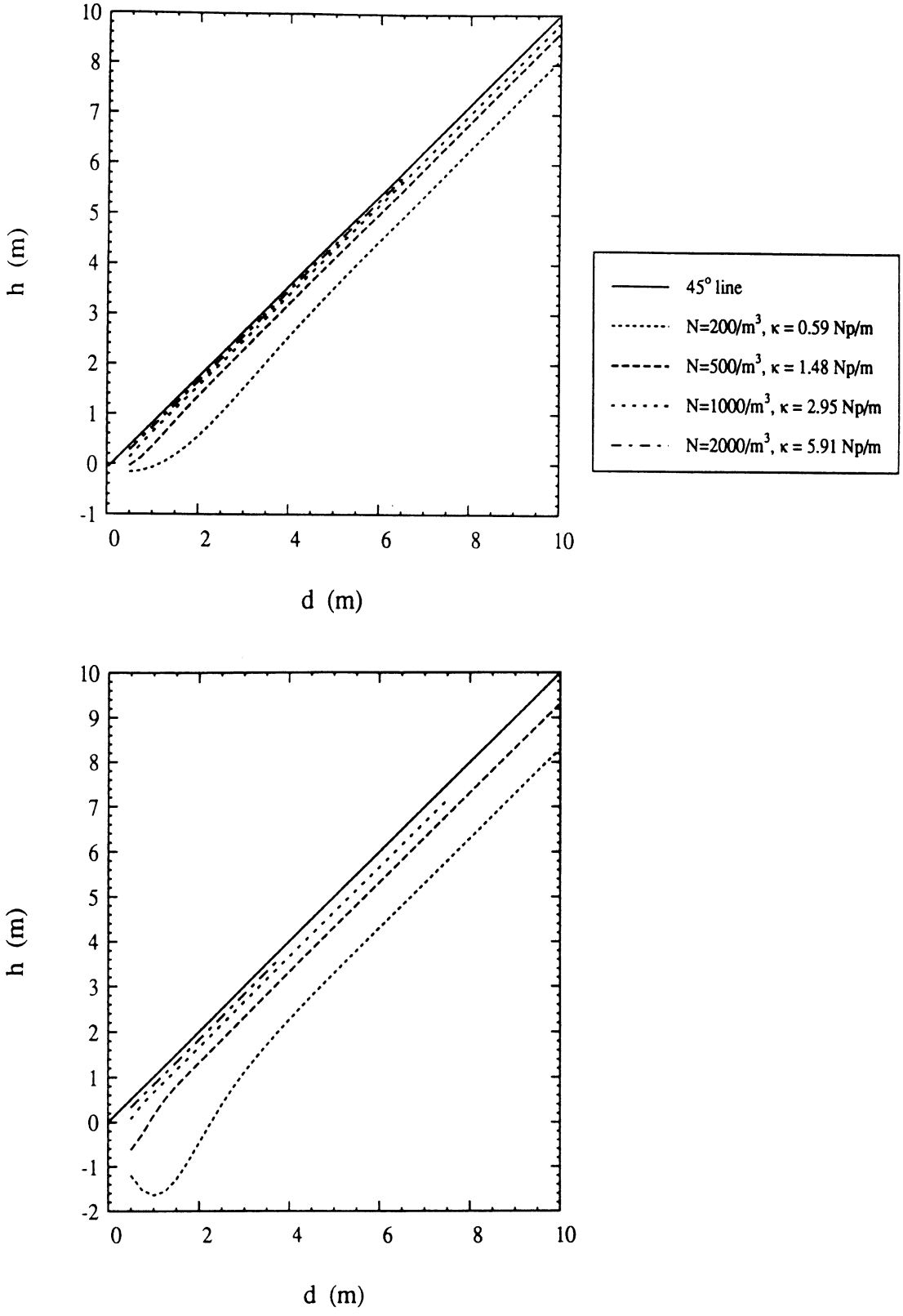

Figure 10: Height of the scattering phase center of the layer above the ground as a function of layer thickness for different values of particle density at $f = 5.3$GHz and $\theta = 30°$ (a) and $\theta = 60°$ (b).

Appendix II

Electromagnetic Scattering Model for a Tree Trunk Above a Ground Plane

Electromagnetic Scattering Model For A Tree Trunk Above A Ground Plane

Yi-Cheng Lin and Kamal Sarabandi

Radiation Laboratory
Department of Electrical Engineering and Computer Science
The University of Michigan
Ann Arbor, MI 48109-2122

ABSTRACT

An efficient and realistic electromagnetic scattering model for a tree trunk above a ground plane is presented in this paper. The trunk is modeled as a finite-length stratified dielectric cylinder with a corrugated bark layer. The ground is considered to be a smooth homogeneous dielectric with an arbitrary slope. The bistatic scattering response of the cylinder is obtained by invoking two approximations. In the microwave region, the height of the tree trunks are usually much larger than the wavelength. Therefore the interior fields in a finite length cylinder representing a tree trunk can be approximated with those of an infinite cylinder with the same physical and electrical radial characteristics. Also an approximate image theory is used to account for the presence of the dielectric ground plane which simply introduces an image excitation wave and an image scattered field. An asymptotic solution based on the physical optics approximation is derived which provides a fast algorithm with excellent accuracy when the radii of the tree trunks are large compared to the wavelength. The effect of a bark layer is also taken into account by simply replacing the bark layer with an anisotropic layer. It is shown that the corrugated layer acts as an impedance transformer which may significantly decrease the backscattering radar cross section depending on the corrugation parameters. It is also shown that for a tilted ground plane a significant cross-polarized backscattered signal is generated while the co-polarized backscattered signal is reduced.

1 Introduction

Because of the important role of the earth's vegetation cover on climatic changes, characterization of physical parameters of the vegetation cover remotely and globally is of great importance. In recent years, considerable effort has been devoted to the development of electromagnetic scattering models for forest canopy [1-3]. In these models the forest canopy is considered to be composed of simple geometrical particles having different sizes, shapes, and dielectric constants. Using vector radiative transfer theory, it has been shown that the backscattering from a typical forest stand can be decomposed into four scattering components : (1) direct backscattering from the crown layer, (2) bistatic scattering from the crown layer reflected from the ground plane, (3) bistatic scattering from the trunk layer reflected from the ground plane , (4) direct backscattering from the ground plane [1]. In lower microwave frequency and/or when the crown layer is tenuous the backscattering is dominated by the ground-trunk interaction. Therefore the accuracy of the scattering model in such cases is directly proportional to the accuracy of the scattering model for tree trunks above a ground plane.

In the mentioned models of forest stands, a tree trunk is simply modeled by a vertical, homogeneous, finite-length dielectric cylinder. The scattering solutions for a finite-length cylinder, reported in the literature, are either based on the eigen-function expansion solution for an infinite cylinder [1-5], or low frequency approximation where all dimensions of the cylinder are small compared to the wavelength [6]. When the cylinder radius is large compared to the wavelength the eigen-function solution becomes, numerically, inefficient due to the poor rate of convergence of the series involved in the solution. This is the case in microwave region where the radius of tree trunks in a forest stand can be significantly larger than the wavelength. An inefficient solution for the calculation of scattering properties of a canopy constituent particles makes the canopy model numerically intractable because the scattering solution for individual particles must be evaluated many times to account for the particle variability in size and orientation. Moreover, in modeling a tree trunk with a dielectric cylinder, an important feature of the tree trunk , the bark layer, has been overlooked. For many trees the bark layer is rough and can be represented by longitudinal grooves on the surface of a dielectric cylinder having possibly a different dielectric constant. The effect of the bark layer on the RCS of a tree trunk was demonstrated recently by representing the bark

layer with a corrugated dielectric layer [7]. Using a hybrid scattering model based on the method of moments and physical optics it was shown that the RCS of a tree trunk is significantly reduced when the effect of the bark layer is taken into account. However this model is not numerically efficient enough to be used in conjunction with the scattering model for a forest canopy.

In this paper a realistic and efficient scattering model for a tree trunk above a ground plane is developed. In this model the effect of the radial inhomogeneity as well as the rough bark layer are taken into consideration. Relying on the fact that the dielectric constants of tree trunks are highly lossy, the physical optics (PO) approximation is used at high frequencies where the radius of curvature is large compared to the wavelength. For finite-length cylinders having radii comparable to the wavelength , the eigen-function expansion in conjunction with the field equivalence principle is used. The bark layer is represented by a periodic corrugated layer and equivalently replaced by an anisotropic layer as suggested in [9]. The ground plane is considered to be a homogeneous medium having a smooth interface and both the cylinder and the ground plane are allowed to have arbitrary orientation with respect to the global coordinate system. Numerical simulations are demonstrated in section 7 where the region of validity of the PO approximation and the effect of a bark layer and a tilted ground plane are investigated.

2 Global Coordinate System

In this paper, the problem of scattering from a cylinder above a ground plane in most general configuration is considered as shown in Fig.1. A global coordinate system (X, Y, Z) is constructed to describe the directional vector $\hat{u}$,

$$\hat{u}(\theta, \phi) = \hat{X} \sin\theta \cos\phi + \hat{Y} \sin\theta \sin\phi + \hat{Z} \cos\theta \tag{1}$$

representing the unit vector along the incidence direction $\hat{k}_i(\theta_i, \phi_i)$, the scattering direction $\hat{k}_s(\theta_s, \phi_s)$, the orientation direction of the cylinder $\hat{z}(\theta_c, \phi_c)$, or the unit normal to the ground plane $\hat{n}_g(\theta_g, \phi_g)$. In this coordinate system , the horizontal and vertical polarization of the incident and the scattered waves are defined by

$$\hat{h_p} = \hat{Z} \times \hat{k_p} / |\hat{Z} \times \hat{k_p}| \tag{2}$$

$$\hat{v_p} = \hat{h_p} \times \hat{k_p} \tag{3}$$

where subscript p can be i or s. In this paper, the forward scatter alignment convention [6] will be used. The components of the scattered field $\mathbf{E^s}$ and the incident field $\mathbf{E^i}$ in the global coordinate system can be related to each other by the scattering matrix $\mathbf{S}$, i.e.,

$$\begin{pmatrix} E_v^s \\ E_h^s \end{pmatrix} = \frac{e^{ik_o r}}{r} \begin{pmatrix} S_{vv} & S_{vh} \\ S_{hv} & S_{hh} \end{pmatrix} \begin{pmatrix} E_v^i \\ E_h^i \end{pmatrix}. \tag{4}$$

The ground is assumed to be smooth having an arbitrary slope in the global coordinate system. It can be shown [8] that when the observation point is away from the ground plane interface and in the far field region of the scatterer, the effect of the ground plane on scattering can simply be taken into account by including the mirror image contributions. Hence the scattering matrix consists only of four components,

$$\mathbf{S} = \mathbf{S_t} + \mathbf{S_{gt}} + \mathbf{S_{tg}} + \mathbf{S_{gtg}} \tag{5}$$

where

$$\mathbf{S_t} = \mathbf{S^0}(\hat{k}_s, \hat{k}_i) \tag{6}$$

$$\mathbf{S_{gt}} = e^{i\tau_s}\mathbf{\Gamma}(\hat{k}_s, \hat{n}_g, \hat{k}_{sg}) \cdot \mathbf{S^0}(\hat{k}_{sg}, \hat{k}_i) \tag{7}$$

$$\mathbf{S_{tg}} = e^{i\tau_i}\mathbf{S^0}(\hat{k}_s, \hat{k}_{gi}) \cdot \mathbf{\Gamma}(\hat{k}_{gi}, \hat{n}_g, \hat{k}_i) \tag{8}$$

$$\mathbf{S_{gtg}} = e^{i(\tau_i+\tau_s)}\mathbf{\Gamma}(\hat{k}_s, \hat{n}_g, \hat{k}_{sg}) \cdot \mathbf{S^0}(\hat{k}_{sg}, \hat{k}_{gi}) \cdot \mathbf{\Gamma}(\hat{k}_{gi}, \hat{n}_g, \hat{k}_i). \tag{9}$$

In the above expressions, the optical lengths τ_i and τ_s account for the extra path lengths of the image excitation and the image scattered waves respectively. $\mathbf{S^0}(\hat{k}_s, \hat{k}_i)$ is the scattering matrix of the isolated target in free space, and $\mathbf{\Gamma}(\hat{k}_r, \hat{n}_g, \hat{k}_i)$ is the reflection matrix which accounts for the specular reflection and polarization transformation due to the tilted ground plane. In order to provide a physical insight for each term in (6)-(9), subscripts t and g are added to represent the scattering from the trunk and the reflection from the ground plane respectively. The order of the subscripts indicates the sequence of scattering in the first order solution. The unit vectors indicating the direction of incident, scattered, and reflected waves, as shown in Fig.1, are also expressed in the arguments of $\mathbf{S^0}$ and $\mathbf{\Gamma}$ in the same order. In most cases the total backscattered signal is dominated by the specular terms $\mathbf{S_{gt}}$ and $\mathbf{S_{tg}}$.

In the following sections, a general reflection matrix $\mathbf{\Gamma}$ for a tilted ground plane with arbitrary slope is first obtained, and then the bistatic expressions for the scattering matrix $\mathbf{S^0}$ of a stratified finite cylinder in free space based on the eigen-function expansion and the PO approximation are derived.

3 Reflection Coefficient Matrix For A Tilted Ground Plane

The existing models for forest stands assume a flat horizontal ground plane with no local slope. In this configuration the tree trunks are positioned normal to the ground plane with possibly a narrow angular distribution around the normal direction. In reality the ground plane may not be horizontal while the tree trunks are still vertically oriented such as forest stands in mountainous areas. The local slope has two significant effects on the backscatterer : (1) depending on the slope angle and the trunk height, the ground-trunk term in the backscattering direction reduces, and (2) a significant cross-polarized component is generated through the reflection from the slanted ground plane which enhances the cross-polarized backscattering coefficient.

Using a simple coordinate transformation the reflection coefficient matrix of the ground plane can be easily computed. Consider a smooth ground plane with a unit normal $\hat{n}_g(\theta_g, \phi_g)$ that is illuminated by a plane wave propagating in $\hat{k}_i$ direction. The direction of the reflected wave is given by

$$\hat{k}_r = \hat{k}_i - 2\hat{n}_g(\hat{n}_g \cdot \hat{k}_i) \tag{10}$$

which is normal to $\mathbf{E}^r$ having E_v^r and E_h^r as its vertical and horizontal components in the global coordinate system. Defining the reflection coefficient matrix $\mathbf{\Gamma}$ by

$$\mathbf{E}^r = \mathbf{\Gamma}(\hat{k}_r, \hat{n}_g, \hat{k}_i) \cdot \mathbf{E}^{\mathbf{i}} \tag{11}$$

the objective is to express the elements of $\mathbf{\Gamma}$ in terms of the Fresnel reflection coefficients of the ground plane. In the local coordinate of the ground plane, the vertical and horizontal polarization of a wave are defined by

$$\hat{h}_p' = \hat{n}_g \times \hat{k}_p / |\hat{n}_g \times \hat{k}_p| \tag{12}$$

$$\hat{v}_p' = \hat{h}_p' \times \hat{k}_p \tag{13}$$

where the subscript p can be i or r. By representing both the incident and reflected field vectors in the local coordinate system $(\hat{v}_p', \hat{h}_p', \hat{k}_p)$ and noting that

$$\begin{pmatrix} E_{v'}^r \\ E_{h'}^r \end{pmatrix} = \begin{pmatrix} \Gamma_{v'} & 0 \\ 0 & \Gamma_{h'} \end{pmatrix} \begin{pmatrix} E_{v'}^i \\ E_{h'}^i \end{pmatrix} \tag{14}$$

the elements of the reflection coefficient matrix can be obtained from

$$\Gamma_{pq} = (\hat{p}_r \cdot \hat{v}_r')\Gamma_{v'}(\hat{v}_i' \cdot \hat{q}_i) + (\hat{p}_r \cdot \hat{h}_r')\Gamma_{h'}(\hat{h}_i' \cdot \hat{q}_i) \quad (15)$$

where p and q can be v or h, and $\Gamma_{v'}$ and $\Gamma_{h'}$ are, respectively, the vertical and horizontal Fresnel reflection coefficients of the ground plane. The inner products in the above expression in terms of the global coordinate parameters are given by

$$\hat{v}_j \cdot \hat{v}_j' = \hat{h}_j \cdot \hat{h}_j' = \frac{\hat{n}_g \cdot \hat{Z} - (\hat{k}_j \cdot \hat{Z})(\hat{n}_g \cdot \hat{k}_j)}{|\hat{n}_g \times \hat{k}_j||\hat{Z} \times \hat{k}_j|}$$

$$\hat{v}_j \cdot \hat{h}_j' = -\hat{h}_j \cdot \hat{v}_j' = \frac{\hat{n}_g \cdot \hat{h}_j}{|\hat{n}_g \times \hat{k}_j|}$$

where j can be i or r.

4 A Semi-Exact Solution

Scattered fields of an infinite stratified cylinder can be obtained by the standard eigen-function expansion method [10]. However, for finite-length cylinders, no exact solution exists. In the microwave region where the length of a tree trunk is much larger than the wavelength and the dielectric constant has a significant imaginary part, the effect of the longitudinal traveling waves on a finite cylinder can be ignored. Therefore, the internal fields of a finite cylinder may be approximated by those of an infinite cylinder having the same radial characteristics. In this paper the scattered fields of a finite cylinder is obtained by invoking the field equivalence principle. That is the dielectric cylinder is replaced by fictitious electric and magnetic surface currents **J** and **M** given by

$$\mathbf{J} = \hat{n} \times \mathbf{H} \quad (16)$$

$$\mathbf{M} = -\hat{n} \times \mathbf{E} \quad (17)$$

where **H** and **E** are the total (incident plus scattered) magnetic and electric fields on the surface of the cylinder, and $\hat{n}$ is the unit vector outward normal to the cylinder surface. These fields are approximated by those of the infinite cylinder, and their tangential components on the surface of the cylinder are given by

$$E_z(\rho' = a, \phi', z') = \sum_n E_{zn} e^{i(\hat{k}_i \cdot \hat{z}' z' + n\phi')} \quad (18)$$

$$Z_0 H_z(\rho' = a, \phi', z') = \sum_n H_{zn} e^{i(\hat{k}_i \cdot \hat{z}' z' + n\phi')} \quad (19)$$

$$E_\phi(\rho' = a, \phi', z') = \sum_n E_{\phi n} e^{i(\hat{k}_i \cdot \hat{z}' z' + n\phi')} \quad (20)$$

$$Z_0 H_\phi(\rho' = a, \phi', z') = \sum_n H_{\phi' n} e^{i(\hat{k}_i \cdot \hat{z}' z' + n\phi')} \quad (21)$$

where Z_0 is the intrinsic impedance of the free space and E_{zn}, H_{zn}, $E_{\phi n}$, and $H_{\phi n}$ are the Fourier components of electric and magnetic field which can be found in a recursive fashion for a stratified cylinder as shown in [11]. In (18)-(21), (ρ', ϕ', z') define a local coordinate system in which the cylinder axis $\hat{Z}_c$ is along $\hat{z}'$ and $\hat{y}' = (\hat{k}_i \times \hat{z}')/|\hat{k}_i \times \hat{z}'|$. Using the fictitious current sources, the electric and magnetic Hertz vector potentials can be evaluated from :

$$\mathbf{\Pi}_e(\bar{r}) = \frac{iZ_0}{4\pi k_0} \frac{e^{ik_o r}}{r} \int_{-b/2}^{b/2} \int_0^{2\pi} \mathbf{J}(z', \phi') e^{-ik_0 \hat{k}_s \cdot \bar{r}'} a d\phi' dz' \quad (22)$$

$$\mathbf{\Pi}_m(\bar{r}) = \frac{iY_0}{4\pi k_0} \frac{e^{ik_o r}}{r} \int_{-b/2}^{b/2} \int_0^{2\pi} \mathbf{M}(z', \phi') e^{-ik_0 \hat{k}_s \cdot \bar{r}'} a d\phi' dz'. \quad (23)$$

where b is the height of the cylinder. The scattered field in the radiation zone (far field region) of the cylinder can be obtained from

$$\mathbf{E}^s = -k_0^2 [\hat{k}_s \times (\hat{k}_s \times \mathbf{\Pi}_e) + \hat{k}_s \times (Z_0 \mathbf{\Pi}_m)]. \quad (24)$$

After some algebraic manipulation as shown in [13], the elements of the scattering matrix for the finite-length cylinder in free space are found to be

$$S^0_{vv} = -\frac{iab}{4\pi k_0} \frac{\sin V}{V} [(\hat{v}_s \cdot \hat{z}') I(\hat{v}_i) + (\hat{h}_s \cdot \hat{z}') K(\hat{v}_i)] \quad (25)$$

$$S^0_{vh} = -\frac{iab}{4\pi k_0} \frac{\sin V}{V} [(\hat{v}_s \cdot \hat{z}') I(\hat{h}_i) + (\hat{h}_s \cdot \hat{z}') K(\hat{h}_i)] \quad (26)$$

$$S^0_{hv} = -\frac{iab}{4\pi k_0} \frac{\sin V}{V} [(\hat{h}_s \cdot \hat{z}') I(\hat{v}_i) - (\hat{v}_s \cdot \hat{z}') K(\hat{v}_i)] \quad (27)$$

$$S^0_{hh} = -\frac{iab}{4\pi k_0} \frac{\sin V}{V} [(\hat{h}_s \cdot \hat{z}') I(\hat{h}_i) - (\hat{v}_s \cdot \hat{z}') K(\hat{h}_i)] \quad (28)$$

where

$$I = \sum_n \{H_{\phi n} u_{1n} + \frac{\hat{k}_s \cdot \hat{z}'}{B} (\sin \tilde{\phi} H_{zn} u_{2n} - \cos \tilde{\phi} H_{zn} u_{1n}) \quad (29)$$

$$
\begin{aligned}
& -\frac{\sin\tilde{\phi}}{B}E_{zn}u_{3n} - \frac{\cos\tilde{\phi}}{B}E_{zn}u_{2n}\} \\
K &= -\sum_n \{E_{\phi n}u_{1n} + \frac{\hat{k}_s\cdot\hat{z}'}{B}(\sin\tilde{\phi}E_{zn}u_{2n} - \cos\tilde{\phi}E_{zn}u_{3n}) \qquad (30)\\
& -\frac{\sin\tilde{\phi}}{B}H_{zn}u_{3n} - \frac{\cos\tilde{\phi}}{B}H_{zn}u_{2n}\}
\end{aligned}
$$

with

$$
\begin{aligned}
V &= \frac{k_0 b}{2}(\hat{k}_i - \hat{k}_s)\cdot\hat{z}' \qquad (31)\\
u_{1n} &= 2\pi(-i)^n J_n(y_0)e^{in\tilde{\phi}} \\
u_{2n} &= 2\pi(-i)^n\{i\cos\tilde{\phi}J_n'(y_0) + \sin\tilde{\phi}\frac{n}{y_0}J_n(y_0)\}e^{in\tilde{\phi}} \\
u_{3n} &= 2\pi(-i)^n\{i\sin\tilde{\phi}J_n'(y_0) - \cos\tilde{\phi}\frac{n}{y_0}J_n(y_0)\}e^{in\tilde{\phi}} \\
B &= \sqrt{(\hat{k}_s\cdot\hat{x}')^2 + (\hat{k}_s\cdot\hat{y}')^2} \\
\tilde{\phi} &= \tan^{-1}\left(\frac{\hat{k}_s\cdot\hat{y}'}{\hat{k}_s\cdot\hat{x}'}\right) \\
y_0 &= k_0 a B.
\end{aligned}
$$

Here J_n and J_n' are, respectively, the Bessel function of first kind and its derivative. It should be noted that I and K as given by (6) and (7) are functions of the polarization of the incident wave.

5 Physical Optics Approximation

The semi-exact solution described in the previous section becomes inefficient at high frequencies where the radius of the cylinder is large compared to the wavelength and fails when the cross section of the cylinder is not circular. These deficiencies can be removed at high frequencies by employing the PO approximation. This approximation is valid when the radius of curvature of the cylinder is large compared to the wavelength and the permittivity of the cylinder has a relatively large imaginary part so that the effect of the glory rays and the creeping waves could be ignored. As before, the cylinder is replaced by fictitious electric and magnetic currents, however in this case, the currents

are approximated by those of the local tangential plane which are proportional to the sum of the incident and reflected waves.

To simplify the integration of the currents over the lit surface, the stationary phase (SP) approximation may be used. This approximation is valid so long as the stationary point falls over the lit region. For convenience, a local coordinate $(\hat{n}, \hat{t}, \hat{l})$ is established at the SP point. The local tangential directions are defined by

$$\hat{t} = \hat{n} \times \hat{k}_i / |\hat{n} \times \hat{k}_i| \tag{32}$$

$$\hat{l} = \hat{n} \times \hat{t} \tag{33}$$

where $\hat{n}$ is a unit vector normal to the cylinder surface at the SP point. For the general case of an anisotropic medium (the bark layer may exhibit anisotropic properties) a dyadic reflection coefficient $\mathbf{R}$ is introduced to relate the polarization coupling between the incident and reflected waves, i.e.

$$\mathbf{E}_T^r = \mathbf{R} \cdot \mathbf{E}_T^i \tag{34}$$

Combining the incident and reflected fields, the total fields $\mathbf{E}(= \mathbf{E^r} + \mathbf{E^i})$ and $\mathbf{H}(= \mathbf{H}^r + \mathbf{H}^i)$ on the surface of the cylinder can be obtained from

$$\begin{pmatrix} E_l \\ E_t \end{pmatrix} = \begin{pmatrix} 1 + R_{vv} & R_{vh} \\ R_{hv} & 1 + R_{hh} \end{pmatrix} \begin{pmatrix} E_l^i \\ E_t^i \end{pmatrix} \tag{35}$$

and

$$\begin{pmatrix} H_l \\ H_t \end{pmatrix} = \begin{pmatrix} 1 - R_{hh} & R_{hv} \\ R_{vh} & 1 - R_{vv} \end{pmatrix} \begin{pmatrix} H_l^i \\ H_t^i \end{pmatrix}. \tag{36}$$

Applying the stationary phase approximation, it can be shown that the Hertz vector potentials are given by

$$\mathbf{\Pi}_e = \frac{iZ_0}{k_0} \frac{e^{ik_o r}}{r} Q\mathbf{J} \tag{37}$$

$$\mathbf{\Pi}_m = \frac{iY_0}{k_0} \frac{e^{ik_o r}}{r} Q\mathbf{M}. \tag{38}$$

where $\mathbf{J}$ and $\mathbf{M}$ are the fictitious currents evaluated from the total fields $\mathbf{E}$ and $\mathbf{H}$ at the SP point ($\phi' = \tilde{\phi}$), and

$$Q = \frac{ik_0}{4\pi} \int_{-b/2}^{b/2} \int_{-\pi/2}^{\pi/2} e^{-ik_0 aB\cos(\phi' - \tilde{\phi})} e^{ik_0(\hat{k}_i - \hat{k}_s)\cdot\hat{z}z'} a d\phi' dz'. \tag{39}$$

$$= \frac{ib}{2\pi}\frac{\sin V}{V}e^{-ik_0Ba}\sqrt{\frac{k_0a}{2B}}\left\{F\left[\sqrt{\frac{k_0Ba}{2}}(\frac{\pi}{2}+\tilde{\phi})\right]+F\left[\sqrt{\frac{k_0Ba}{2}}(\frac{\pi}{2}-\tilde{\phi})\right]\right\}$$

with

$$B = \left\{[(\hat{k}_s-\hat{k}_i)\cdot\hat{x}']^2+[(\hat{k}_s-\hat{k}_i)\cdot\hat{y}']^2\right\}^{1/2}$$
$$\tilde{\phi} = \tan^{-1}(\frac{(\hat{k}_s-\hat{k}_i)\cdot\hat{y}'}{(\hat{k}_s-\hat{k}_i)\cdot\hat{x}'})$$

and $F(\cdot)$ is the Fresnel Integral. This approximation is valid provided $k_0aB >> 1$ and $\tilde{\phi}$ is away from the shadow boundary.

Using a similar procedure as in the previous section, the scattering matrix elements are found to be

$$S^0_{vv} = Q[(\hat{l}\cdot\hat{v}_s)Z_0J_{lv}+(\hat{t}\cdot\hat{v}_s)Z_0J_{tv}+(\hat{l}\cdot\hat{h}_s)M_{lv}+(\hat{t}\cdot\hat{h}_s)M_{tv}] \quad (40a)$$
$$S^0_{vh} = Q[(\hat{l}\cdot\hat{v}_s)Z_0J_{lh}+(\hat{t}\cdot\hat{v}_s)Z_0J_{th}+(\hat{l}\cdot\hat{h}_s)M_{lh}+(\hat{t}\cdot\hat{h}_s)M_{th}] \quad (40b)$$
$$S^0_{hv} = Q[(\hat{l}\cdot\hat{h}_s)Z_0J_{lv}+(\hat{t}\cdot\hat{h}_s)Z_0J_{tv}-(\hat{l}\cdot\hat{v}_s)M_{lv}-(\hat{t}\cdot\hat{v}_s)M_{tv}] \quad (40c)$$
$$S^0_{hh} = Q[(\hat{l}\cdot\hat{h}_s)Z_0J_{lh}+(\hat{t}\cdot\hat{h}_s)Z_0J_{th}-(\hat{l}\cdot\hat{v}_s)M_{lh}-(\hat{t}\cdot\hat{v}_s)M_{th}] \quad (40d)$$

where J_{pq} and M_{pq} are the currents along $\hat{p}$ direction induced by a $\hat{q}$ polarized incident wave (p can be t or l and q can be v or h). The inner products of the vectors in the above expressions can easily be calculated in terms of the global coordinates.

The above results fail in the case of forward scattering for which $B = 0$. However, in directions close to the forward direction, an alternative approximation for the scattered field is possible and is given by [13]

$$\mathbf{E}^s = \frac{-2iab}{\lambda_0}(\hat{k}_i\cdot\hat{x}')\frac{\sin V}{V}\frac{\sin W}{W}\frac{e^{ik_or}}{r}\mathbf{E}^i \quad (41)$$

where $W = k_0a(\hat{k}_s\cdot\hat{y}')$ and V is given in (31).

6 Modeling of A Corrugated Bark Layer

For some tree species, the bark layer is corrugated with grooves along the longitudinal direction. In this paper, the bark is simply modeled as a periodic

corrugated layer with period L and width d as shown in Fig.2a. It is shown in [9] that ,when $L < \lambda_0/2$ (single Bragg mode), the corrugated layer can be equivalently replaced by an anisotropic layer (see Fig.2b) with the same thickness whose permittivity tensor is given by

$$\epsilon = \begin{pmatrix} \epsilon_{11} & 0 & 0 \\ 0 & \epsilon_{22} & 0 \\ 0 & 0 & \epsilon_{33} \end{pmatrix}. \tag{42}$$

The entries of the tensor in terms of the permittivity, period, and width of the corrugated layer , when $L \leq 0.2\lambda_0$, are approximated by

$$\epsilon_{11} = \frac{\epsilon_r}{\epsilon_r(1 - d/L) + d/L} \tag{43}$$

$$\epsilon_{22} = \epsilon_{33} = 1 + (\epsilon_r - 1)d/L. \tag{44}$$

Assuming that the radius of the cylinder is much larger than the wavelength, the permittivity of the bark layer can be represented by $\epsilon(\phi, z, n)$ where $\epsilon_{\phi\phi} = \epsilon_{11}$ and $\epsilon_{zz} = \epsilon_{nn} = \epsilon_{22}$.

To employ the PO approximation, a coordinate transformation from the local (ϕ, z, n) to (t, l, n) at SP point is needed. The resultant permittivity tensor in coordinate (t, l, n) is

$$\epsilon = \begin{pmatrix} \epsilon_{zz}\sin^2\phi_z + \epsilon_{\phi\phi}\cos^2\phi_z & (\epsilon_{\phi\phi} - \epsilon_{zz})\sin\phi_z\cos\phi_z & 0 \\ (\epsilon_{\phi\phi} - \epsilon_{zz})\sin\phi_z\cos\phi_z & \epsilon_{zz}\cos^2\phi_z + \epsilon_{\phi\phi}\sin^2\phi_z & 0 \\ 0 & 0 & \epsilon_{nn} \end{pmatrix} \tag{45}$$

where

$$\phi_z = \cos^{-1}\left(\frac{\hat{k}_i \cdot \hat{z}}{\sqrt{1 - (\hat{n} \cdot \hat{k}_i)^2}}\right) \tag{46}$$

The reflected fields from a stratified anisotropic dielectric half space is computed using the method described in [12].

7 Numerical Results

In this section a number of numerical examples for the scattering from a finite cylinder above a ground plane are presented. In all the considered examples

the normalized RCS, defined by

$$\sigma_{pq} = \frac{4\pi |S_{pq}|^2}{k_0 a b^2}, \tag{47}$$

are displayed for a two-layered cylinder with height b, exterior radius a_1 and interior radius a_2. The permittivity of the exterior and interior layers are chosen to be : $\epsilon_1 = 4 + i1$ and $\epsilon_2 = 10 + i5$ respectively. Also the cylinder is positioned vertically ($\theta_c = 0$) on a tilted ground with permittivity $\epsilon_g = 10 + i5$.

First, the validity region of the PO approximation in backscatter direction is examined. Figure 3 compares σ_{vv} and σ_{hh} using the PO and semi-exact solutions. It is found that the PO solution agrees well with the semi-exact solution when $k_0 a > 10$. For small values of $k_0 a$ the resonance behavior of backscatter is shown by the semi-exact solution. Figures 4-6 show the monostatic and bistatic scattering patterns which are simulated for a two-layered cylinder with and without a corrugation. The thickness of the corrugated layer and its filling factor are respectively chosen to be $t = 0.1\lambda_0$ and $d/L = 0.7$ (see Fig.2). Figure 4 shows the backscattering pattern as a function of incidence angle. At small angles of incidence, the PO approximation differs slightly from the semi-exact solution because the radial component of the propagation constant ($k_\rho = k_0 \sin\theta$) is small in this region and the condition $k_\rho a > 10$ is not satisfied. The vv-polarized backscattering RCS has two minima corresponding to the two Brewster angles one occurring on the surface of the cylinder ($\theta \simeq 25^o$) and the other occurring on the ground plane ($\theta \simeq 75^o$). The backscattering RCS vanishes at $\theta = 0^o$ and 90^o since the four components contributing to the backscattering RCS interfere destructively. The ripples on the curves are due to the components $\mathbf{S_t}$ and $\mathbf{S_{gtg}}$ (see equation (1)), which become significant for angles of incidence close to 90^o; and the oscillation rate is proportional to the cylinder length. This figure also shows the effect of the bark layer on the backscattering RCS. Depending on the incidence angle the RCS of the cylinder may be reduced as high as 10 dB. The reduction in the RCS is a function of the cylinder length and the corrugation parameters. Basically the corrugated layer behaves as an impedance transformer between the air and the vegetation material. Figure 5 shows the bistatic scattering pattern as a function of elevation angle when $\theta_i = 120^o, \phi_i = 180^o$ and the observation point is moving in the XZ-plane. Figure 6 shows the bistatic scattering pattern as a function of azimuth angle (ϕ_s) with $\theta_i = 120^o, \phi_i = 180^o$, and $\theta_s = 60^o$. The discontinuities found on the PO solution near the forward directions are because of

switching the expression for scattering from (9) to (10).

Figures 7-9 show the effect of the tilted ground plane on the backscattering RCS. All the parameters in Fig.7 are the same as those given in Fig.4 except for the tilt angle of the ground ,$\theta_g = 20^o$ and $\phi_g = 90^o$. Comparing Fig.4 with Fig.7, it can be seen that a significant cross-polarized backscattered signal is generated due to the slope of the ground plane. Figure 8 shows the variation of backscattering RCS as a function of the ground azimuth angle ϕ_g where $\theta_i = 135^o$, $\phi_i = 180^o$ and $\theta_g = 20^o$. One can observe that the peak of the backscattering RCS occurs at $\phi_g = 70^o (= \pi - \theta_g)$. Figure 9 shows the backscattering RCS as a function of the ground elevation angle θ_g where $\theta_i = 135^o, \phi_i = 180^o$ and $\phi_g = 0^o$ and 180^o. The regions in the positive and the negative θ_g represent the ascending and the descending sides of a mountain respectively. In this case no cross-polarized signal is generated because the cylinder is in the principal plane (X-Z plane). Note that there are two maxima occuring at $\theta_g = 0^o$ and $\theta_g = -22.5^o$. The first maximum corresponds to the dihedral-like ground -trunk interaction. The second maximum corresponds to a reflection from the ground plane which illuminates the cylinder at normal incidence. The backscatter from the cylinder bounce off from the ground plane and returns toward the radar (see Fig.10). This strong backscatter component can be observed where $\hat{k}_i, \hat{n}_g$ and $\hat{Z}_c$ are in the same plane and $\theta_i = 2\theta_g + \pi/2$.

8 Conclusions

An efficient and realistic electromagnetic scattering model for a tree trunk above a ground plane is presented in this paper. The trunk is modeled as a finite-length stratified dielectric cylinder with a corrugated bark layer. The ground is considered to be a smooth homogeneous dielectric with an arbitrary slope. An asymptotic solution based on the PO approximation for high frequencies is derived. This solution provides a fast algorithm with excellent accuracy when the radii of tree trunks are large compared to the wavelength. The effect of the bark layer is also taken into account by simply replacing the bark layer with an anisotropic layer. It is shown that the corrugated layer acts as an impedance transformer which may significantly decrease the backscattering RCS. The RCS reduction depends on the corrugation parameters. It is also shown that for a tilted ground plane a significant cross-polarized backscattered signal is generated while the co-polarized backscattered signal is reduced.

References

[1] F. T. Ulaby, K. Sarabandi, K. MacDonald, M. Whitt, and M. C. Dobson, " Michigan Microwave Canopy Scattering Model", *Int. J. Remote Sensing*, Vol. 11, NO. 7, pp. 1223-1253, 1990

[2] L. Tsang, C. H. Chan, J. A. Kong, and J. Joseph, " Polarimetric signature of a canopy of dielectric cylinders based on first and second order vector radiative transfer theory," *J. Electromag. Waves and Appli.* Vol. 1, No. 1, pp. 19-51, 1992.

[3] S. L. Durden, J. J. van Zyl, and H. A. Zebker,"Modeling and observation of the radar polarization signature of forested areas", *IEEE Trans. Geosci. Remote Sensing*, Vol. 27, No. 3, pp. 290-301, 1989.

[4] S. S. Seker and A. Schneider,"Electromagnetic scattering from a dielectric cylinder of finite length", *IEEE Trans. Antenna Propagat.*, Vol. 36, No. 2, pp. 303-307, 1988

[5] M. A. Karam and A. K. Fung, " Electromagnetic scattering from a layer of finite-length, randomly oriented dielectric circular cylinder over a rough interface with application to vegetation", *Int. J. Remote Sensing*, Vol. 9, No. 6, pp. 1109-1134, 1988

[6] F. T. Ulaby and C. Elachi,*Radar Polarimetry for Geoscience Applications*, Artech House, 1990.

[7] K. Sarabandi and F. T. Ulaby,"High frequebcy scattering from corrugated stratified cylinders", *IEEE Trans. Antennas Propag.*, Vol. 39, No. 4, pp. 512-520, 1991.

[8] K. Sarabandi, "Scattering from dielectric structures above impedance surfaces and resistive sheets," *IEEE Trans. Antennas Propag.,* Vol. 40, No. 1, pp. 67-78, Jan. 1992.

[9] K. Sarabandi, " Simulation of a periodic dielectric corrugation with an equivalent anisotropic layer," *International Journal of Infrared and Millimeter Waves,* Vol. 11, pp. 1303-1321, 1990

[10] G. T. Ruck, D. E. Barrick, W. D. Staurt, and C. K. Krichbaum, *Radar Cross Section Handbook*, pp. 259-263 and pp. 479-484, New York: Plenum Press , 1970.

[11] M. O. Kolawole," Scattering from dielectric cylinders having radially layered permittivity, " *J. Electromag. Waves and Appli.*, Vol. 16, No. 2, pp. 235-259, 1992

[12] M. A. Morgan, "Electromagnetic Scattering by Stratified Inhomogeneous Anisotropic Media," *IEEE Trans. Antennas Propag.*, Vol. 35, pp. 191-197, 1987

[13] K. Sarabandi, *Electromagnetic Scattering from Vegetation Canopies*, Ph.D. Dissertation, pp. 224, eq. 7.40, University of Michigan, 1989.

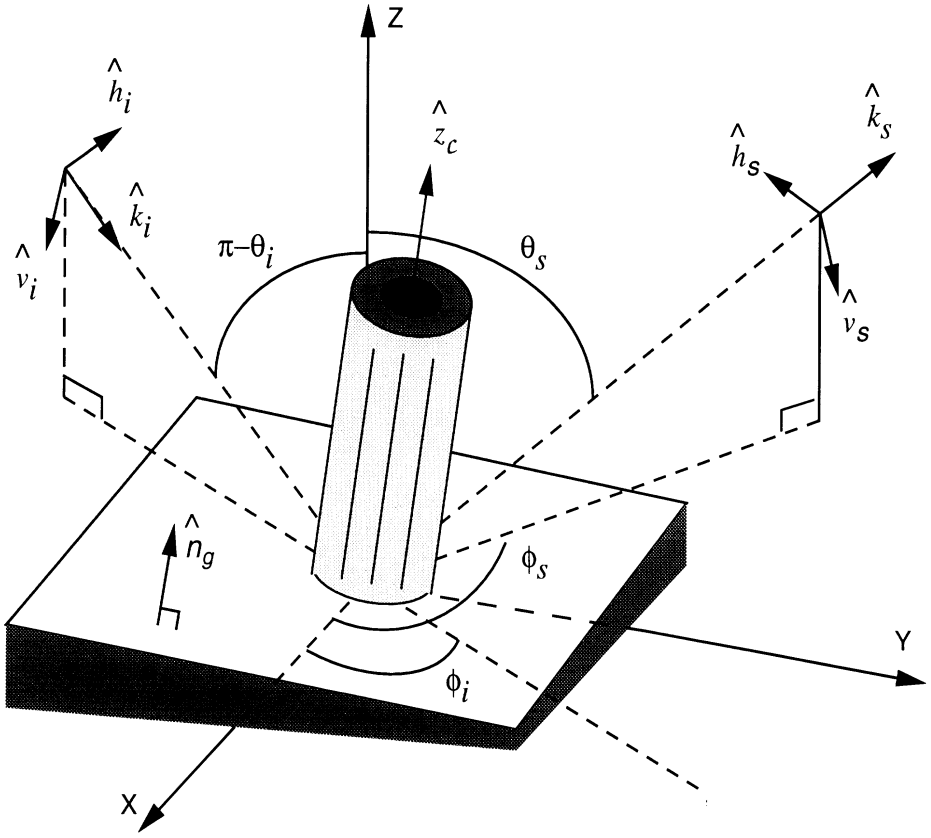

Figure 1: Global coordinate system

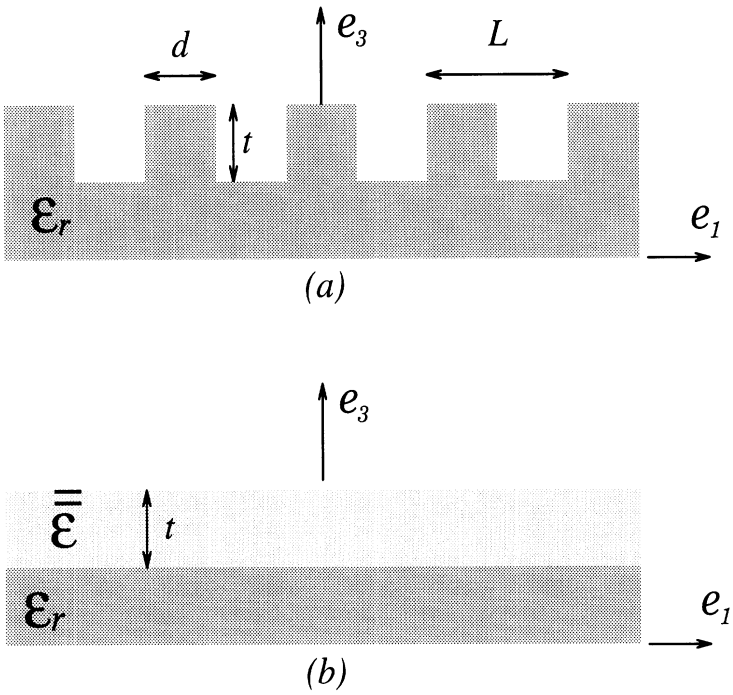

Figure 2: A corrugated layer and its equivalent anisotropic layer.

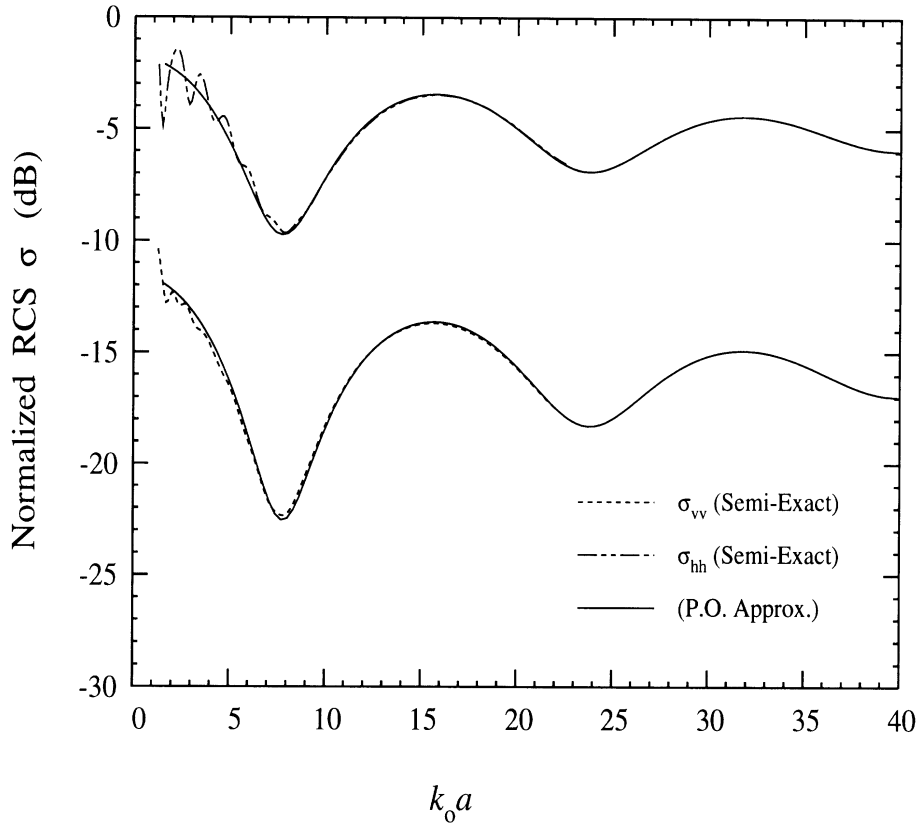

Figure 3: Comparison of the PO approximation with the semi-exact solution. The ratio of the interior radius a_2 and the exterior radius $a_1(=a)$ is kept constant $(a_2/a_1 = 0.9)$. Other parameters are : $b = 20\lambda_0, \epsilon_1 = 4 + i1, \epsilon_2 = \epsilon_g = 10 + i5, \theta_i = 120^o, \phi_i = 180^o, \theta_s = 60^o, \phi_s = 0^o, \theta_g = \theta_c = 0^o$.

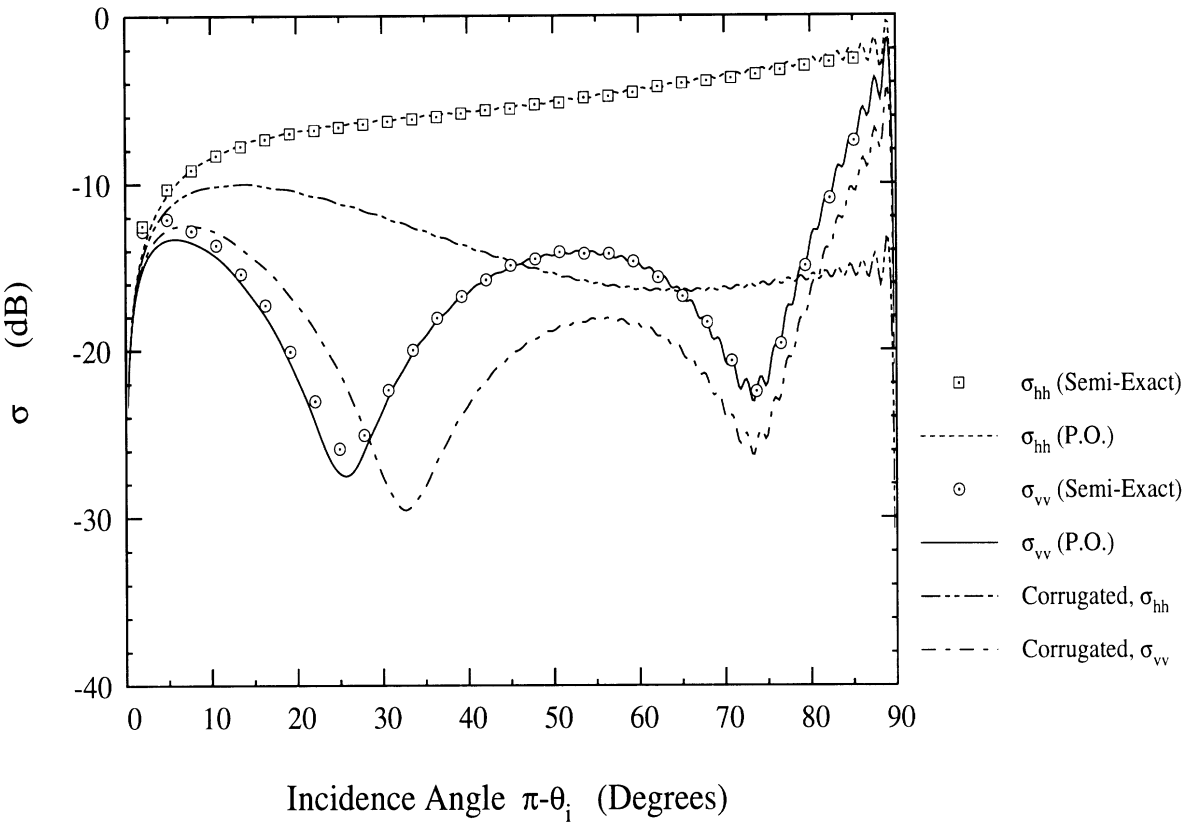

Figure 4: The normalized backscattering RCS as a function of the incidence angle $\theta = \pi - \theta_i$ for a two layered cylinder with and without the corrugation. Other parameters are : $b = 20\lambda_0, a_1 = 2\lambda_0, a_2 = 1.8\lambda, t = 0.1\lambda_0, d/L = 0.7, \phi_i = 180^o, \phi_s = 0^o, \theta_g = \theta_c = 0^o$.

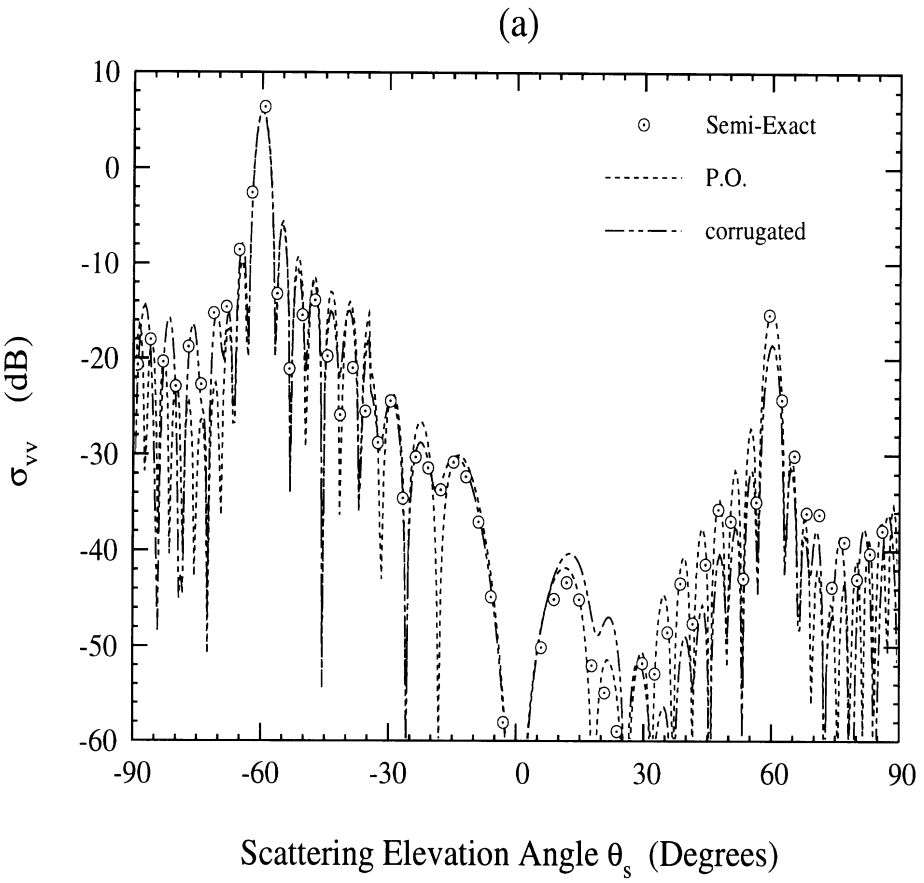

Figure 5: The normalized bistatic σ_{vv} (a) and σ_{hh} (b) as a function of the scattering elevation angle θ_s in XZ-plane ($\theta_s > 0$ when $\phi_s = 0^o; \theta_s < 0$ when $\phi_s = 180^o$). The backscattered and the specular directions are shown at $\theta_s = 60^o$ and $\theta_s = -60^o$ respectively. Other parameters are : $\theta_i = 120^o, \phi_i = 180^o, \theta_g = \theta_c = 0^o, b = 10\lambda_0, a_1 = 2\lambda_0, a_2 = 1.8\lambda_0$.

(b)

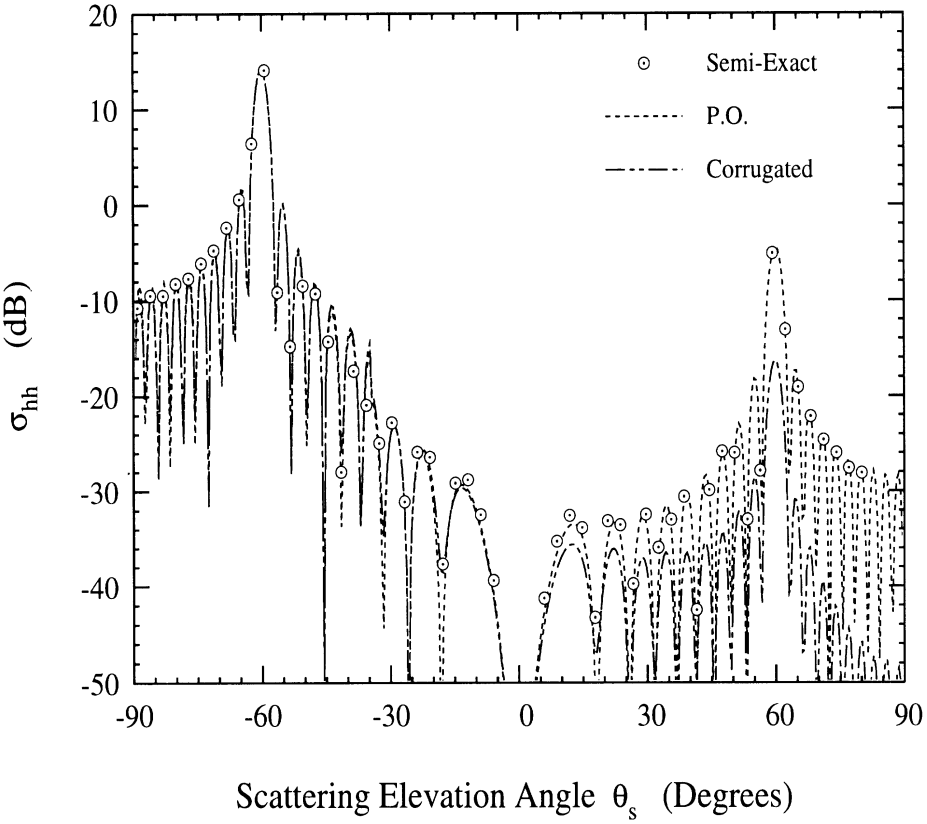
Semi-Exact
P.O.
Corrugated
σ_{hh} (dB)
20
10
0
-10
-20
-30
-40
-50
-90
-60
-30
0
30
60
90
Scattering Elevation Angle θ_s (Degrees)

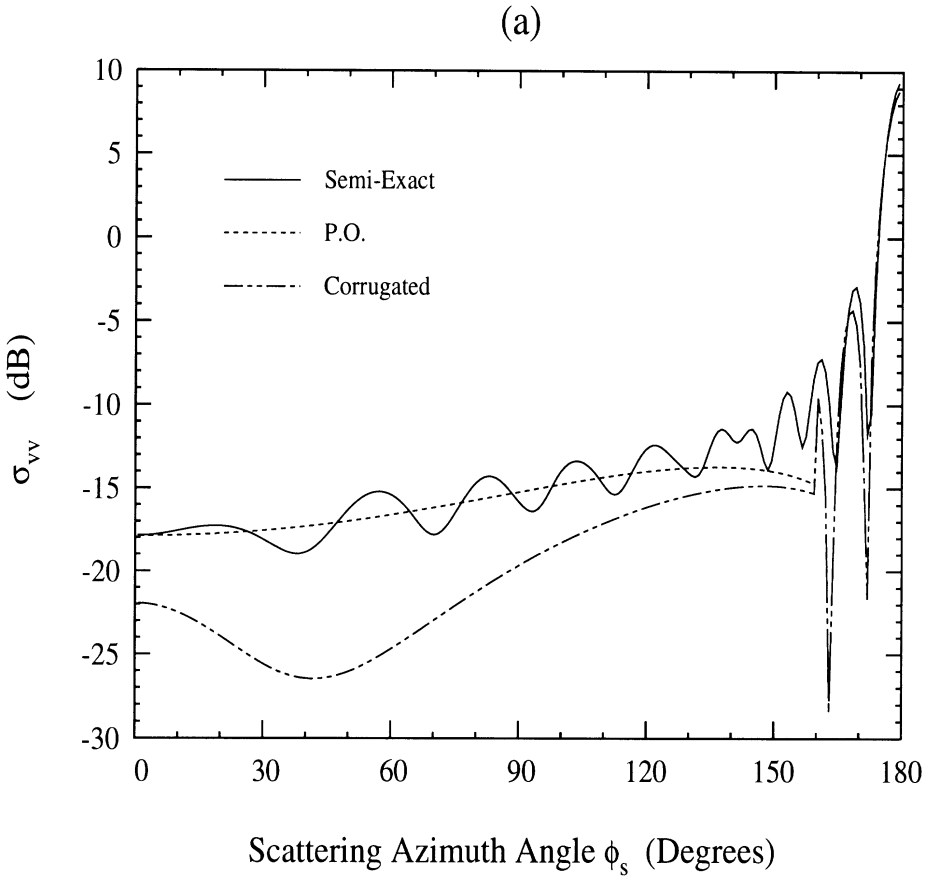

Figure 6: The normalized bistatic σ_{vv} (a) and σ_{hh} (b) as a function of the scattering azimuth angle ϕ_s. The backscattered and forward-scattered direction are shown at $\phi_s = 0^o$ and $\phi_s = 180^o$ respectively. Other parameters are : $\theta_i = 120^o, \phi_i = 180^o, \theta_s = 60^o, \theta_g = \theta_c = 0^o, b = 20\lambda_0, a_1 = 4\lambda_0, a_2 = 3.6\lambda_0$.

(b)

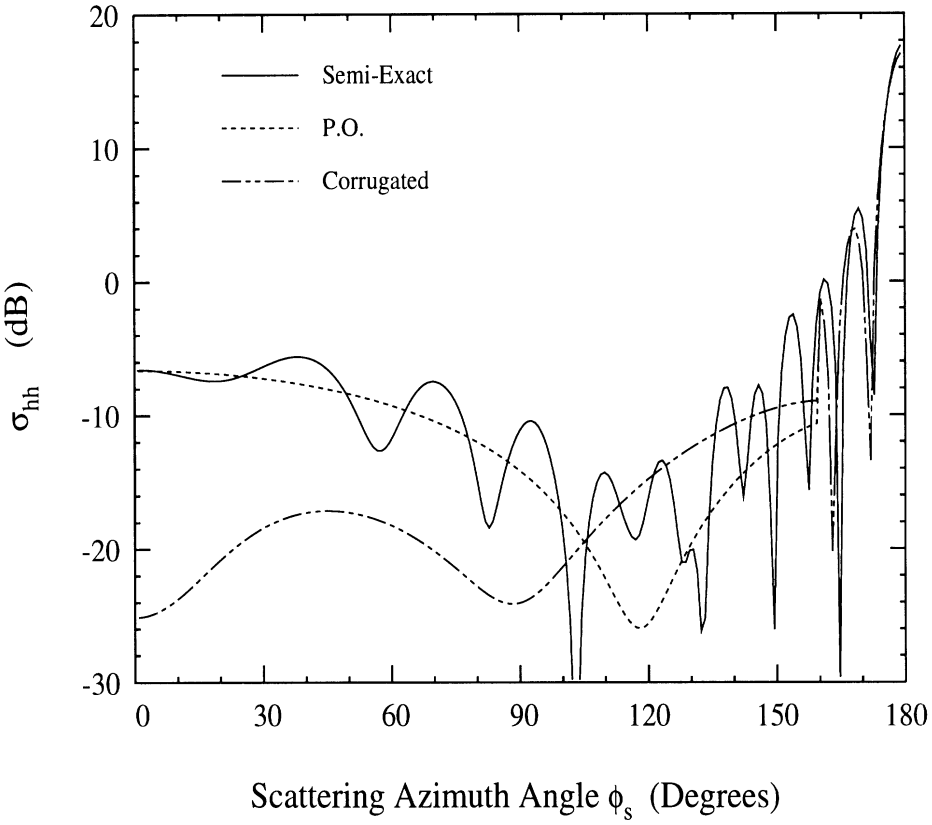
Semi-Exact
P.O.
Corrugated
20
10
0
-10
-20
-30
0
30
60
90
120
150
180
σ_{hh} (dB)
Scattering Azimuth Angle ϕ_s (Degrees)

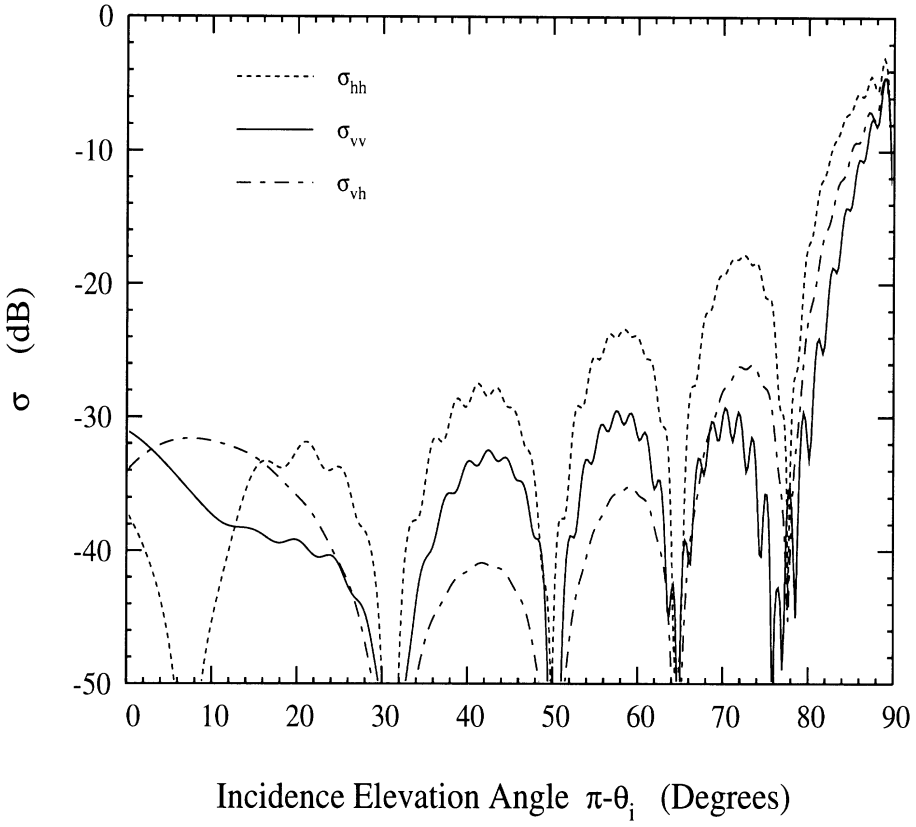

Figure 7: The normalized backscattering RCS as a function of the incidence angle $\pi - \theta_i$ for a two layered cylinder above a tilted ground plane. Other parameters are : $\theta_g = 20^o, \phi_g = 90^o, \theta_c = 0^o, \phi_i = 180^o, \phi_s = 0^o, \theta_s = \pi - \theta_i, b = 20\lambda_0, a_1 = 2\lambda_0, a_2 = 1.8\lambda_0$.

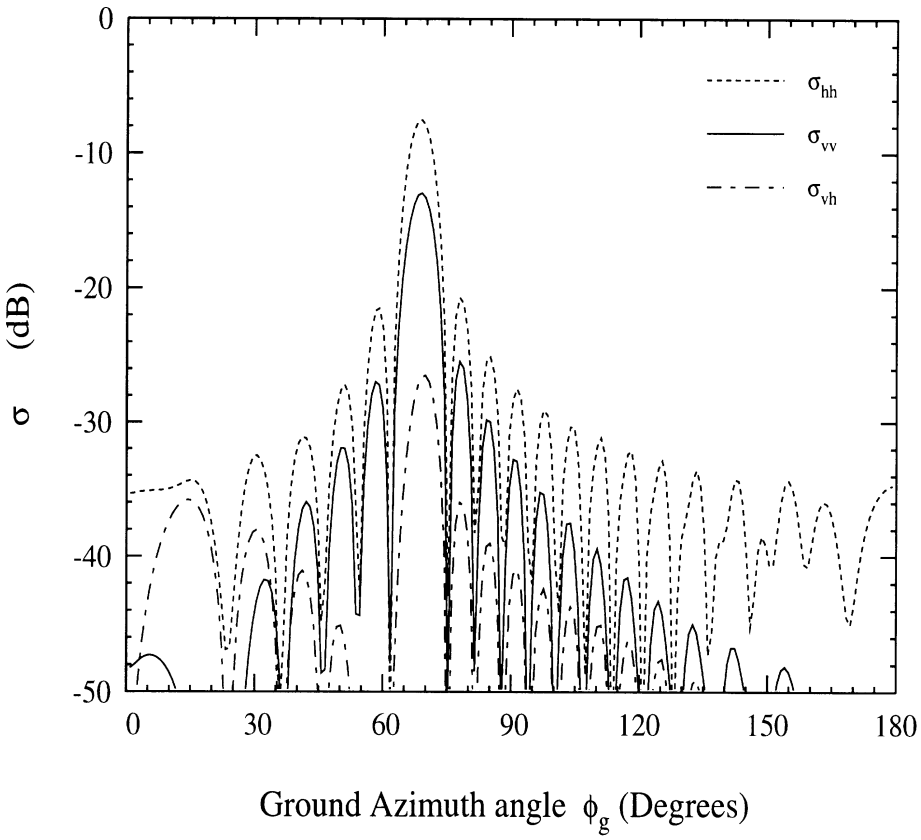

Figure 8: The normalized backscattering RCS as a function of the ground azimuth angle ϕ_g. Other parameters are : $\theta_g = 20^o, \theta_c = 0^o, \theta_i = 135^o, \phi_i = 180^o, \theta_s = 45^o, \phi_s = 0^o, b = 20\lambda_0, a_1 = 2\lambda_0, a_2 = 1.8\lambda_0$.

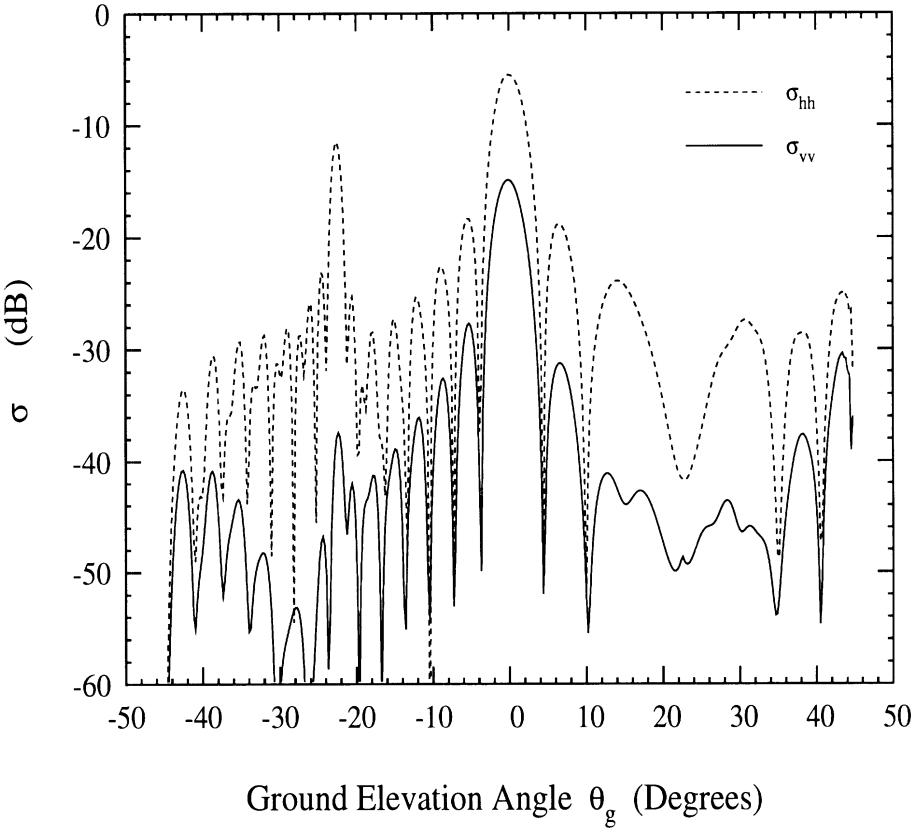

Figure 9: The normalized backscattering RCS as a function of the ground elevation angle θ_g ($\theta_g > 0$ when $\phi_g = 0^o; \theta_g < 0$ when $\phi_g = 180^o$). Other parameters are : $\theta_i = 135^o, \phi_i = 180^o, \theta_s = 45^o, \phi_s = 0^o, b = 10\lambda_0, a_1 = 2\lambda_0, a_2 = 1.8\lambda_0$.

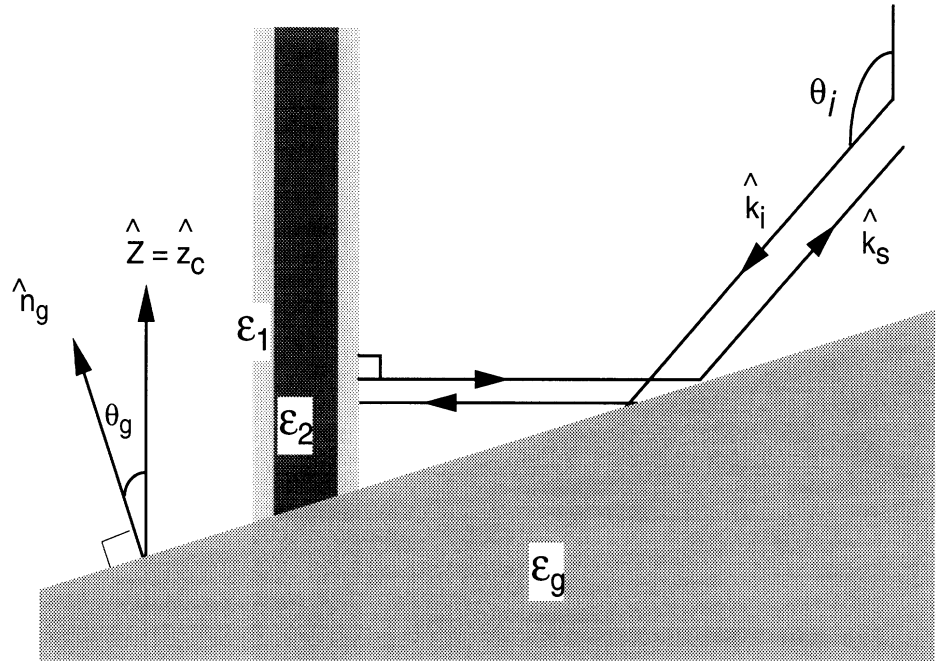

Figure 10: The geometry of the scattering configurations for a cylinder over a tilted ground where a strong backscatter can be observed.

Appendix III

A Monte Carlo Coherent Scattering Model For Forest Canopies Using Fractal-Generated Trees

A Monte Carlo Coherent Scattering Model For Forest Canopies Using Fractal-Generated Trees

Yi-Cheng Lin and Kamal Sarabandi

Radiation Laboratory
Department of Electrical Engineering and Computer Science
The University of Michigan
Ann Arbor, MI 48109-2122

ABSTRACT

A coherent scattering model for tree canopies based on a Monte Carlo simulation of scattering from fractal-generated trees is developed and verified in this paper. In contrast to incoherent models, the present model calculates the coherent backscatter from forest canopies composed of realistic tree structures where the relative phase information from individual scatterers is preserved. Computer generation of tree architectures faithful to the real stand is achieved by employing fractal concepts and Lindenmayer systems as well as incorporating the in-situ measured data. The electromagnetic scattering problem is treated by considering the tree structure as a cluster of scatterers composed of cylinders (trunks and branches) and disks (leaves) above an arbitrary tilted plane (ground). Using the single scattering approximation, the total scattered field is obtained from the coherent addition of the individual scattering from each scatterer illuminated by a mean field. Foldy's approximation is invoked to calculate the mean field within the forest canopy which is modeled as a multi-layer inhomogeneous medium. Backscatter statistics are acquired via a Monte Carlo simulation over a large number of realizations. The accuracy of the model is verified using the measured data acquired by a multi-frequency and multi-polarization SAR (SIR-C) from a maple stand at many incidence angles. A sensitivity analysis shows that the ground tilt angle and the tree structure may significantly affect the polarimetric radar response, especially at lower frequencies.

1 Introduction

Microwave radar remote sensing has been accepted as a viable instrument for monitoring and assessing significant parameters of forest ecosystems such as LAI and vegetation biomass [1]. Over the past decade much effort has been devoted to the development of scattering models for vegetation canopies as a step towards retrieving the forest biophysical parameters from a set of radar measurements [2].

Radiative transfer (RT) theory [3] is the most widely used model for characterization of scattering from a forest canopy [4]. When the medium consists of sparse scatterers that are small compared to the field correlation length within the random medium, RT theory can accurately predict the second moments of the radar backscatter statistics. However, no information regarding the absolute phase, an important quantity required for investigating the response of a forest to an interferometric SAR, can be extracted from a RT model. The other shortcoming of RT theory is its inability to account for the coherent effects that may exist between different scatterers or scattering mechanisms. Recent investigations on scattering behavior of tree canopies have shown that both backscattering and attenuation are significantly influenced by tree architecture [5]. Therefore, development of a coherent scattering model that accounts for tree architecture is crucial for the accurate estimation of radar behavior of forest canopies.

Modeling vegetation using coherent approaches has attained prominence over the past decades. The distorted Born approximation has been known as one of the basic approaches used for coherent modeling of vegetation [6], where each scatterer is illuminated by a mean field and the backscattered fields are added coherently. For short vegetation Yueh et al. [7] considered the effect of the soybean plant structure on radar backscatter using a two-scale branching model. Similarly, a coherent model for cultural grass canopies, where the dimensions of the vegetation particles such as grass blades and stems are comparable to the medium height dimension, has also been developed [8]. It was shown that at low microwave frequencies the relative positions of scatterers and plants with respect to each other affect the polarimetric backscatter response of vegetation canopies. In these models the structure of the vegetation is considered from a statistical point of view and therefore only the second moments of the scattered fields are provided, that is, the absolute phase information is lost.

Further investigations have explored the coherent scattering from a 3-D tree structure. In [9] the radar backscatter was simulated for various deciduous tree types using fractal theory [10] for the tree structure. In a more recent paper [11] Lindenmayer Systems (L-systems) [12], useful tools for implementation of fractal patterns or structures, were employed to develop simple 3-D tree structures of the order of few wavelengths to examine the importance of coherent and multiple scattering. A straightforward approach in constructing the tree structure was carried out in [13] where an accurate description of particle positions was characterized for a red pine tree using surveying tools. In this model the tree structure is divided into cylinders whose backscattered fields are added coherently via the distorted Born approximation.

The purpose of this paper is to develop and validate a comprehensive coherent scattering model for forest canopies, which can account for the coherent effect due to

the tree structure and provide information about the absolute phase of the backscattered field. The proposed model is comprised of three major components: (1) accurate generation of tree structures based on few physical parameters, (2) evaluation of scattered fields, and (3) Monte Carlo simulation. In the tree structure modeling, fractal-based L-systems are employed to construct a realistic tree structure incorporating the ground truth data of the desired stand. As will be shown, the spatial and angular distribution of branches strongly influences the behavior of radar backscatter, indicating the importance of the tree-generating code in constructing the fine features of tree structures. In the scattering model, individual tree components located above a tilted dielectric plane are illuminated by the mean field, and the scattered fields are computed and then added coherently. The branches and tree trunks are modeled by stratified dielectric cylinders and leaves are modeled by dielectric disks and needles of arbitrary cross sections. The mean field at a given point within the tree structure, which accounts for the phase change and the attenuation due to the scattering and absorption losses of vegetation particles, is calculated using Foldy's approximation [3]. Finally, a Monte Carlo simulation is performed on a large number of fractal generated trees to characterize the statistics of the backscattered signals. Another feature of the proposed coherent model is its capability in accounting for the effect of a nonuniform extinction profile within a forest canopy. The accuracy of the model is compared with the backscatter measurements acquired by SIR-C from a forest test site in Raco, Michigan.

In what follows, we first describe the procedure for generation of tree structures using stochastic L-systems. Next the construction of the coherent scattering model and the Monte Carlo simulation is explained. Then, the validity of the model is examined against L- and C-band backscatter measurements of a well characterized forest stand. A sensitivity study is also carried out to examine the degree of dependency of polarimetric backscatter on forest parameters.

2 Fractal Model for Generation of Tree Structures

2.1 Fractal Theory and Lindenmayer Systems

Tree structures in nature are complex and their mathematical description seems to require a large number of independent parameters. Contrary to this observation, it has been shown that geometrical features of most botanical structures can be explained using fractal theory where only a few parameters are required to specify the vegetation structure. The mathematical concept of fractals was originated by Mandelbrot [10] in the early seventies. Currently fractal theory is the most popular mathematical model used for relating natural structures to abstract geometries. Mandelbrot defined a fractal as a set whose Hausdorff-Besicovitch dimension strictly exceeded the topological dimension. In other words, the notion of fractal is defined only in the limit. However, in order to apply the fractal concept to practical problems, a finite curve is usually considered as an approximation of an infinite fractal so long as the significant properties of both are closely related. A distinctive feature of a finite fractal is the

self-similarity which is kept through the derivation process.

To implement fractal theory, L-systems have been well-known tools for the construction of fractal patterns or structures where the *self-similarity* is preserved through a so-called rewriting process [12]. L-systems were originally proposed by Lindenmayer [14], who applied it to the development of lower forms of plant life, such as red algae. L-systems, also called developmental systems, have since been applied in many fields, including formal language theory and biomathematics. The features of L-systems consist of the structural grammar rules and recursive processes which can easily be implemented by modern computers.

In L-systems, a tree structure G is specified by three components: (1) a set of edge labels V, (2) an initiator w, called *axiom*, with labels from V, and (3) a set of tree growth productions P. In compact notation this tree-growing process is symbolized by $G =< V, w, P >$. Given a tree structure G, a tree T_2 is directly derived from a tree T_1 ($T_1 \Rightarrow T_2$) if T_2 is obtained from T_1 by simultaneously replacing each edge in T_1 by its successor according to the production set P. A tree T is generated by G in a derivation of length n if there exists a sequence of trees T_0, T_1, ..., T_n such that $T_0 = w$, and $T_0 \Rightarrow T_1 \Rightarrow ... \Rightarrow T_n = T$. Figure 1 shows an example of a simple two-dimensional fractal tree of length 4, where the *self-similarity* can be easily observed through each successive process.

2.2 Botanical Modeling

In order to simulate realistic tree structures, botanical properties must be incorporated into the tree generation. In this section, several botanical features such as branch dimension rules, leaf attachment, and tree type development are described.

The cross section and the length of younger branches decrease as the branching process progresses. At a node where a branch splits into two or more branches, a common practice for determining the relationship between the radius of the originating branch (r_a) and the radius of the younger branches (r_b and r_c) is the application of the conservation law of the cross sectional area, given by:

$$r_a^2 = r_b^2 + r_c^2. \tag{1}$$

The relationship between the radius of the new branches (i.e. r_b and r_c) is specific to the tree type, and should be specified according to the ground truth measurements. Another parameter to be specified is the relationship between the length of the new and old branches (l_a and l_b, respectively). Defining g as the growth rate parameter, we have

$$l_b = l_a/g. \tag{2}$$

For a three-dimensional branching structure, two branching angles, the tilt angle θ and rotation angle ϕ, must be specified to characterize the relationship between the orientation of the new and the old branches.

Most leaves are attached to the end of the final branches noting that the term leaf here refers to a general composite leaf which may be comprised of many leaflets. The

number of leaves surrounding a branch is a function of many factors including the tree species, tree density, and the local environment. The tree generation algorithm developed in this paper allows the user to specify the number of leaves per final branch as well as a local orientation distribution for the leaves. The orientation of a leaf, defined by the unit normal to the leaf surface, is mostly characterized by the associated position and orientation of the end branch with respect to the global coordinate system. However some relatively narrow distribution function is added to allow for natural variations of leaf orientations.

Based on the architectural characteristics, tree structures can be categorized into three primary classes: columnar, decurrent, and excurrent, which may be represented by coconut, maple, and pine trees respectively [15]. In the majority of deciduous trees, the lateral branches grow as fast as, or faster than, the terminal shoot, giving rise to the deliquescent growth habit where the central stem eventually disappears from repeated forking to form a large spreading crown. This branching pattern is termed decurrent. On the other hand, most coniferous species belong to the excurrent class, where the main stem outgrows the lateral branches giving rise to cone-shaped crowns and a clearly defined bole. In this study, a library of typical tree structures is constructed that can easily be fine-tuned to simulate the desired tree stands. Figure 2 shows two fractal trees of decurrent and excurrent types generated by the developed tree-generating algorithms of this study.

2.3 Computer Implementation

The computer work in the development of the tree structure consists of three main components: the encoding, decoding, and visualization. In L-systems, the encoding is accomplished by iterating the labels with prescribed productions and length. A long label string, like DNA in biology, is obtained at the end of the processes, holding embedded information about the tree structure. Then this long label string is decoded (or translated) into a tree structure through a so called *turtle graph* interpreter [12]. Numerical calculation is performed in this stage to quantify the geometries of the entire tree structure.

Once the fractal tree is created, the tree data file usually contains a large number of tree components and it is difficult to examine the accuracy by manual inspection of the numerical data. Visual inspection of the tree image is a better way at this point. In addition, real-time visualization of the tree structure during the developing stage can also assist the user in learning the sensitivity of the fractal parameters to the tree structure. In this study, a visualization program is developed using the PostScript language where real-time display and printout can be easily performed without any extra software. This program is capable of projecting a 3-D fractal tree structure into a 2-D image with the functions of arbitrary scaling and perspective view. The red pine shown in Figure 2(b) is viewed at 20° measured from the horizontal plane.

3 Coherent Scattering from Forest Canopies

In this section, a coherent scattering model is developed to calculate the polarimetric radar response of the fractal-generated trees. Once a tree is created, it is treated as a cluster of scatterers composed of cylinders (trunks and branches) and disks (leaves) with specific position, orientation, and geometric shape and size, as shown in Figure 3. It is assumed that the entire tree is illuminated by a plane wave, whose direction of propagation is denoted by a unit vector $\hat{k}_i$ and is given by

$$\mathbf{E^i}(\mathbf{r}) = \mathbf{E}_o^i e^{ik_o \hat{k}_i \cdot \mathbf{r}}. \tag{3}$$

The scattered field in the far zone is next calculated for individual trees. Since the uncertainty in the relative position of trees with respect to each other is usually of the order of many wavelengths, the total scattered power can simply be determined by the incoherent addition of scattered power from individual trees. To the first order of approximation, the scattering from a tree is approximated by the superposition of the scattered field from each scatterer within the tree structure. Hence, neglecting the effect of multiple scattering among the scatterers, the total scattered field from a single tree can be evaluated from

$$\mathbf{E}^s = \frac{e^{ikr}}{r} \sum_{n=1}^{N} e^{i\phi_n} \mathbf{S}_n \cdot \mathbf{E}_o^i, \tag{4}$$

where N is the total number of the scatterers within a tree structure, $\mathbf{S}_n$ is the scattering matrix of the n-th scatterer above a dielectric plane and ϕ_n is a phase compensation term accounting for the shift of the phase reference from the local coordinate system of the n-th scatterer to the global coordinate phase reference. Denoting the position of the n-th scatterer in the global coordinate system by $\mathbf{r_n}$, ϕ_n is given by

$$\phi_n = (\hat{k}_i - \hat{k}_s) \cdot \mathbf{r_n}, \tag{5}$$

where $\hat{k}_s$ is the unit vector representing the propagation direction of the scattered field.

In order to compute the local scattering matrix $\mathbf{S}_n$ let us consider a single scatterer above a dielectric plane, as shown in Figure 4. Neglecting the multiple scattering between the scatterer and its mirror image, each scatterer mainly contributes four scattering components, denoted by: (1) direct scattering denoted by $\mathbf{S}_n^t$, (2) ground-scatterer scattering denoted by $\mathbf{S}_n^{tg}$, (3) scatterer-ground scattering denoted by $\mathbf{S}_n^{gt}$, and (4) ground-scatterer-ground scattering denoted by $\mathbf{S}_n^{gtg}$, as shown in Figure 4. The scattering matrix $\mathbf{S}_n$ in terms of its components can be written as

$$\mathbf{S}_n = \mathbf{S}_n^t + \mathbf{S}_n^{gt} + \mathbf{S}_n^{tg} + \mathbf{S}_n^{gtg}, \tag{6}$$

where

$$\mathbf{S}_n^t = \mathbf{S}_\mathbf{n}^\mathbf{0}(\hat{k}_s, \hat{k}_i), \tag{7}$$

$$\mathbf{S}_n^{gt} = e^{i\tau_s} \mathbf{R}(\hat{k}_s, \hat{k}_{gs}) \cdot \mathbf{S}_\mathbf{n}^\mathbf{0}(\hat{k}_{gs}, \hat{k}_i), \tag{8}$$

$$\mathbf{S}_n^{tg} = e^{i\tau_i} \mathbf{S}_\mathbf{n}^\mathbf{0}(\hat{k}_s, \hat{k}_{gi}) \cdot \mathbf{R}(\hat{k}_{gi}, \hat{k}_i), \tag{9}$$

$$\mathbf{S}_n^{gtg} = e^{i(\tau_i + \tau_s)} \mathbf{R}(\hat{k}_s, \hat{k}_{gs}) \cdot \mathbf{S}_\mathbf{n}^\mathbf{0}(\hat{k}_{gs}, \hat{k}_{gi}) \cdot \mathbf{R}(\hat{k}_{gi}, \hat{k}_i), \tag{10}$$

and

$$\hat{k}_{gi} = \hat{k}_i - 2\hat{n}_g(\hat{n}_g \cdot \hat{k}_i), \tag{11}$$

$$\hat{k}_{gs} = \hat{k}_s - 2\hat{n}_g(\hat{n}_g \cdot \hat{k}_s), \tag{12}$$

$$\tau_i = -2k_0(\mathbf{r_n} \cdot \hat{n}_g)(\hat{n}_g \cdot \hat{k}_i), \tag{13}$$

$$\tau_s = 2k_0(\mathbf{r_n} \cdot \hat{n}_g)(\hat{n}_g \cdot \hat{k}_s). \tag{14}$$

In the expressions given by (7)-(10), $\mathbf{S_n^0}$ is the bistatic scattering matrix of the n-th scatterer in free space. The direction of incidence and scattering are denoted by unit vectors in the argument of $\mathbf{S_n^0}$. In the above expressions, $\hat{n}_g$ is the unit vector normal to the tilted ground surface. The phase terms τ_i and τ_s account for the extra path lengths of the image excitation and the image scattered waves respectively. $\mathbf{R}$ is the reflection matrix of the dielectric plane whose elements are derived in terms of the Fresnel reflection coefficients and the polarization transformation due to the ground tilt angle. The explicit expressions of the reflection matrix of a tilted dielectric plane ($\mathbf{R}$) with an arbitrary slope and the expressions for the bistatic scattering matrices ($\mathbf{S_n^0}$) of large scatterers like trunks and primary branches are given in [16], where the semi-exact solution together with the physical optics approximation are derived for the calculation of scattering from a stratified dielectric cylinder above a tilted dielectric plane. The formulae for the scattering matrices of small scatterers like twigs and leaves are constructed based on the expressions given in [17,18].

The above analysis is not quite complete since in the calculation of scattering from the n-th scatterer the other scatterers are assumed to be transparent. The second or higher-order analysis, which takes into account the multiple scattering among the tree structures, is fairly complicated and is beyond the scope of this paper. However, the effect of attenuation and phase change of the coherent wave propagating in the random media can be readily modeled by calculating the mean field within the random medium.

Consider a coherent radar wave propagating in a statistically uniform random medium. Based on Foldy's approximation [3], the variation of the mean field $\mathbf{E}$ with respect to the distance s along the direction $\hat{k}$ is generally governed by

$$\frac{d\mathbf{E}}{ds} = i\mathbf{K} \cdot \mathbf{E}, \tag{15}$$

where

$$\mathbf{K} = \begin{bmatrix} k_0 + M_{vv} & M_{vh} \\ M_{hv} & k_0 + M_{hh} \end{bmatrix}, \tag{16}$$

and

$$M_{pq} = \frac{2\pi n_0}{k_0} < S_{pq}^0(\hat{k}, \hat{k}) > . \tag{17}$$

Here k_o is the wave number of free space; n_0 is the volume density of the scatterer; and $< S_{pq}^0(\hat{k}, \hat{k}) >$ is the ensemble average of the forward scattering matrix, (p and q can be v or h). Using the standard eigen-analysis, the differential equation (15) can easily be solved and the solution is given by

$$\mathbf{E}(s) = e^{ik_0 s}\mathbf{T}(s, \hat{k}) \cdot \mathbf{E}^0, \tag{18}$$

where $\mathbf{E^0}$ is the field at $s = 0$ and $\mathbf{T}$ is the transmissivity matrix accounting for the extinction due to scattering and absorption. In most natural structures, azimuthal symmetry can be assumed where $M_{vh} = M_{hv} = 0$ and the transmissivity matrix is reduced to

$$\mathbf{T} = \begin{bmatrix} e^{iM_{vv}s} & 0 \\ 0 & e^{iM_{hh}s} \end{bmatrix}. \tag{19}$$

Note that the transmissivity matrix defined in (18) excludes the phase terms due to free space path lengths, and merely accounts for the perturbation in propagation caused by the vegetation.

To include the effect of wave extinction in the scattering model, consider a situation when the entire tree structure is embedded in an effective medium with an effective propagation constant given by (16). Under the aforementioned approximations the expressions for the components of the n-th scattering matrix in the backscatter direction should be modified as follows:

$$\mathbf{S}_n^t = \mathbf{T}_n^i \cdot \mathbf{S}_n^0(-\hat{k}_i, \hat{k}_i) \cdot \mathbf{T}_n^i, \tag{20}$$

$$\mathbf{S}_n^{gt} = e^{i\tau_n}\mathbf{T}^t \cdot \mathbf{R} \cdot \mathbf{T}_n^r \cdot \mathbf{S}_n^0(-\hat{k}_r, \hat{k}_i) \cdot \mathbf{T}_n^i, \tag{21}$$

$$\mathbf{S}_n^{tg} = e^{i\tau_n}\mathbf{T}_n^i \cdot \mathbf{S}_n^0(-\hat{k}_i, \hat{k}_r) \cdot \mathbf{T}_n^r \cdot \mathbf{R} \cdot \mathbf{T}^t, \tag{22}$$

$$\mathbf{S}_n^{gtg} = e^{i2\tau_n}\mathbf{T}^t \cdot \mathbf{R} \cdot \mathbf{T}_n^r \cdot \mathbf{S}_n^0(-\hat{k}_r, \hat{k}_r) \cdot \mathbf{T}_n^r \cdot \mathbf{R} \cdot \mathbf{T}^t, \tag{23}$$

with

$$\hat{k}_r = \hat{k}_i - 2\hat{n}_g(\hat{n}_g \cdot \hat{k}_i), \tag{24}$$

$$\tau_n = 2k_0(\mathbf{r_n} \cdot \hat{n}_g)(\hat{n}_g \cdot \hat{k}_r), \tag{25}$$

where $\mathbf{T}_n^i, \mathbf{T}_n^r$, and $\mathbf{T}^t$ are the transmissivity matrices, respectively, for the direct, reflected, and total traveling path as shown in Figure 5. In the derivation of (20)-(23) the reciprocal property of wave propagation, is employed, i.e., $\mathbf{T}(s, \hat{k}) = \mathbf{T}(s, -\hat{k})$, which results in the expected reciprocal scattering relation $\mathbf{S_n^{gt}} = (\mathbf{S_n^{tg}})^{-t}$. Here the superscript $(\cdot)^{-t}$ denotes the operation of matrix transposition followed by negation of the cross-polarized elements in order to be consistent with the the forward scattering alignment convention [1].

Distributions of vegetation particle type and size is non-uniform along the vertical extent of most forest stands unlike what has been assumed in the aforementioned existing scattering models mostly for the lack of knowledge of such distributions. In the proposed model where the exact description of particle distributions are available, propagation and scattering of the mean field within the forest medium can be characterized rather accurately. To account for the vertical inhomogeneity, consider an M-layered random media above a tilted ground surface illuminated by a plane wave. Each layer, with thickness $d_m (m = 1, 2, ..., M)$, is assumed to be parallel to the ground surface. It is also assumed that the boundaries between the layers are diffuse where no reflection or refraction can take place. Suppose the n-th scatterer is located in the m-th layer, then the objective is to calculate the transmissivity matrices $\mathbf{T}_n^i, \mathbf{T}_n^r$, and $\mathbf{T}^t$.

In the backscatter case, only the incident directions $\pm\hat{k}_i$ and the reflected directions $\pm\hat{k}_r$ are of interest. Therefore for each scatterer the forward scattering matrix should be calculated for both $\hat{k}_i$ and $\hat{k}_r$ directions. Then for each layer (say the m-th layer), the layered transmissivity matrix is computed by

$$\mathbf{T}_m^{i/r}(L_m) = \begin{bmatrix} e^{iM_{vv,m}^{i/r}L_m} & 0 \\ 0 & e^{iM_{hh,m}^{i/r}L_m} \end{bmatrix} \tag{26}$$

where $L_m = d_m/(\hat{n}_g \cdot \hat{k}_r)$ is the path length, and

$$\mathbf{M}_m^{i/r} = \frac{2\pi D_t}{k_0 d_m} \sum_n^{N_m} \mathbf{S}_n^0(\hat{k}_{i/r}, \hat{k}_{i/r}). \tag{27}$$

is the effective propagation constant for the m-th layer. In the above expression D_t is the tree density (number/m^2) and N_m is the number of particles of a single tree in the m-th layer. The final expressions for the transmissivity matrices can be written as

$$\mathbf{T}^t = \mathbf{T}_1^i(L_1)\mathbf{T}_2^i(L_2)...\mathbf{T}_M^i(L_M), \tag{28}$$

$$\mathbf{T}_n^i = \mathbf{T}_m^i(L_{mn}^i)\mathbf{T}_{m+1}^i(L_{m+1})...\mathbf{T}_M^i(L_M), \tag{29}$$

$$\mathbf{T}_n^r = \mathbf{T}_m^r(L_{mn}^r)\mathbf{T}_{m-1}^i(L_{m-1})...\mathbf{T}_1^i(L_1), \tag{30}$$

where L_{mn}^i and L_{mn}^r are the path length from the n-th scatter to the top and bottom of the m-th layer boundary along the $\hat{k}_i$ and $\hat{k}_r$ directions, respectively, as shown in Figure 5. These distances are given by $L_{mn}^i = (H_m - \mathbf{r}_n \cdot \hat{n}_g)/(\hat{n}_g \cdot \hat{k}_r)$ and $L_{mn}^r = (\mathbf{r}_n \cdot \hat{n}_g - H_{m-1})/(\hat{n}_g \cdot \hat{k}_r)$ where $H_m = \sum_{k=1}^m d_k$ represents the height of the upper interface of the m-th layer.

For distributed targets, the radar backscattering coefficients and phase difference statistics, instead of the scattering matrix, are usually the quantities of interest. These quantities can be derived from the second moments of the backscattered field components [19]. The statistics of the scattered field are approximated from a Monte Carlo simulation where a large number of tree structures are generated using stochastic L-systems and then the scattering matrix of all generated trees are computed. Computation of the scattering matrices is accomplished in the following manner. First the canopy height is discretized into M layers and the extinction coefficient of each layer and the integrated transmissivity matrices are computed as outlined previously. Then these quantities are used in (20)-(23) for calculating the scattering matrix of individual trees.

The computation involved in the calculation of the scattering matrices of individual leaves for many trees is too excessive to be carried out even with the fastest available computers. To solve this problem, the 4π solid angle covering the entire vector space representing the orientation direction of a leaf is discretized into a finite number and a look-up table for scattering matrices of a leaf oriented along all the discrete directions is generated for the three principal backscattering ($\mathbf{S}_n^0(-\hat{k}_i, \hat{k}_i)$ and $\mathbf{S}_n^0(-\hat{k}_r, \hat{k}_r)$) , forward scattering ($\mathbf{S}_n^0(\hat{k}_i, \hat{k}_i)$ and $\mathbf{S}_n^0(\hat{k}_r, \hat{k}_r)$), and bistatic scattering

($\mathbf{S}_n^0(-\hat{k}_r, \hat{k}_i)$ and $\mathbf{S}_n^0(-\hat{k}_i, \hat{k}_r)$) directions. The number of discrete orientation directions is determined from the ratio of a typical leaf dimension to the wavelength (a/λ). According to this scheme the number of the discrete points should increase with increasing a/λ. A similar scheme may be used for branches, however, we found that this may unnecessarily increase the CPU time due to a large variability in diameter and length of the branches.

In order to calculate the desired backscatter statistics, the differential covariance matrix of the backscattered field must be evaluated. As described earlier, the backscattered fields of adjacent trees in a forest are uncorrelated at microwave frequencies and above. Therefore the backscattered power from individual trees can be added and the covariance matrix elements are proportional to the tree density D_t and are given by

$$W_{pqst}^0 = D_t < S_{pq} S_{st}^* >, \tag{31}$$

where $p, q, s, t \in \{v, h\}$. According to this definition for the differential covariance matrix, the backscattering coefficient can be obtained from

$$\sigma_{pq}^0 = 4\pi W_{pqpq}^0. \tag{32}$$

4 Model Verification

In this section, the accuracy and validity of the developed model is examined using a set of measured data acquired by the Space-shuttle Imaging Radar-C/X-Band Synthetic Aperture Radar (SIR-C/X-SAR). The collected ground truth and the radar parameters, such as frequency and incidence angle, are used as model input. In this section we also present some examples to demonstrate the sensitivity of radar backscatter to some important forest parameters.

4.1 SIR-C/X-SAR

The SIR-C/X-SAR radar system [22] was flown aboard the shuttle Endeavor in the spring (SRL-1) and fall (SRL-2) of 1994. This mission was the first of its kind where a beam-steerable, multi-frequency, and multi-polarization space-borne synthetic aperture radar was deployed. The SIR-C/X-SAR system operated at L- (1.25 GHz), C- (5.3 GHz), and X-band (9.6 GHz). The L- and C-band SARs were configured to collect polarimetric data whereas the X-band SAR was a single channel radar and collected the backscatter data at vv polarization. The look angle of the system was varied from 15^o to 60^o. In this study, the polarimetric SIR-C data (L- and C-band) during the SRL-2 is selected for comparison with the results predicted by the model developed in this paper.

4.2 Ground Truth

Raco, located in the eastern part of Michigan's Upper Peninsula, was designated by NASA as a calibration and ecological Supersite and has been a test site for our radar

Tree Density :	1700/Hectare
Tree Height :	16.8 m
Trunk Diameter (DBH) :	14 cm
Leaf Density :	382 $\#/m^3$
Leaf Area :	50 $cm^2/\#$
Leaf Thickness :	0.2 mm
Leaf Moisture (m_g) :	0.51
Wood Moisture (m_g) :	0.60
Soil Moisture (m_v) :	0.18

Table 1: Ground Truth of Stand 31

	L-band	C-band
Leaf	$17.9 + i6.0$	$14.7 + i4.7$
Wood	$32.1 + i10.0$	$27.7 + i8.4$
Soil	$9.7 + i1.6$	$9.4 + i1.5$

Table 2: Dielectric properties of Stand 31

remote sensing activities since 1991 [20,21]. Great efforts have been devoted towards characterizing ground inventories and the site has been imaged by ERS-1, JERS-1, SIR-C/X-SAR, and JPL AIRSAR. The main research objective at this site has been relating the measured SAR backscatter data to the forest ecological/biophysical parameters, which are essential input parameters for the ecological models used for the study of land and atmosphere processes.

The Raco Supersite contains most boreal forest species and many of the temperate species. The SIR-C/X-SAR overflight occurred in the fall, a time of some seasonal change where trees begin to dry and the deciduous leaves begin to undergo their fall color change. During the SIR-C overflight (October 1994), the leaves were still predominantly green. Color change happened towards the end of the mission.

In this study, a deciduous forest stand, denoted in the existing report [20] as Stand 31, is selected as a test stand. This stand consists of a large number of red maple as well as a few sugar maple, uniformly covering an area about 300 m by 300 m on flat terrain. The ground truth of this stand has been collected since 1991, and a summary of its pertinent parameters is reported in Table 1. The vegetation and soil dielectric constants during the SIR-C overflights are reported in Table 2, and are derived from the measured moisture values using the empirical models described in [23,24].

4.3 Simulation Results

The first step in obtaining the model prediction is to generate fractal trees faithful to the real tree structure of the desired forest stand. There are two phases for determining the input parameters for the tree generating code. The first phase is to characterize the coarse parameters such as the branching nature of the trees, the growth factors, and the finite fractal order. In the second phase, some of the fine input

parameters, such as the branch tilt angle and its distribution, are slightly tuned in order to minimize the difference between the simulated and measured backscattering coefficients σ^0. In general accomplishing the second phase is much more difficult than the first phase because there is no apparent rule for adjusting the parameters. To establish a set of rules of thumb for fine-tuning the parameters of tree structures, we performed a sensitivity analysis. The gradient of the desired radar backscatter parameters with respect to the desired tree structure parameters was determined and used for determining the fine tuning procedure. In this procedure, we allowed the fine tree parameters to be adjusted to within 10% of the measured ground truth parameter to account for the uncertainty in the ground truth measurements. It is assumed that the model (including tree generation and coherent scattering) is verified if the simulation results can simultaneously match the polarimetric SIR-C data for both frequencies and different incidence angles.

Figure 6 shows a photo of Stand 31 (taken in April, 1994), the fractal tree structure generated by the model, and its corresponding extinction coefficient (imaginary part of $\mathbf{M}_m^i$ in (17)) profile. It is noted that the wave attenuation at C-band is much greater than L-band, and the extinction coefficient for vertical polarization is slightly greater than that for horizontal polarization at both frequencies. This extinction coefficient profile is shaped according to the tree architecture and composition, which plays an important role in radar backscatter parameters including the position of the scattering phase center [25]. In this example, the entire tree canopy is divided into eleven layers, and the extinction coefficient is calculated as described in the previous section. It should be pointed out that the number of layers can be determined by imposing a step discontinuity threshold. Basically the algorithm starts with a moderate number of layers, calculates the extinction coefficient for each layer, and examines the step discontinuity. If the discontinuity between any two layers is larger than the prescribed threshold, these layers are divided into finer layers.

In performing Monte Carlo simulations, one should be careful of the convergence properties of the simulation. In all simulation results reported in this paper convergence was achieved to within ± 0.5 dB of the estimated mean values for less than 100 tree realizations. Figures 7(a) and 7(b) show, respectively, the convergence behavior of the backscattering coefficients at L- and C-band for forest Stand 31.

Figure 8 shows the comparison between the model prediction and the measured backscattering coefficients for three consecutive SIR-C overflights as a function of incidence angle at L- and C-band respectively. It is shown that an excellent agreement is achieved for all incidence angles and polarizations except for the C-band cross-polarized backscattering coefficient. The lack of accuracy for this polarization can be attributed to the effect of multiple scattering between branches or branches and leaves in the canopy crown. It shows that the measured C-band data is consistently higher than the simulated results by 1.3 dB which can be attributed to the overestimation of radiometric calibration constants. The computation time for each incidence angle point is about 35 minutes at L-band and 65 minutes at C-band on a Sun Sparc 20 workstation.

As mentioned in section 3, the total backscatter is comprised of different scattering components. Simulation results show that in all cases except for L-band hh

polarization the backscattering coefficients are dominated by the direct backscatter component (σ_t^0). The hh-polarized backscattering coefficient σ_{hh}^0 at L-band, depending on the incidence angle, is mostly dominated by the direct backscatter or the ground bounce term (σ_{gt}^0). The double ground bounce component (σ_{gtg}^0) is negligible for all cases because of the low transmissivity for this canopy (see Figure 12 for LAI=12). Figure 9 shows the scattering components of σ_{hh}^0 as a function of incidence angle. The analysis for characterizing the contribution of each scattering component is essential in determining the position of the scattering phase center of the forest.

It is also important to examine the effect of the inhomogeneity of the extinction profile (see Figure 6(d) on the backscattering coefficient. Figure 10 compares the co-polarized backscattering coefficients of Stand 31 where the forest is both modeled by a 2-layer medium and by an 11-layer medium. In the 2-layer model the tree canopy is composed of a trunk layer extending from 0–5 m and a crown layer which extends from 5–17 m. It can be observed that the 2-layer model overestimates the backscatter at lower incidence angles and underestimates at higher incidence angles. The discrepancy in this example is as high as 2.5 dB, and can be even higher for stands with higher leaf density. It is also found that the discrepancy increases with increasing frequency. For example, the discrepancy at L-band is only less than 0.3 dB. It should be mentioned that the CPU time for calculation of the backscattering coefficient for a 2-layer and an 11-layer forest is almost the same, because the mean field profile of the canopy is calculated before the Monte Carlo simulation is carried out.

The statistical behavior of the backscatter can also be obtained from the present model. Through the Monte Carlo simulations the desired histograms can be constructed by recording the backscatter results for each realization. Figure 11 shows the estimated probability density function (pdf) of backscattering coefficients in dB at incidence angle 43.6°. The pdf can provide additional information about the distributed target if the backscatter statistics are non-Gaussian. For instance, although the mean values of σ_{hh}^0 and σ_{vv}^0 at L-band are nearly identical, their pdfs are somewhat different from each other.

The transmissivity is another quantity with which to characterize a stand. Based on the extinction profile of the forest canopies, the transmissivity can be computed by integrating the attenuation of each layer. In Figure 12, the one-way transmissivity (from top to bottom) is calculated as a function of leaf area index (LAI), defined as the total leaf area (single side) per unit area of forest. It is shown that the horizontally polarized wave can more easily penetrate the canopies than the vertically polarized wave. This phenomenon results from the fact that the tree trunk and branches are oriented mostly along the vertical direction.

To demonstrate the effect of tree structures on the radar backscatter, two examples are considered in this study. In the first example, denoted as Case 1, we change the branching angle $\Delta\theta$ from $22^o \pm 5^o$ (used in Stand 31) to $15^o \pm 3^o$ while keeping the other parameters the same. Figure 13 compares the orientation distribution of the branches for Stand 31 and Case 1 example. The pdfs of branch orientation are obtained by counting the number of branches in small increments of orientation angle for all the branch segments of a fractal tree, which included about 7500 branch segments in

Tree Structures	L-band			C-band		
	σ^o_{vv} (dB)	σ^o_{vh} (dB)	σ^o_{hh} (dB)	σ^o_{vv} (dB)	σ^o_{vh} (dB)	σ^o_{hh} (dB)
Stand 31	-8.8	-14.6	-8.2	-9.3	-16.4	-10.1
Case 1	-8.4	-16.1	-7.1	-7.9	-16.2	-8.7
Case 2	-13.2	-19.6	-9.1	-11.4	-21.6	-10.3

Table 3: Effect of tree structures on backscattering coefficients, simulated at $\theta_i = 43.6^o$.

more than 20 classes of diameters and lengths. In the second example referred to as Case 2, we changed the tree height and trunk diameter while keeping the dry biomass unchanged (14.4 kg/m^2). A tree structure of Case 2 having height 8.6 m and trunk diameter $17cm$ is shown in Figure 2(a). The backscattering coefficients calculated for these three tree structures are given in Table 3, which indicates a significant variability in the backscattering coefficients among the three simulated forest stands of different geometrical structures having identical biomass.

The effect of the ground tilt angle on the radar backscatter from the forest canopy is also investigated in this study. Using the same parameters of Stand 31 except for changing the ground tilt angle θ_g from 0^o to 10^o, the backscattering coefficients are computed as a function of the azimuthal look angle ϕ_i for incidence angle θ_i at 25.4^o. As expected, simulation results show that the radar backscatter is not sensitive to the tilt plane at C-band since most of the backscattered field emanates from the crown layer. However, at L-band the radar backscatters, especially σ^o_{hh} and σ^o_{vh}, show sensitivity to the ground tilt angle (see Figure 14(a)). Near the azimuthal look angle $\phi_i = 70^o$, there are noticeable increases in σ^0_{hh} and σ^0_{vh} which can be attributed to a ground-trunk interaction. To illustrate this point, consider a single cylinder oriented along the $\hat{z}_c$ direction standing on a tilted ground surface with a unit normal $\hat{n}_g$, as shown in Figure 14(b). The ground-trunk scattered ray is parallel to the incident ray when the following relationship is satisfied:

$$\hat{k}_i \cdot \hat{z}_c = (\hat{k}_i \cdot \hat{n}_g)(\hat{n}_g \cdot \hat{z}_c). \tag{33}$$

Assuming $\hat{z}_c$ is along the vertical direction Z (most trees grow vertically in spite of the tilted ground), the above equation can be readily reduced to an explicit expression given by

$$\cos\phi_i = \frac{2\sin^2\theta_g}{\tan\theta_i \sin 2\theta_g}. \tag{34}$$

Using this expression a maximum backscatter is expected at $\phi_i = 68^o$ when $\theta_g = 10^o$ and $\theta_i = 25.4^o$. For this particular look angle significant hh-polarized and cross-polarized backscatters are generated, as shown in Figure 14(c) which has a very good coincidence with Figure 14(a). The radar cross section in Figure 14(c) is simulated from a cylinder of radius $a = 7.2cm$, length $b = 7.2m$, and dielectric constant $\epsilon = 32.1 + i10.0$ vertically standing on a tilted dielectric plane with $\theta_g = 10^o$ and $\epsilon_g = 9.7 + i1.6$ illuminated by a plane wave with incidence angle $\theta_i = 25.4^o$.

5 Conclusions

A coherent scattering model for forest canopies based on a Monte Carlo simulation of fractal-generated trees is developed in this paper. A coherent model offers three major advantages over the existing incoherent scattering models: (1) the model preserves the effect of architectural structure of the trees which manifest itself in the extinction and scattering profiles, (2) the model provides complete statistics of the scattered field instead of just its second moments, and (3) the model is capable of simulating the scattering from forest canopies on a tilted ground surface. In general the coherent scattering model is comprised of two main components: (1) a tree structure generating model which is developed based on stochastic L-systems, (2) a first-order scattering model which can handle radially stratified cylinders and dielectric disks and needles of arbitrary cross section.

The validity and accuracy of the model was demonstrated by comparing the results based on the model simulation with the backscattering coefficients measured by polarimetric L- and C-band SIR-C at three different incidence angles. A very good agreement between the measured quantities and the model predictions is obtained with the exception of σ^0_{vh} for C-band which is believed due to the existence of multiple scattering in the crown layer. A sensitivity study was also carried out to demonstrate the effects of tilted ground surfaces and tree structures on the radar backscattering coefficients.

6 Acknowledgment

This investigation was supported by NASA Office of Mission to Planet Earth under contract NAGW 4555. The authors are thankful to Dr. L. Pierce for helping in extracting the SIR-C data used in this paper.

Appendix

The parameters for L-systems for generating the maple tree used in this paper is given below. Note that some user-defined symbols other than those used by L-systems [12] are rendered to account for the sophisticated features of the tree structures. For example, the branch tapering symbols (),[], and {} are used to denote small, medium, and large branch tapering respectively.

• Fractal Coding Parameters:
Length (number of iteration) n: 4
Axiom/initiator w:
FFF!(+A){!FF(+A){!FF(++A){!F(+B)!(++B){F!(+A)!(++A)[!F[++B]![++B]![+B]]}}}}
Production p_1:
A: → ff(+A)!f(+A){!(++A){!f[+A]!f[+B]}}}
Production p_2:
B: → f(+A)[!f(++B)[!f[++B]!f[+B][-B]]]
Production p_3:
F: → FF
Production p_4:
f: → ff
where F and f are respectively vertical and horizontal forward steps.

• Geometrical parameters include tree diameter at breast height (DBH), branching angle (θ_b) and rotation angle (ϕ_b), trunk tilt angle (θ_t), leaf orientation angle (θ_l), number of leaflet ($N_{leaflet}$), leaf radius (a_l), leaf thickness (t_l), stem radius (a_s), and stem length (l_s).

mean(DBH),	std(DBH),	mean(F),	std(F),	mean(f),	std(f)	(cm)
14.	3.	9.	1.	7.5	1.	
mean(θ_b),	std(θ_b),	mean(ϕ_b),	std(ϕ_b)	(deg)		
22.	5.	137.5	10.			
mean(θ_t),	std(θ_t),	mean(θ_l),	std(θ_l)	(deg)		
0.	3.	5.	10.			
$N_{leaflet}$,	a_l,	t_l,	a_s,	l_s,	(cm)	
5	4.0	0.02	0.1	8.		

where mean(·) and std(·) refers to the statistical mean and the standard deviation of the parameters respectively.

• Display postscript parameters:

Xstart,	Ystart,	Zstart,	θ_{view},	ϕ_{view},	Scale
300	300	80	90	0	25

References

[1] F. T. Ulaby and C. Elachi, *Radar Polarimetry for Geoscience Applications*, Artech House, 1990.

[2] M. C. Dobson, F. T. Ulaby, T. Le Toan, A. Beaudoin, and E. S. Kasischke, "Dependence of radar backscatter on conifer forest biomass," *IEEE Trans. Geosci. Remote Sensing*, vol. 30, pp. 402-415, 1992.

[3] L. Tsang, J. A. Kong, and R. T. Shin, *Theory of Microwave Remote Sensing*, New York : Wiley Interscience, 1985.

[4] F. T. Ulaby, K. Sarabandi, K. MacDonald, M. Whitt, and M. C. Dobson, " Michigan Microwave Canopy Scattering Model", *Int. J. Remote Sensing*, Vol. 11, NO. 7, pp. 1223-1253, 1990.

[5] M. L. Imhoff, "A theoretical analysis of the effect of forest structure on SAR backscatter and the remote sensing of biomass", *IEEE Trans. Geosci. Remote Sensing*, Vol. 33, No. 2, pp. 341-352, 1995.

[6] N. S. Chauhan, R. H. Lang, and K. J. Ranson, "Radar Modeling of a Boreal Forest" *IEEE Trans. Geosci. Remote Sensing*, Vol. 29, No. 4, pp. 627-638, 1991.

[7] S. H. Yueh, J. A. Kong, J. K. Jao, R. T. Shin, and T. L. Toan, "Branching model for vegetation," *IEEE Trans. Geosci. Remote Sensing*, Vol. 30, No. 2, pp. 390-402, 1992.

[8] J. M. Stiles and K. Sarabandi, "Scattering from cultural grass canopies: a phase coherent model," Proceedings of IGARSS'96 held in Lincoln, pp. 720-722, 1996.

[9] C. C. Borel and R. E. McIntosh, "A backscattering model for various foliated decidous tree types at millimeter wavelengths," Proceedings of IGARSS'86 held in Zurich, pp. 867-872, 1986

[10] B. Mandelbrot, *Fractal Geometry of Nature*, New York, W. H. Freeman Company, 1983.

[11] G. Zhang, L. Tsang, and Z. Chen, "Collective scattering effects of trees generated by stochastic Lindenmayer systems," *Microwave and Optical Technology Letters* , vol. 11, no. 2, pp. 107-111, 1996.

[12] P. Prusinkiewicz and A. Lindenmayer, *The Algorithmic Beauty of Plants*, Spring-Verlag, New York, 1990.

[13] R. H. Lang, R. Landry, O. Kavakhioglu and J. C. Deguise,"Simulation of microwave backscatter from a red pine stand," in Multispectral and Microwave Sensing of Forestry, Hydrology, and Natural Reources, SPIE, Rome, Italy, vol. 2314, pp. 538-548, 1994.

[14] A. Lindenmayer, "Developmental algorithms for multicellular organisms: a survey of L-systems", *Journal of theoretical biology*, Vol. 54, pp. 3-22, 1975.

[15] M. H. Zimmermann and C. L. Brown, *Tree Structures and Function* , Springer-Verlag, New York, 1971.

[16] Y. C. Lin and K. Sarabandi, "Eletromagnetic scattering model for a tree trunk above a tilted ground plane", *IEEE Trans. Geosci. Remote Sensing*, Vol. 33. No. 4, pp.1063-1070, 1995.

[17] K. Sarabandi and T. B. A. Senior, "Low-frequency scattering from cylindrical strutures at oblique incidence," *IEEE Trans. Geosci. Remote Sensing*, Vol. 28, No. 5, pp. 879-885, 1990.

[18] M. A. Karam, A. K. Fung, and Y. M. M. Antar, "Electromagnetic wave scattering from some vegetation samples," *IEEE Trans. Geosci. Remote Sensing*, vol. 26, no. 6, pp. 799-808, 1988.

[19] K. Sarabandi, "Derivation of phase statistics from the Mueller matrix", *Radio Science*, Vol. 27, No. 5, pp. 553-560, 1992.

[20] K. M. Bergen, M. C. Dobson, T. L. Sharik, and I. Brodie, "Structure, Composition, and above-ground biomass of SIR-C/X-SAR and ERS-1 forest test stands 1991-1994, Raco Michigan Site ", Rep. 026511-7-T, The University of Michigan Radiation Laboratory, Oct., 1995

[21] K. M. Bergen, M. C. Dobson, L. E. Pierce, J. Kellndorfer, and P. Siqueira, "October 1994 SIR-C/X-SAR Mission : Ancilary data report, Raco Michigan Site ", Rep. 026511-6-T, The University of Michigan Radiation Laboratory, Oct., 1995

[22] R. L. Jordan, B. L. Huneycutt, and M. Werner, "The SIR-C/X-SAR synthetic aperture radar system," *IEEE Trans. Geosci. Remote Sensing*, vol. 33, pp. 829-839, July 1996.

[23] M. T. Hallikainen, F. T. Ulaby, M. C. Dobson, M. A. El-Rayes, and L.-K. Wu, "Microwave dielectric behavior of wet soil – Part I : empirical models and experimental observations," *IEEE Trans. Geosci. Remote Sensing*, vol. GE-23, pp. 25-34, 1985.

[24] F. T. Ulaby and M. A. Elrayes, "Microwave dielectric spectrum of vegetation, Part II: Dual-dispersion model," *IEEE Trans. Geosci. Remote Sensing*, vol. GE-25, pp. 550-557, 1987.

[25] K. Sarabandi, "Δk-Radar equivalent of interferometric SARs: a theoretical study for determination of vegetation height," *IEEE Trans. Geosci. Remote Sensing*, vol. 35, no. 5, pp. 1267-1276, 1997.

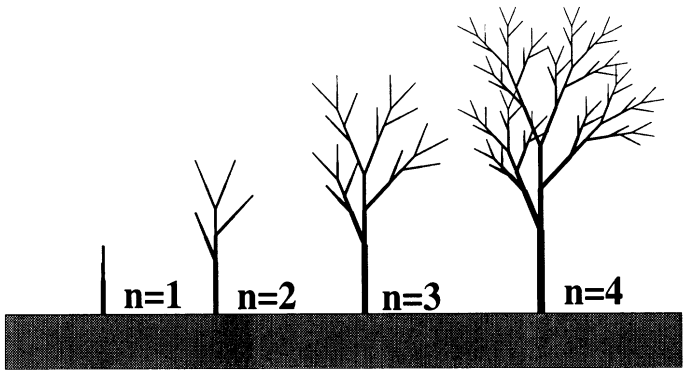

Figure 1: The growing process of a fractal tree.

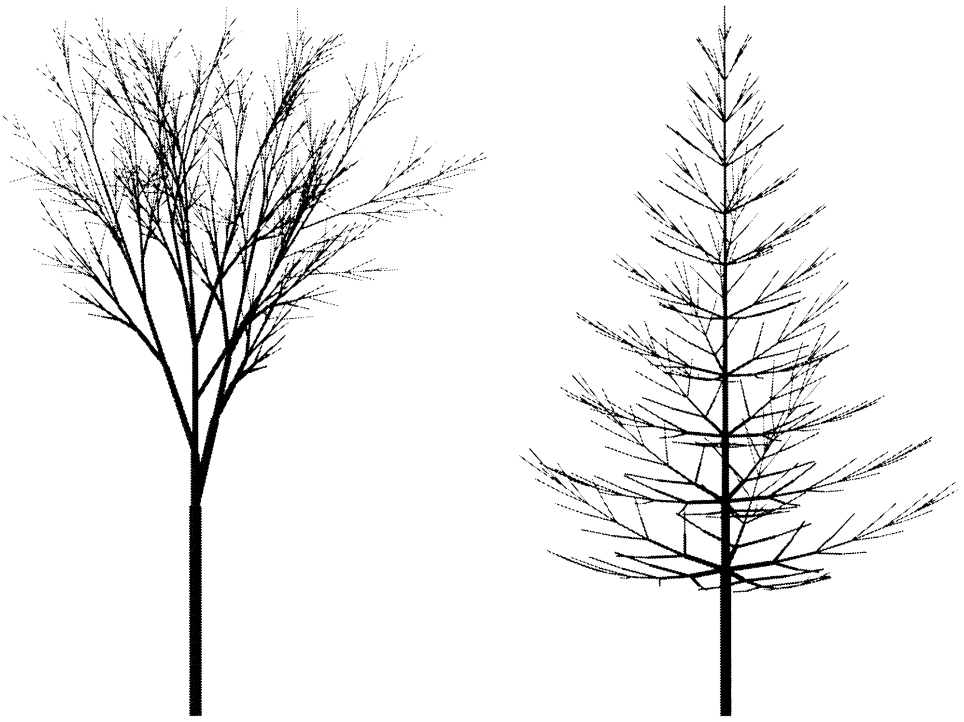

(a) Decurrent (b) Excurrent

Figure 2: Two fractal trees simulated for (a) decurrent and (b) excurrent types.

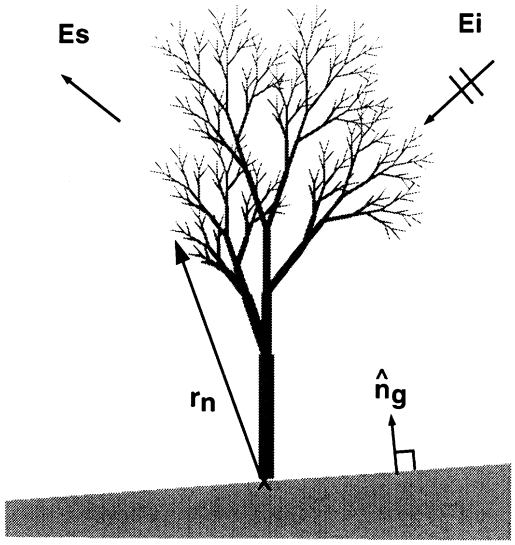

Figure 3: Scattering from a cluster of scatterers above a tilted ground surface.

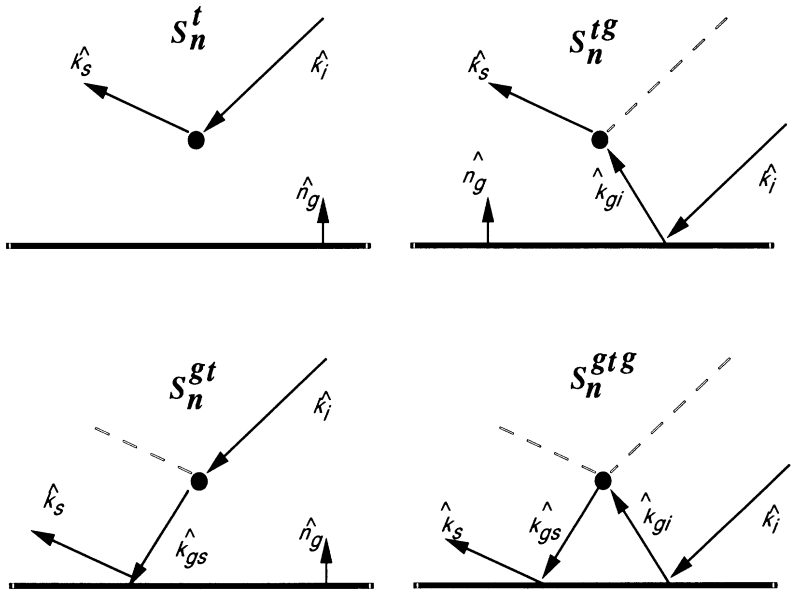

Figure 4: Four scattering components from an object above a tilted dielectric plane.

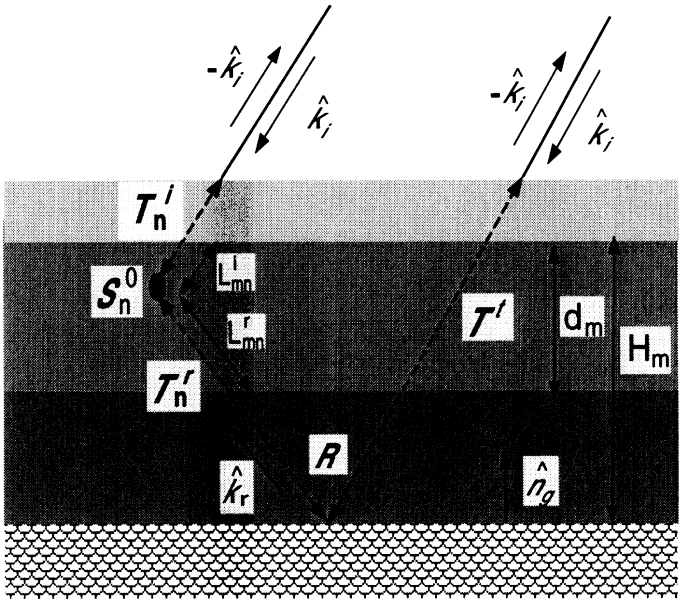

Figure 5: Extinction of a coherent wave in random media.

(a) Stand 31 (b) Fractal Tree (c) Fractal Tree (d) Extinction Profile

Figure 6: Visual verificatiin of the fractal model: photograph of the test maple stand (a), the generated fractal tree without (b) and with leaves (c), and the calculated extinction profile (d).

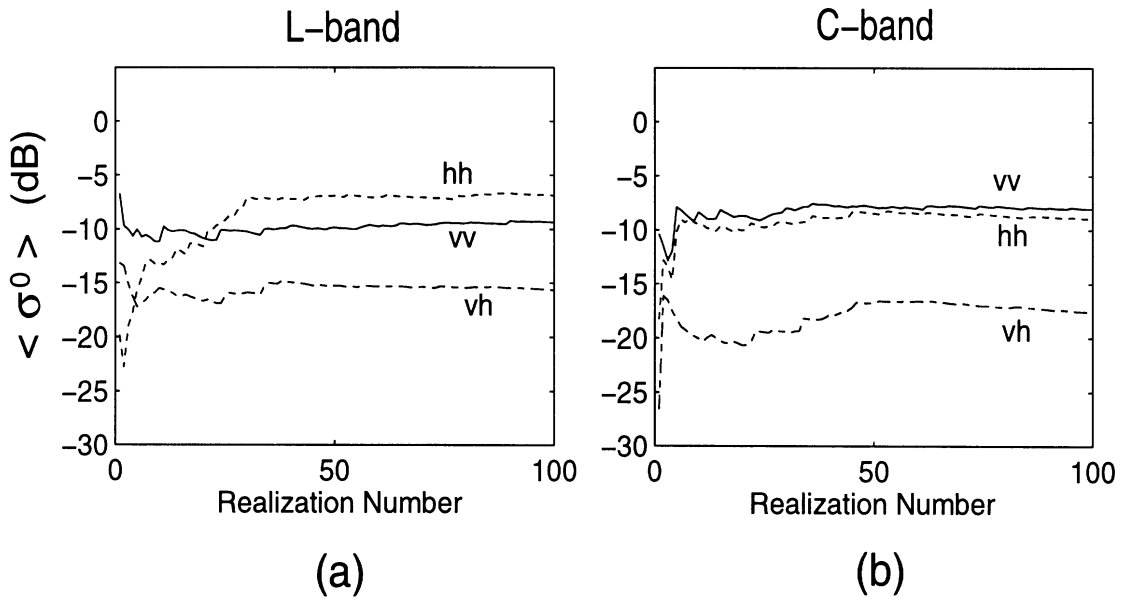

Figure 7: Convergence behavior of the Monte Carlo simulation for Stand 31 at L-band(a) and C-band (b) at incidence angle $\theta_i = 30^o$.

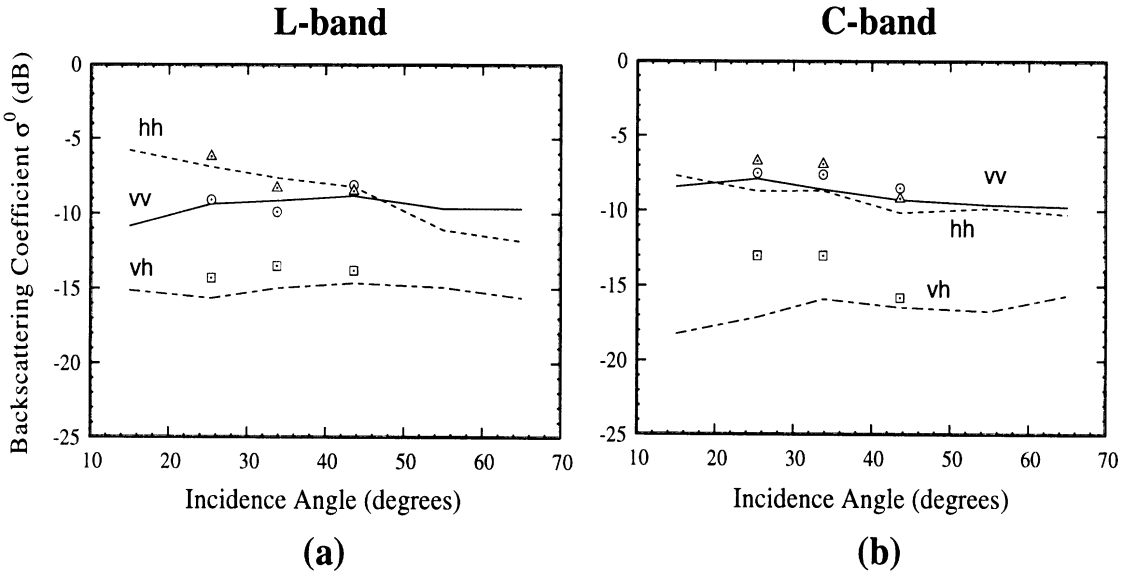

Figure 8: Comparison between the model predictions (lines) and SIR-C data (symbols) at (a) L-band and (b) C-band.

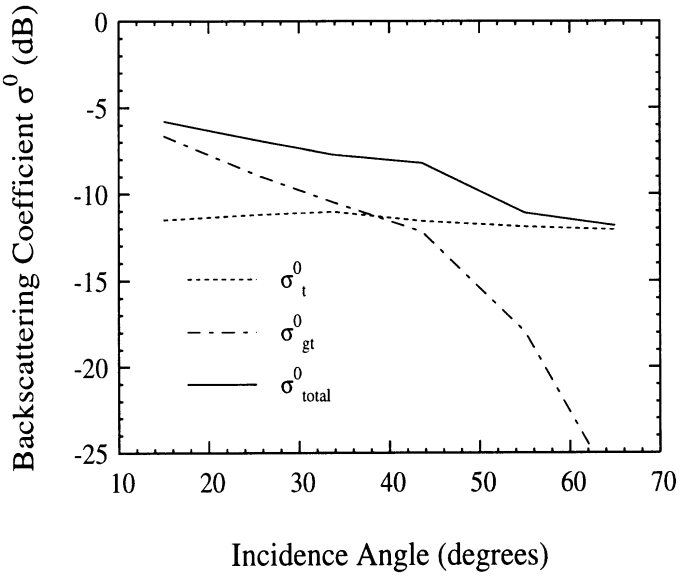

Figure 9: Contribution of different scattering components (σ_t^0-direct and σ_{gt}^0-ground-trunk) to the overall backscattering coefficient (σ_{total}^0) as a function of incidence angle.

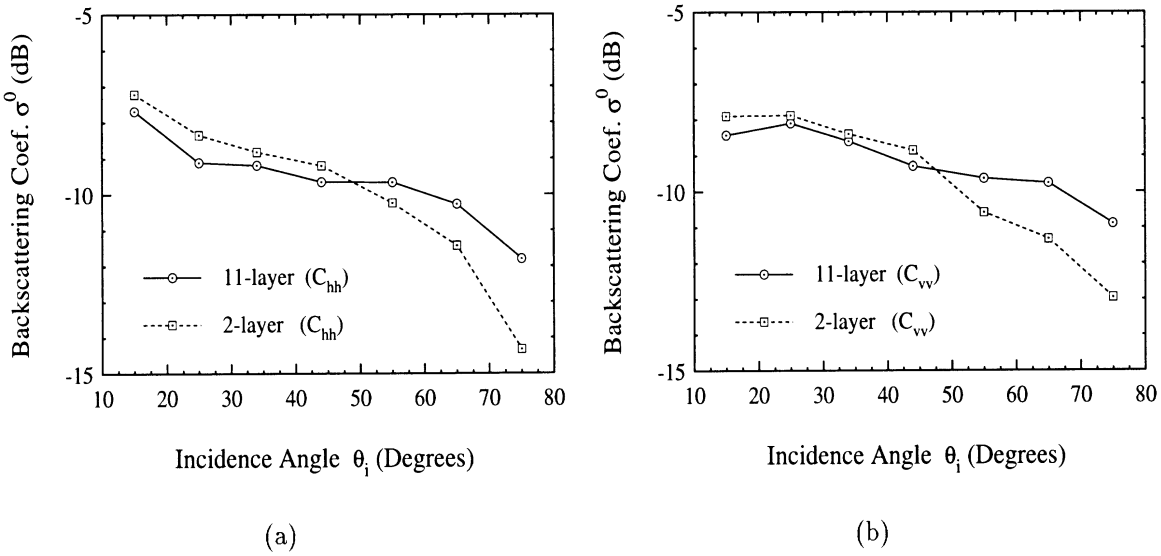

Figure 10: Comparison of the 11-layer and 2-layer extinction models simulated at C-band for *hh* polarization (a) and *vv* polarization (b).

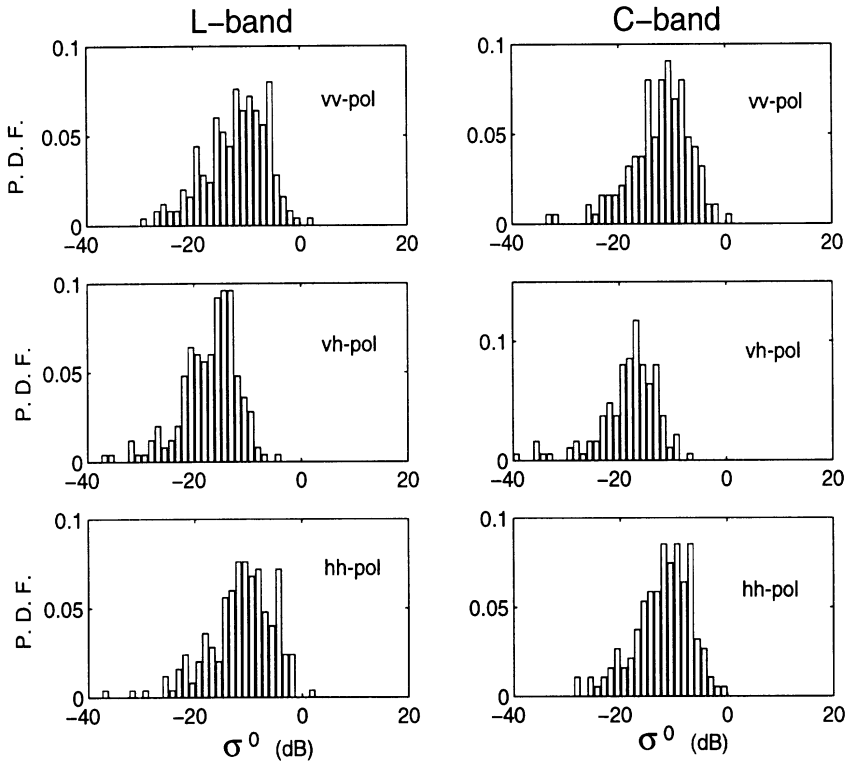

Figure 11: Histogram of the backscattering coefficients for Stand 31 at $\theta_i = 43.6^o$.

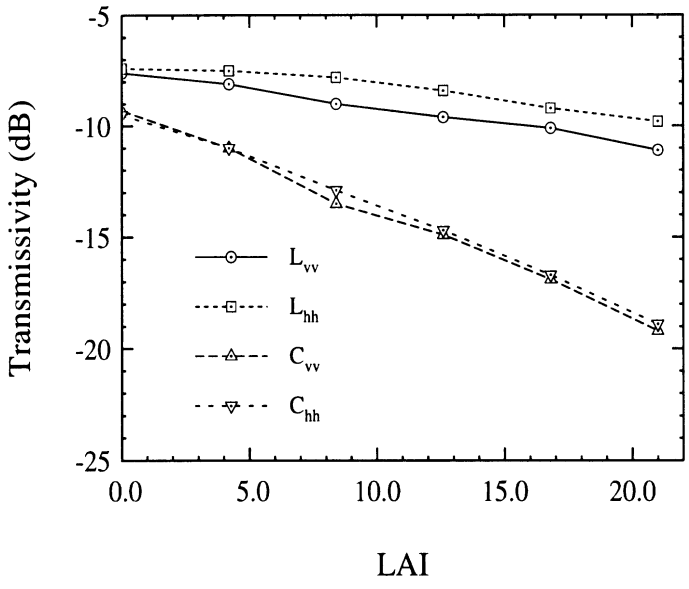

Figure 12: One-way transmissivity as a function of leaf area index (LAI).

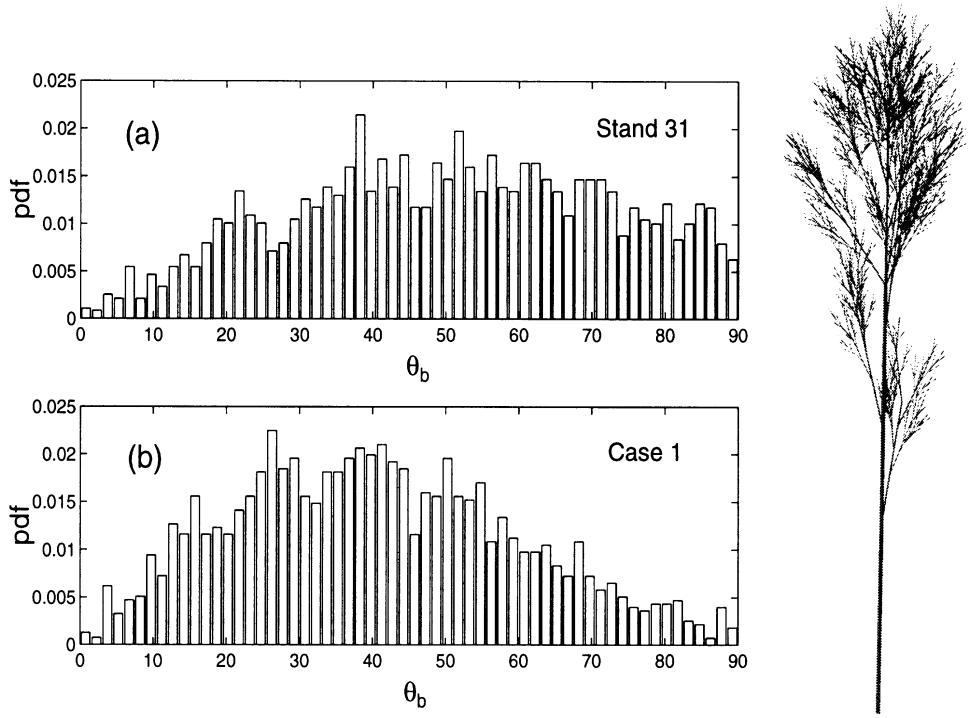

Figure 13: Histogram of branch orientation resulting from two branching angles : (a) $\Delta\theta_b = 22^o \pm 5^o$ (Stand 31); (b)$\Delta\theta_b = 15^o \pm 3^o$ (Case 1). The tree structure of (b) is also shown on the right.

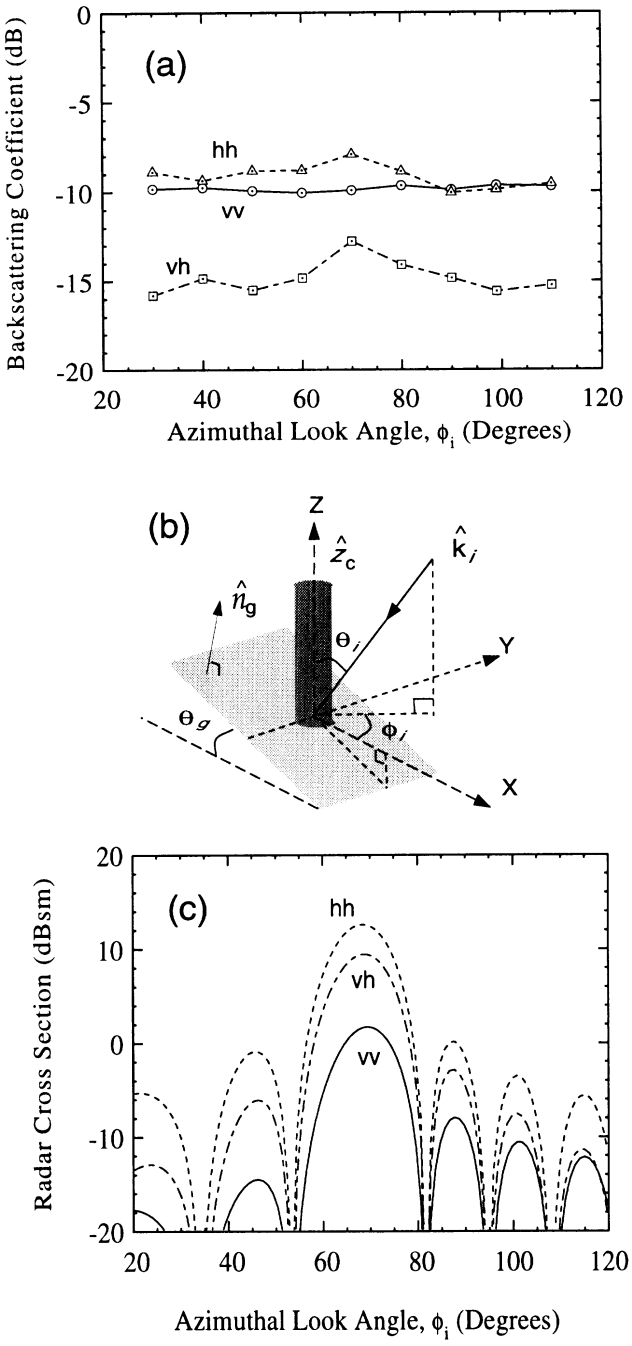

Figure 14: The effect of the ground tilt angle on radar backscatter: (a) backscattering coefficients for Stand 31 over a tilted ground with $\theta_g = 10^o$ simulated at L-band with incidence angle $\theta_i = 25.4^o$, (b) a vertical cylinder on a tilted dielectric plane and the associated coordinates, (c) RCS simulation for (b).

Appendix IV

Simulation of Interferometric SAR Response for Characterization of Scattering Phase Center Statistics of Forest Canopies

Simulation of Interferometric SAR Response for Characterizing the Scattering Phase Center Statistics of Forest Canopies

Kamal Sarabandi and Yi-Cheng Lin

Radiation Laboratory
Department of Electrical Engineering and Computer Science
The University of Michigan
Ann Arbor, MI 48109-2122

Abstract

A coherent scattering model for tree canopies is employed in order to characterize the sensitivity of an interferometric SAR (INSAR) response to the physical parameters of forest stands. The concept of an equivalent scatterer for a collection of scatterers within a pixel, representing the vegetation particles of tree structures, is used for identifying the scattering phase center of the pixel whose height is measured by an INSAR. Combining the recently developed coherent scattering model for tree canopies and the INSAR Δk-radar equivalence algorithm, for the first time accurate statistics of the scattering phase center location of forest stands are obtained numerically. The scattering model is based on a Monte Carlo simulation of scattering from fractal generated tree structures, and therefore is capable of preserving the absolute phase of the backscatter. The model can also account for coherent effects due to the relative position of individual scatterers and the inhomogeneous extinction experienced by a coherent wave propagating through the random collection of vegetation particles. The location of the scattering phase center and the correlation coefficient are computed using the Δk-radar equivalence, simply by simulating the backscatter response at two slightly different frequencies. The model is successfully validated using the measured data acquired by JPL TOPSAR over a selected pine stand in Raco, Michigan. A sensitivity analysis is performed to characterize the response of coniferous and deciduous forest stands to a multi-frequency and multi-polarization INSAR in order to determine an optimum system configuration for remote sensing of forest parameters.

1 Introduction

Accurate estimation of gross forest parameters such as total vegetation biomass, total leaf area index, and tree height in global scale has long been an important goal within the remote sensing community. Over the past two decades much effort has been devoted to the development of scattering models [1–6] for understanding the interaction of electromagnetic waves with vegetation, and to the construction and development of advanced imaging radars for acquiring test data and examining the feasibility of the remote sensing problem [7,8]. In most practical situations the number of vegetation parameters influencing the radar response usually exceeds the number of radar observation parameters. For this reason the application of a multi-frequency and multi-polarization radar system was proposed and such a system was flown aboard the Shuttle Endeavor in April and October 1994 [8]. Preliminary results indicate that the classification and retrieval of vegetation biophysical parameters indeed require many simultaneous radar channels; however, free-flight of such systems is not practical due to the exorbitant power requirements.

Recent advancements in the field of radar interferometry have opened a new door to the radar remote sensing of vegetation. In addition to the backscattering coefficient, radar interferometers measure two additional quantities that contain target information [9]. These quantities are the correlation coefficient and the interferogram phase. To interpret these quantities and to characterize their dependency on the physical parameters of the target, a thorough understanding of the coherent interaction of electromagnetic waves with vegetation particles is required. The premise of this investigation with regard to retrieving vegetation parameters from INSAR data stems from the fact that the location of the scattering phase center of a target is a strong function of the target structure. For example the scattering phase centers of non-vegetated terrain are located at or slightly below the surface depending upon the wavelength and the dielectric properties of the surface media, whereas for vegetated terrain, these scattering phase centers lie at or above the surface depending upon the wavelength of the SAR and the vegetation attributes. It also must be recognized that the vegetation cover adds noise in many interferometric SAR applications where the vegetation itself is not the primary target, such as geological field mapping or surface change monitoring. In these cases it is also important to identify and characterize the effect of vegetation on the topographic information obtained from the interferometric SAR.

In recent years some experimental and theoretical studies have been carried out to demonstrate the potential INSARs in retrieving forest parameters. For example in [10,11] and [12] experimental data using ERS-1 SAR repeat-pass and DO-SAR single-pass are employed to show the applications of SAR interferometry for classification of forest types and retrieval of tree heights. Also theoretical models have been developed to establish relationships between the interferogram phase and correlation coefficient to the physical parameters of vegetation and the underlying soil surface [13–15]. Although these models give qualitative explanation for the measured data and provide a basic understanding of the problem, due to the oversimplified assumptions in the description

of vegetation structure, they are not accurate enough for most practical applications. For example the shape, size, number density, and orientation distributions of vegetation in forest stands are nonuniform along the vertical direction. The nonuniform distributions of physical parameters of vegetation particles (such as leaves, and branches) give rise to inhomogeneous scattering and extinction which significantly affects the correlation coefficient and the location of the vegetation scattering phase center.

The purpose of this investigation is to develop a robust scattering model for forest canopies capable of predicting the response of INSARs. Although there are a number of EM scattering models available for vegetation canopies [1–3, 5, 6], they are of little use with regard to INSAR applications due to their inability to predict the absolute phase of the scattered field. The absolute phase of the scattered field is the fundamental quantity from which the interferogram images are constructed. The proposed model described in Section 2 is basically composed of two recently developed algorithms: 1) a fully coherent scattering model for tree canopies based on a Monte Carlo simulation of scattering from fractal generated trees [16], and 2) extraction of the scattering phase center based on a Δk-radar equivalence relationship with INSAR [13]. In Section 3 the validity of the model in predicting the backscatter coefficients and the location of the scattering phase center of forest canopies is demonstrated by comparing the simulated results with those measured by JPL TOPSAR [17]. Finally a sensitivity study is conducted to demonstrate the variations of the scattering phase center of a forest stand in terms of target parameters such as tree density, soil moisture, tree type, and ground tilt angle, as well as INSAR parameters such as polarization, frequency and incidence angle.

2 Model Description

In this section an overview is given of the approaches which are employed to extract statistics of the scattering phase center of forest canopies. Three tasks must be undertaken for the calculation of the correlation coefficient and the location of the scattering phase center. These include: 1) accurate simulation of tree structures, 2) development of the scattering model, and 3) development of an algorithm for evaluation of the location of the scattering phase center.

2.1 Fractal Model

It will be shown that the location of the scattering phase center of a tree is a strong function of the tree structure. For an accurate estimation of the scattering phase center and the backscattering coefficients, the algorithm for generating desired tree structures must be capable of producing realistic tree structures and yet be as simple as possible. It has been shown that geometrical features of most botanical structures can be described by only a few parameters using fractal theory [18, 19]. A distinctive feature of fractal patterns is the *self-similarity* which is kept through the derivation process. To generate fractal patterns we use Lindenmayer systems [20] which are versatile tools for

implementing the *self-similarity* throughout a so-called rewriting process. For a tree-like structure, some essential botanical features must be added to the fractal process, including branch tapering in length and cross section, leaf placement, and randomizing the fractal parameters according to some prescribed probability density functions. The botanical features and the probability density functions must be characterized according to in-situ measurements of a given stand.

Although there are many computer graphics available for generating tree-like structures, most are not appropriate for the purpose of scientific modeling. At microwave frequencies, the radar return and its statistics strongly depend on tree structures, which necessitates the application of a realistic model for generating accurate tree structures. Therefore, the final and most important step in the fractal model is to incorporate the information about the tree structure and its statistics obtained from the in-situ measurements of the ground truth. Figures 1 and 2 compare the simulated trees produced by the fractal model developed in this paper with the photographs of the actual forest stands. These simulated structures are generated according to in-situ measurements collected from two test sites denoted by Stand 22 (red pine) and Stand 31 (red maple) in Raco, Michigan. The fractal pine shown in Figure 1(b) consists of 792 branch segments, 391 end needle clusters, and 747 needle-covered stems. The fractal maple in Figure 2(b) comprises 7494 branch segments and 14818 leaves consistent with the ground truth data [16]. To visualize the generated 3-D tree structure, the fractal model is equipped with a fast algorithm which displays the real-time projected tree image with arbitrary scaling and perspective view.

2.2 Scattering Model

In contrast to the existing scattering models for tree canopies, the coherent model used in this investigation is capable of preserving the absolute phase of the backscatter as well as the relative phases of individual scatterers which give rise to coherent effects. Once a tree structure is generated, the scattered field is computed by considering the tree structure as a cluster of scatterers composed of cylinders (trunks and branches) and disks/needles (leaves) with specified position, orientation, and size. The attenuation and phase shift due to the scattering and absorption losses of vegetation particles within the tree canopy are taken into account in the computation of the scattered field from individual particles. To the first order of scattering approximation, the backscatter from the entire tree is calculated from the coherent addition of the individual scattering terms. Hence, neglecting the multiple scattering among the scatterers, the total scattered field can be written as

$$\mathbf{E}^s = \frac{e^{ikr}}{r} \sum_{n=1}^{N} e^{i\phi_n} \mathbf{S}_n \cdot \mathbf{E}_o^i, \tag{1}$$

where N is the total number of the scatterers, $\mathbf{S}_n$ is the individual scattering matrix of the n-th scatterer which may be a tree trunk [21] or a vegetation needle [22], and ϕ_n is the phase compensation accounting for the shifting of the phase reference from the local

to the global phase reference, given by $\phi_n = k_0(\hat{k}_i - \hat{k}_s) \cdot \mathbf{r_n}$, where $\mathbf{r_n}$ is the position vector of the n-th scatterer in the global coordinate system.

In order to compute the scattering matrix of the n-th particle $\mathbf{S}_n$, consider a single particle above a ground plane. Ignoring the multiple scattering between the scatterer and its mirror image, the scattering matrix is composed of four components : 1) direct component $\mathbf{S}_n^t$, 2) ground-scatterer component $\mathbf{S}_n^{tg}$, 3) scatterer-ground component $\mathbf{S}_n^{gt}$, and 4) ground-scatterer-ground component $\mathbf{S}_n^{gtg}$. Therefore, the individual scattering matrix $\mathbf{S}_n$ can be written as

$$\mathbf{S}_n = \mathbf{S}_n^t + \mathbf{S}_n^{gt} + \mathbf{S}_n^{tg} + \mathbf{S}_n^{gtg}, \tag{2}$$

where

$$\begin{aligned}
\mathbf{S}_n^t &= \mathbf{T}_n^i \cdot \mathbf{S}_n^0(-\hat{k}_i, \hat{k}_i) \cdot \mathbf{T}_n^i, && (3)\\
\mathbf{S}_n^{gt} &= e^{i\tau_n}\mathbf{T}^t \cdot \mathbf{R} \cdot \mathbf{T}_n^r \cdot \mathbf{S}_n^0(-\hat{k}_r, \hat{k}_i) \cdot \mathbf{T}_n^i, && (4)\\
\mathbf{S}_n^{tg} &= e^{i\tau_n}\mathbf{T}_n^i \cdot \mathbf{S}_n^0(-\hat{k}_i, \hat{k}_r) \cdot \mathbf{T}_n^r \cdot \mathbf{R} \cdot \mathbf{T}^t, && (5)\\
\mathbf{S}_n^{gtg} &= e^{i2\tau_n}\mathbf{T}^t \cdot \mathbf{R} \cdot \mathbf{T}_n^r \cdot \mathbf{S}_n^0(-\hat{k}_r, \hat{k}_r) \cdot \mathbf{T}_n^r \cdot \mathbf{R} \cdot \mathbf{T}^t, && (6)
\end{aligned}$$

with $\hat{k}_r = \hat{k}_i - 2\hat{n}_g(\hat{n}_g \cdot \hat{k}_i)$ and $\tau_n = 2k_0(\mathbf{r_n} \cdot \hat{n}_g)(\hat{n}_g \cdot \hat{k}_r)$. In the above expressions, $\hat{n}_g$ is the unit vector normal to the ground plane, which in general is tilted with respect to the horizontal plane of the global coordinate system. The optical length τ_n accounts for the extra path length experienced by the ground-scatterer or the scatterer-ground scattering components compared to the direct scattering component. $\mathbf{S_n^0}$ is the scattering matrix of the n-th scatterer isolated in free space. $\mathbf{R}$ is the reflection matrix of the ground plane which includes the surface reflection coefficient and the polarization transformation due to the tilted ground plane. $\mathbf{T}_n^i$ and $\mathbf{T}_n^r$ are transmissivity matrices accounting for the attenuation and phase change of the mean-field from the canopy top and the ground to the scatterer respectively, and $\mathbf{T}^t$ is the total canopy transmissivity (see Figure 3).

A forest stand with a closed canopy can be regarded as a multi-layered random medium where the properties of each layer can be characterized according to the particle distribution along the vertical extent of the forest canopy. The particle size, shape, position, and orientation distributions are obtained directly from the fractal model. A continuous multi-layer random medium is not an accurate representation for the discontinuous canopies such as coniferous forest stands. In these cases, the mean field within the canopy is a function of both the vertical and horizontal positions as shown in Figure 4. The scattering model developed for this study has the ability to keep track of the attenuation and phase shift of the incident and reflected rays as they traverse through the discontinuous canopies. This is accomplished by defining an envelope obtained from the fractal model for the tree canopy. Depending on the incidence angle, the incident or reflected rays may traverse through the neighboring trees [23]. In the Monte Carlo simulation the position of the neighboring trees are chosen randomly according to the tree density and plantation.

2.3 Algorithms for Evaluating the Location of the Scattering Phase Center

As mentioned earlier, the overall objective of this investigation is to study the relationship between the phase and correlation coefficient of an INSAR interferogram and the physical parameters of a forest stand. An INSAR system measures the backscatter of a scene at two slightly different look angles, and the phase difference between the two backscattered fields is used to derive the elevation information. In a recent study [13] it has been established that similar information can be obtained by measuring the backscatter of the scene at two slightly different frequencies provided that the look angle is known. For an INSAR system with known baseline distance (B) and angle α operating at frequency f_0, the frequency shift (Δf) of an equivalent Δk-radar is given by

$$\Delta f = \frac{f_0 B}{mr} \sin(\alpha - \theta) \tag{7}$$

where θ is the looking angle, $m = 1, 2$ for repeat-pass, and two-antenna INSAR configurations respectively, and r is the distance between the antenna and the scatterer. This equivalence relationship is specifically useful for numerical simulations and controlled experiments using stepped-frequency scatterometer systems. In Monte Carlo simulations, once the tree structure and the scattering configuration are determined, the backscatter signals are calculated twice at two slightly different frequencies. The backscatter at $f_1 = f_0$ and $f_2 = f_0 + \Delta f$ are represented by E_1 and E_2 respectively, which are computed from

$$E_1 = \sum_{n=1}^{N} e^{2ik_0 \hat{k}_i \cdot \mathbf{r_n}} \mathbf{S}_n(k_0) \cdot \mathbf{E}_o^i, \tag{8}$$

$$E_2 = \sum_{n=1}^{N} e^{2i(k_0+\Delta k) \hat{k}_i \cdot \mathbf{r_n}} \mathbf{S}_n(k_0 + \Delta k) \cdot \mathbf{E}_o^i. \tag{9}$$

It is also shown that the height of the equivalent scatterer above the x-y plane of the global coordinate system can be determined from

$$z_e = \frac{-\Delta\Phi}{2\Delta k \cos\theta}, \tag{10}$$

where $\Delta k = 2\pi\Delta f/c$, and $\Delta\Phi = \angle(E_1^* E_2)$ represents the phase difference between E_1 and E_2. Note that the equivalent frequency shift for most practical INSAR configurations is only a small fraction of the center frequency ($\Delta f/f_0 < 0.1\%$) and therefore the far field amplitudes of individual isolated scatterers (S_n^0) do not change when the frequency is changed from f_0 to $f_0 + \Delta f$, that is, $S_n^0(k_0) \simeq S_n^0(k_0 + \Delta k)$. This approximation speeds up the Monte Carlo simulation without compromising the overall accuracy of scattering phase center height estimation.

For a random medium like a forest stand, the scattering phase center height (z_e) is a random variable whose statistics are of interest. Usually the mean value and the second

moment of this random variable are sought. Based on a rigorous statistical analysis [13] it is shown that the statistics of $\Delta\Phi$ can be obtained from the frequency correlation function of the target by computing

$$\alpha e^{i\zeta} = \frac{< E_1^* E_2 >}{\sqrt{< |E_1|^2 >< |E_2|^2 >}}, \tag{11}$$

where α is the correlation coefficient, and ζ is the coherent phase difference. In (11) $< \cdot >$ denotes the ensemble averaging which is evaluated approximately using a sufficiently large number of realizations through the Monte Carlo simulation. When the backscatter statistics are Gaussian, α and ζ provide a complete description of the statistics of $\Delta\Phi$. The apparent height of the scattering phase center of a forest stand is proportional to ζ and can be obtained from

$$z_e = \frac{-\zeta}{2\Delta k \cos\theta}. \tag{12}$$

Note that ζ is not the statistical mean of $\Delta\Phi$, but rather the phase value at which the probability density function of $\Delta\Phi$ assumes its maximum. In fact, using the mean value may result in a significant error for calculating the apparent height z_e. To demonstrate this, two cases may be considered where in one case $\zeta = 0$ and in the other case $\zeta = 180°$ (see [?] for plots of $\Delta\phi$ pdf). In both cases the mean value of $\Delta\Phi$ is zero whereas the apparent heights calculated from (12) are obviously different.

In order to develop some intuition about the scattering phase center and to examine the validity of the above equivalence algorithms, let us consider a simple case where the target is a single scatterer above a ground plane. Through this illustrative case the relationship between the location of the scattering phase center and the scattering mechanisms can be demonstrated. Consider a dielectric cylinder of radius $a = 5cm$, length $b = 3m$, dielectric constant $\epsilon_t = 22 + i10$, which is located at height $h = 6m$ above a ground plane having a complex permittivity $\epsilon_g = 9.7 + i1.6$. Suppose the target is illuminated by a plane wave whose direction of propagation is determined by the incident angles $\theta_i = 30°, \phi_i = 180°$, as shown in Figure 5. As mentioned previously, the backscattered field is mainly composed of four scattering components with different path lengths. In general it is quite difficult to characterize the location of the scattering phase center of a scatterer analytically when multi-path scattering mechanisms are involved. However, in cases where a single scattering mechanism is dominant it is found that the location of the scattering center is strongly dependent upon the path length of the dominant scattering component.

Here we illustrate this fact through an experimental study where the orientation of the cylinder is properly arranged in four configurations, as shown in (a)-(d) of Figure 5, such that the total backscatter is dominated by (a) S^t, (b) S^{gb}, (c) S^{gtg}, and (d)$S^t + S^{gb}$ respectively. Note that S^{gb} is the combination of the reciprocal pair S^{gt} and S^{tg}. The simulation results at f_0 =1.25 GHz are shown in Table 1, which includes the scattering phase center height normalized to the physical height z_e/h, the ratio of the amplitude of individual scattering components to the total backscattered field $|S^{(\cdot)}/S|$, and the overall radar cross section (RCS) of the target for each orientation configuration and for

both polarizations. It is obvious from the results reported in Table 1 that in scattering configuration (a) where the backscatter is dominated by the direct component ($S^t/S = 0.99$) the location of the scattering phase center appears at the physical location of the scatterer above the ground ($z_e/h \simeq 1$). Similarly in scattering configurations (b) and (c) where the backscatter is dominated, respectively, by the single ground bounce component and the double ground bounce component, the locations of the scattering phase center appear on the ground surface and at the mirror image point as shown in Figure 5. In scattering configuration (d), the direct and the single ground bounce components of the backscatter are comparable in magnitude and as shown in Table 1 the location of the scattering phase center in this case appears at a point between the physical location of the scatterer and the ground surface. When the number of scatterers is large the location of the scattering phase center is a convoluted function of physical locations of the constituent scatterers and the relative magnitudes and phases of the scattering components. Note that $|z_e/h|$ and $|S^{(\cdot)}/S|$ in Table 1 may exceed 1 since the total backscattered field S is the superposition of four scattering components which are not necessarily in phase.

3 Comparison with Measured Data and Sensitivity Study

In this section full simulations of forest stands are carried out. As a first step, the model predictions are compared with the JPL TOPSAR measurements over a selected pine stand, denoted as Stand 22. Then a sensitivity study is conducted to characterize the variations of the scattering phase center height and correlation coefficient as a function of both forest and INSAR parameters.

Stand 22 is a statistically uniform red pine forest located within Raco Airport, Raco, Michigan. This scene was selected for this study because the stand is over a large flat terrain which reduces the errors in the measured tree height due to possible surface topographic effects. In addition, the nearby runway provides a reference target at the ground level. Ground truth data for this stand have been collected since 1991 [24] and careful in-situ measurements were conducted by the authors during the overflights of TOPSAR in late April, 1995. The relevant physical parameters of this stand are summarized in Table 2. The vegetation and soil dielectric constants are derived from the measured moisture contents using the empirical models described in [25,26].

The JPL TOPSAR is an airborne two-antenna interferometer, operating at C-band (5.3 GHz) with vv polarization configuration [17]. During this experiment, Stand 22 was imaged twice at two different incidence angles 39° and 53°. Figure 6 shows a portion of the 39° radar image which includes the test stand. Each side of the dark triangle in this image is a runway of about 2 miles long. The measured height of the stand is obtained from the elevation difference between the stand and the nearby runway. Using the ground truth reported in Table 2, the backscattering coefficient and the location of the scattering phase center as a function of the incidence angle were simulated at 5.3 GHz.

As shown in Figures 7 and 8, excellent agreement between the model predictions and TOPSAR measurements is achieved. The simulated height of the scattering phase center of the same forest for an hh-polarized INSAR having the same antenna configuration and operating at the same frequency is also shown in Figure 7. It is shown that the estimated height at the hh-polarization configuration is lower than that obtained from the vv-polarization configuration. This result is usually true for most forest stands since the ground-trunk backscatter for hh-polarization is much higher than that for vv-polarization. Also noting that the location of the scattering phase center for a ground-trunk backscatter component is at the air-ground interface, the location of the scattering phase center of trees for hh-polarization is lower than that for vv-polarization.

The comparison between the simulated σ^0_{vv} and the measured σ^0_{vv} acquired by TOPSAR as a function of the incidence angle is shown in Figure 8. Also shown in this figure is the contribution of each scattering component (the direct backscatter σ^t and the ground-bounce backscatter σ^{gb}) to the overall backscattering coefficient. It was found that the contribution of the double ground-bounce component σ^{gtg} was relatively small and for most practical cases can be ignored. In this case, at low incidence angles ($\theta_i < 30°$) the ground-bounce backscatter is the dominant component, whereas at higher incidence angles the direct backscatter becomes the dominant factor. This trend is the cause for the increasing behavior of the scattering phase center height as a function of the incidence angle found in Figure 7. It is worth mentioning that the contribution of pine needles to the overall backscattering coefficient was found to be negligible compared to the contribution from the branches and tree trunks. However, inclusion of the needles in the scattering simulation was necessary because of their significant effect on the extinction.

With some confidence in the scattering model and the algorithm for evaluation of the scattering phase center height, further simulation can be performed to characterize the dependence of the scattering phase center height of a forest stand on the system parameters such as frequency, polarization, and incidence angle, and the forest parameters such as tree density, soil moisture, and tree types. In addition, we demonstrate the capability of the present model as a tool for determining an optimum system configuration for retrieving physical parameters of forest canopies. Figure 9 shows the estimated height of Stand 22 for two principal polarizations at C-band (5.3 GHz) and L-band (1.25 GHz) as a function of the ground soil moisture, simulated at $\theta_i = 45°$. As the soil moisture increases, the ground plane reflection will also increase, which in turn causes the ground bounce scattering component to increase. As a result of this phenomenon, the scattering phase center height decreases with soil moisture as shown in Figure 9. This effect is more pronounced for L-band vv-polarization than other INSAR configurations, suggesting a practical method for monitoring the soil moisture using the apparent height of the forest stand. This high sensitivity at L_{vv} is achieved because of the existence of competitive scattering components. Basically, at low soil moisture the direct backscatter component is comparable with the ground bounce component and the scattering phase center lies amidst the canopy. As the soil moisture increases, the ground bounce scattering component becomes more dominant, which results in lowering the apparent height of the stand. On the other hand, the least sensitive configuration is L_{hh} since the dominant scattering

component, independent of the soil moisture, is the ground bounce component.

Figure 10 shows the effect of the tree density on the estimated height of a red pine stand having a similar structure as that of Stand 22 at $\theta_i = 45°$. As the tree density increases, the extinction within the canopy increases, which reduces the ground-bounce component. Increasing the tree density would also increase the direct backscatter component. As a result of these two processes, the apparent height of the canopy increases with increasing tree density as demonstrated in Figure 10. As before, the apparent height for L_{hh} configuration does not show any sensitivity to the tree density indicating that the ground bounce component remains dominant over the entire simulation range of 700–1200 trees/Hectare. This lack of sensitivity to the apparent height of coniferous stands for L_{hh} suggests that this configuration is most suitable for mapping the surface height of coniferous forest stands.

Now let us examine the response of INSAR when mapping deciduous forest stands. For this study a red maple stand, denoted by Stand 31, is selected whose structure and scatterers are different from the previous example. A fractal generated red maple tree and a picture of the stand are shown in Figure 2. This stand was selected as a test stand to validate the previously developed coherent scattering model [16], using the SIR-C data. The average tree height and tree number density were measured to be $16.8m$ and 1700 trees/Hectare respectively. Table 3 provides the detailed ground truth data from Stand 31. The simulations for estimating the scattering phase center height are performed fully-polarimetrically at L-band and C-band. Figure 11 shows the variation of the apparent height of Stand 31 as a function of the incidence angles for co- and cross-polarized L- and C-band INSAR configurations. Simulation results at C-band show that except at very low angles of incidence, the scattering phase center is near the top of the canopy. In this case the backscatter in all three polarizations is dominated by the direct backscatter components of particles near the canopy top. The same is true for L_{vv} and L_{vh} configurations; however, since penetration depth at L-band is higher than C-band, the location of the scattering phase center appears about 1–3 m below the apparent height at C-band. The scattering phase center height for L_{hh} configuration, on the other hand, is a strong function of the incidence angle where it appears near the ground surface at low incidence angles and increases to a saturation point near grazing angles. At low incidence angles the ground-trunk interaction is the dominant scattering mechanism for hh polarization and since the location of the scattering phase for all single ground bounce terms is on the ground, the overall scattering phase center height appears close to the ground. Close examination of this figure indicates that a pair of C_{vv} and L_{hh} INSAR data at low incidence angles can be used to estimate the tree height of deciduous forest stands with closed canopies. A C-band foliated canopy behaves as a semi-infinite medium and as shown in [13] the knowledge of extinction would reveal the distance between the location of the scattering phase center and the canopy top (Δd) using $\Delta d = \cos\theta/(2\kappa)$. If an average extinction coefficient (κ) of $0.2N_p/m$ is used in the above equation, a distance $\Delta d = 1.77m$ is obtained at $\theta = 45°$. However, a simple relation for evaluating the apparent height for L_{hh} does not exist yet.

Figure 12 shows the effect of the ground tilt angle on the estimated scattering phase

center height. This simulation is obtained by setting a ground tilt angle $\theta_g = 10°$ for a forest stand similar to Stand 31 and calculating the estimated scattering phase center height as a function of the azimuthal incidence angle ϕ_i at $\theta_i = 25.4°$. As mentioned in [16], there is a strong ground-trunk backscatter around $\phi_i = 70°$, particularly for L_{hh} and L_{vh}. This accounts for the dip in the apparent height simulations for L_{hh} and L_{vh} configurations at $\phi_i = 70°$ shown in Figure 12.

So far only the behavior of the mean value of the scattering phase center height has been investigated; however, the model has the ability to provide an approximate probability distribution function of the scattering phase center height. The histograms of the scattering phase center height can be constructed by recording the simulated results for each scattering simulation. Figure 13 shows the simulated probability density function (PDF) of the scattering phase center height of Stand 22 at $\theta = 45°$ for the three principal polarizations and for both L- and C-band. At L-band the scattering phase center height has a narrow distribution for hh-polarization, indicating that a relatively small number of independent samples are sufficient for estimating the apparent height. At C-band the scattering phase center height of the cross-polarized backscatter exhibits a narrower PDF.

As mentioned earlier, the correlation coefficient (α) is an independent parameter provided by INSARs which, in principle, may be used for inversion and classification processes. The measured correlation coefficient is a function of INSAR parameters such as look angle, baseline distance and angle, radar range to target and target parameters. To examine the behavior of α as a function of target parameters, the Δk-radar equivalence relationship given by (7) is used where the dependence on INSAR parameters are lumped into one parameter, namely, the frequency shift. Figure 14 shows the calculated correlation coefficients (α) as a function of the normalized frequency shift ($\Delta f/f_0$) (corresponding to the baseline distance in an INSAR), simulated for Stand 22 and Stand 31 at $\theta_i = 45°$. As shown in [13] the correlation coefficient is inversely proportional to the width of the PDF, that is, a high value of α indicates a narrow distribution. A comparison between the histograms shown in Figure 13 and the values of α shown in Figure 14(a) demonstrates this relationship. It is interesting to note that simulated α for Stand 31 at L_{hh} is significantly smaller than the correlation coefficients at other polarizations (see Figure 14(b)). This behavior is a result of the fact that the direct backscatter and ground-bounce backscatter components are comparable.

It is shown that for the same baseline to distance ratio (B/r) which corresponds to a constant $\Delta f/f_0$, α at C-band is smaller than α at L-band independent of polarization. It should be mentioned here that for most practical situations $\Delta f/f_0$ is of the order of 10^{-4} or smaller which renders a value for α near unity ($\alpha > 0.99$). That is, for practical INSAR configurations, the effect of forest parameters on the correlation coefficient appears on the third digit after the decimal point. It can be shown that the measured correlation coefficient is a product of three factors: 1) target decorrelation which is a function of target parameters only and is proportional to B/r, 2) system decorrelation which is a function system slant range resolution and B/r , and 3) temporal decorrelation which a function of target change between the two backscatter measurements. Unfortunately the

decorrelation caused by the target is far less than those caused by the other two factors. This puts a serious limitation on the applicability of α for inversion and classification algorithms, since accurate measurement of α with three significant digits is not practical even with two antenna INSARs. For repeat-pass interferometry, the α values reported for forest stands is below 0.7 which is caused mostly by the temporal decorrelation of the target. Therefore, it does not seem logical to use α as a parameter for classifying forest types. The TOPSAR measured αs for Stand 22 at incidence angles 39° and 53° are, respectively, 0.935 and 0.943 which are below the calculated values of 0.998 and 0.999. This discrepancy can be attributed to processing errors and thermal noise.

4 Conclusions

In this paper a scattering model capable of predicting the response of interferometric SARs when mapping forest stands is described. The model is constructed by combining a first-order scattering model applied to fractal generated tree structures and a recently developed equivalence relation between an INSAR and a Δk-radar. Using this model, for the first time accurate statistics of the scattering phase center height and the correlation coefficient of forest stands are calculated numerically. The validity and accuracy of the model are demonstrated by comparing the measured backscattering coefficient and the scattering phase center height of a test stand with those calculated by the model. Then an extensive sensitivity analysis is carried out to characterize the dependence of the scattering phase center height on forest physical parameters, such as soil moisture, tree density, and tree types, and INSAR parameters such as frequency, polarization, and incidence angle. The ability of the model to predict the PDF of the scattering phase center height and the correlation coefficient is also demonstrated. It is shown that for practical INSAR configurations, the correlation coefficient of forest stands is near unity, much larger than what can be measured by existing INSAR systems.

Acknowledgments:
This investigation was supported by NASA under contract NAG5-4939. The authors appreciate the help of the JPL Radar Science group in providing the TOPSAR image data used in this study.

References

[1] F. T. Ulaby, K. Sarabandi, K. MacDonald, M. Whitt, and M. C. Dobson, " Michigan Microwave Canopy Scattering Model", *Int. J. Remote Sensing*, Vol. 11, No. 7, pp. 1223-1253, 1990.

[2] L. Tsang, C. H. Chan, J. A. Kong, and J. Joseph, " Polarimetric signature of a canopy of dielectric cylinders based on first and second order vector radiative transfer theory," *J. Electromag. Waves and Appli.* Vol. 6, No. 1, pp. 19-51, 1992.

[3] M. A. Karam, A. K. Fung, R. H. Lang, and N. H. Chauhan, " A microwave scattering model for layered vegetation," *IEEE Trans. Geosci. Remote Sensing*, Vol. 30, No. 4, pp. 767-784, July 1992.

[4] K. Sarabandi, *Electromagnetic Scattering from Vegetation Canopies*, Ph.D. Dissertation, University of Michigan, 1989.

[5] G. Sun, and K.J. Ranson, "A three-dimensional radar backscatter model of forest canopies," *IEEE Trans. Geosci. Remote Sensing*, Vol. 33, No. 2, 1995.

[6] K.C. McDonald and F.T. Ulaby, "Radiative transfer modeling of discontinuous tree canopies at microwave frequencies," *Int. J. Remote Sensing,* Vol. 14, No. 11, 1993.

[7] J. B. Cimino, C. Elachi, and M. Settle, "SIR-B the second shuttle image radar experiment," *IEEE Trans. Geosci. Remote Sensing*, vol. 24, pp. 445-452, July 1986.

[8] R. L. Jordan, B. L. Huneycutt, and M. Werner, "The SIR-C/X-SAR synthetic aperture radar system," *IEEE Trans. Geosci. Remote Sensing*, vol. 33, pp. 829-839, July 1996.

[9] E. Rodriguez and J.M. Martin, "Theory and design of interferometric synthetic aperture radars," *IEE Proceedings,* vol. F139, no. 2, pp. 147-159, 1992.

[10] J. O. Hagberg, L. M. H. Ulander, and J. Askne, "Repeat-pass SAR Interferometry over forested terrain," *IEEE Trans. Geosci. Remote Sensing*, Vol. 33, pp. 331-340, March, 1995.

[11] U. Wegmuller and C. L. Werner, "SAR Interferometry Signature of Forest," *IEEE Trans. Geosci. Remote Sensing*, vol. 33, pp. 1153-1161, Sep. 1995.

[12] N.P. Faller and E.H. Meier, "First results with the airborne single-pass DO-SAR interferometer," *IEEE Trans. Geosci. Remote Sensing*, vol. 33, No. 5, Sep. 1995.

[13] K. Sarabandi, "Δk-Radar equivalent of interferometric SARs: a theoretical study for determination of vegetation height," *IEEE Trans. Geosci. Remote Sensing*, vol. 35, no. 5, Sept. 1997.

[14] R. N. Treuhaft, S. N. Madsen, M. Moghaddam, and J. J. van Zyl, "Vegetation characteristics and underlying topography from interferometric radar," *Radio Science*, Vol. 31, No. 6, pp. 1449-1485, 1996.

[15] J.I.H. Asken , P.B.G. Dammert, L.M.H. Ulander, and G. Smith, "C-band repeart-pass interferometric SAR observations of the forest," *IEEE Trans. Geosci. Remote Sensing*, Vol. 35, No.1, 1997.

[16] Y. C. Lin and K. Sarabandi, "A Monte Carlo Coherent Scattering Model For Forest Canopies Using Fractal Generated Trees,"*IEEE Trans. Geosci. Remote Sensing*, accepted for publication.

[17] H. A. Zebker, S. N. Madsen, J. Martin, K. B. Wheeler, T. Miller, Y. Lou, G. Alberti, S. Vetrella, and A. Cucci, " The TOPSAR interferometric radar topographic mapping instrument," *IEEE Trans. Geosci. Remote Sensing*, Vol.30, No.5, pp.933-940, 1992.

[18] B. Mandelbrot, *Fractal Geometry of Nature*, New York, W. H. Freeman Company, 1983.

[19] C. C. Borel and R. E. McIntosh, "A backscattering model for various foliated deciduous tree types at millimeter wavelengths," Proceedings of IGARSS'86 held in Zurich, pp. 867-872, 1986

[20] P. Prusinkiewicz and A. Lindenmayer, *The Algorithmic Beauty of Plants*, Spring-Verlag, New York, 1990.

[21] Y. C. Lin and K. Sarabandi, "Electromagnetic scattering model for a tree trunk above a tilted ground plane", *IEEE Trans. Geosci. Remote Sensing*, Vol. 33. No. 4, pp.1063-1070, 1995.

[22] K. Sarabandi and T. B. A. Senior, "Low-frequency scattering from cylindrical structures at oblique incidence," *IEEE Trans. Geosci. Remote Sensing*, Vol. 28, No. 5, pp. 879-885, 1990.

[23] Y. C. Lin, "A fractal-based coherent microwave scattering model for forest canopies," Ph.D. Dissertation, The University of Michigan, 1997.

[24] K. M. Bergen, M. C. Dobson, T. L. Sharik, and I. Brodie, "Structure, Composition, and above-ground biomass of SIR-C/X-SAR and ERS-1 forest test stands 1991-1994, Raco Michigan Site ", Rep. 026511-7-T, The University of Michigan Radiation Laboratory, Oct., 1995

[25] M. T. Hallikainen, F. T. Ulaby, M. C. Dobson, M. A. El-Rayes, and L.-K. Wu, "Microwave dielectric behavior of wet soil – Part I : empirical models and experimental observations," *IEEE Trans. Geosci. Remote Sensing*, vol. GE-23, pp. 25-34, 1985.

[26] F. T. Ulaby and M. A. Elrayes, "Microwave dielectric spectrum of vegetation, Part II: Dual-dispersion model," *IEEE Trans. Geosci. Remote Sensing*, vol. GE-25, pp. 550-557, 1987.

Configuration	(a)		(b)		(c)		(d)	
Polarization	vv	hh	vv	hh	vv	hh	vv	hh
z_e/h	1.00	0.99	0.01	-0.01	-1.06	-0.96	0.49	0.43
$\|S^t/S\|$	0.99	0.97	0.02	0.01	0.05	0.05	0.62	0.42
$\|S^{gb}/S\|$	0.03	0.02	0.99	1.01	0.13	0.08	0.62	0.59
$\|S^{gtg}/S\|$	0.00	0.00	0.01	0.00	1.10	1.03	0.00	0.00
RCS (dBsm)	8.06	5.19	-0.46	6.16	-6.05	-5.23	-17.2	-15.1

Table 1: The normalized height of the scattering phase center, the normalized scattering components, and the radar cross section for four different scattering configurations as shown in Figure 5.

Tree Density :	1142#/Hectare
Tree Height :	8.9 m
Trunk Diameter (DBH) :	14.6 cm
Dry Biomass :	53 (tons/ha)
Needle Length :	10 cm
Needle Diameter :	1.2 mm
Needle Moisture (m_g) :	0.62
Wood Moisture (m_g) :	0.42
Soil Moisture (m_v) :	0.18

Table 2: Ground truth data of Stand 22

Tree Density :	1700/Hectare
Tree Height :	16.8 m
Trunk Diameter (DBH) :	14 cm
Dry Biomass :	140 (tons/ha)
Leaf Density :	382 $\#/m^3$
Leaf Area :	50 $cm^2/\#$
Leaf Thickness :	0.2 mm
Leaf Moisture (m_g) :	0.51
Wood Moisture (m_g) :	0.60
Soil Moisture (m_v) :	0.18

Table 3: Ground Truth of Stand 31

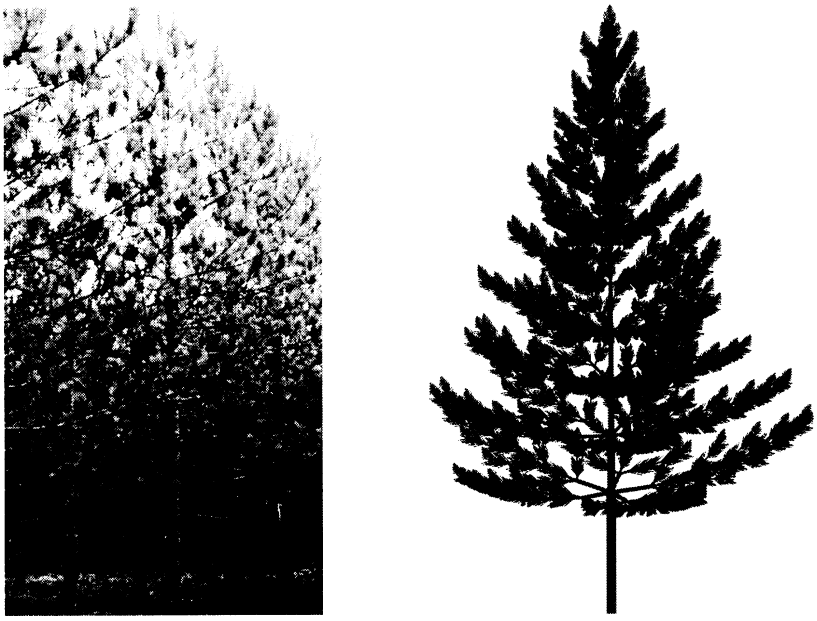

(a) Stand 22 (b) Fractal Pine

Figure 1: The photograph of a red pine stand (Stand 22), and the simulated tree structure using the fractal model.

(a) Stand 31 (b) Fractal Maple

Figure 2: The photograph of a red maple stand (Stand 31), and the simulated tree structure using the fractal model.

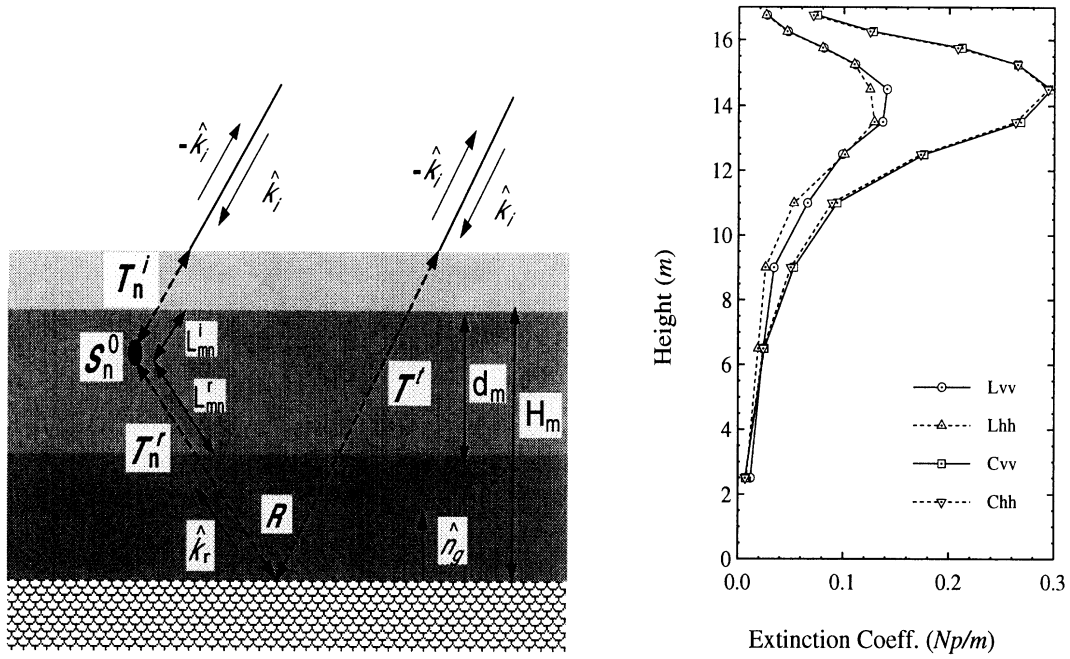

(a) (b)

Figure 3: Propagation of a coherent wave in a continuous canopy (a), and an example of extinction profile calculated for Stand 31 (b).

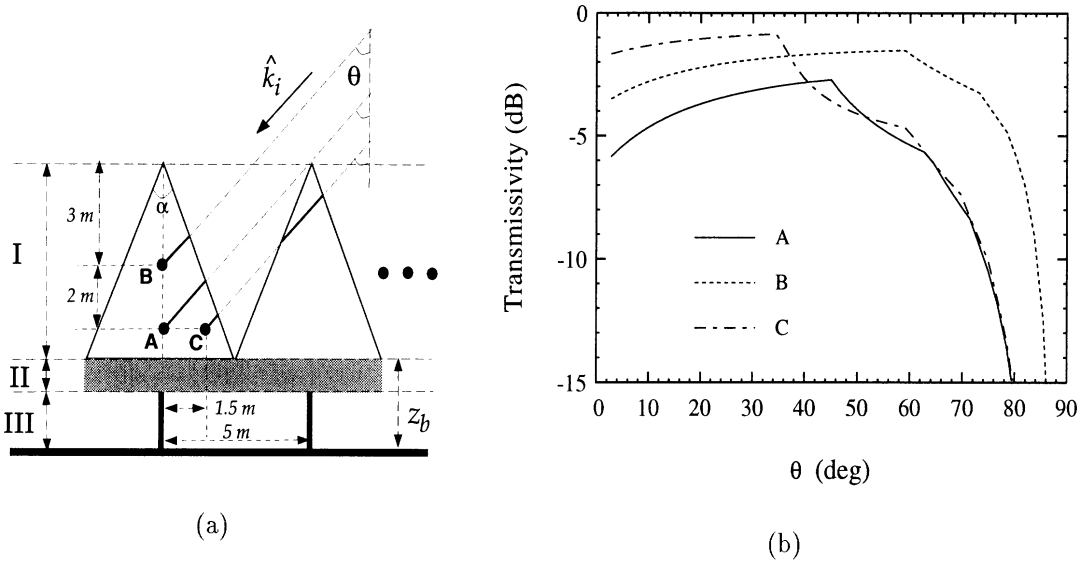

(a) (b)

Figure 4: The position dependence of the transmissivity for coniferous trees and the shadow effect caused by neighboring trees.

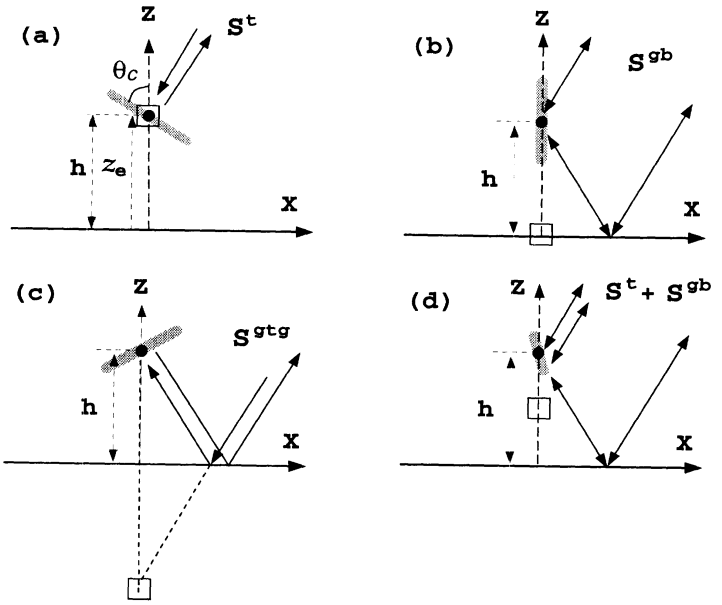

Figure 5: Four configurations for a cylinder above a ground plane with orientation angles: (a) $\theta_c = 60°, \phi_c = 180°$, (b) $\theta_c = 0°, \phi_c = 0°$, (c) $\theta_c = 60°, \phi_c = 0°$, (d) $\theta_c = 45°, \phi_c = 150°$, and their principal scattering mechanisms respectively. The center of the scatterer is denoted by (•) and equivalent scattering phase center by (□).

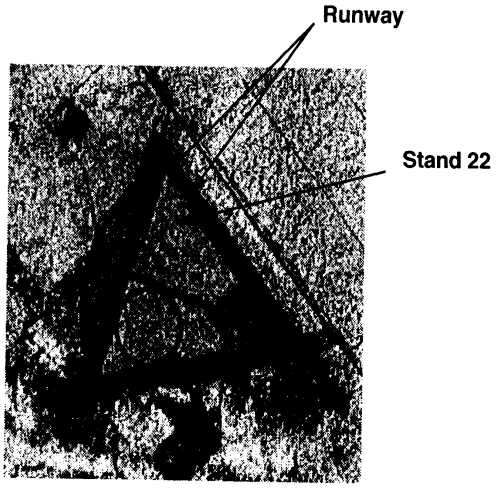

Figure 6: A portion of a TOPSAR C-band image (σ^0_{vv}), indicating Stand 22 at an airport near Raco, Michigan.

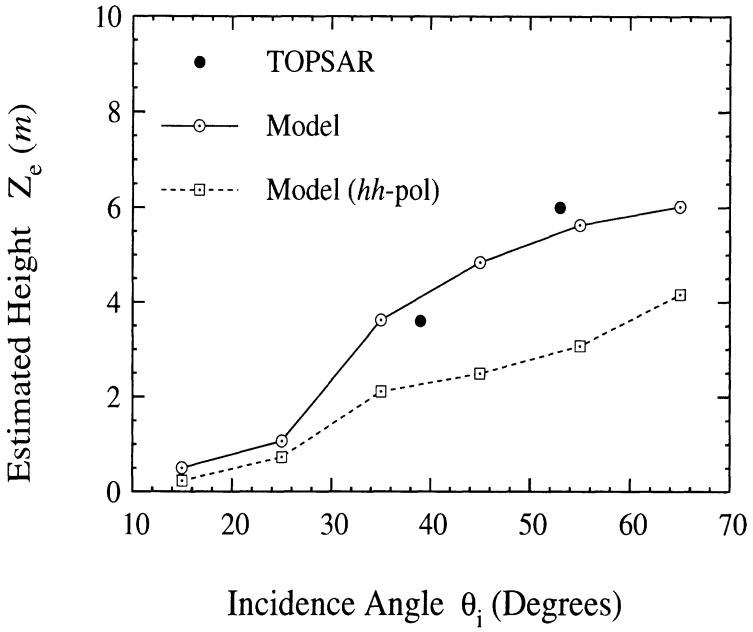

Figure 7: The estimated height of scattering phase center of Stand 22, compared with the data extracted from two TOPSAR images of the same stand.

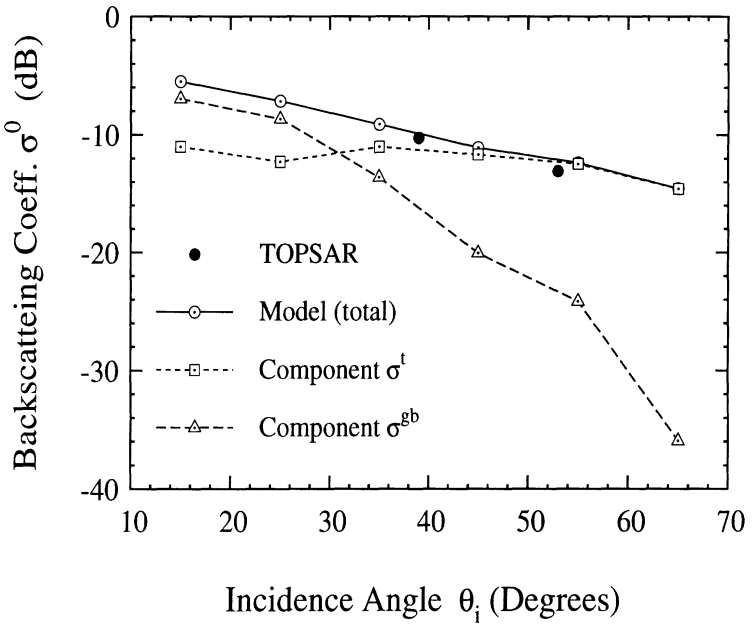

Figure 8: The simulated backscattering coefficient of Stand 22, compared with the measured σ^0_{vv} extracted from two TOPSAR images of the same stand.

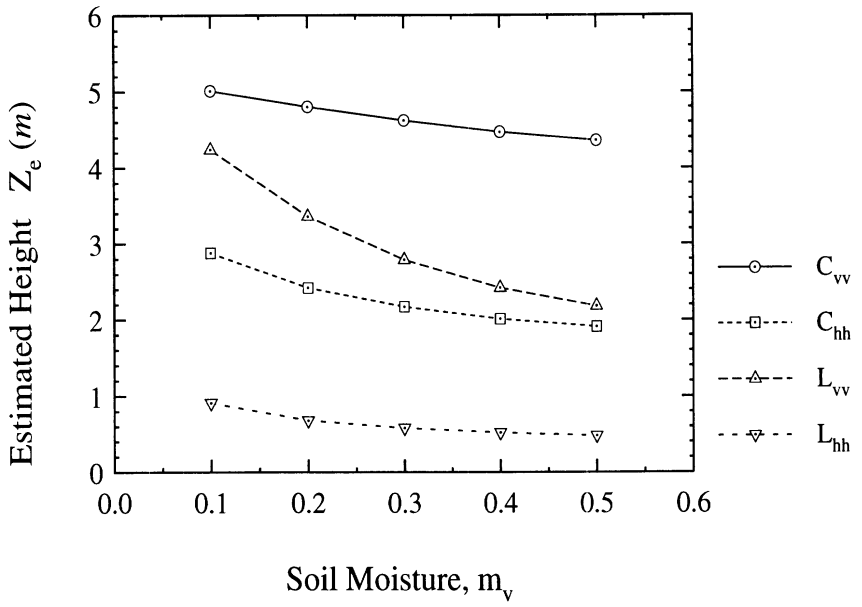

Figure 9: The estimated scattering phase center height of Stand 22 as a function of soil moisture, simulated at $\theta_i = 45°$.

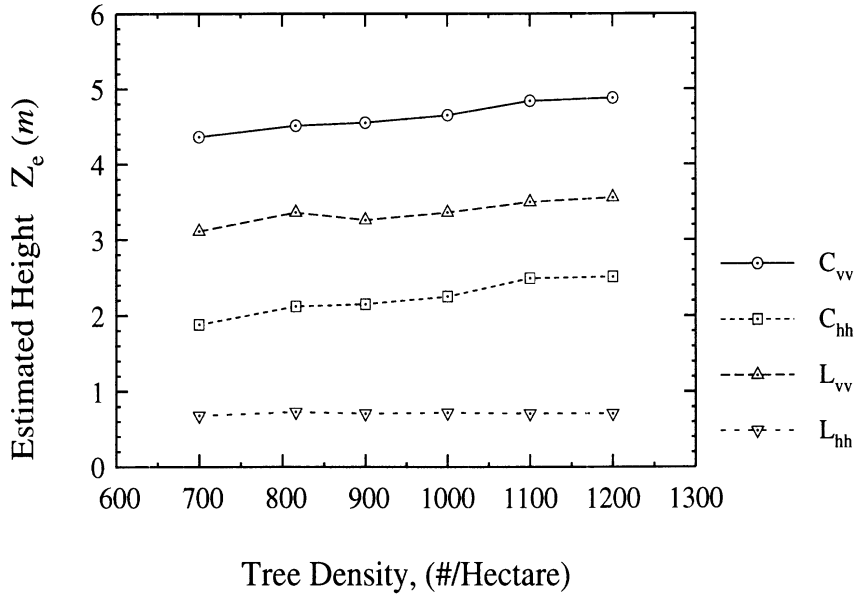

Figure 10: The estimated scattering phase center height of Stand 22 as a function of tree density, simulated at $\theta_i = 45°$.

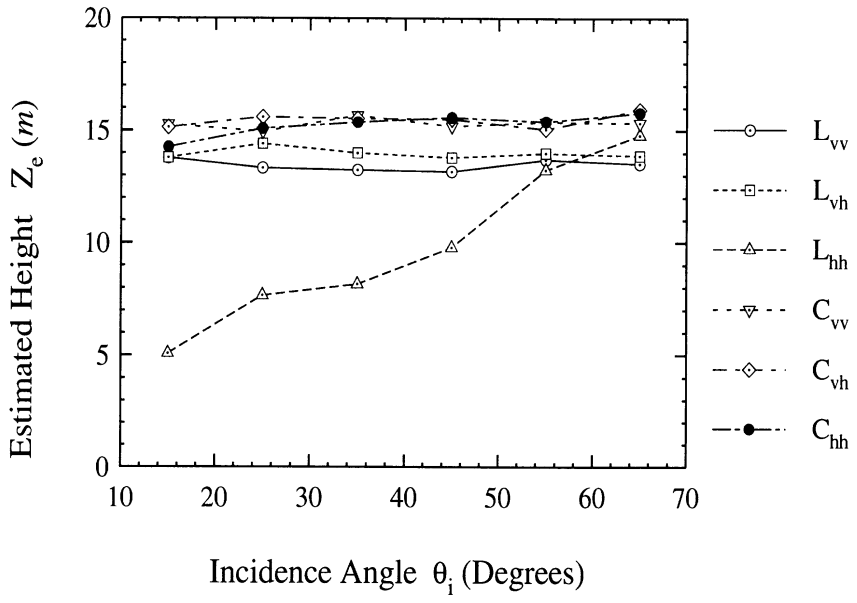

Figure 11: The estimated scattering phase center height of Stand 31 as a function of incidence angle, with fully-polarimetric L- and C-and response.

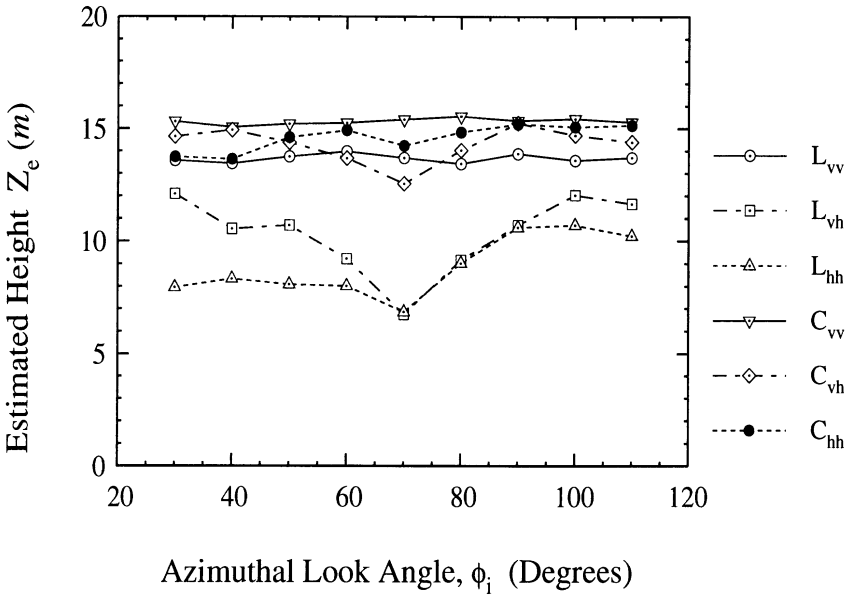

Figure 12: The estimated scattering phase center height of Stand 31 over a tilted ground with tilt angle $\theta_g = 10°$, at $\theta_i = 25.4°$.

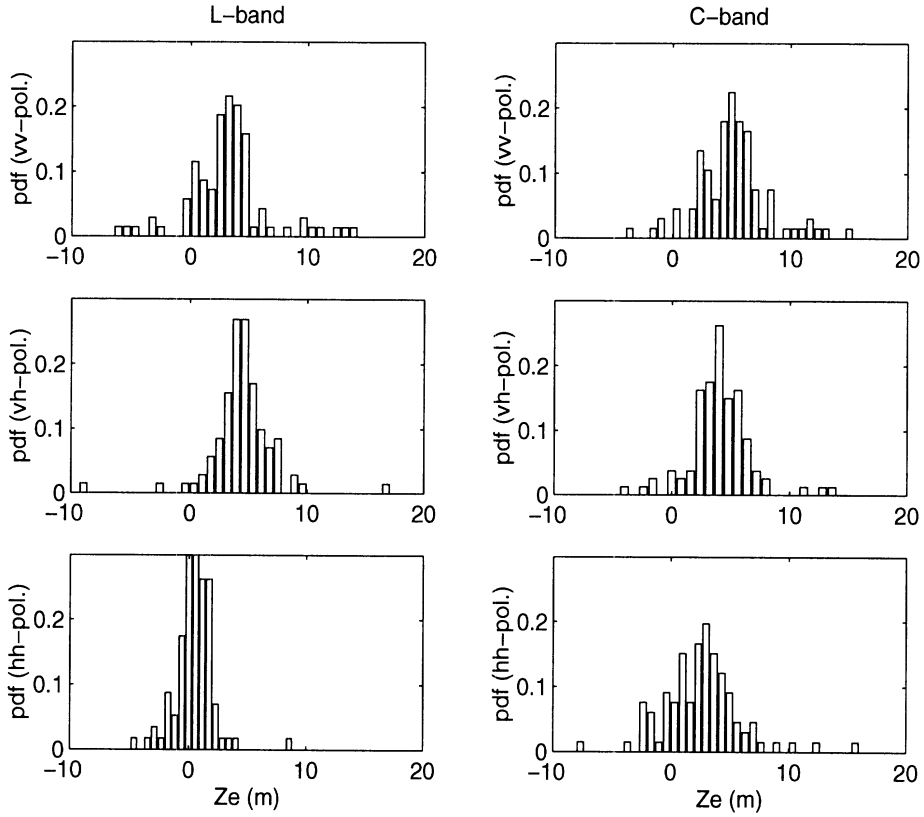

Figure 13: PDF of the scattering phase center height of Stand 22 at $\theta_i = 45°$ as a function of frequency and polarization.

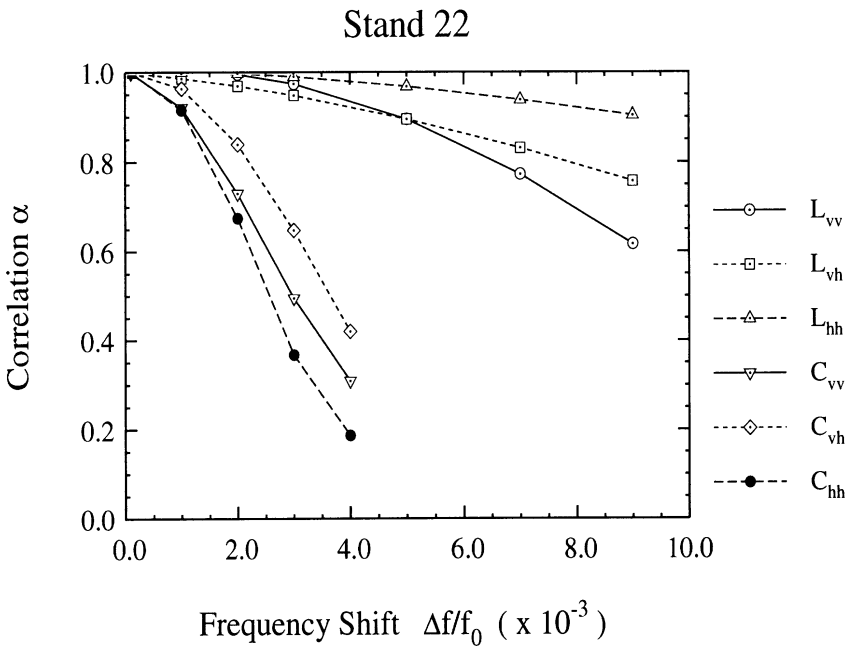

(a)

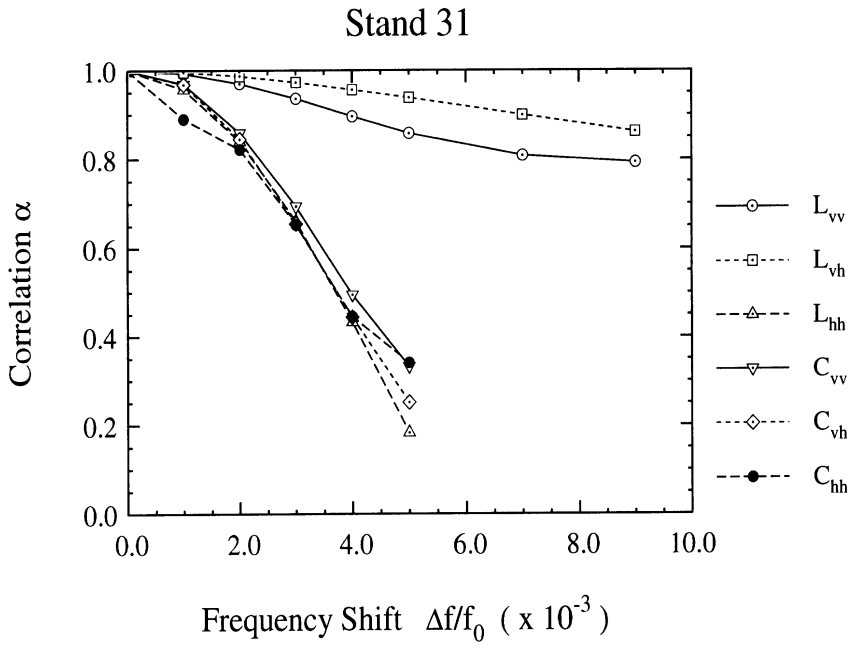

(b)

Figure 14: The correlation coefficient as a function of the frequency shift, simulated from (a) Stand 22 and (b) Stand 31.

Appendix V

Electromagnetic Scattering from Short Branching Vegetation

Electromagnetic Scattering from Short Branching Vegetation

Tsenchieh Chiu and Kamal Sarabandi
Department of Electrical Engineering and Computer Science
The University of Michigan, Ann Arbor, MI 48109-2122
Tel:(313) 936-1575, Fax:(313) 747-2106
Email: tcchiu@eecs.umich.edu

Abstract – A polarimetric coherent electromagnetic scattering model for short branching vegetation is developed in this paper. With the realistic structures which reasonably describe the relative positions of the particles, this model is able to consider the coherent effect due to the phase difference between the scattered fields from different particles, and account for the second-order near-field interaction between particles to which the relative positions and orientation of the particles are essential. The model validation with measurements is also presented, and excellent agreement is obtained. The polarimetric radar backscatter measurements for soybean plants using truck-mounted scatterometers were conducted at L-band and C-band under different soil-moisture conditions. Through an extensive ground truth, the important plant and rough surface parameters, such as the soil moisture and surface roughness, vegetation dielectric constant, and geometry of the soybean plants, were characterized for model verification. It is found that the second-order near-field scattering is significant at C-band for fully-grown soybeans due to the high vegetation particle density, and at L-band the contribution from the second-order near field is negligible. The coherence effect is shown to be important at L-band and to a much lower extent at C-band. This model is then used to demonstrate its ability for estimating the physical parameters of a soybean field including soil moisture from a polarimetric set of AIRSAR images.

1 Introduction

Microwave remote sensing has evolved into an important tool for monitoring the atmosphere and surface of the earth. Electromagnetic waves at microwave frequencies are able to penetrate more deeply into vegetation, and, therefore, retrieving parameters of vegetation and underlying ground surfaces has become one of the major applications of microwave remote sensing. With the advent of polarimetric synthetic aperture radars (SAR) and the development of radar polarimetric techniques, microwave remote sensing has attained significant prominence. While a large amount of data can be collected very efficiently, there are still difficulties in accurately predicting the physical parameters of the targets from the collected radar information. To accomplish this task, a necessary step is to construct a high-fidelity scattering model by which the relationship between all targets' physical parameters to the radar backscatter can be established.

In the early vegetation scattering models, the vegetation medium was simplified in terms of a homogeneous random medium and the single scattering theory was applied to account for the scattering and propagation in the random medium [1, 2, 3]. For example, in [1] a forest stand is represented in terms of a two-layer random medium including a crown layer composed of randomly oriented cylinders and disks representing branches and leaves and a trunk layer containing nearly vertical cylinders representing tree trunks below the crown layer. Although these models are capable of predicting the scattering behavior of vegetation qualitatively, they are incapable of predicting the scattering behavior quantitatively due to their simplifying assumptions. An important feature of a high fidelity scattering model is to preserve the structure of vegetation as different species of vegetation have their own unique structures, which are expected to exhibit their own scattering behaviors. An important effect of the vegetation structure is the coherence effect caused by the relative position of the vegetation particles which produce certain interference pattern. It is shown that the coherence effects caused by the vegetation structure become more significant at lower frequencies [4]. In the remote sensing of vegetation-covered terrain where the underlying soil surface is the target of interest , low microwave frequencies are recommended and therefore the coherence effects must be carefully accounted for. The model developed by Yueh et al. [5] may be among the first to address the coherence effects caused by the vegetation structure. In their scattering model for soybeans, a two-scale branching vegetation structure was constructed, and the scattered fields from particles were added coherently. Lin et al. [6] also proposed a coherent scattering model for forest canopies in which rather realistic tree-like structures are constructed using the fractal theory. In both models, the scattering solutions are formulated using the single scattering theory.

Another important issue in modeling the scattering from vegetation is the effect of the multiple scattering among vegetation particles. Vegetation particles are usually arranged in clusters within a single plant, such as leaves around end branches and branches around main stems and trunks. Therefore, a vegetation medium may be appropriately considered as locally dense. In such cases, the near-field multiple scattering is strong and may significantly affect the overall response. To accurately evaluate the near-field interaction, the realistic description of the relative positions and orientations of the vegetation particles and accurate and efficient scattering formulations are required. In recent years, some advanced scattering solutions that account for the near-field interaction between scatterers have been presented [7, 8]. However, vegetation scattering models which can handle the near-field interaction with realistic vegetation structures have not been developed yet. The evaluation of the near-field interaction is usually numerically intensive, considering the huge number of particles in the medium.

In this paper, a scattering model for soybeans is presented which incorporates realistic

computer-generated vegetation structures and accounts for the second-order near-field scattering interaction. Soybeans are erect branching plants composed of components which can be often found in many vegetation: stems, branches, leaves and fruits (pods) arranged in a very well-defined manner. Hence it is very appropriate for studying the effect of the vegetation structure on the radar backscatter. Also because of its moderate number of particles, the computation of the second-order near-field interaction is not formidable. Also from the experimental point of view, the dimensions of soybean plants are small enough to allow for conducting controlled experiments using truck-mounted scatterometers. Due to the uniformity of the plants and underlying soil surface, gathering the ground truth data is rather simple. The paper is organized as follows: Section 2 gives the theoretical description of the model, including the vegetation structure modeling and the scattering solution. In Section 3 the experimental procedures using the University of Michigan truck-mounted scatterometer and AIRSAR are discussed. Finally in Section 4 model validation using the measured data and a sensitivity analysis are presented.

2 Theoretical Analysis

Consider a global coordinate system with x-y plane parallel to a horizontal ground plane and z-axis along the vertical direction, as shown in Fig. 1. Suppose a plane wave given by

$$\mathbf{E}^{\mathbf{i}}(\mathbf{r}) = \mathbf{E}_{\mathbf{0}}^{\mathbf{i}} e^{ik_0 \hat{k}_i \cdot \mathbf{r}} \ . \tag{1}$$

is illuminating the ground plane from the upper half-space, where $\hat{k}_i$ is the unit vector along the propagation direction given by

$$\hat{k}_i = \hat{x} \sin\theta_i \cos\phi_i + \hat{y} \sin\theta_i \sin\phi_i - \hat{z} \cos\theta_i \ . \tag{2}$$

The vector $\mathbf{E}_{\mathbf{0}}^{\mathbf{i}}$ in (1) is expressed in terms of a local coordinate system ($\hat{v}_i$,$\hat{h}_i$,$\hat{k}_i$) where $\hat{h}_i = \hat{k}_i \times \hat{z}/|\hat{k}_i \times \hat{z}|$ and $\hat{v}_i = \hat{h}_i \times \hat{k}_i$ denote the horizontal and vertical unit vectors, respectively. Representing the direction of the observation point by $\hat{k}_s$, the polarization of the scattered field can also be expressed in terms of a local coordinated system ($\hat{v}_s$,$\hat{h}_s$,$\hat{k}_s$) where

$$\hat{k}_s = \hat{x} \sin\theta_s \cos\phi_s + \hat{y} \sin\theta_s \sin\phi_s + \hat{z} \cos\theta_s \ , \tag{3}$$

and $\hat{v}_s$ and $\hat{h}_s$ can be obtained using similar expressions as those given for $\hat{v}_i$ and $\hat{h}_i$, respectively.

2.1 Vegetation Structure Modeling

To make the proposed scattering solution tractable, simple geometries are chosen to represent vegetation particles. Leaves are represented by elliptical thin dielectric disks. The other particles, which include stems, branches, and pods, are modeled using circular cylinders. Analytical scattering solutions are available for both geometries and will be introduced in the next section.

The orientation and dimension of each particle are described by four parameters, as shown in Fig. 2. The values of these parameters are determined by random number generators during the simulation with predescribed probability distribution functions (pdf). The orientation parameters of the particles are described by two angles: β(elevation angle) and γ(azimuth angle). Azimuthal symmetry is assumed for γ, and its pdf is given by

$$p(\gamma) = \frac{1}{2\pi}, \qquad \gamma \in [0, 2\pi) \ . \tag{4}$$

However, for β, a bell-shaped pdf is chosen:

$$p(\beta) = \frac{e^{-((\beta-\beta_m)/\beta_s)^2}}{\int_0^\pi e^{-((\beta'-\beta_m)/\beta_s)^2}\, d\beta'}, \qquad \beta \in [0, \pi] \,. \tag{5}$$

For leaves, the axis ratio (b/a) assumed constant and the thickness and major axis (a) are given Gaussian pdfs. Three types of cylinders are considered for main stems, branches, and pods. For these cylinders, Gaussian pdfs are chosen to describe the statistics of their radii and lengths.

The branching structure of soybeans is rather simple and can be developed using the following algorithm:

1. All parameters of main stem are determined using random number generators. The main stem is then divided into subsections, whose lengths are again decided by Gaussian random number generator.

2. At each node (connecting point of two subsections of the stem), a branch is placed whose orientation is obtained from (4) and (5). Depending on the growth stage, pods may be added at each node.

3. To each branch end a leaf is attached. In this paper, the number of leaflets at each branch end is three (this may be different for other soybean species). Azimuthal orientation angle of leaves is determined from the orientation angle of the branches they are connected to.

Figure 9 shows a typical computer-generated soybean structures according to the aforementioned algorithm.

2.2 Scattering Mechanism and Scattering Formulations for the Vegetation Particles and Rough Surfaces

Several scattering mechanisms are considered for the scattering model. Figure 3 depicts 6 different mechanisms including: (1) direct backscatter from the underlying rough surface, (2) direct backscatter from vegetation particles, (3) single ground bounce, (4) double ground bounce, (5) second-order scattering interaction among vegetation particles, and (6) scattering interaction between main stem and the rough surface. The first four mechanisms are included in almost all existing vegetation scattering models. Mechanism #5 is a second-order solution which accounts for the near-field interaction within a single plant. Mechanism #6 is only considered for predicting the cross-polarized scattering at L-band according to a study reported in [10] where it is shown that the co-polarized scattering of mechanism #6 at L-band is weak compared to that of Mechanism #2. Mechanism #6 is also ignored at C-band, because of attenuation experienced by the wave propagating through the vegetation layer. In what follows, the scattering solutions for each mechanism is briefly described.

1. **Mechanism #1:**

   There exist many rough-surface scattering models available in the literature. In this paper, a second-order small perturbation model(SPM) [17] and a physical optic (PO) model [18] are incorporated to handle the backscatter from the rough surface.

2. **Mechanisms #2~#4:**

   These mechanisms are often referred to as the single scattering solutions in which only the scattering solutions for the isolated vegetation particles are considered. The effect of

the ground surface in mechanisms #3 and #4 are considered by introducing the ground reflection coefficients. If the SPM is used in mechanism #1, the Fresnel reflection coefficients are used directly. If the PO is needed according to the surface roughness condition, the reflection coefficients are modified by $e^{-2(ks\cos\theta_i)^2}$ to account for the reduction in the surface reflectivity [11]. The single scattering solutions for dielectric disks and cylinders are obtained from the following formulations:

(a) **Elliptical disk:**

The thickness of the soybean leaves ($\approx 0.2 - 0.3mm$) is usually small compared to the wavelength in microwave region and the ratio of the thickness to the diameter of the leaves is much less than unity. Also by noting that the dielectric constant of vegetation is lossy, the Rayleigh-Gans formulation [12] can be applied to derive the scattering solution for the elliptical disks representing the vegetation leaves. For an elliptical disk, the scattering matrix elements are found to be

$$S_{pq}^{d} = \hat{p} \cdot (\bar{\bar{\mathbf{P}}}_{\mathbf{d}} \cdot \hat{q}) \frac{A_d k_0^2}{2\pi} \frac{J_1(\sqrt{(aA)^2 + (bB)^2})}{\sqrt{(aA)^2 + (bB)^2}} , \tag{6}$$

where A_d, a and b are the area, major axis, and minor axis of the disk respectively. In (6), $\bar{\bar{\mathbf{P}}}_{\mathbf{d}} = \bar{\bar{\mathbf{U}}}_{\mathbf{d}}^{-1} \bar{\bar{\mathbf{P}}}_{\mathbf{d}}^{0} \bar{\bar{\mathbf{U}}}_{\mathbf{d}}$, where $\bar{\bar{\mathbf{P}}}_{\mathbf{d}}^{0}$ is the disk's polarizability tensor which can be found in [12, 13], and $\bar{\bar{\mathbf{U}}}_{\mathbf{d}}$ is the matrix of coordinate transformation which transfers the global coordinate system to a local coordinate system defined by the major axis, minor axis, and the normal of the disk respectively. The explicit expression for $\bar{\bar{\mathbf{U}}}_{\mathbf{d}}$ can be obtained from [14]. Also A and B are given by

$$\begin{aligned} A &= k_0 \left[\bar{\bar{\mathbf{U}}}_{\mathbf{d}}^{-1} \cdot (\hat{k}_i - \hat{k}_s) \right] \cdot \hat{x} \\ B &= k_0 \left[\bar{\bar{\mathbf{U}}}_{\mathbf{d}}^{-1} \cdot (\hat{k}_i - \hat{k}_s) \right] \cdot \hat{y} . \end{aligned} \tag{7}$$

(b) **Circular cylinder:**

Exact scattering solution does not exist for cylinders of finite length, but an approximated solution, which assumes the internal field induced within the finite cylinder is the same as that of the infinite cylinder with the same cross section and dielectric constant, can be used [15]. Generally, this solution is valid when the ratio of the length to the diameter is large.

3. **Mechanism #5:**

The second-order scattered field between two particles is formulated using an efficient algorithm based on the reciprocity theorem [7]. For two adjacent particles we have

$$\hat{p} \cdot \mathbf{E_{21}} = \int_{V_1} \mathbf{E}_{e2} \cdot \mathbf{J}_1 \, dv . \tag{8}$$

where $\mathbf{E}_{e2}$ is the scattered field from particle #2 illuminated by an infinitesimal current source at the observation point in the absence of particle #1, and $\mathbf{J}_1$ is the induced polarization current of particle #1 illuminated by the incidence field in the absence of particle #2. $\mathbf{E_{12}}$ can be obtained using the reciprocity theorem. Hence the second-order scattered field are conveniently obtained from the plane wave solution of the induced polarization current and near field of individual particles. These quantities for disks and cylinders are given by:

(a) **Disk:** The induced polarization current is obtained from Rayleigh-Gans approximation and is given by

$$\mathbf{J_1(r)} = -ik_oY_o\bar{\bar{\mathbf{P}}}_\mathbf{d} \cdot \mathbf{E_0^i} e^{ik_0\hat{k}_i\cdot\mathbf{r}} , \tag{9}$$

where $\bar{\bar{\mathbf{P}}}_\mathbf{d}$ is the polarizability tensor. The exact near-field scattered field must be numerically evaluated from

$$\mathbf{E_{e2}(r)} = \frac{ik_0Z_0}{(4\pi)^2}\frac{e^{ik_0r_0}}{r_0}\left(\bar{\bar{\mathbf{P}}}_\mathbf{d}\cdot\hat{p}\right)\cdot\int_{S_2}\bar{\bar{\mathbf{G}}}(k,R)e^{ik_0(-\hat{k}_s\cdot\mathbf{r}'+R)}\,ds' , \tag{10}$$

where

$$\bar{\bar{\mathbf{G}}}(k_0,R) = \left(\frac{-1+ik_0R+k_0^2R^2}{R^3}\right)\bar{\bar{\mathbf{I}}} + \left(\frac{3-3ik_0R-k_0^2R^2}{R^3}\right)\hat{R}\hat{R} , \tag{11}$$

and $\hat{R}$ is a unit vector defined by $\hat{R} = (\mathbf{r}-\mathbf{r}')/|\mathbf{r}-\mathbf{r}'|$.

(b) **Cylinder:** The formulation for finite finite cylinders is used again to calculate the induced polarization current and the near-field scattered field. The formulation of the scattered field in the vicinity of the cylinder is given by [7]

$$\mathbf{E_{e2}(r)} = -\frac{ik_oZ_oe^{ik_or_o}}{4\pi r_o}\mathbf{F}(\phi-\phi_s)H_o^{(1)}(k_o\sin\theta_s\rho)e^{k_o\cos\theta_sz} . \tag{12}$$

Equation (12) is derived using the stationary phase approximation along the axial direction of the cylinder axis. This solution has been verified by the method of moments [7, 16], and the region of validity is given by

$$\rho > 2d_c^2/\lambda , \tag{13}$$

where d_c is the diameter of the cylinder, and ρ is the radial distance between the observation point and the cylinder axis. For the main stem of soybeans, the radius is usually less than 5mm. Applying (13) it is found that $\rho > 3.5mm$ at C-band (5.3 GHz). Therefore, (12) is appropriate for calculating the near-field interaction.

4. **Mechanism #6:**

The incoherent interaction between the main stems and rough surface is formulated using the reciprocity technique introduced in [7]. The details and lengthy formulation for the cylinder-rough surface scattering interaction can be found in [19]. This model is only applied to calculate the scattering interaction between the main stem and underlying rough surface. The reason for this is that for a titled cylinder with large elevation angle (β) such as branches, the cross-polarized scattering from mechanisms #2 and #3 is dominant. However, main stems often grow nearly vertically and its interaction with the ground becomes a important source of the cross-polarized scattering, noting that the mechanisms #2 and #3 of nearly vertical cylinders do not produce significant cross-polarized scattering field. As will be shown later, the cross-polarized scattering at L-band is mainly dominated by two scattering mechanisms #2 and #6.

2.3 Propagation in a Lossy Layered Media

2.3.1 Foldy's Approximation

The scattering solutions provided in the previous section are for targets in free space. However, for vegetation canopies the targets are within a lossy random medium. Thus, a particle is illuminated by not only the incident plane wave, but also by the scattered fields from other particles. To calculate the total scattered field from a particle, it is usually assumed that the particle is embedded in homogeneous lossy medium, as shown in Fig. 4(a). The vegetation layer can be divided into many sub-layers which contain different types and number density of vegetation particles, and thus each layer exhibits different equivalent propagation constants.

Foldy's approximation [14] has been widely used in many vegetation scattering models to account for the attenuation experienced by the wave traveling through the vegetation medium. According to the Foldy's approximation the vertical and horizontal components of the mean electric field in a sparse random medium satisfy

$$\begin{aligned} \frac{dE_h}{ds} &= i\left(k_0 + M_{hh}\right) E_h + iM_{hv}E_v \\ \frac{dE_v}{ds} &= iM_{vh}E_h + i\left(k_0 + M_{vv}\right) E_v \ , \end{aligned} \tag{14}$$

where s is the length along the propagation path within the medium and

$$M_{pq} = \frac{2\pi n_0}{k_0}\langle S_{pq}(\hat{k},\hat{k})\rangle \ , \qquad p,q \in \{h,v\} \ . \tag{15}$$

Here n_0 is the number density of the scatterers within the medium, and $\langle S_{pq}(\hat{k},\hat{k})\rangle$ is the averaged forward scattering matrix element of the scatterers. Since the vegetation structure exhibits statistical azimuthal symmetry, there is no coupling between horizontal and vertical components of the coherent field and therefore $M_{hv} = M_{vh} = 0$. From (14), the effective propagation constants for both polarizations are given by

$$\begin{aligned} k_h^e &= k_0 + M_{hh} \\ k_v^e &= k_0 + M_{vv} \ . \end{aligned} \tag{16}$$

As mentioned previously, the second-order near-field interaction is incorporated in this model, and it will only be calculated for the scatterers within a single plant. It is reasonable to assume that no extinction should be considered for the calculation of the near-field interaction. However, since both particle are still embedded in the vegetation layer, extinction is considered for the incident wave and secondary scattered fields. As shown in Fig. 4(b), the space between two scatterers is considered as free space, and Foldy's approximation is still used on paths #1 and #2.

2.3.2 Propagation Paths

In this section, the phase difference and extinction caused by the wave propagating in the vegetation layer will be formulated using the method presented in [20]. To build a coherent scattering model, the phase of each scattering mechanism has to be calculated with respect to a phase reference point. Figure 5(a) shows the propagation geometry for the direct path. The reference phase point is taken to be the origin of the coordinate system. Using ray optics, the propagation from the equi-phase plane (shown in Fig. 5(a)) directly to the scatterer is given by

$$\Phi_d'(\hat{k}_0, \mathbf{r}', p) = k_0 \mathbf{r_1} \cdot \hat{k}_0 + k_p^e(\mathbf{r}' - \mathbf{r_1}) \cdot \hat{k}_e \ , \tag{17}$$

where $\mathbf{r_1}$ denotes the location where the ray intersects the interface between the vegetation layer and free-space. Here the effect of refraction is ignored assuming a diffuse boundary between the vegetation layer and free-space ($\hat{k}_e = \hat{k}_0$) and p denotes the polarization of the wave. Substituting (16) into (17), it is found that

$$\Phi'_d(\hat{k}_0, \mathbf{r}', p) = k_0 \mathbf{r}' \cdot \hat{k}_0 + M_{pp}(\mathbf{r}' - \mathbf{r_1}) \cdot \hat{k}_0 \ . \tag{18}$$

The first term on the right-hand side of (18) is the free-space propagation term and will be included in the scattering matrix elements of the scatterer. The second-term on the right-hand side is the extra phase difference and extinction caused by the propagation in the lossy vegetation media, and will be denoted as $\Phi_d(\hat{k}_0, \mathbf{r}', p)$. The free space-vegetation interface is set to be the x-y plane, so it is found that

$$(\mathbf{r}' - \mathbf{r_1}) \cdot \hat{k}_0 = \frac{z'}{\hat{k}_o \cdot \hat{z}} \ . \tag{19}$$

Therefore, $\Phi_d(\mathbf{r}', p)$ can be written as

$$\Phi_d(\hat{k}_0, \mathbf{r}', p) = M_{pp} \frac{z'}{\hat{k}_o \cdot \hat{z}} \ . \tag{20}$$

The ground-bounce path, as shown in Fig. 5(b), includes a reflection from the ground plane. In Fig. 5(b), the image position is given by

$$\mathbf{r}'_{image} = x'\hat{x} + y'\hat{y} - (z' + 2d)\hat{z} \ , \tag{21}$$

where d is the thickness of the layer. Using (20), it is found that $\Phi_g(\hat{k}_0, \mathbf{r}', p)$, which only accounts for the extra phase difference and extinction caused by the propagation in the lossy vegetation media, can be written as

$$\Phi_g(\hat{k}_0, \mathbf{r}', p) = -M_{pp} \frac{z' + 2d}{\hat{k}_o \cdot \hat{z}} \ . \tag{22}$$

2.4 Scattering from Soybean Fields and Monte-Carlo Simulation

Consider an area of soybean field with N_p soybean plants per unit area. For a given computer-generated soybean plant (the k-th plant with N_s particles), the total scattering amplitude can be written as

$$S_{pq,k} = \left\{ \sum_{i=1}^{N_s} \left[S^d_{pq,ki} + S^{gg}_{pq,ki} + S^{g1}_{pq,ki} + S^{g2}_{pq,i} \right] + \sum_{i=1}^{N_s} \sum_{\substack{j=1 \\ j \neq i}}^{N_s} S^{2nd}_{pq,kij} \right\} e^{ik_0(\hat{k}_i - \hat{k}_s) \cdot \mathbf{r_k}} \ , \tag{23}$$

where $\mathbf{r_k}$ is the location of the plant. In (23) each term includes the attenuation and phase shift due to the propagation:

$$\begin{aligned}
\text{direct:} \qquad & S^d_{pq,ki} = S_{pq,ki}(\hat{k}_s, \hat{k}_i) e^{i\Phi_d(-\hat{k}_s, \mathbf{r}_{ki}, p)} e^{i\Phi_d(\hat{k}_i, \mathbf{r}_{ki}, q)} \\
\text{ground-plant:} \qquad & S^{g1}_{pq,ki} = S_{pq,ki}(\hat{k}_s, \hat{k}'_i) R_p e^{i\Phi_g(-\hat{k}_s, \mathbf{r}_{ki}, p)} e^{i\Phi_d(\hat{k}_i, \mathbf{r}_{ki}, q)} \\
\text{plant-ground:} \qquad & S^{g1}_{pq,ki} = S_{pq,ki}(\hat{k}'_s, \hat{k}_i) R_q e^{i\Phi_d(-\hat{k}_s, \mathbf{r}_{ki}, p)} e^{i\Phi_g(\hat{k}_i, \mathbf{r}_{ki}, q)} \\
\text{ground-ground:} \qquad & S^{gg}_{pq,ki} = S_{pq,ki}(\hat{k}'_s, \hat{k}'_i) R_q R_q e^{i\Phi_g(-\hat{k}_s, \mathbf{r}_{ki}, p)} e^{i\Phi_g(\hat{k}_i, \mathbf{r}_{ki}, q)} \\
\text{near-field 2nd-order:} \qquad & S^{2nd}_{pq,kij} = S^{2nd}_{pq,kij}(\hat{k}_s, \hat{k}_i) e^{i\Phi_d(-\hat{k}_s, \mathbf{r}_{ki}, p)} e^{i\Phi_d(\hat{k}_i, \mathbf{r}_{kj}, q)} \ ,
\end{aligned} \tag{24}$$

where $\hat{k}_i' = \hat{k}_i - 2(\hat{k}_i \cdot \hat{z})\hat{z}$ and $\hat{k}_s' = \hat{k}_s - 2(\hat{k}_s \cdot \hat{z})\hat{z}$. Note that all scattering mechanisms are added coherently to capture the coherence effect caused by the vegetation structure.

The scattering coefficient of the soybean field is then computed by incoherent addition of the scattered powers from vegetation, rough surface, and main stem-rough surface interaction. Hence

$$\sigma^0_{pqpq} = \sigma^0_{pqpq}(\text{vegetation}) + \sigma^0_{pqpq}(\text{rough surace}) + \sigma^0_{pqpq}(\text{stem-rough surface}) \ , \tag{25}$$

where

$$\sigma^0_{pqpq}(\text{vegetation}) = 4\pi \left\langle \left| \sum_{k=1}^{N_p} S_{pq,k} \right|^2 \right\rangle \tag{26}$$

$$\sigma^0_{pqpq}(\text{rough surface}) = \sigma^0_{pqpq,r} \left| e^{i\Phi_d(-\hat{k}_s,-d\hat{z},p)} e^{i\Phi_d(\hat{k}_i,-d\hat{z},q)} \right|^2 \tag{27}$$

$$\begin{aligned} \sigma^0_{pqpq}(\text{stem-rough surface}) = 4\pi N_p \Big\langle \Big| & S^{rc}_{pq} e^{i\Phi_d(-\hat{k}_s,-d\hat{z},p)} e^{i\Phi_d(\hat{k}_i,(-d+0.5l_c)\hat{z},q)} \\ & + S^{cr}_{pq} e^{i\Phi_d(\hat{k}_i,-d\hat{z},p)} e^{i\Phi_d(-\hat{k}_s,(-d+0.5l_c)\hat{z},q)} \Big|^2 \Big\rangle \ . \end{aligned} \tag{28}$$

In calculation of the contribution from the direct rough surface and the stem-rough surface, the propagation attenuation through vegetation layer is also included. S^{rc}_{pq} and S^{cr}_{pq} are, respectively, the rough surface-cylinder and cylinder-rough surface scattering amplitudes. The ensemble averaging in (28) is carried out analytically using the SPM formulation, and the details are reported in [10]. As mentioned earlier, the contribution from this term is only significant at L-band for the cross-polarized term.

The ensemble averaging in (26) is carried out using a Monte-Carlo simulation. For each realization in the Monte-Carlo simulation, a group of computer-generated soybean plants are generated and distributed on a square area of 1 m^2, and then the scattered fields are computed. This procedure will be repeated until a convergence is reached. To examine the coherence effect, the scattered power from the vegetation is also calculated incoherently from

$$\begin{aligned} \sigma^0_{pqpq}(\text{vegetation}) = 4\pi \Bigg\langle \sum_{k=1}^{N_p} \Bigg\{ \sum_{i=1}^{N_s} \left[\left| S^d_{pq,ki} \right|^2 + \left| S^{gg}_{pq,ki} \right|^2 + \left| S^{g1}_{pq,ki} \right|^2 + \left| S^{g2}_{pq,i} \right|^2 \right] \\ + \sum_{i=1}^{N_s} \sum_{\substack{j=1 \\ j\neq i}}^{N_s} \left| S^{2nd}_{pq,kij} \right|^2 \Bigg\} \Bigg\rangle \ . \end{aligned} \tag{29}$$

3 Experimental Results

In this section, the experimental procedure and the multi-frequency multi-polarization backscatter measurements using polarimetric scatterometer systems and JPL AIRSAR are presented.

3.1 Measurement Using the University of Michigan's POLARSCAT

In August of 1995, a series of polarimetric measurements were conducted on a soybean field near Ann Arbor, MI. These measurement were conducted using the University of Michigan polarimetric scatterometer systems (POLARSCAT) [21]. The polarimetric backscatter data were

collected at two different frequencies (L-band and C-band) over a wide range of incidence angles (from 20^o to 70^0 at 10^o increment). The overall goal of these experiments was to investigate the feasibility of soil-moisture retrieval of vegetation-covered terrain from radar backscatter data. Experiments were designed to observe the radar-backscatter variations due to the change in soil moisture while the vegetation parameters were almost the same. Two sets of data were collected. In one measurement the angular polarimetric data were collected on August 14 when the underlying soil surface was dry, and in another a similar data was collected right after a heavy rain on August 18. At the time of experiments the soybean plants were fully grown with significant number of pods. In fact the vegetation biomass was at its maximum. Since the separation between the time of experiments were only about 4 days, no significant change in the vegetation parameters were observed.

The vegetation structural parameters and moisture in addition to the soil surface roughness and moisture were carefully characterized. The dielectric constant of the soil surface was measured by using a C-band field-portable dielectric probe [22]. The measured relative dielectric constant (ϵ_r) was used to estimate the moisture contents (m_v) by inverting a semi-empirical model [23] which give ϵ_r in terms of m_v. The mean m_v, which is shown in Table 1, is then used to estimate ϵ_r at L-band.

Two dielectric measurement techniques [24, 25] were used to measure the dielectric constant of leaves and stems. These measurement were performed at C-band using WR-187 waveguide sample holder, and the results are shown in Fig. 6. The corresponding dielectric constants at L-band was then calculated using the empirical model provided in [26]. The gravimetric moisture content (m_g) of the vegetation was also measured on the day of radar measurement to monitor the variation of the biomass. As shown in Table 1, the vegetation moisture remained almost the same on both dates of the experiments.

The dimensions and orientations of vegetation particles were also recorded. Table 2 shows the means and standard deviations of vegetation parameters. Unlike most cultivated fields where the plants are planted in row structures, the soybean plants of this field were distributed in a rather random pattern, as shown in Fig. 7. This picture shows the top-view at the end of the season where all the leaves were fallen. The surface roughness parameters were also measured and reported in Table 1.

3.2 Measurement Using AIRSAR

JPL Airborne Synthetic Aperture Radar (AIRSAR) [27] was deployed to conduct backscatter measurements on a number of cultivated fields. Although AIRSAR is capable of measuring polarimetric backscatter at three microwave frequencies (P-,L-, and C-band), only L-band and C-band data were collected. The backscatter data were collected by AIRSAR during its flight over the Kellogg Biological Station near Kalamazoo, Michigan, on July 12, 1995. Also these data sets were collected at three different incidence angles: 30, 40, 45 degree. Unfortunately the soybean fields were not within the research site of the station and the ground truth data was rather limited. The only available informations are that the soybean were about a month old and the volumetric soil moisture content was less than 0.1. Figure 8 shows the composite L-band and C-band SAR image at 45^o incidence angle.

4 Data Simulation and Analysis

The vegetation scattering model is first validated using the data collected by POLARSCAT. Guided by the ground truth data, many soybean plant structures were generated in order to

carry on the data simulation (see Fig. 9(a)). The computer-generated plants were uniformly distributed using a random number generator. The Monte-Carlo simulations are performed at incidence angles ranging from 20^o to 70^o at 5^o increment. Figures 10(a) and 11(a) show the simulated and measured backscattering coefficients versus incidence angle at L-band and C-band, respectively. Good agreement is achieved by allowing the dielectric constants of vegetation particles vary within the confidence region shown in Fig. 6. In figures 10(b), (c), and (d), the contributions from individual scattering mechanisms are plotted as functions of incidence angle at L-band. The cross products of among different mechanisms, which account for the coherence effect, are not presented in these figures. It is quite obvious that the contribution from the second-order near-field interaction at L-band is negligible for both co- and cross-polarized terms. It is also shown that for co-polarized backscattering coefficient the direct backscatter from soybean, direct backscatter from rough surface, and single ground-bounce are sufficient to characterize the scattering behavior. For cross-polarization, however, the two most significant mechanisms are the direct backscatter from vegetation and the incoherent rough surface-stem interaction. The later mechanism contains information regarding the underlying soil surface including the soil moisture. Figures 11(b), (c), and (d) show scattering contributions from different mechanisms versus incidence angle at C-band. The direct backscatter form vegetation and the second-order near-field interaction are the dominant scattering mechanisms at C-band. Because of larger near-field region, the near-field interaction is stronger at C-band than at L-band. Also the second-order near-field interaction has more profound effect on the vv- and cross-polarization, because the orientation of the main stems is nearly vertical. The other mechanisms, which include the soil moisture information, are not significant for two reasons: (1) high extinction through the vegetation layer, and (2) surface roughness which decreases the reflectivity of the ground surface.

From these analysis it is found that the backscatter at C-band or higher frequencies are mainly sensitive to vegetation parameters for sufficiently high vegetation biomass (in this case, biomass = 1.97 kg/m^2). At L-band or lower frequencies, it is possible to sense the soil moisture for surfaces covered with short vegetation and relatively high biomass. Figures 12(a), (b), and (c) demonstrate the sensitivity of the backscatter to soil moisture as a function of incidence angle for the soybean field. The simulations are performed under four different soil-moisture conditions: $m_v = 0.1, 0.2, 0.3$ and 0.4 at L-band. The backscatter data collected on August 14 and August 18 are also plotted in these figures for comparison. These results suggest that the appropriate range of incidence angle for the the purpose of soil-moisture retrieval is $\theta_i < 50^o$ where there is about 6-dB of dynamic range. At incidence angles larger than 50^o, the sensitivity to soil moisture decreases due to the high extinction caused by the vegetation. To retrieve the soil moisture accurately, vegetation parameters must be estimated as accurately as possible. It seems a combination of high and low frequency backscatter data is needed to estimate the vegetation and soil moistures accurately.

Due to the limited ground-truth data, the AIRSAR data set is used for estimating the vegetation and surface roughness parameters. Although the retrieval algorithm presented here is based on trial and error, it indicates the feasibility of estimating vegetation parameters and soil moisture from image radars. The procedure for estimating these parameters is described below:

1. Based on a series of trial simulations, it is found that the second-order near-field interaction can be ignored at L- and C-band for the one-month old soybeans. In this case the soybean plants are still young with shorter branches and stems and much fewer number of vegetation particles. Also there are no pods on the plants whose interaction with the

main stem is the major source of the near-field interaction.

2. Judging from the measured values of the co-polarized scattering coefficients reported in Fig. 13(a), it is inferred that the vegetation biomass is rather low. In this case, depending on the surface roughness, the surface scattering mechanism can be dominant at low incidence angles. If the surface scattering is dominant entirely, it is expected that σ^o_{vv} be larger than σ^o_{hh}. However, this is not observed from the measured data at 30^o. Hence, there is at least a comparable backscattering contribution from the vegetation. Under this condition, a significant contribution to the backscatter at C-band comes from the vegetation.

3. At relatively low biomass, it is found that cross-polarized scattering coefficient is dominated by the direct backscatter from the soybean at both frequency bands. The size of the main stems for one-month-old soybean is small, so the rough surface-stem interaction is not significant. Also at C-band the direct backscatter from the rough surface is weak due to the small rms height and extinction through the vegetation layer. Therefore, the dimension, the number density, and the dielectric constant of the soybean can be estimated by matching the cross-polarized backscatter at C-band. This is done by confining the range of the vegetation dielectric constants to those reported in Fig. 6. The elevation angles of all vegetation particles can be estimated by matching the co-polarized scattering coefficient ratio $\sigma^0_{vv}/\sigma^0_{hh}$ and cross-polarized scattering coefficient. The vegetation parameters as a first iteration is decided by matching the data at C-band. Then, by matching the data at L-band with the same vegetation structure, the parameters of the rough surface is estimated. The simulation is then iterated between L-band and C-band until the simulated and measured data match at both frequency bands.

After matching the backscatter data at both L- and C-band, the final estimated target parameters are shown in Tables 3 and 4. A typical corresponding computer-generated soybean plant is shown in Fig. 9(b). Figures 13(a) and 14(a) show the simulated and measured scattering coefficients versus incidence angle at L- and C-band, respectively. Monte-Carlo simulation are performed at 5 degree increments. Figures 13(b), (c), and (d) show scattering contributions from different mechanisms versus incidence angle at L-band. As predicted, the scattering between stems and rough surface is not significant due to the shorter and slimmer main stems and smaller surface roughness. Figures 13(b), (c), and (d) show scattering contributions from different mechanisms versus incidence angle at C-band. As predicted, the second-order scattering can be neglected.

Finally, Figs. 15 and 16 show the coherence effect of the vegetation structure. The scattering coefficients do not include the contribution from the main stems-rough surface scattering and the direct backscatter from the rough surface. In these figures the coefficients denoted as "coherent" are calculated using (26), while those which are denoted as "incoherent" are calculated using (29). It is shown that for a fully grown soybean, the coherence effect is significant at L-band for co-polarized components, while the effect is not observable at C-band. However, for low biomass condition (AIRSAR data), it is found that the coherent effect is also significant at C-band. This can be explained noting that a fully-grown soybean plant has more complex structure with more particles than a one-month-old plant. Nevertheless, it should be noted that the second-order near-field interaction is significant for POLARSCAT data at C-band, and can be evaluated only when the relative distance and orientation of particles are given. Therefore, to some extent, the coherence effect of structure embedded in this mechanism is also

important at C-band. For the cross-polarized scattering, the coherence effect is less significant in both low and high biomass conditions at both frequencies.

5 Conclusions

In this paper, an electromagnetic scattering model for short branching vegetation is presented. The vegetation particles are modeled as simple geometries such as cylinders and disks for which analytical scattering solutions are available. With the realistic structures which reasonably describe the relative positions of the particles, this model is is constructed so that the coherence effect due to the phase difference between the scattered fields from different particles and the second-order near-field interaction among particles are accounted for. Also the interaction between the main stems and underlying rough surface is incorporated into this model which is shown to be important only at low frequencies (L-band) and for cross-polarized backscattering coefficient.

The model accuracy is verified using polarimetric radar backscatter measurements of a soybean field obtained from truck-mounted scatterometers. Through an extensive ground-truth data collection, target parameters such as the soil and vegetation moisture contents, geometry of the soybean plants, and surface roughness were characterized. Monte-Carlo simulations were carried out simulating the statistical properties of the backscatter at different incidence angles. Good agreement is obtained between the model prediction and measured backscattering coefficients. From a sensitivity analysis, it is found that: (1) the second-order near-field interaction is more significant at C-band than at L-band, (2) the interaction between the main stems and rough surfaces could be significant for cross-polarized scattering at L-band, (3) the double ground-bounce mechanism is generally not important, and (4) high-frequency data (C-band or higher) can be used to probe the vegetation, and low-frequency data (L-band or lower) is needed to probe the soil moisture through vegetation.

The model was also used to estimate the parameters of a soybean field using the AIRSAR data, and reasonable results which agree with the limited ground-truth data was obtained. The coherence effect was also examined using the model simulation.

Acknowledgment: This research was supported by NASA under contract NAGW-4180 and JPL under contract JPL-958749.

References

[1] Ulaby, F.T., K. Sarabandi, K. McDonald, M. Whitt, and M.C. Dobson, "Michigan microwave canopy scattering model," *Int. J. Remote Sensing*, vol. 11, no. 7, pp. 2097-2128, 1990.

[2] Karam, M.A. and A.K. Fung,"Electromagnetic scattering from a layer of finite length, randomly oriented, dielectric circular cylinders over a rough interface with application to vegetation," *Int. J. Remote Sensing*, vol. 9, pp. 1109-1134, 1988.

[3] Lang, R.H. and J.S. Sidhu,"Electromagnetic backscattering from a layer of vegetation: a discrete approach," *IEEE Trans. Geosci. Remote Sensing,* vol. 21, pp. 62-71, 1983.

[4] Zhang G., L. Tsang, and Z. Chen, "Collective scattering effects of trees generated by stochastic Lindenmayer systems," *Microwave and Optical Technology Letters,* vol 11, no. 2, pp. 107-111, Feb. 1995.

[5] Yueh, S.H., J.A. Kong, J.K. Jao, R.T. Shin, and T.L. Toan, "Branching model for vegetation," *IEEE Trans. Geosci. Remote Sensing,* vol. 30, no. 2, pp. 390-402, March 1992.

[6] Lin, Y.C. and K. Sarabandi, "A Monte Carlo Coherent Scattering model for forest canopies using fractal generated trees," to be submitted to *IEEE Trans. Geosci. Remote Sensing.*

[7] Sarabandi, K. and P.F. Polatin, "Electromagnetic scattering from two adjacent objects," *IEEE Trans. Antennas Propagat.*, vol. 42, no. 4, pp. 510-517, 1994.

[8] Tsang L., K. Ding, G. Zhang, C.C. Hsu, and J.A. Kong, "Backscattering enhancement and Clustering effects of randomly distributed dielectric cylinders overlying a dielectric half space based on Monte-Carlo simulations," *IEEE Trans. Antennas Propagat.*, vol. 43, no. 5, pp. 488-499, May 1995.

[9] Raven, P.H., R.F. Evert, and S.E. Eichhorn, *Biology of Plants*, Worth Publishers, INC., New York, NY, 1986.

[10] Chiu, T. and K. Sarabandi, "Electromagnetic scattering interaction between a dielectric cylinder and a slightly rough surface," submitted to *IEEE Trans. Antennas Propagat..*

[11] Ishimaru A. *Wave Propagation and Scattering in Random media,* vol. 2, New York: Academic, 1978.

[12] Schiffer, R. and K.O. Thielheim, "Light Scattering by Dielectric Needles and Disks," *J. Appl. Phys.*, 50(4), April 1979.

[13] Sarabandi, K. and T.B.A. Senior, "Low-frequency Scattering from Cylindrical Structures at Oblique Incidence," *IEEE Trans. Geosci. Remote Sensing*, vol. 28, no. 5, pp. 879-885, 1990.

[14] Tsang, L., J. Kong, and R.T. Shin, *Theory of Microwave Remote Sensing*, John Wiley and Sons, New York, 1985.

[15] Seker S.S. and A. Schneider, "Electromagnetic Scattering from a dielectric cylinder of finite length," *IEEE Trans. Antennas Propagat.*, vol. 36, no. 2, pp. 303-307, Feb. 1988.

[16] Polatin P.F., K. Sarabandi, and F.T. Ulaby, "Monte-Carlo simulation of electromagnetic scattering from a heterogeneous two-component medium," *IEEE Trans. Antennas Propagat.*, vol. 43, no. 10, pp. 1048-1057, Oct. 1995.

[17] Sarabandi K. and T. Chiu, "Electromagnetic scattering from slightly rough surface with inhomogeneous dielectric profiles," *IEEE Trans. Antennas Propagat.*, vol. 45, no. 9, pp. 1419-1430, Sep. 1997.

[18] Ulaby F.T., R.K. More, and A.K. Fung, *Microwave Remote Sensing: Active and Passive*, vol. 2, Artech House, Norwood, MA., 1982.

[19] Chiu T. and K. Sarabandi, "Electromagnetic scattering interaction between a dielectric cylinder and a slightly rough surface," submitted to *IEEE Trans. Antennas Propagat.*.

[20] Stiles J., *A coherent polarimetric microwave scattering models for grassland structures and canopies,* Ph.D. dissertation, the University of Michigan, Ann Arbor, 1996.

[21] Tassoudji M.A., K. Sarabandi, and F.T. Ulaby, "Design consideration and implementation of the LCX polarimetric scatterometer (POLARSCAT)," Rep. 022486-T-2, Radiation Laboratory, The University of Michigan, June 1989.

[22] Brunfeldt D.R., "Theory and design of a field-portable dielectric measurement system," *IEEE Int. Geosci. Remote Sensing Symp. (IGARSS) Digest,* vol. 1, pp. 559-563, 1987.

[23] Hallikainen M.T., F.T. Ulaby, M.C. Dobson, M.A. El-Rayes, and L. Wu, "Microwave dielectric behavior of wet soil - Part I: Empirical models and experimental observations," *IEEE Trans. Geosci. Remote Sensing,* vol. GE-23, pp. 25-34, 1985.

[24] Sarabandi K. and F.T. Ulaby, "Technique for measuring the dielectric constant of thin materials," *IEEE Trans. Instrum. Meas,* vol. 37, no. 4, pp. 631-636, Dec. 1988.

[25] Sarabandi K., "A technique for dielectric measurement of cylindrical objects in a rectangular waveguide," *IEEE Trans. Instrum. Meas,* vol. 43, no. 6, pp. 793-798, Dec. 1994.

[26] Ulaby F.T. and M.A. El-Rayes, "Microwave dielectric spectrum of vegetation, part II: Dual-dispersion model," *IEEE Trans. Geosci. Remote Sensing,* vol. GE-25, pp. 550-557, 1987.

[27] http://www.jpl.nasa.gov/mip/airsar.html

	Aug. 14	Aug. 18
soil (m_v)	0.06	0.17
rms height(s)	$0.0115m$	
correlation length(l)	$0.0879m$	
vegetation (m_g)	0.769	0.767
number density of plant	34 ± 13 plants/m^2	
biomass	1.97 kg/m^2	

Table 1: Measured ground truth for the POLARSCAT data set.

	β_m, β_s (degree)	radius (cm)	length or thickness (cm)
stem	5, 5	0.3 ± 0.09	73.0 ± 3.4
node	5, 5	0.3 ± 0.09	5.4 ± 1.4
branch	45.8, 25.6	0.12 ± 0.031	20.7 ± 6.5
pod	135.5, 30.8	0.35 ± 0.03	3.7 ± 0.48
leaf	45.6, 30.1	$3.8 \pm 0.07(0.576)$	0.022 ± 0.002

Table 2: Measured vegetation parameters of soybeans for the POLARSCAT data set.

soil (m_v)	0.05
rms height(s)	0.0038 m
correlation length(l)	0.038 m
number density of plant	19 plants/m^2
biomass	0.22 kg/m^2

Table 3: Estimated ground truth for the AIRSAR data set.

	β_m, β_s (degree)	radius (cm)	length or thickness (cm)
stem	7.5, 5	0.18 ± 0.05	30.2 ± 3.4
node	7.5, 5	0.18 ± 0.05	5.0 ± 1.0
branch	60.8, 25.6	0.12 ± 0.031	14.7 ± 4.5
leaf	47.0, 30.0	$3.7 \pm 0.08(0.6)$	0.02 ± 0.001

Table 4: Estimated vegetation parameters of soybeans for the AIRSAR data set.

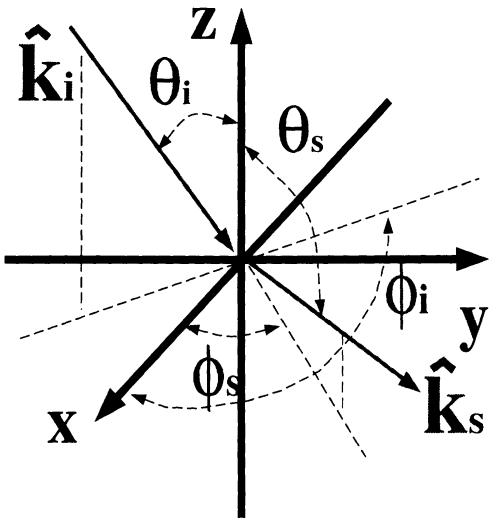

Figure 1: Definition of the incident and scattering angles.

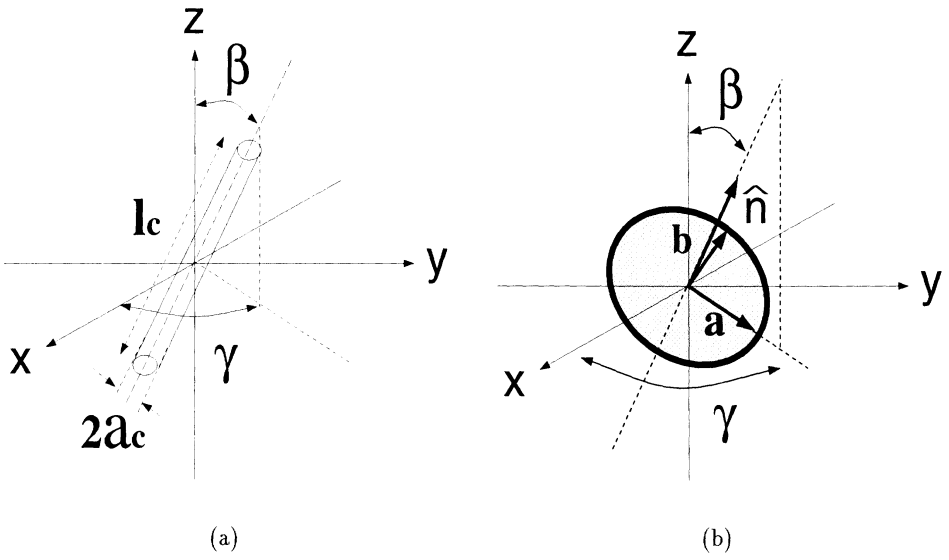

(a) (b)

Figure 2: Denotation of the dimensional and orientational parameters for (a) a cylinder and (b) a disk.

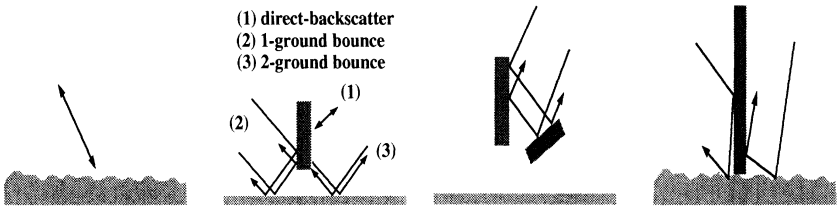

(a) (b) (c) (d)

Figure 3: Scattering mechanisms. (a) direct backscatter from rough surface, (b) direct backscatter from vegetation, single ground-bounce, and double ground-bounce, (c) second-order near-field interaction, and (d) incoherent main stem-rough surface interaction.

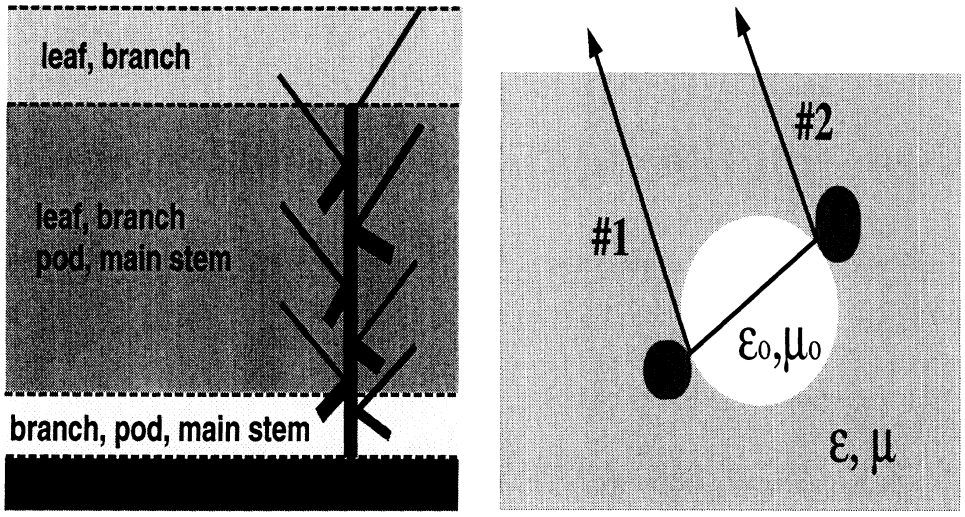

(a) (b)

Figure 4: Vegetation particles embedded in the lossy medium. (a) Stratified structure for the calculation of the equivalent propagation constant. (b) Free space is assumed in the calculation of the second-order near-field interaction.

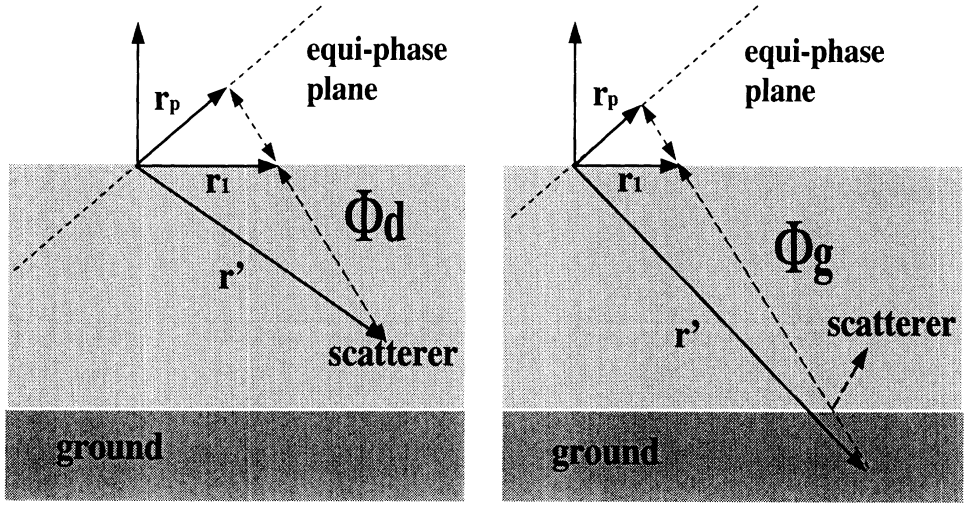

(a) (b)

Figure 5: Propagation paths in the vegetation layer. (a) direct and (b) ground bounce.

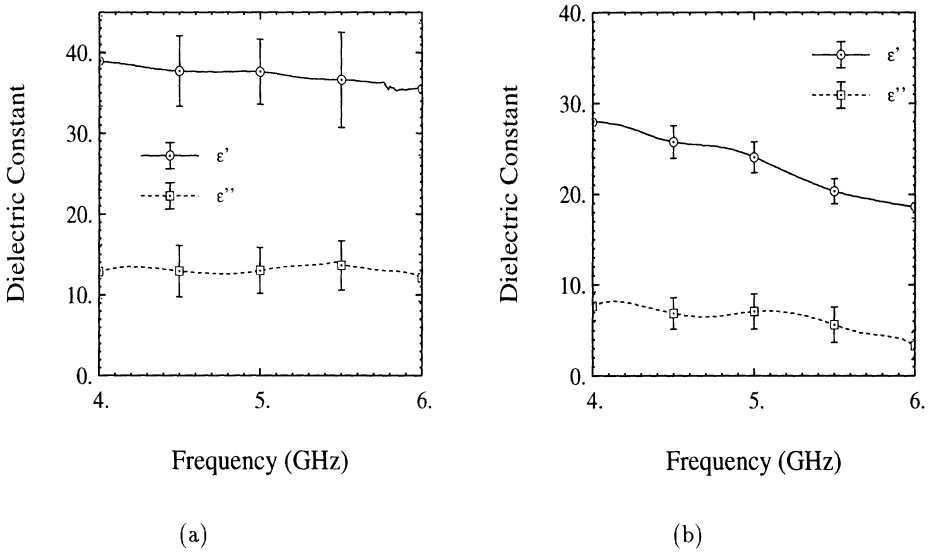

Figure 6: Measured dielectric constants for (a) branches and main stems, and (b) leaves at C-band using the procedure outlined in [24, 25].

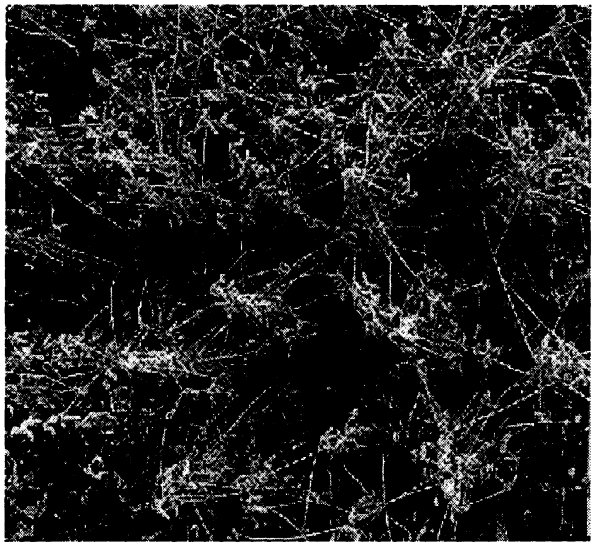

Figure 7: Picture of the soybean plant distribution for POLARSCAT data set. It was taken from the top of the field when plants were dry. Unlike the row structure which is often seen in many cultivated field, the distribution pattern is rather random.

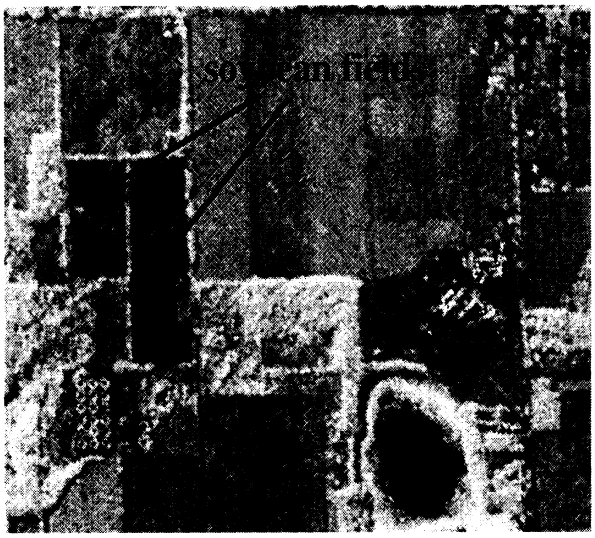

Figure 8: AIRSAR image of the Kellogg Biological Station in July of 1995. This image combined the L-band and C-band backscatter data at 45 degree of incidence angle. Two soybean field is on the left side of the image with dark color.

(a) (b)

Figure 9: Computer-generated soybean plants for (a) POLARSCAT data set and (b) AIRSAR data set.

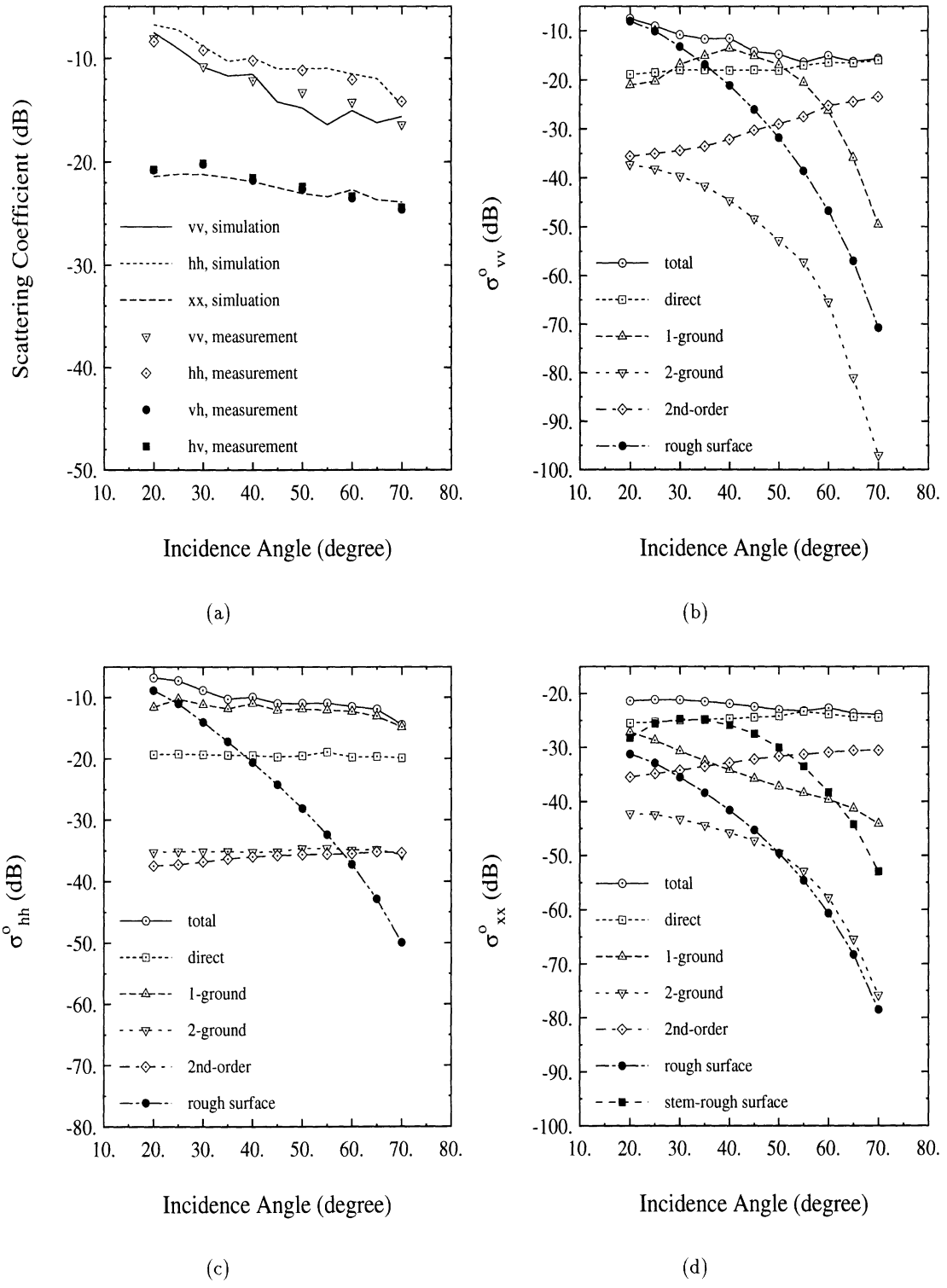

Figure 10: Scattering coefficients versus incidence angle at L-band for August 14 POLARSCAT data set: (a) model validation, and (b)(c)(d) scattering mechanism analysis for vv-, hh-, and cross-polarizations, respectively.

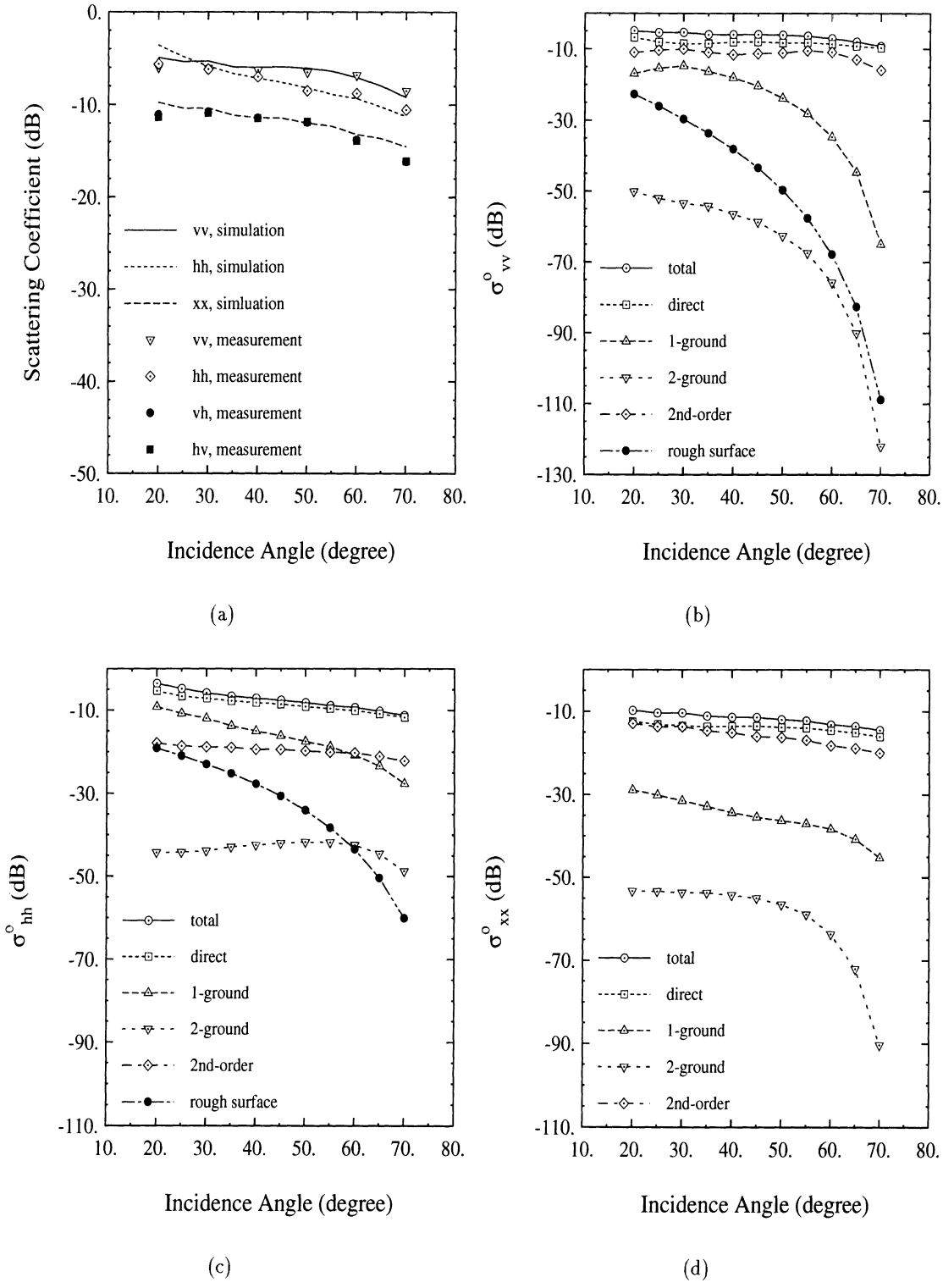

Figure 11: Scattering coefficients versus incidence angle at C-band for August 14 POLARSCAT data set: (a) model validation, and (b)(c)(d) scattering mechanism analysis for vv-, hh-, and cross-polarizations, respectively.

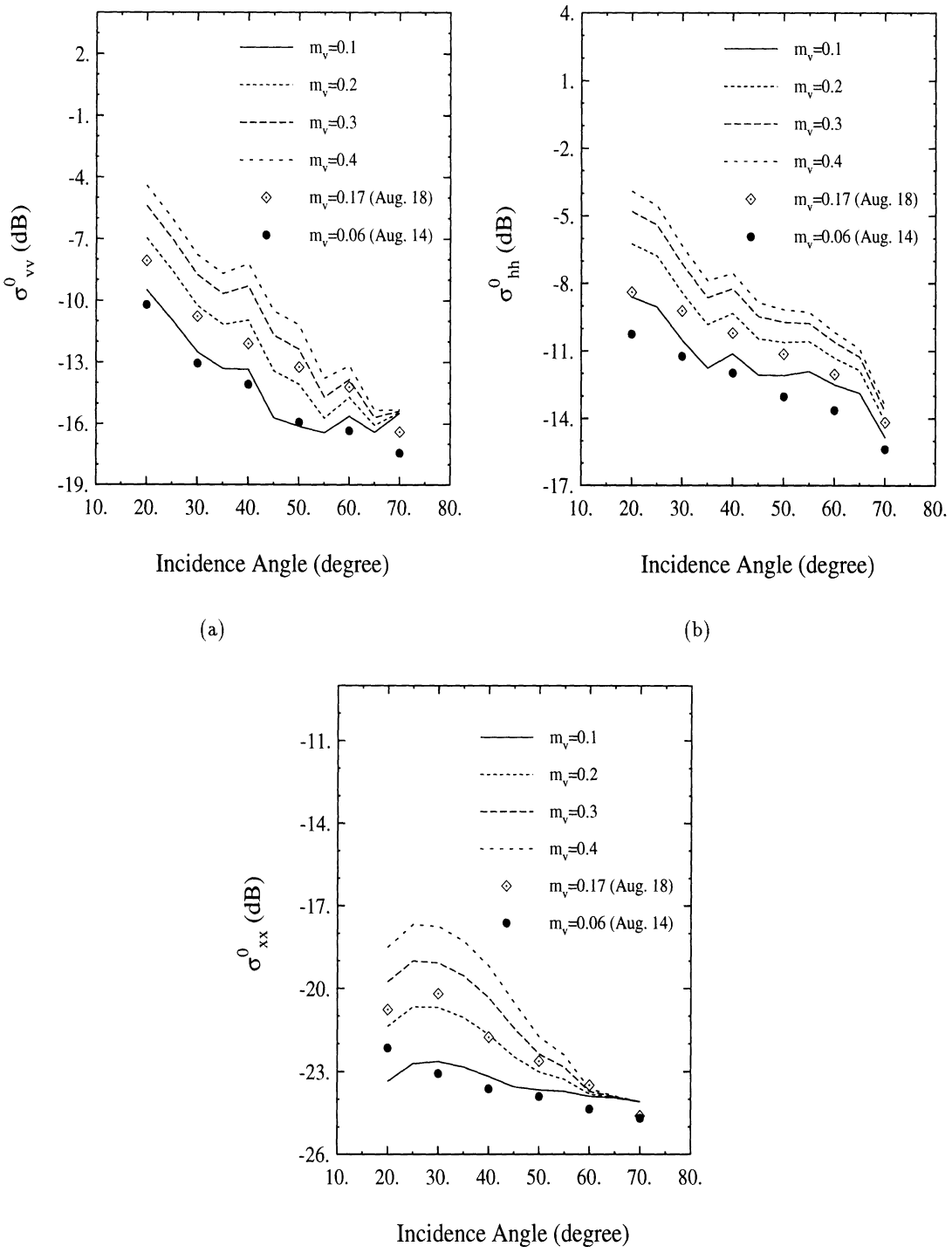

Figure 12: Analysis of sensitivity to the variation of the soil moisture for the POLARSCAT data set at L-band.(a) vv-polarization, (b) hh-polarization, and (c) cross-polarization.

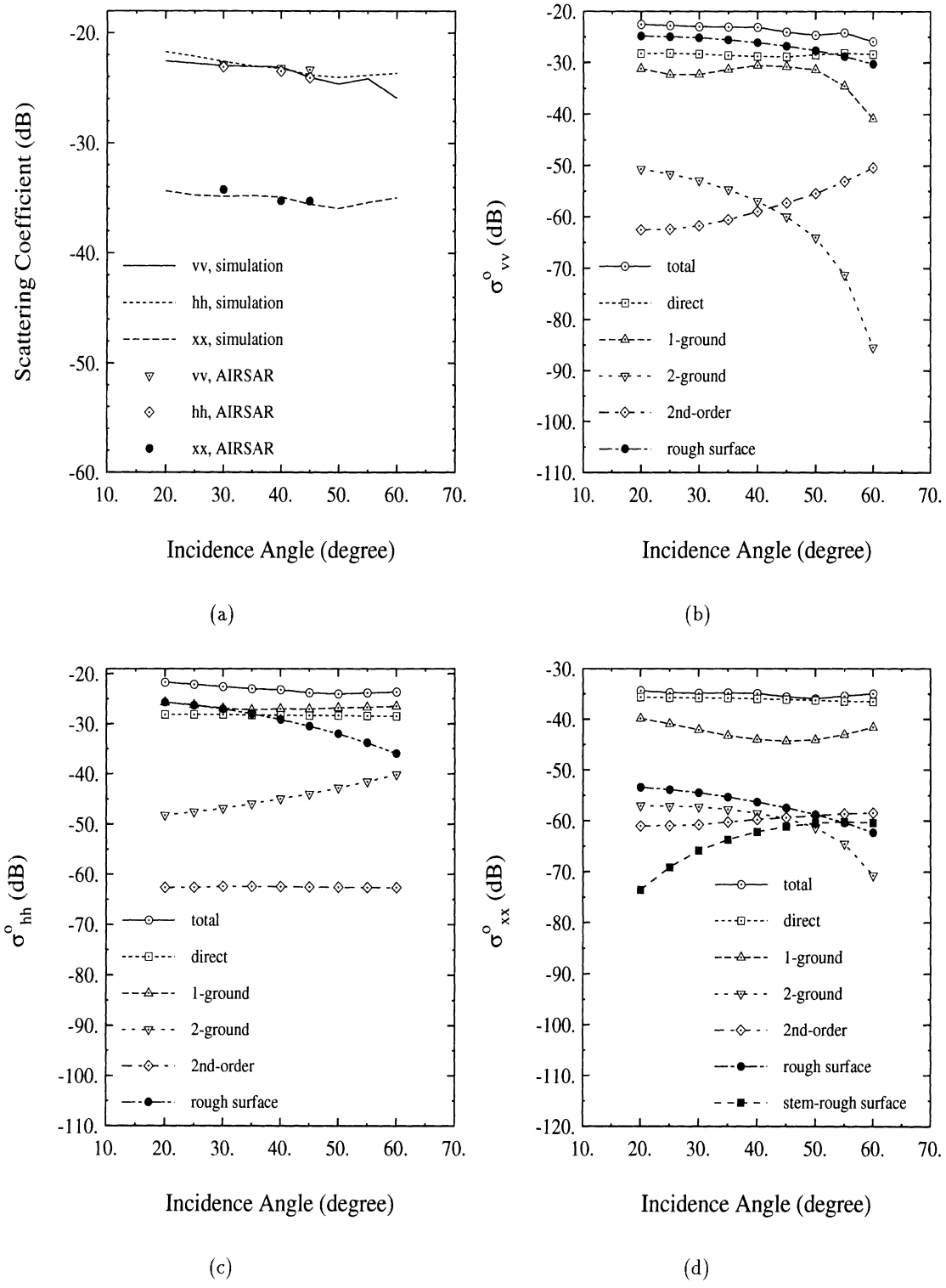

Figure 13: Scattering coefficients versus incidence angle at L-band for AIRSAR data set: (a) model validation, and (b)(c)(d) scattering mechanism analysis for vv-, hh-, and cross-polarizations, respectively.

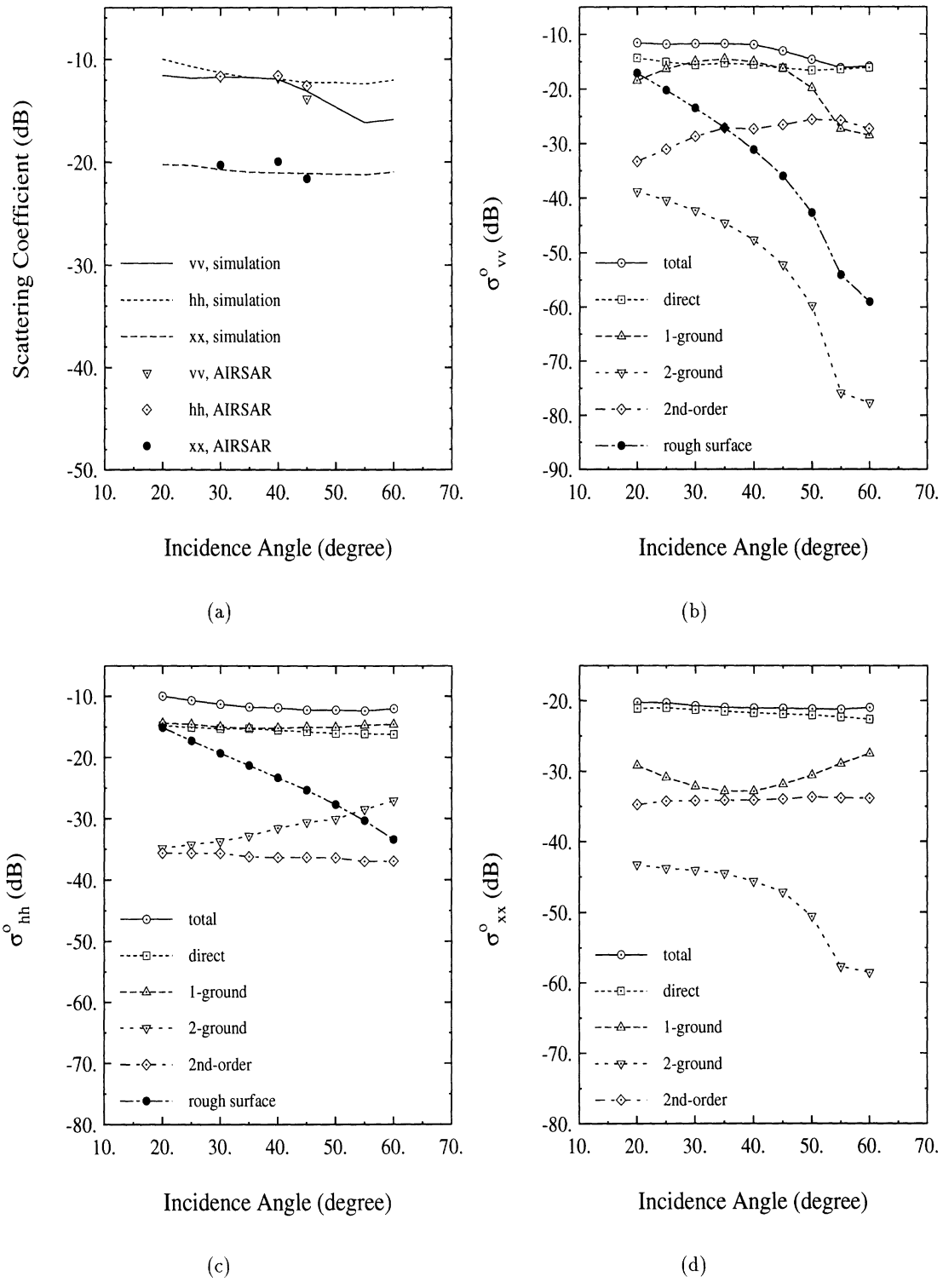

Figure 14: Scattering coefficients versus incidence angle at C-band for AIRSAR data set: (a) model validation, and (b)(c)(d) scattering mechanism analysis for vv-, hh-, and cross-polarizations, respectively.

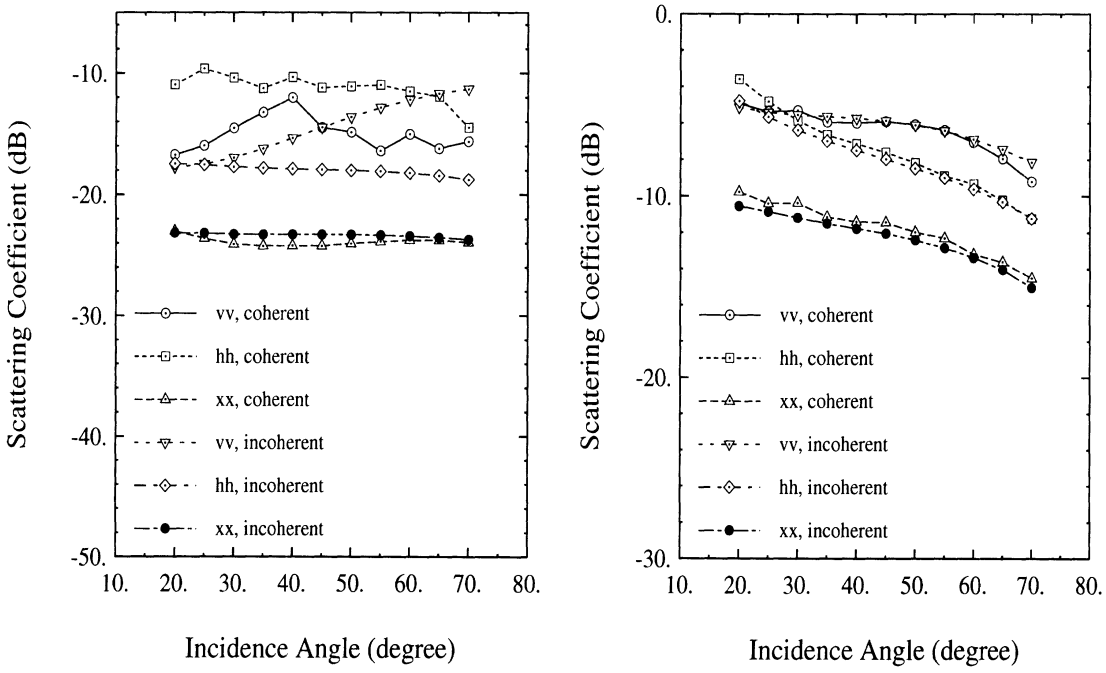

Figure 15: Demonstration of the coherence effect caused by the soybean plant structure for a fully grown soybean field at (a) L-band and (b) C-band.

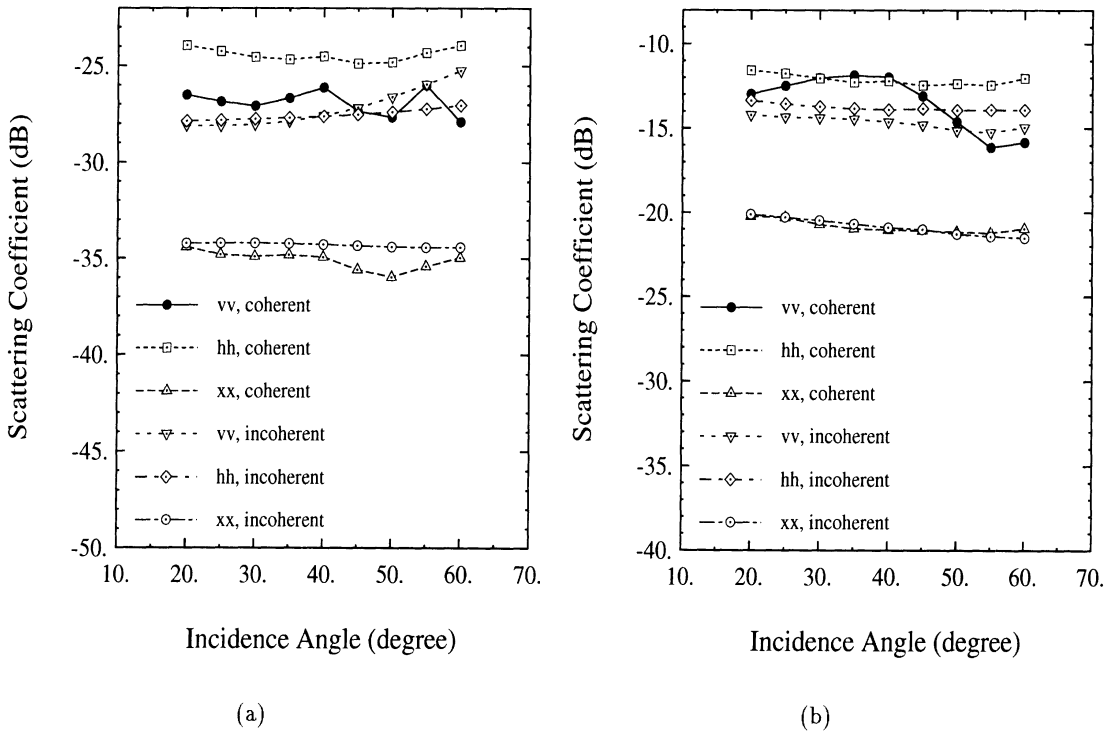

Figure 16: Demonstration of the coherence effect caused by the soybean plant structure for a young soybean field at (a) L-band and (b) C-band.

Appendix VI

Retrieval of Forest Parameters Using a Fractal-Based Coherent Scattering Model and a Genetic Algorithm

Submitted to *IEEE Trans. Geosci. Remote Sensing* (October 7, 1997)

Retrieval Of Forest Parameters Using A Fractal-Based Coherent Scattering Model And A Genetic Algorithm

Yi-Cheng Lin and Kamal Sarabandi

Radiation Laboratory
Department of Electrical Engineering and Computer Science
The University of Michigan
Ann Arbor, MI 48109-2122

ABSTRACT

In this paper a procedure for retrieval of forest parameters is developed using the recently developed fractal-based coherent scattering model (FCSM) and a stochastic optimization algorithm. Since the fractal scattering model is computationally extensive, first a simplified empirical model with high fidelity for a desired forest stand is constructed using FCSM. Inputs to the empirical model are the influential structural and electrical parameters of the forest stand such as the tree density, tree height, trunk diameter, branching angle, wood moisture, and soil moisture. Other finer structural features are embedded in the fractal model. The model outputs are the polarimetric and interferometric response of the forest as a function of the incidence angle. In this study a genetic algorithm is employed as a global search routine to characterize the input parameters of a forest stand from a set of measured polarimetric/interferometric backscatter responses of the stand. The success of the inversion algorithm is demonstrated using a set of measured single-polarized interferometric SAR data and several FCSM simulation results.

1 Introduction

Retrieval of gross biophysical parameters of forest stands, such as basal area, tree height, and leaf area index (LAI), is of great importance in many environmental research programs. Radar remote sensing at lower microwave frequencies has been proposed as a sensitive instrument for such applications [1,2]. In support of programs pertaining to radar remote sensing of vegetation, many advanced polarimetric (SIR-C, AIRSAR) [3] and interferometric (TOPSAR) [4] radar instruments have been developed.

The study of the inversion problems in geophysical science and engineering has been of great importance from the onset of the remote sensing science [5, 6]. For example, in microwave remote sensing of vegetation the inverse problem is defined as the application of the measured quantities such as the polarimetric backscattering coefficients (from a SAR) [7] and/or the scattering phase center heights (from an interferometric SAR) [8,9] in an algorithm in order to retrieve forest parameters such as tree type, tree density and height, and moisture content of vegetation and soil.

Over the past two decades significant effort has been devoted towards the development of scattering models for vegetation canopies [10–15] as well as inversion models to retrieve forest parameters from the measured data [16–18]. So far the emphasis of the scattering model development has been on the construction of simplified models with as few input parameters as possible so that the inversion problem becomes tractable. In this process the importance of structural features of the canopy (particle arrangement), coherence effects, and multiple scattering were ignored. Even with these simplifications, the inversion process is rather complex. In [16, 18] neural network approaches are suggested for the inversion process where extensive computer simulations or experimental results are used to train a neural network in a reverse order (the model outputs are fed as the input to the program). This method is computationally extensive and its success depends on the fidelity and the extent of the training data. In [17] a gradient-based search routine is applied to a nested linearized model. This model is computationally efficient; however, its applicability is limited to models with small dimensionality and its success depends on the fidelity of the forward model.

This paper describes the application of a high fidelity scattering model in an inversion process based on a stochastic global search method. Basically, a recently-developed coherent scattering model that preserves the structural features of tree canopies using fractal models is employed to generate simplified empirical models (for different tree species) that can predict the polarimetric and interferometric radar response of a forest stand efficiently and accurately. The premise for the successful

development of such empirical models stems from the fact that the model outputs are averaged quantities, such as backscattering coefficients or the mean height of the scattering phase center, and therefore are very gentle functions of model inputs.

As demonstrated in [15], the fractal-based coherent scattering model (FCSM) offers two advantages over the traditional scattering models, namely, FCSM is more versatile and accurate. Basically, FCSM is a first-order scattering model and is capable of simulating the fully polarimetric (including the phase statistics) and polarimetric-interferometric (scattering phase centers and correlation coefficients for any polarization configuration [19]) radar responses of coniferous and deciduous forest stands. High accuracy is achieved by FCSM through incorporating the coherent effects among the individual scatterers and scattering components and by accounting for the accurate position of scatterers which is manifested in inhomogeneous scattering and extinction profiles. However, this versatility and accuracy has been achieved at the expense of the model complexity which demands extensive computational power. For example, the number of input parameters needed to accurately characterize the tree structures and the environment may easily exceed 30 (it should be noted that once a tree type is chosen much fewer free parameters are needed to model the natural variabilities). On the other hand, to obtain a solution with a reasonable accuracy in the Monte Carlo simulation, a sufficiently large number ($\geq$ 100) of realizations are required. The required computational time for each simulation limits the model's utility in inverse processes which may demand the calculation of the forward problem many times.

To circumvent the aforementioned problem, development of empirical models based on FCSM is proposed. Construction of an empirical model can be achieved using a standard procedure such as curve-fitting and regression method. Unlike physical models, empirical models are simple mathematical expressions formed from a set of data acquired from measurements or a physical model prediction. Once empirical formulae are obtained, they are easy to use and require minimal computation time. However, it should be noted that an empirical model is usually valid only for a specific case within a certain range of the parameter space over which the model is constructed.

For the development of the empirical model used in this study, first a sensitivity analysis is conducted in order to determine the significant parameters, the number of which determines the dimensionality of the input vector space. A red pine stand is chosen in this paper and six parameters are selected as the input parameters. Each selected parameter is allowed to have about 30% variation with respect to a centroid. Using the Monte Carlo simulation results obtained from FCSM a database is constructed by varying the individual parameters over a prescribed range of the

input vector space around the centroid. The parameters at the centroid are obtained from the ground truth data of a red pine test stand (Stand 22) in Raco, Michigan.

For the inversion process, first a least-square estimator is used and is shown to work properly when the number of measured channels is equal to or larger than the dimension of the input vector space. But since this may not be the case in general situations, a genetic algorithm (GA) [20] is developed and employed as a search routine for the nonlinear optimization problem. GAs are known to be very successful when the dimension of the input vector space is large and/or when the objective function is nonlinear.

2 Empirical Model Development

In general, the output of the Monte Carlo coherent scattering model can be expressed as

$$\mathbf{M} = \mathcal{L}(f, p, \theta; d_a, H_t, D_t, \theta_b, m_s, m_w), \tag{1}$$

where $\mathcal{L}$ is a complex operator relating the input and output of the model and the output $\mathbf{M}$ is a vector which may contain the backscattering coefficient $(\sigma^0_{vv}, \sigma^0_{vh}, \sigma^0_{hh})$, scattering matrix phase difference statistics, the scattering phase center height Z_e, or the interferogram correlation coefficient. The input parameters are divided into two categories: 1) radar system parameters, and 2) target parameters. Radar parameters include the radar frequency f, the polarization configuration p, and the incidence angle θ. The number of target parameters can be very large, consisting of the tree structural parameters and the dielectric properties of the constituent components. However, the number of these parameters is reduced drastically once a tree type is chosen. In this case only a few structural parameters are sufficient to allow for natural variabilities observed for that type of tree. The rest of the structural parameters are embedded in the fractal code of the tree. In this paper we demonstrate development of an empirical model for a red pine tree where only six free parameters are sufficient to describe the stand. These include the trunk diameter d_a, tree height H_t, tree density D_t, branching angle θ_b, soil moisture m_s and wood moisture m_w. It should be noted that these parameters themselves are statistical in the coherent model with prescribed distribution functions and here we are referring to their mean value.

Multi-frequency polarimetric SAR systems operate at discrete frequencies, usually at P-, L-, C-, and X-band, and the polarization configuration p are vv, vh, and hh. In this study, we demonstrate a model with three fundamental backscattering coefficients and the associated mean scattering phase center height as the model output and fix the frequency at C-band (5.3 GHz). The empirical model is developed to

operate over the angular range 25°– 70°. Therefore the output and input vectors $\mathbf{M}$ and $\mathbf{x}$ are defined as:

$$\mathcal{L} = \begin{bmatrix} Z_e^{vv} \\ Z_e^{vh} \\ Z_e^{hh} \\ \sigma_{vv}^0 \\ \sigma_{vh}^0 \\ \sigma_{hh}^0 \end{bmatrix}, \quad \text{and } \mathbf{x} = \begin{bmatrix} d_a \\ H_t \\ D_t \\ \theta_b \\ m_s \\ m_w \end{bmatrix}.$$

As mentioned earlier since no resonance behavior is expected, the output vector $\mathbf{M}$ is a gentle function of the input vector $\mathbf{x}$ and the incidence angle θ which may be related to each other via a simple empirical relationship

$$\widetilde{\mathbf{M}} = \tilde{\mathcal{L}}(\theta; \mathbf{x}), \tag{2}$$

where $\tilde{\mathcal{L}}$ is the simple empirical operator and $\widetilde{\mathbf{M}}$ is the output of the empirical model. It is expected that $\widetilde{\mathbf{M}}$ be as close to $\mathbf{M}$ as possible.

In general, the output parameters are non-linear functions of the incidence angle and other input parameters. In order to establish these relationships the coherent model must be run by varying the incidence angles and other input parameters. Through an extensive sensitivity study it was found that over a finite domain of the input vector space a logarithmic relationship between the backscattering coefficient (linear in dB scale) and a linear relation between the scattering phase center height and the input parameters exist. The dependence on the incidence angle was found to be nonlinear.

The first step in the construction of the empirical model is to choose the domain of the input vector space. In this investigation we chose the structural parameters of a young red pine stand, a test forest stand in Raco Michigan (Stand 22), and the seasonal average of soil and vegetation moisture as the centroid of the input domain. These parameters and their range of variation used in the model development are shown in Table 1. The range of parameter space is chosen so that the measured parameters of a red pine test stand (see Table 2) is at the centroid of the parameter space. The Monte Carlo simulation was then carried out for specific incidence angles by varying the six free parameters within the prescribed ranges. The average scattering phase center heights (Z_e) for each polarization configuration and backscattering coefficients (σ^0 in dB) are shown in Figures 1 and 2 as a function of each parameter respectively. These figures clearly demonstrate the linear relationship previously described. Hence the output vector can be readily approximated by the Taylor series expansion of the exact model to the first order, and is given by

$$\tilde{\mathcal{L}}(\mathbf{x}) = \mathcal{L}(\mathbf{x}_0) + \mathbf{A} \cdot (\mathbf{x} - \mathbf{x}_0) \tag{3}$$

where $\mathbf{x_0}$ denotes the input vector at the centroid and $\mathbf{A}$ is the matrix of partial derivatives whose ij-th element is given by

$$a_{ij} = \frac{\partial \mathcal{L}_i}{\partial x_j}|_{\mathbf{x}=\mathbf{x_0}}. \tag{4}$$

a_{ij} simply represents the derivative of the i-th output channel $\mathcal{L}_i$ with respect to the j-th input parameter x_j, evaluated at the centroid $\mathbf{x_0}$.

In this matrix, each element was evaluated by calculating the slope of a fitting line over 5 sample points based on a least square method. In Figures 1 and 2 the symbols $(*)$ are the simulation results and the lines are the best linear estimation. It should be pointed out that each point in each figure represents an ensemble average of 200 realizations of the Monte Carlo simulation. This indicates that the initial task of generating a matrix of coefficients is very tedious and time-consuming. However, once the empirical model is obtained, it can provide a highly accurate solution to an arbitrary input in almost real-time. This property of the empirical model is especially important in the inversion processes.

Results in Figures 1 and 2 are for a fixed incidence angle $\theta = 25°$. However, the simulations at other incidence angles show that the general form of (3) is valid for all incidence angles with the exception that $\tilde{\mathcal{L}}(\mathbf{x_0})$ and $\mathbf{A}$ are functions of the incidence angle, i.e.,

$$\tilde{\mathcal{L}}(\theta; \mathbf{x}) = \mathcal{L}^0(\theta) + \mathbf{A}(\theta) \cdot (\mathbf{x} - \mathbf{x_0}). \tag{5}$$

It is found that $\mathcal{L}^0(\theta)$ and $\mathbf{A}(\theta)$ are non-linear, but gentle, functions of the incidence angle θ over the range of interest (25° to 70°). In order to obtain the functional form of $\mathcal{L}^0$ and $\mathbf{A}$ on θ, the aforementioned Monte Carlo simulation was repeated at several different incidence angles, and the corresponding values $\mathcal{L}^0$ and $\mathbf{A}$ were evaluated. Polynomial functions are used to capture the angular variations of $\mathcal{L}^0$ and $\mathbf{A}$. It was found that $\mathcal{L}^0$ and $\mathbf{A}$ can be accurately expressed by

$$\mathcal{L}^0(\theta) = \mathcal{L}_0 + \mathcal{L}_1\theta + \mathcal{L}_2\theta^2 + \mathcal{L}_3\theta^3, \tag{6}$$

and

$$\mathbf{A}(\theta) = \mathbf{A}_0 + \mathbf{A}_1\theta + \mathbf{A}_2\theta^2 + \mathbf{A}_3\theta^3 + \mathbf{A}_4\theta^4, \tag{7}$$

where $\mathcal{L}_i$ and $\mathbf{A_i}$ are 6×1 and 6×6 matrices whose values are reported in the Appendix. Figure 3 compares the results of the empirical model given by (5) with those of the Monte Carlo simulation at the centroid $(\mathbf{x} = \mathbf{x_0})$. It should be noted that the choice of the output parameters are arbitrary and depends on the available set of input data. For example, an empirical model for a two-frequency system with three backscattering coefficients could be developed using the same procedure.

Equation (5) represents the overall empirical model whose accuracy can be evaluated through a comparison with the Monte Carlo simulations. For this comparison a large number Monte Carlo simulations with independent input vectors were carried out. Figures 4, 5, and 6 show the comparison between the results of the empirical model and those of the Monte Carlo coherent model using 200 independent input data sets randomly selected within the aforementioned domain of the empirical model. The figures show excellent agreement between the empirical model and the Monte Carlo coherent model, noting that the convergence criteria for the Monte Carlo model is ± 0.5 dB. Having confidence on a fast and accurate empirical model, the inversion processes can be attempted which is the subject of the next section.

3 Inversion Algorithms

Consider a physical system whose input-output relation is expressed by $\mathbf{M} = \tilde{\mathcal{L}}(\mathbf{x})$ where in general $\mathbf{M}$ and $\mathbf{x}$ are multi-dimensional vectors of arbitrary length. The inverse problem is mathematically defined as $\mathbf{x} = \tilde{\mathcal{L}}^{-1}(\mathbf{M})$ subject to certain physical constraints. Although the inverse problem may be well-defined mathematically, in practice the inverse solution may not exist for two reasons: 1) mathematical construction of the model may not be exact, and 2) the measured vector $\mathbf{M}$ may not be exact because of measurement errors. Hence, instead of casting the problem in terms of an inverse problem, the problem of finding $\mathbf{x}$ is usually cast in terms of a constraint minimization problem.

Suppose there exists a set of measurements $\widetilde{\mathbf{M}}$, the problem is defined as characterization of $\mathbf{x}$ so that the objective function (or error function), defined by

$$\mathcal{E}(\mathbf{x}) = \|\mathcal{L}(\mathbf{x}) - \widetilde{\mathbf{M}}\|^2. \tag{8}$$

is minimized over a pre-defined domain for $\mathbf{x}$. Here, $\|\cdot\|$ denotes the norm of the argument. As mentioned earlier there are a number of inversion processes available in the literature; however, in this paper by constructing a simple empirical model a traditional least-square minimization approach and a stochastic global minimization method are examined.

3.1 Least-Square Approach

As it was shown in Section 2, the scattering problem can be cast in terms of a linear system of equations of the form $\tilde{\mathcal{L}}(\mathbf{u}) = \mathbf{A}\mathbf{u}$ where $\mathbf{A}$ is an $m \times n$ matrix and $\mathbf{u}$ is an n-dimensional vector in D, $D \subset R^n$. For a given m-dimensional vector $\widetilde{\mathbf{G}}$, (8) can be

expanded as

$$\mathcal{E} = \sum_{i=1}^{m}(\sum_{j=1}^{n} a_{ij}u_j - \tilde{g}_i)^2. \tag{9}$$

A solution that minimizes $\mathcal{E}$ must satisfy

$$\frac{\partial \mathcal{E}}{\partial u_j} = 0, \qquad j = 1, 2, ..., n \tag{10}$$

and is referred to as the least-square solution. It is shown that the solution of (10) ($\mathbf{u_m}$) can be obtained from the solution of the following matrix equation [21]:

$$(\mathbf{A^*A}) \cdot \mathbf{u_m} = \mathbf{A^*} \cdot \widetilde{\mathbf{G}}. \tag{11}$$

Here, A^* is the transpose of A. It is also demonstrated that the solution $\mathbf{u_m} = (\mathbf{A^*A})^{-1}\mathbf{A^*}\widetilde{\mathbf{G}}$ exists if $rank(\mathbf{A}) = n$. This requirement states that the number of independent equations should exceed the number of unknowns.

To apply (11) to our empirical model using (3), it is noted that

$$\tilde{\mathcal{L}}(\mathbf{x}) - \mathcal{L}^0 = \mathbf{A} \cdot (\mathbf{x} - \mathbf{x_0}), \tag{12}$$

thus we use the substitution $\mathbf{u} = \mathbf{x} - \mathbf{x_0}$ and $\widetilde{\mathbf{G}} = \widetilde{\mathbf{M}} - \mathcal{L}^0$. Here $\mathcal{L}^0$ and $\mathbf{A}$ are evaluated from (6) and the solution is given by

$$\mathbf{x_m} = \mathbf{x_0} + (\mathbf{A^*A})^{-1}\mathbf{A^*}(\widetilde{\mathbf{M}} - \mathcal{L}^0). \tag{13}$$

The least-square solution may not be suitable for the inverse problem at hand for two reasons. First, the number of output channels m is usually less than that of unknown parameters n. In this case, $rank(A) < n$, and A^*A is not invertible. Even when the number of channels is larger than the unknowns, the solution provided by (13) may not be accurate. This happens when $\mathbf{A^*A}$ is ill-conditioned. Basically, some elements of $(A^*A)^{-1}$ become very large which amplify the errors in $\widetilde{\mathbf{M}}$ [22].

3.2 Genetic Algorithms

In recent years, applications of genetic algorithms to a variety of optimization problems in electromagnetics have been successfully demonstrated [24, 25]. The fundamental concept of genetic algorithms (GAs) is based on the concept of natural selection in the evolutionary process which is accomplished by genetic recombination and mutation. The algorithms are based on a number of ad hoc steps including: 1) discretization of the parameter space, 2) development of an arbitrary encoding algorithm to establish a one-to-one relationship between each code and the discrete

points of the parameter space, 3) random generation of a trial set known as the initial population, 4) selection of high performance parameters according to the objective function known as natural selection, 5) mating and mutation, 6) recursion of steps 4 and 5 until a convergence is reached. Figure 7 shows the flow chart of GAs. Note that the population size is provided by the user and an initial population of the given size is generated randomly.

In this study, since we have as many as six input ground truth parameters and six output channels, it is expected that the objective function is complex and highly non-linear containing many local minima. In this case, the traditional gradient-based optimization methods usually converge to a local minimum and fail to locate the inverted data. One interesting feature of GAs is that the method would provide a list of optimal solutions instead of a solution. This is important in a sense that a solution that best meets the physical constraints (not included in the objective function) may be selected from the list of optimal solutions.

For this problem, each of the input parameters was discretized and encoded into a 4-bit binary code, creating a discrete input vector space with 2^{24} members. A population of 240 members was used for each generation and the objective function was defined by

$$\mathcal{E}(\mathbf{x}) = \|\mathbf{w} \cdot \left[\widetilde{\mathbf{M}} - \mathcal{L}^{\mathbf{0}} - \mathbf{A} \cdot (\mathbf{x} - \mathbf{x}_0)\right] \|^2, \tag{14}$$

where $\mathbf{w}$ is a user-defined weighting function assigned to individual output channels. To examine the performance of this GA-based inversion algorithm, many arbitrary points within the domain of the input vector space were selected and then the Monte Carlo simulation was used to evaluate the polarimetric backscattering coefficients and the scattering phase center heights at 5.3 GHz. The output of FCSM for these simulations were used as a synthetic measured data set $\widetilde{\mathbf{M}}$ for the inversion algorithm. Figures 8(a)–8(f) show the performance of the inversion algorithm through comparisons of the input parameters $\mathbf{x}$ and the inverted parameters $\mathbf{x}'$. Also shown in each of the figures is the calculated average error η, defined by

$$\eta = \frac{\sum_{j=1}^{N} |x_j - x'_j|}{N\Delta x}, \tag{15}$$

where N is the number of points (N=10 in this case), and Δx is the range of validity of the parameter according to the empirical model. It should be noted here that the quantization error for 4-bit quantization ($\pm 3\%$) is also included in the results. To examine the importance of the quantization error and the stochastic nature of the solution in the inversion process, the inversion process was applied to another set of synthetic measurement data generated by the empirical model. Figures 9(a)–9(f) show the comparison between the actual input $\mathbf{x}$ and the inverted solution $\mathbf{x}'$. It is

noticed that the error in Figures 9(a)–9(f) are slightly smaller than those obtained from Figures 8(a)–8(f). This indicates that the quantization error and the stochastic nature of the solution are considerable factors on the overall error. Increasing the quantization level to 5 bits increases the members of the input vector space by factor of 2^6. This slows down the inversion process since the population in each generation must also be increased. However, this does not improve the overall accuracy drastically as the errors inherent in the empirical model and those caused by the stochastic nature of the GA solution are independent of quantization error.

At last, the developed inversion algorithm is tested using the real measured data acquired by the JPL TOPSAR over a test stand of red pine forest in Raco, Michigan. Although only four data points (C-band vv-polarized backscattering coefficients and scattering phase center heights at incidence angles $\theta = 39°$ and $53°$) are available, the inversion algorithm can be easily modified via the objective function of the GA. In this case, the objective function is given by

$$\mathcal{E}(\mathbf{x}) = \mathcal{E}_1(\mathbf{x}) + \mathcal{E}_2(\mathbf{x}), \tag{16}$$

where

$$\mathcal{E}_1(\mathbf{x}) = \|\mathbf{w} \cdot \left[\widetilde{\mathbf{M}}_1 - \mathcal{L}_1^0 - \mathbf{A}_1 \cdot (\mathbf{x} - \mathbf{x}_0)\right]\|^2, \tag{17}$$

$$\mathcal{E}_2(\mathbf{x}) = \|\mathbf{w} \cdot \left[\widetilde{\mathbf{M}}_2 - \mathcal{L}_2^0 - \mathbf{A}_1 \cdot (\mathbf{x} - \mathbf{x}_0)\right]\|^2. \tag{18}$$

Here the subscript 1 and 2 denotes, respectively, the case for the incidence angle $\theta = 39°$ and $53°$. Note that the weighting function and the measured vectors in this case are written as

$$\mathbf{w} = \left[\begin{array}{cccccc} 1 & 0 & 0 & 1 & 0 & 0 \end{array}\right], \tag{19}$$

$$\widetilde{\mathbf{M}}_1 = \left[\begin{array}{cccccc} Z_e^{vv}(\theta = 39°) & 0 & 0 & \sigma_{vv}^0(\theta = 39°) & 0 & 0 \end{array}\right]^t, \tag{20}$$

$$\widetilde{\mathbf{M}}_2 = \left[\begin{array}{cccccc} Z_e^{vv}(\theta = 53°) & 0 & 0 & \sigma_{vv}^0(\theta = 53°) & 0 & 0 \end{array}\right]^t. \tag{21}$$

The simulation results are compared with ground truth data [2] in Table 2 where a very good agreement is shown.

4 Conclusions

In this paper, a simplified empirical model was developed using a high fidelity Monte Carlo coherent scattering model to be incorporated in an efficient inversion algorithm. The empirical model was specifically developed for a red pine forest stand which provides simple expressions for the polarimetric backscattering coefficients and scattering

phase center heights at C-band as a function of the incidence angle. The accuracy of the empirical model was examined by comparing its output with that of the Monte Carlo fractal-based coherent scattering model. The empirical model in conjunction with a stochastic search algorithm (genetic algorithm) were used to construct an inversion algorithm. The accuracy of the inversion algorithm was demonstrated by first using synthetic measured data generated from the empirical model and the Monte Carlo FCSM. It was shown that the inversion algorithm can accurately estimate the input parameters where synthetic data were used. Next we applied the inversion algorithm to an actual data set, obtained from TOPSAR, composed of vv-polarized backscattering coefficient and scattering phase center height at C-band and at two incidence angles. Excellent agreement was obtained between the ground truth data and the output of the inversion algorithm.

5 Acknowledgment

This investigation was supported by NASA Office of Earth Science Enterprise under contract NAG5 4939. and the Jet Propulsion Laboratory under contract JPL 958749.

Appendix

In this appendix, the values of coefficient matrices $\mathcal{L}_i$ and $\mathbf{A_i}$ used in (6) and (7) are reported for the red pine stand investigated in this study.

$$\begin{bmatrix} \mathcal{L}_0 & \mathcal{L}_1 & \mathcal{L}_2 & \mathcal{L}_3 \end{bmatrix} = \begin{bmatrix} -3.1051 & 0.2642 & -0.0020 & 0.0000 \\ 3.6061 & -0.0659 & 0.0029 & 0.0000 \\ 3.6264 & -0.3188 & 0.0094 & -0.0001 \\ -12.2843 & 0.2713 & -0.0079 & 0.0000 \\ -50.1483 & 2.1623 & -0.0431 & 0.0003 \\ 3.5502 & -0.3062 & -0.0005 & 0.0000 \end{bmatrix},$$

and

$$\mathbf{A}_0 = \begin{bmatrix} 1.5294 & -0.2244 & 49.0879 & 10.8663 & 5.2289 & -59.6487 \\ -0.6424 & 0.2687 & -0.5762 & 0.7727 & -2.4209 & -7.0918 \\ 7.1314 & 0.1875 & 10.3344 & -7.0854 & -3.6540 & -2.5728 \\ -13.5348 & -1.8434 & -45.9425 & 16.2122 & 2.2269 & -108.8944 \\ -1.0359 & -1.0341 & 22.6264 & 5.2748 & 6.6677 & -73.7306 \\ -4.7396 & -2.3518 & -224.1260 & -6.9444 & -4.8994 & 114.7993 \end{bmatrix},$$

$$\mathbf{A}_1 = \begin{bmatrix} -0.1943 & 0.0320 & -4.2781 & -0.9772 & -0.7657 & 5.5036 \\ 0.0581 & -0.0244 & 0.0609 & -0.0693 & 0.1572 & 0.5872 \\ -0.7710 & -0.0071 & -0.5252 & 0.6810 & 0.3879 & 0.3659 \\ 1.3292 & 0.1763 & 3.9880 & -1.3883 & 0.3188 & 11.9278 \\ 0.0508 & 0.1137 & -2.1445 & -0.2531 & -0.5110 & 6.0220 \\ 0.6771 & 0.1919 & 19.5566 & 0.7884 & 0.9928 & -10.1014 \end{bmatrix},$$

$$\mathbf{A}_2 = \begin{bmatrix} 0.0086 & -0.0013 & 0.1302 & 0.0316 & 0.0312 & -0.1844 \\ -0.0019 & 0.0010 & -0.0025 & 0.0029 & -0.0038 & -0.0198 \\ 0.0297 & -0.0002 & 0.0005 & -0.0233 & -0.0161 & -0.0121 \\ -0.0469 & -0.0057 & -0.1266 & 0.0433 & -0.0218 & -0.4499 \\ -0.0010 & -0.0040 & 0.0673 & 0.0035 & 0.0144 & -0.1697 \\ -0.0305 & -0.0052 & -0.6039 & -0.0325 & -0.0354 & 0.3303 \end{bmatrix},$$

$$\mathbf{A}_3 = \begin{bmatrix} -0.0002 & 0.0000 & -0.0017 & -0.0004 & -0.0005 & 0.0027 \\ 0.0000 & -0.0000 & 0.0000 & -0.0001 & 0.0000 & 0.0003 \\ -0.0005 & 0.0000 & 0.0002 & 0.0003 & 0.0003 & 0.0001 \\ 0.0007 & 0.0001 & 0.0017 & -0.0006 & 0.0004 & 0.0072 \\ 0.0000 & 0.0001 & -0.0009 & -0.0000 & -0.0002 & 0.0021 \\ 0.0005 & 0.0001 & 0.0079 & 0.0006 & 0.0005 & -0.0047 \end{bmatrix},$$

$$\mathbf{A}_4 = \begin{bmatrix} 0.0097 & -0.0013 & 0.0795 & 0.0222 & 0.0306 & -0.1417 \\ -0.0014 & 0.0009 & -0.0025 & 0.0033 & -0.0016 & -0.0148 \\ 0.0278 & -0.0008 & -0.0218 & -0.0176 & -0.0142 & -0.0044 \\ -0.0390 & -0.0038 & -0.0831 & 0.0302 & -0.0284 & -0.4111 \\ -0.0003 & -0.0033 & 0.0469 & -0.0002 & 0.0079 & -0.0906 \\ -0.0339 & -0.0023 & -0.3794 & -0.0357 & -0.0218 & 0.2407 \end{bmatrix} \cdot 10^{-4}.$$

References

[1] M. C. Dobson, F. T. Ulaby, T. L. Toan, A. Beaudoin, and E. S. Kasischke, "Dependence of radar backscatter on conifer forest biomass," *IEEE Trans. Geosci. Remote Sensing*, vol. 30, pp. 402–415, 1992.

[2] M. C. Dobson, F. T. Ulaby, L. E. Pierce, T. L. Sharik, K. M. Bergen, J. Kellndorfer, E. L. J. R. Kendra, Y. C. Lin, A. Nashashibi, K. Sarabandi, and P. Siqueira, "Estimation of forest biophysical characteristics in Northern Michigan with SIR-C/X-SAR," *IEEE Trans. Geosci. Remote Sensing*, vol. 33, pp. 877–895, 1995.

[3] R. L. Jordan, B. L. Huneycutt, and M. Werner, "The SIR-C/X-SAR synthetic aperture radar system," *IEEE Trans. Geosci. Remote Sensing*, vol. 33, pp. 829–839, 1996.

[4] H. A. Zebker, S. N. Madsen, J. Martin, K. B. Wheeler, T. Miller, Y. Lou, G. Alberti, S. Vetrella, and A. Cucci, "The topsar interferometric radar topographic mapping instrument," *IEEE Trans. Geosci. Remote Sensing*, vol. 30, pp. 933–940, 1992.

[5] V. Dimri, *Deconvolution and Inverse Theory : application to geophysical problems.* Elsevier, 1992.

[6] M. K. Sen, *Global Optimization Methods in Geophysical Inversion.* Elsevier, 1995.

[7] F. T. Ulaby and C. Elachi, *Radar Polarimetry for Geoscience Applications.* Artech House, 1990.

[8] K. Sarabandi, "Δk-Radar equivalent of interferometric SARs: a theoretical study for determination of vegetation height," *IEEE Trans. Geosci. Remote Sensing*, vol. 35, no. 5, pp. 1267-1276, 1997.

[9] R. N. Treuhaft, S. N. Madsen, M. Moghaddam, and J. J. van Zyl, "Vegetation characteristics and underlying topography from interferometric radar," *Radio Science*, vol. 31, pp. 1449–1485, 1996.

[10] K. Sarabandi, *Electromagnetic Scattering from Vegetation Canopies.* PhD thesis, University of Michigan, 1989.

[11] F. T. Ulaby, K. Sarabandi, K. MacDonald, M. Whitt, and M. C. Dobson, "Michigan microwave canopy scattering model," *Int. J. Remote Sensing*, vol. 11, pp. 1223–1253, 1990.

[12] L. Tsang, C. H. Chan, J. A. Kong, and J. Joseph, "Polarimetric signature of a canopy of dielectric cylinders based on first and second order vector radiative transfer theory," *J. Electromag. Waves and Appli.*, vol. 6, pp. 19–51, 1992.

[13] M. A. Karam, A. K. Fung, R. H. Lang, and N. H. Chauhan, "A microwave scattering model for layered vegetation," *IEEE Trans. Geosci. Remote Sensing*, vol. 30, pp. 767–784, 1992.

[14] N. S. Chauhan, R. H. Lang, and K. J. Ranson, "Radar modeling of a boreal forest," *IEEE Trans. Geosci. Remote Sensing*, vol. 29, pp. 627–638, 1991.

[15] Y. C. Lin and K. Sarabandi, "A Monte Carlo coherent scattering model for forest canopies using fractal-generated trees," revised for *IEEE Trans. Geosci. Remote Sensing*, September 1997.

[16] L. Pierce, K. Sarabandi, and F. Ulaby, "Application of an artificial neural network in canopy scattering inversion," *Int. J. Remote Sensing*, vol. 15, pp. 3263–3270, 1994.

[17] P. F. Polatin, K. Sarabandi, and F. T. Ulaby, "An iterative inversion algorithm with application to the polarimetric radar response of vegetation canopies," *IEEE Trans. Geosci. Remote Sensing*, vol. 32, pp. 62–71, 1994.

[18] F. Amar, M. S. Dawson, and A. K. Fung, "Inversion of the relevant forest and vegetation parameters using neural networks," in *Proc. of Progress in Electromagnetic Research Symposium (PIERS)*, 1993.

[19] K. Sarabandi and Y. C. Lin, "Simulation of interferometric SAR response for characterizing the scattering phase center statistics of forest canopies," *IEEE Trans. Geosci. Remote Sensing*, submitted March 1997.

[20] D. E. Goldberg, *Genetic Algorithms in Search, Optimization and Machine Learning.* Addison-Wesley, 1989.

[21] S. H. Friedberg, A. J. Insel, and L. E. Spence, *Linear Algebra.* Prentice Hall, Inc., 1979.

[22] A. Ishimaru, *Wave propagation and scattering in random media*, Section 22-4, Vol. II. Academic Press, 1978.

[23] J. Bosworth, "Comparison of genetic algorithms with conjugate gradient methods : technical report," Tech. Rep. UMR0554, The University of Michigan, Computer and Communication Sciences Dept., 1972.

[24] K. Sarabandi and E. S. Li, "Characterization of optimum polarization for multiple target discrimination using genetic algorithms," *IEEE Trans. Antennas Propag.*, accepted for publication, 1997.

[25] R. L. Haupt, "An introduction to genetic algorithms for electromagnetics," *IEEE Ant. and Propagat. Magazine*, vol. 37, pp. 7–15, 1995.

Parameter	Range	Variation
Trunk Diameter	$10.9 \sim 14.9(cm)$	31 %
Tree Height	$8.0 \sim 9.9(m)$	21 %
Tree Density	$807 \sim 1027$ (trees/Hectare)	24 %
Branching Angle	$13.8 \sim 15.8$ (deg)	14 %
Soil Moisture	$0.36 \sim 0.56$ (g/g)	43 %
Wood Moisture	$0.28 \sim 0.48$ (g/g)	52 %

Table 1: The ranges of the selected ground truth parameters and the corresponding percentage variations to the centroid.

Measured Channels $\widetilde{\mathbf{M}}$	$Z_e^{vv}(\theta = 39°) = 3.6m$			$\sigma_{vv}^0(\theta = 39°)$= -10.26 dB		
	$Z_e^{vv}(\theta = 53°) = 6.1m$			$\sigma_{vv}^0(\theta = 53°)$= -13.07 dB		
Parameters	$d_a(cm)$	$H_t(m)$	$D_t(\#/Hectare)$	θ_b	m_s	m_w
Ground truth$\mathbf{x}$	12.9	9.00	907	14.8°	0.46	0.38
Inverted $\mathbf{x}'$	12.4	9.37	945	13.9°	0.44	0.37

Table 2: The inversion results using the interferometric TOPSAR data as the measured channels $\widetilde{\mathbf{M}}$. Here $\mathbf{x}$ is the actual ground truth data and $\mathbf{x}'$ is the output of the inversion process.

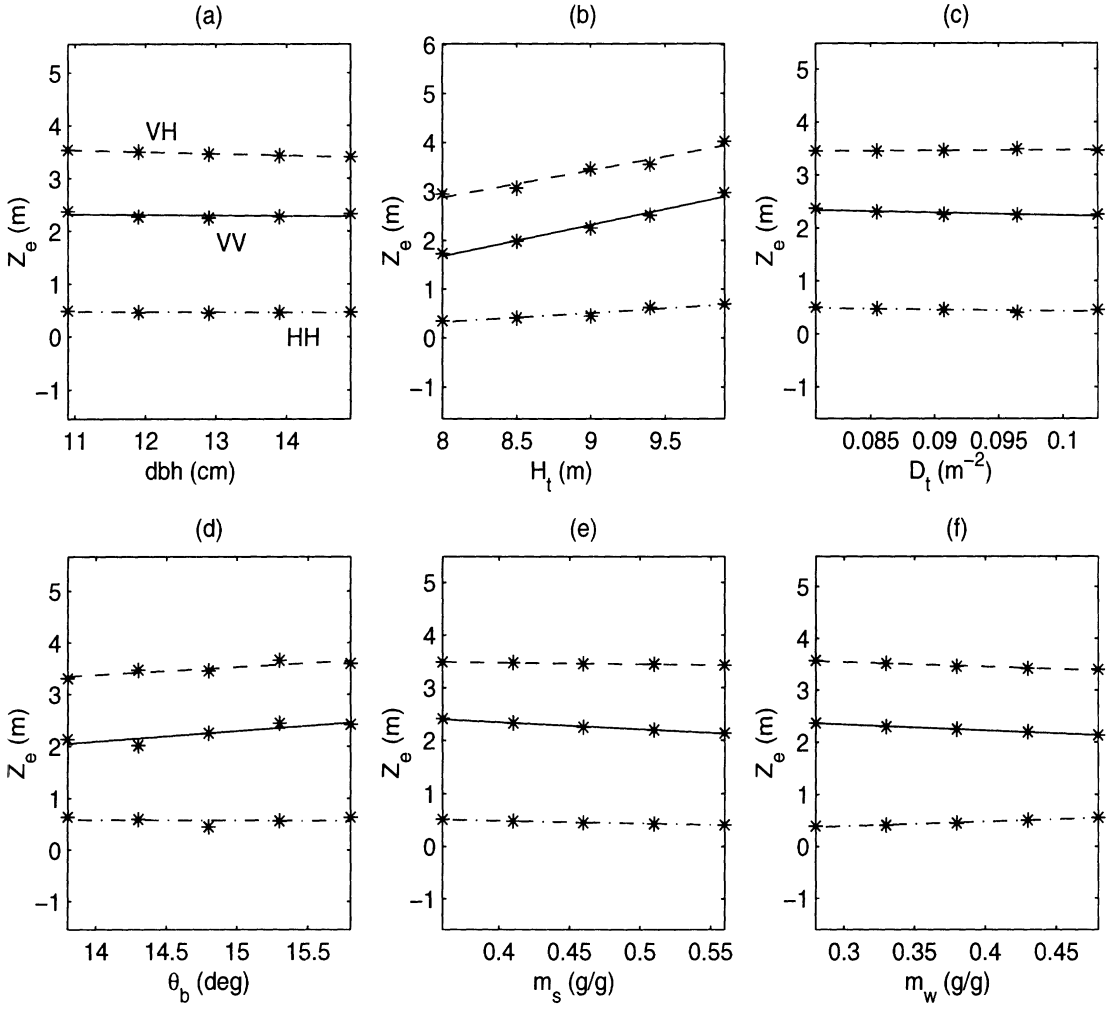

Figure 1: The sensitivity analysis of the C-band polarimetric scattering phase center height as a function of the physical parameters: (a) trunk diameter, (b) tree height, (c) tree density, (d) branching angle, (e) soil moisture, and (f) wood moisture, simulated at incidence angle $\theta = 25^o$.

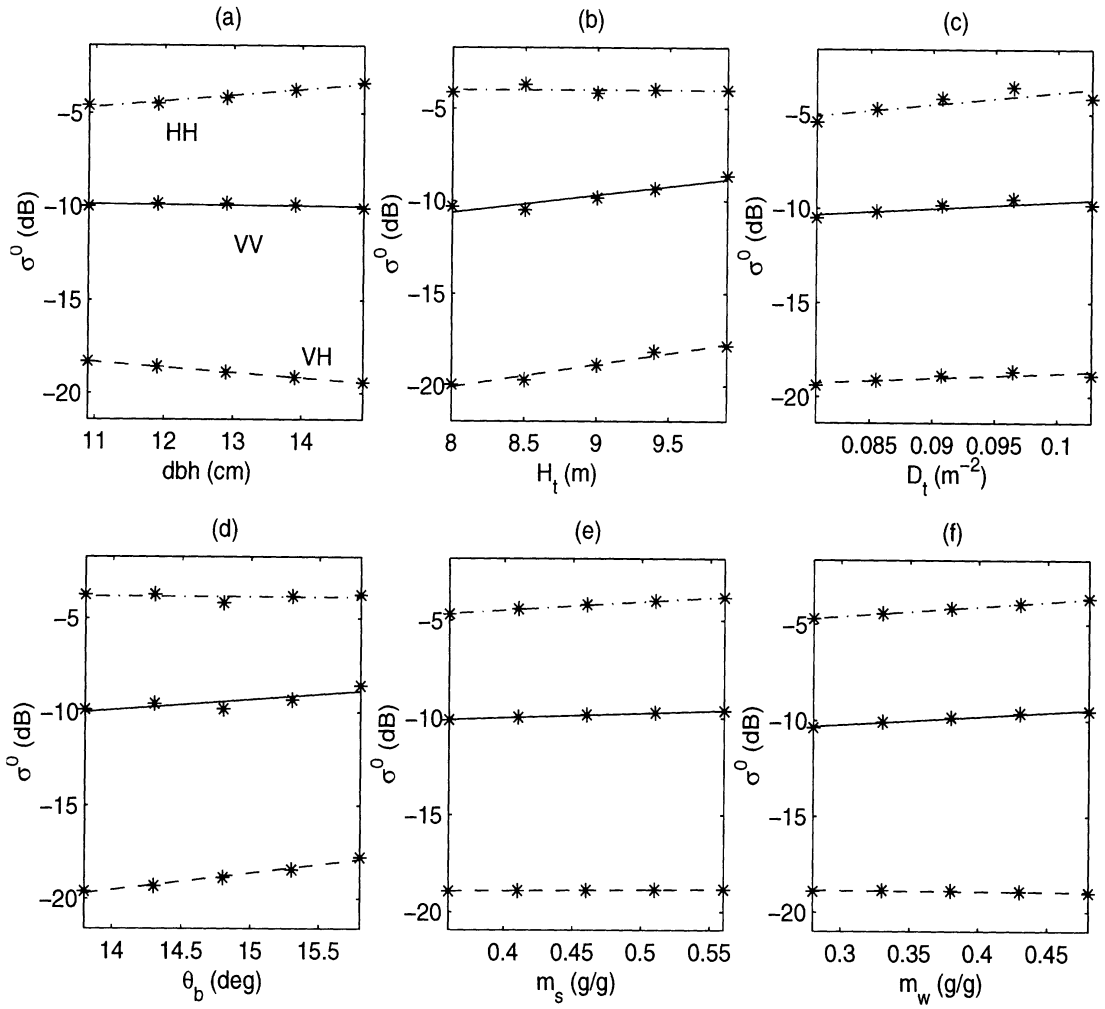

Figure 2: The sensitivity analysis of the C-band polarimetric backscattering coefficient as a function of the physical parameters: (a) trunk diameter, (b) tree height, (c) tree density, (d) branching angle, (e) soil moisture, and (f) wood moisture, simulated at incidence angle $\theta = 25^o$.

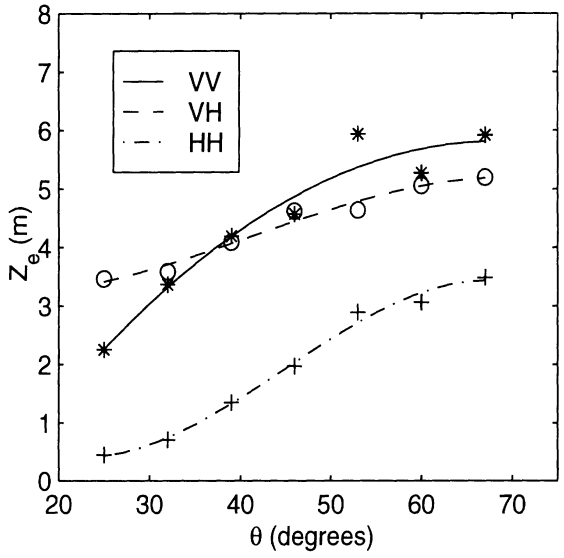

(a)

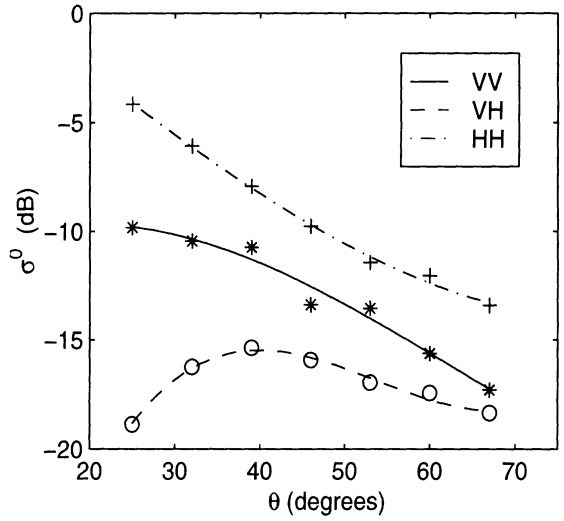

(b)

Figure 3: The angular dependence of the polarimetric backscatter in terms of: (a) the scattering phase center height Z_e and (b) the backscattering coefficient σ^0. The simulation results are fitted with polynomials of degree 3.

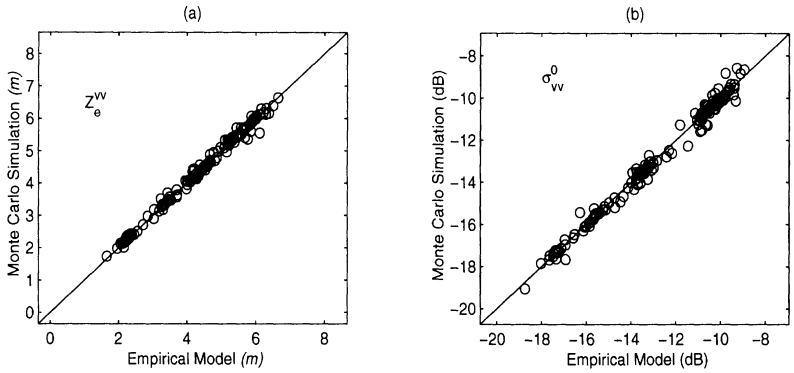

Figure 4: A comparison between the empirical model and the Monte Carlo coherent scattering model for a red pine stand at vv polarization configuration.

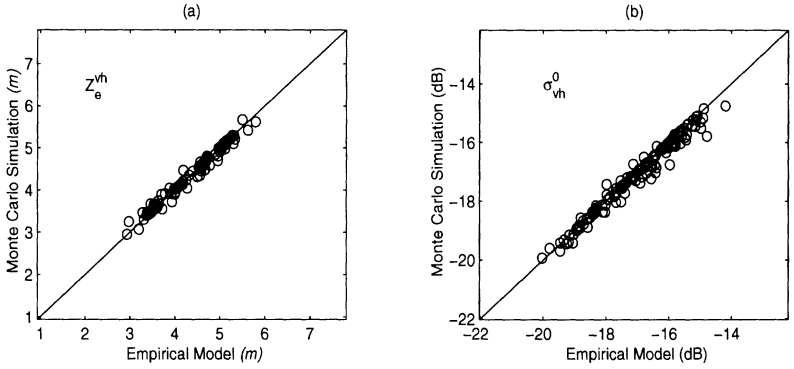

Figure 5: A comparison between the empirical model and the Monte Carlo coherent scattering model for a red pine stand at vh polarization configuration.

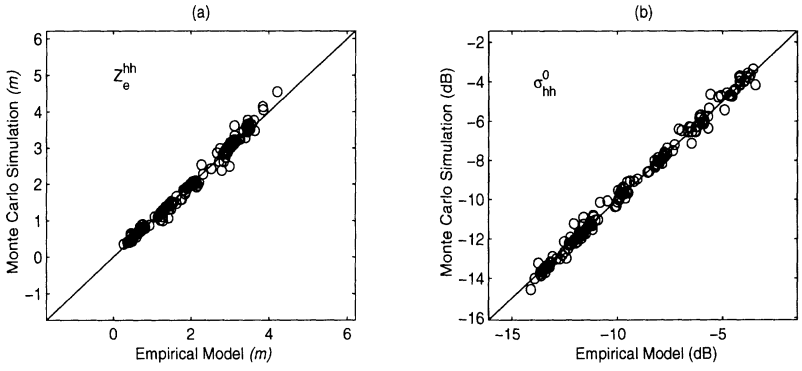

Figure 6: A comparison between the empirical model and the Monte Carlo coherent scattering model for a red pine stand at hh polarization configuration.

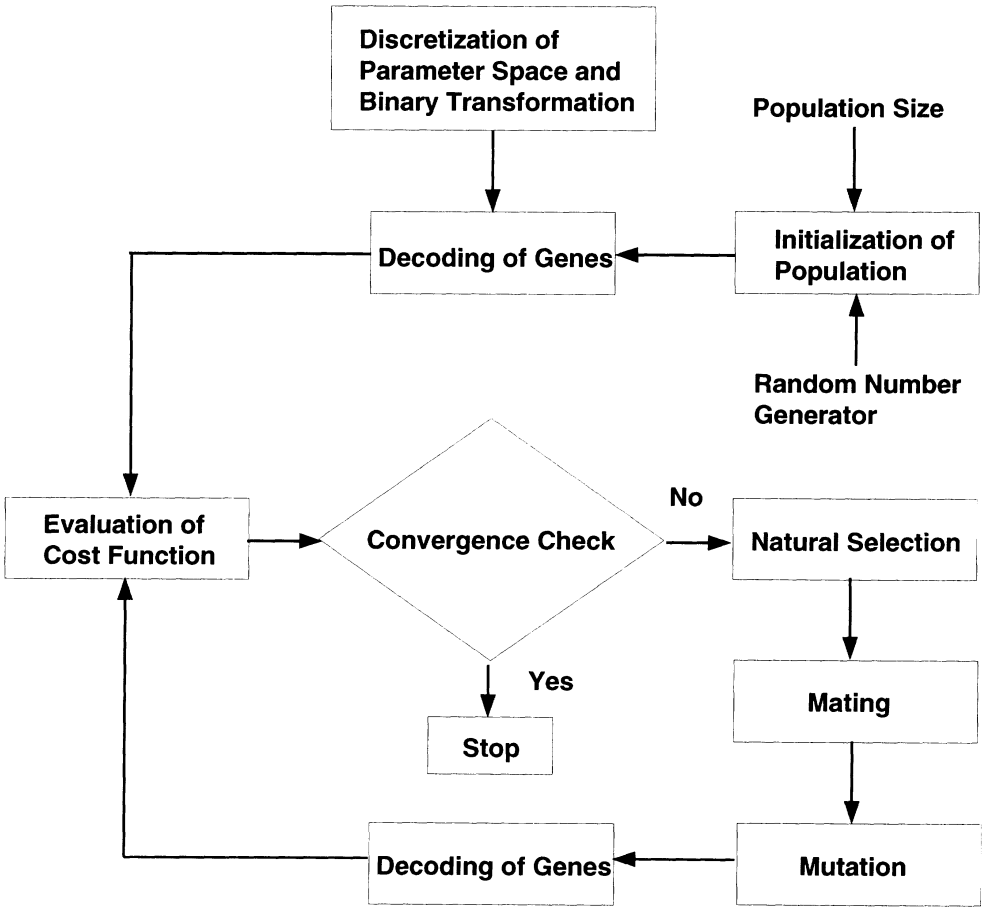

Figure 7: A flow chart of a genetic algorithm.

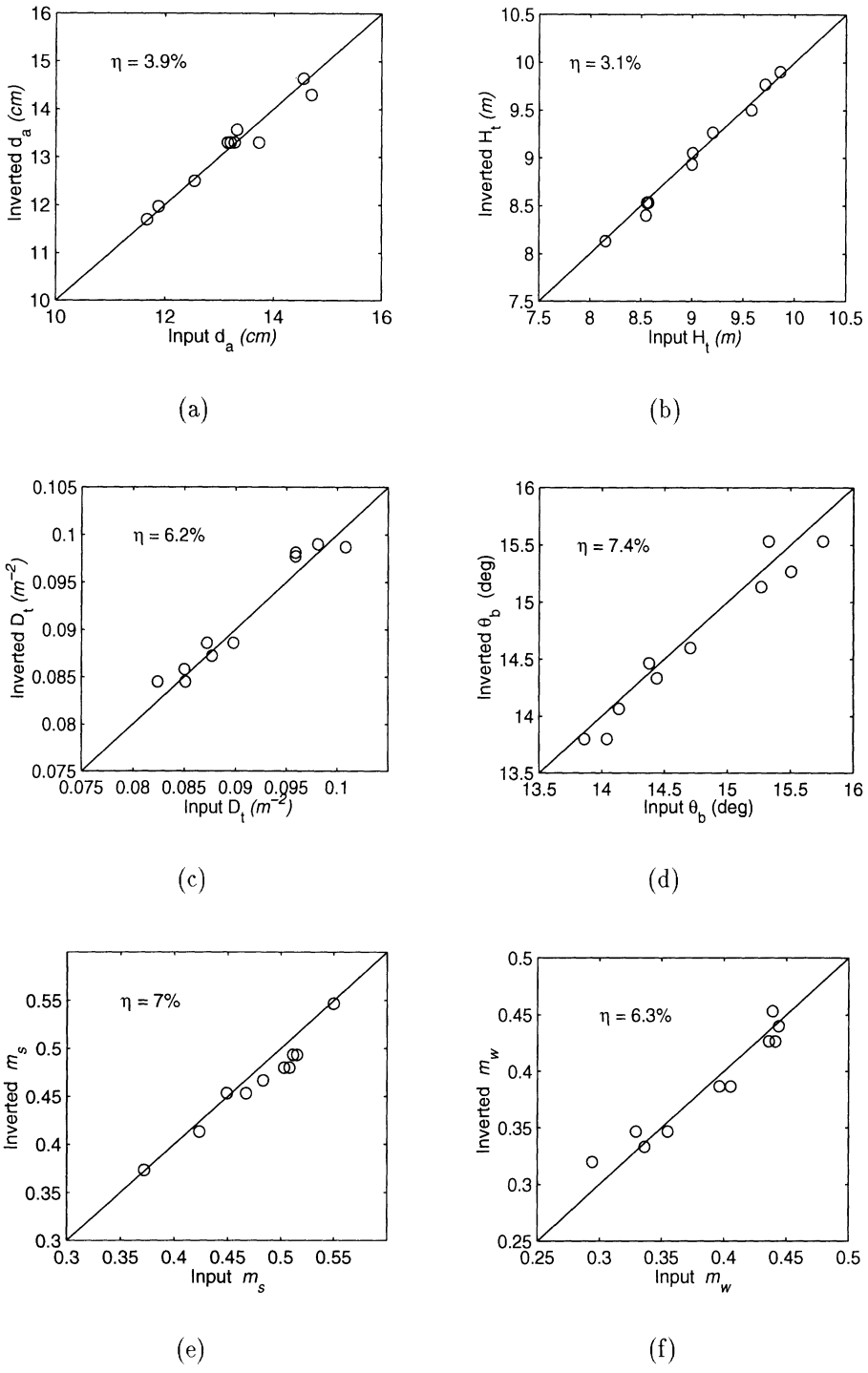

Figure 8: Comparison of the input parameters ($\mathbf{x}$) and the output of the inversion algorithm ($\mathbf{x}'$) using the synthetic data obtained from the Monte Carlo simulation, for (a) trunk diameter d_a, (b) tree height H_t, (c) tree density D_t, (d) branching angle θ_b, (e) soil moisture m_s, and (f) vegetation moisture m_w. Here η is a measure of the average error in the inversion process defined by equation(15).

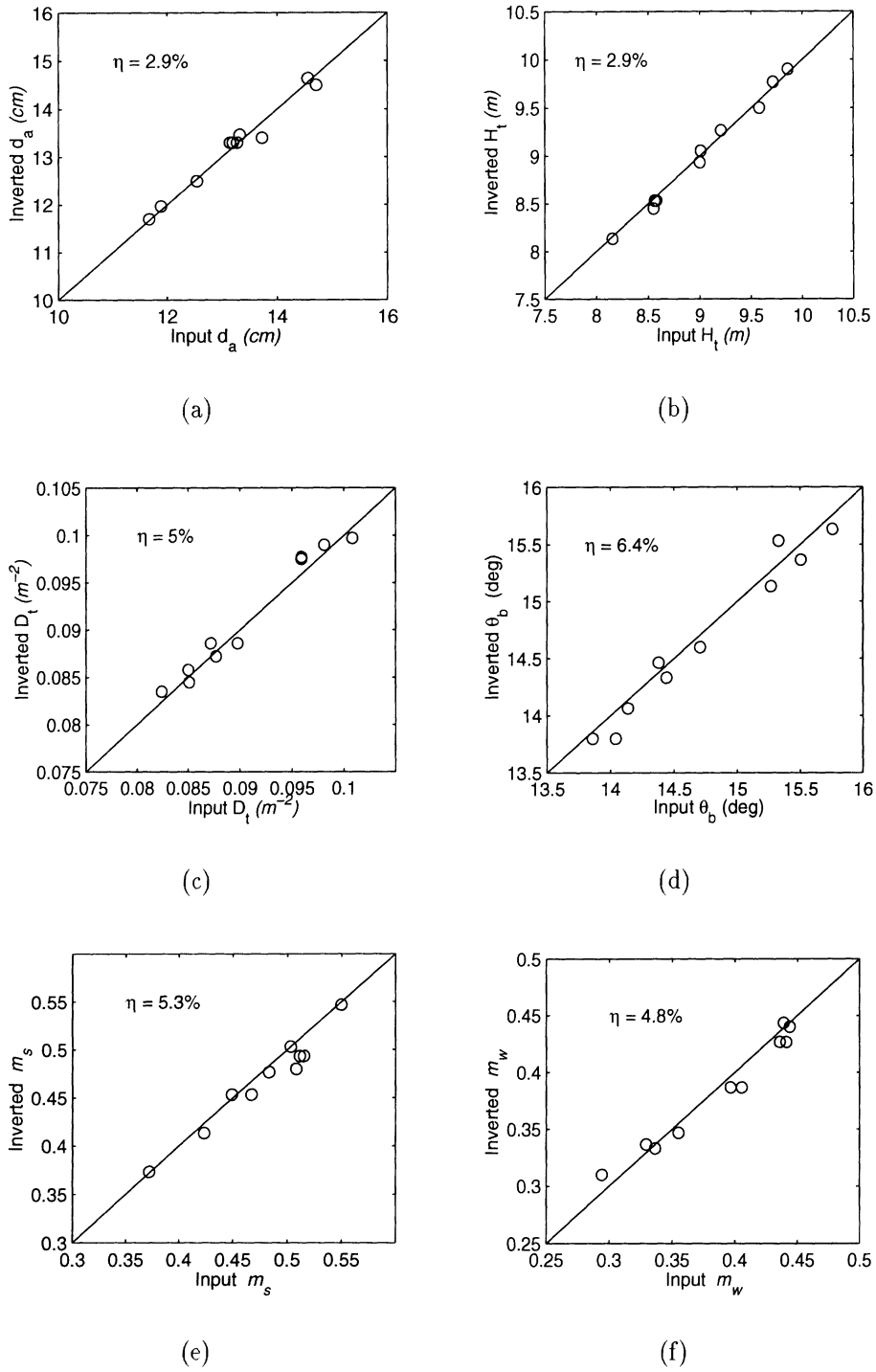

Figure 9: Comparison of the input parameters ($\mathbf{x}$) and the output of the inversion algorithm ($\mathbf{x}'$) using the synthetic data obtained from the empirical model, for (a) trunk diameter d_a, (b) tree height H_t, (c) tree density D_t, (d) branching angle θ_b, (e) soil moisture m_s, and (f) vegetation moisture m_w. Here η is a measure of the average error in the inversion process defined by equation (15).

Appendix VII

An Evaluation of JPL TOPSAR for Extracting Tree Heights

An Evaluation of the JPL TOPSAR for Extracting Tree Heights

Yutaka Kobayashi, Kamal Sarabandi, Leland Pierce, and M. Craig Dobson

Radiation Laboratory
Department of Electrical Engineering and Computer Science
The University of Michigan
Ann Arbor, MI 48109-2122
Phone: (734) 936-1575 FAX: (734) 647-2106
Email: saraband@eecs.umich.edu

ABSTRACT

In this paper the accuracy of the Digital Elevation Model (DEM) generated by the JPL TOPSAR for extracting canopy height is evaluated. For this purpose an experiment using C-band TOPSAR at the Michigan Forest Test Site (MFTS) in Michigan's Upper peninsula was conducted. Nearly 25 forest stands were chosen in MFTS which included a variety of tree types, tree heights and densities. For these stands, extensive ground data were also collected. The most important and difficult-to-characterize ground truth parameter was the forest ground level data which is required for extracting the height of the scattering phase center from the interferometric SAR(INSAR) DEM. To accomplish this, differential GPS (Global Positioning System) measurements were done to accurately ($\pm$ 5 cm) characterize the elevation of (1) a grid of points over the forest floor of each stand, and (2) numerous ground control points (GCPs) over unvegetated areas.

Significant discrepancies between GPS and TOPSAR DEMs and between the two TOPSAR DEMs of the same area were observed. The discrepancies are attributed to uncompensated aircraft roll and multipath. An algorithm is developed to remove the residual errors in roll angle using elevation data from (1) 100-meter resolution U.S. Geological Survey DEM and (2) the GPS-measured GCPs. With this algorithm the uncertainties are reduced to within 3 m. Still, comparison between the corrected TOPSAR DEMs shows an average periodic height discrepancy along the cross-track direction of about $\pm$5 m. Simulation results show that this might have been caused by multipath from an object near one of the INSAR antennas. Careful examination of the coherence image and the backscatter image also show such periodic patterns. Recommendations are provided for the extraction of the best estimate of the scattering phase center height and a model is provided to estimate actual tree height. It is accurate to within 1 meter or 10% for the red pine test stands used here.

1 Introduction

One of the most critical biophysical parameters that is needed for accurate Global Climate Model (GCM) predictions is biomass. Radar has been used extensively in attempts to estimate this parameter, especially for trees. Previous work of ours has used the strategy of accurately classifying the trees to several structural categories followed by class-specific inversion models for various biomass-related terms [4,5]. One of the most important of these parameters is the height of the tree canopy. Because a Synthetic Aperture Radar (SAR) records both amplitude and phase of the target reflections, two such observations from different locations can be used to infer the elevation of the target. This is called interferometric SAR, or INSAR.

Besides the backscattering coefficient image, interferometric SARs provide two additional images that are sensitive to the target parameters. These are the magnitude and phase of the backscatterer cross correlation between the signals received by the two antennas of INSAR. The phase of the interferogram is the quantity from which the height of the pixel (with respect to a reference) is retrieved. The magnitude of the cross correlation, or simply the correlation coefficient, characterizes the uncertainty with which the height can be measured [18]. For random media in which the radar signal can penetrate to some extent, such as a vegetation canopy, the measured height is somewhere within the random volume depending on the location and relative strengths of the scatterers comprising the medium. The measured height is the location of the scattering phase center for each pixel which of course is a random variable. The statistics of this scattering phase center height is a function of size, orientation, spatial distribution and the vertical extent of the random medium. Therefore the measured scattering phase center height can be used as an independent and sensitive parameter for remote sensing of vegetation.

The coherence was used in an attempt to obtain tree height from repeat-pass ERS-1 data [1,7]. In those studies a model was used to predict tree height from the time variation of the coherence. Another study [3] used polarimetric phase differences to obtain images of the phase difference due to the presence of trees, but made no attempt to model the actual height, as there was no ground truth.

In an attempt to establish the relationship between the canopy parameters and the INSAR parameters (phase of interferogram and correlation coefficient) simplified theoretical models based on the distorted Born approximation have been developed [17,18]. These models are first order and are capable of explaining the phenomenology of the problem rather accurately. However, due to their underlying simplifying assumptions they are not capable of producing very accurate quantitative results. To rectify this deficiency, a sophisticated scattering model based on Monte Carlo simulation of fractal-generated trees was developed recently [14,15].

For verifying these models and eventually developing an inversion algorithm experimental data are needed. Since the height of most forest stands range from 10 m to 60 m, accuracy in height measurement of the order of $\pm$ 0.5 m is needed. Initially we excluded INSAR data generated by repeat-pass interferometry as the temporal decorrelation and problems with baseline estimation hamper height evaluation with such required accuracy. Two-antenna

systems such as the JPL TOPSAR are potentially capable of height measurements of the required accuracy.

To examine the feasibility of using INSAR data for estimating tree height, we conducted a set of experiments with JPL TOPSAR over a well-characterized forest test site. The test stands at the Michigan Test Site (MFTS) are chosen to include different tree species at different growth stages and densities. The wealth of data collected at this site over the past several years makes this an ideal area to use: species composition, diameter, height, and stand densities have been meticulously measured with ground-based tools [2]. Also, much of our previous classification work was done at this test site [6,8], and so we are very familiar with the types and distribution of the vegetation.

This paper is organized as follows: section two describes the test site and the ground-based measurements. Section three presents the two height estimation algorithms and Section four gives the conclusions.

2 Ground Measurements

2.1 Tree height measurements

The MFTS is located in the eastern part of Michigan's Upper Peninsula. The surveyed forest stands cover an area of approximately 20 Km x 20 Km centered at Raco. The species composition, diameters, heights and number densities were measured over a period of several years ending in 1994 [2]. In some cases heights of trees were measured with calibrated height poles, in others heights were estimated based on their diameters and species using equations appropriate to that species under similar growing conditions. Because over 70,000 individual trees were measured in 70 different stands we feel that the dataset is one of the best available for testing algorithms for tree height estimation.

To supplement this dataset we wanted closely-spaced and accurate measurements of ground elevation. The data available from the USGS (U.S. Geological Survey) was neither accurate enough nor dense enough (100 m spacing), and so we used differential GPS (Global Positioning System) measurements to obtain our own elevation data.

2.2 GPS Measurements

GPS consists of many satellites in known orbits that are constantly sending signals to receivers on the ground. The ground receiver uses the known orbits and the time it takes for each message to propagate from the satellite to triangulate its own position in three dimensions. The accuracy of the measured position increases with more satellites and more messages.

We used the Trimble Site Surveyor GPS receiver in order to obtain accuracies on the order of 2 cm. This involves the use of a fixed base station and any number of rovers. The base station is a GPS receiver set up over a surveyed benchmark with known three-dimensional

coordinates. It broadcasts its own signal to the rovers to supplement the satellite signals and a difference vector is calculated that relates the rover to the base station.

The benchmarks we used were surveyed by the U.S. National Geodetic Survey and are brass plates set in concrete pilings in the ground. The coordinates of these benchmarks can be obtained from NGS at their web site. Note that the coordinates given are referenced to various earth models called ellipsoids. There are many of these, and it is best to convert from those given to one named WGS-84, as that is the one the GPS receivers use internally. A good review of the ellipsoids used throughout the world is given in Schreier [9].

A typical rover measurement involves: (1) setting the antenna on a measured height pole with a level bubble; (2) finding a clear view of the satellites through the trees (the L-band signal is significantly attenuated by even a few branches); (3) initializing so the satellites are tracked and the position fix is within a meter; and lastly (4) taking a data point by keeping the pole very still and level, waiting for about 10 seconds for the averaging process to converge to a given error tolerance, usually 2 cm.

There were two kinds of measurements we needed to take with the GPS receivers: (1) Ground Control Points, (2) Forest Stand Floor. The ground control points were specially chosen areas on the ground that we could identify in the SAR images. This usually meant road intersections. These points were needed in order to assure ourselves of the accuracy of the USGS and TOPSAR DEMs. The forest stand floor was measured in order to be able to calculate tree heights above the ground using a simple difference with the TOPSAR DEM. In order to deal with ground height variability in a stand a grid of points was used. This was the same grid of points used to measure the tree heights originally and consisted of 40 points per 200 m $\times$ 200 m forest stand. The tree stands chosen for this study were monocultures all planted at the same time, resulting in a very uniform height distribution. It took between 1 and 3 hours to measure a stand, depending on how often we had to reinitialize because of lost signal from the overlying canopy. In some large, dense stands it was impossible to use the GPS receivers at all, and we contented ourselves with measurements along the stand periphery and field notes about the approximate elevation variation within the stand.

Of course, the USGS and GPS data did not agree exactly, however the errors were within the expected range given the large (100m) horizontal spacing of the USGS data.

3 Tree Height Estimation

3.1 INSAR Overview

In single-pass INSAR the platform has two antennas as shown in Figure 1. One antenna transmits and both receive. The path-length differences (δ) between the two signals results in a phase difference (ϕ) given by:

$$\phi = \frac{2\pi}{\lambda}\delta, \tag{1}$$

where λ is the carrier wavelength. Since the geometry of the two antennas is known the baseline length (B) and the baseline angle (α) can be used to determine the look angle (θ):

$$\sin(\alpha - \theta) = -\frac{(r+\delta)^2 - r^2 - B^2}{2rB}, \tag{2}$$

where r is the range of the target from the transmitting antenna. Using the height of the radar platforms (H) as an arbitrary reference, the target elevation is given by:

$$h = H - r\cos\theta. \tag{3}$$

The height h is really the height of the scattering phase center for a given pixel. In the case of trees the height is somewhere below the height of the top of the canopy. The pertinent parameters for the JPL TOPSAR are given in Table 1, while the details concerning the data are given in Table 2.

The raw data was processed by JPL into three standard products: (1) Cvv power, (2) DEM, (3) coherence. It is these standard products that are used in this study. Note that the TOPSAR flights occurred in April of 1995 and that the most recent height measurements were taken in the fall of 1994. Since the growing season had not yet started in April, we believe that there was no significant change in the height of the trees during this time.

3.2 Uncompensated Aircraft Roll Correction

Since the TOPSAR platform [10] is an aircraft, significant effort is expended in measuring and compensating for the deviation of the airplane from smooth level flight. This is called motion compensation and has been successfully applied in the AirSAR data which uses the same platform but different antennas. Motion compensation must correct for variations from steady, level flight, which includes variations in: height, heading, pitch, and roll. As mentioned in [16] the compensation of the roll angle variability is very important, and for TOPSAR the accuracy of this correction is approximately 0.01°.

In comparing the TOPSAR DEMs of the same area from two different TOPSAR images we noticed that there was serious disagreement between them. This prompted us to examine the data more carefully. Eventually we came up with a way of explaining much of the discrepancy with an uncompensated roll angle error of less than 0.3°.

First, we attempted to match the USGS DEM to the TOPSAR DEM which has an expected height-error of about 2 m [11]. This involved converting the USGS DEM into height over the NAD27 ellipsoid, and then manually warping it to the TOPSAR image geometry. Residual errors in aircraft altitude and roll angle are lumped into one parameter, namely roll angle error, which is a good approximation for very small values of residual altitude and roll angle errors. The roads and other sparsely-vegetated areas were compared as seen in Figure 2. Apart from a constant difference between the USGS DEM and the TOPSAR DEM, Fig. 2c shows a significant variation in the height difference (about 50 m) as a function of along-track distance. This variation far exceeds the expected uncertainties in the TOPSAR and USGS DEMs. We interpreted this as a height error caused by the residual errors in the roll angle. The error in roll angle is directly proportional to the error in the look angle, which is used to calculate the height. Equation 3 can be used to obtain what the height error due to an incorrect look angle would be:

$$dh/d\theta = r\sin\theta = x \tag{4}$$

where x is ground range. This shows that the height error is $x\,\Delta\theta$, and so will increase with range and with look-angle error. This is shown in Fig. 2b from a given cut along the cross-track direction (about 13 m for 900 pixels). The look angle error can be caused by an uncompensated roll angle error. Unfortunately a constant roll angle error does not work well for the entire image as can be seen from Fig. 2c. Hence, we used an azimuth-dependent error model. For each azimuth line, j, we can write:

$$\Delta h_j = x\Delta\theta_j + h_{offset}, \tag{5}$$

where h_{offset} is some constant height error that can be used to adjust the offset between the TOPSAR and USGS reference planes. In order to use the USGS DEM to correct the TOPSAR DEM we used only areas in the TOPSAR DEM that were bare spaces or short vegetation. Hence we classified the images using the C_{vv} power to three classes: bare, short vegetation, and trees. Because we only had one channel the approach was based on simple thresholds with trees being greater than -15 dB, and bare less than -20 dB.

The error model given by (5) is used in a statistical sense over the entire image. This is done to minimize the error between the USGS and TOPSAR DEMs as the USGS DEM is coarse and has a height uncertainty of approximately $\pm$ 3–5 m. Determination of the best value for h_{offset} requires the minimization of the following equation:

$$S = \sum_{i=1}^{M}\sum_{j=1}^{N}(\Delta h_{ij} - x_i\Delta\theta_j - h_{offset})^2 \tag{6}$$

where i and j refer to the range and azimuth (along-track) coordinates, respectively, and $\Delta h = h_{TOPSAR} - h_{USGS}$. For estimation of h_{offset} (a constant over the entire image) we did not use every azimuth line in the image because the resultant matrix equation was too large; instead we subsampled in azimuth, using about 100 lines.

The minimization is carried out by finding a stationary point:

$$\frac{\partial S}{\partial h_{offset}} = 0, \text{ and } \frac{\partial S}{\partial \theta_j} = 0, \quad \text{for all j.} \tag{7}$$

This results in the following set of equations:

$$\begin{aligned} h_{offset}MN + \sum_{j=1}^{N}\left(\sum_{i=1}^{M}x_i\right)\Delta\theta_j &= \sum_{i=1}^{M}\sum_{j=1}^{N}\Delta h_{ij} \\ h_{offset}\left(\sum_{i=1}^{M}x_i\right) + \Delta\theta_j\left(\sum_{i=1}^{M}x_i^2\right) &= \sum_{i=1}^{M}x_i\Delta h_{ij}, \quad \text{for all j,} \end{aligned} \tag{8}$$

which can be solved for the $\Delta\theta_j$'s and h_{offset}. This h_{offset} is then used for each azimuth line to get $\Delta\theta_j$ using a linear least-squares fit to equation 5. The resulting roll angle error is a

continuous function of azimuth, which makes this believable as an error mechanism since the airplane cannot have a very high frequency roll angle change. Figure 3 shows the calculated roll angle error for the two TOPSAR scenes. Note that the error is quite small, less than 0.3° in all cases.

Finally the calculated height error is compensated for in the TOPSAR DEM pixel-by-pixel. To assess how well we did, we used the ground control points (GCPs) that were collected using GPS. The GCP locations are shown in Figure 4, and the height errors before and after the roll angle correction are shown in Table 3. This shows that the height error has been reduced to an average of about 2 meters, although there are still a few points where the error is much worse.

Note that in calculating the TOPSAR DEM height for a given point involves averaging over at least 4×4 pixels in the neighborhood of that point. This is because the phase noise standard deviation is large, and averaging will result in a decreased height error, which in this case is about 3–5 meters, comparable to the USGS DEM height errors. This allows comparisons using these heights to be meaningful.

3.3 Multipath

Despite our efforts in correcting for the roll angle error there still appears to be some residual errors left. This is most apparent when looking at the C_{vv} power images, as seen in Figure 5, where a quasi-periodic sinusoid is apparent with the crests parallel to the azimuth direction. The spacing of these crests increases from about 60 pixels in the near range to about 130 in the far range. The same pattern is seen in the DEM data. The magnitude of those errors is approximately 8 dB and 10 meters peak-to-peak, in the power and elevation images, respectively. This is a significant effect that must be dealt with in order to estimate tree heights accurately. In all fairness, these errors are not present at all with some of the TOPSAR data we have. Unfortunately, for this application this is the only data we could use.

This problem may be due to multipath [12,13] where an object near the antennas is reflecting the returned pulse into the antennas. The coherent addition of the direct return and the multipath return could cause such a pattern. Assume that the multipath object only reflects into the upper of the two antennas. Also assume that the object is near the upper antenna. These assumptions are made according to the arrangement of the TOPSAR and other AirSAR antennas. As shown in Figure 6, we can then model the fields at each antenna as:

$$\begin{aligned} r_{A_1} &= E_s e^{ik2A_1T} \\ r_{A_2} &= E_s[e^{ik(A_1T+A_2T)} + de^{ik(A_1T+TC+CA_2)}] \end{aligned} \tag{9}$$

where $k = 2\pi/\lambda$ is the wave number, the terms A_1T, A_2T, TC, and CA_2 are the path lengths, and d is a diffraction coefficient. If we represent the additional path length due to the multipath object as $\Delta L = TC + A_2C - A_2T$ we can write the amplitude error as:

$$\frac{|r_{A_2}|^2 - |E_s|^2}{|E_s|^2} = d^2 + 2d\cos(k\Delta L) \approx 2d\cos(k\Delta L). \quad (10)$$

It can easily be shown that $(TC - TA_2)$ increases with increasing range in a nonlinear fashion which gives rise to a sinusoid whose period increases with range. We can also derive an expression for the phase difference that this would induce in the interferogram phase. Representing this error in phase by ϕ_{error} and noting that $d \ll 1$ it can be shown that

$$\phi_{error} = L[e^{ik(A_2T - A_1T)} + de^{ik(TC + CA_2 - A_1T)}] - Le^{ik(A_2T - A_1T)} \approx d\sin(k\Delta L). \quad (11)$$

Equations (10) and (11) indicate that the phase and power errors are in phase quadrature.

These equations were used to calculate the expected multipath error which was compared to the known error. First, the period of the oscillation as a function of range was used to narrow in on the best position for a single scatterer, then the peak-to-peak variation was used to get the best diffraction coefficient. Unfortunately, the best we could do with a single scatterer did not match the range-varying period exactly and so there remained residual errors. The result was unsatisfactory.

This led us to try another approach. Apparently the TOPSAR processing involves a step where a measured phase screen is applied to the data in order to remove any multipath that is repeatable. This phase screen is calculated by JPL at the beginning of each deployment season, and depends on a very accurate DEM that is compared with the TOPSAR data to produce the phase error as a function of the look angle. We obtained a copy of this phase screen and used it as in the multipath equations above in order to correct both the DEM and power data from TOPSAR. Unfortunately the variations due to this correction still did not exactly cancel the variations in the data we had, and so this method did not work either.

Consequently, we gave up in our attempt to correct for the multipath error. Unfortunately this limited the number of forest test stands we could use, since only a few had bare spots near them that were unaffected by the multipath errors.

3.4 Tree Height Estimation

The corrected DEM is now as consistent with the USGS DEM and the GCP's collected with GPS as was possible. The determination of the height of the trees is next. While the C-band, vv-polarized signal scatters significantly from branches and needles or leaves in the crown, the scattering phase center is rarely at the top of the trees, so we need a model that relates it to the true height. Such a model has been developed using fractal-generated trees by Lin and Sarabandi [14,15].

Using cylinders, disks, and needles a full-wave Monte Carlo simulation was used to estimate powers and scattering phase center heights for several different tree stands, at several incidence angles. The major lessons are that the height of the scattering phase center varies with incidence angle and with the extinction distribution in the tree canopy. Typically the height was higher for large incidence angles and for large total extinctions. However, the calculated phase center height never achieved the true tree height, and often was significantly

less, down to one-tenth or less of the true height. This means that some kind of model must be used in order to obtain tree heights from a TOPSAR DEM, even after we estimate the phase center height.

An heuristic model for tree height of red pine stands given the phase center height, incidence angle, and extinction [or correlation] is now developed. Figure 7 shows the results for the fractal model described above as applied to one stand at the MFTS. Recall that the tree stands chosen for this study were monocultures all planted at the same time, resulting in a very uniform height distribution. The sigmoidal shape can be modeled with

$$h_{ph} = h_o \frac{(\theta/\theta_o)^n}{1 + (\theta/\theta_o)^n} \tag{12}$$

where h_{ph} is the phase center height, h_o is the true height, θ is the incidence angle, θ_o is a free parameter that corresponds to the incidence angle where the curve has an inflection point, and the power n is also a free parameter, but could depend on extinction, with higher n corresponding to higher extinction. The best-fit curve to the C_{vv} data is also shown in Fig. 7. For that data a simple least-squares fit gives $n = 2.7$ and $\theta_o = 45°$. As a first approximation, for all the other data in this study we will assume that only h_o changes. This gives us a family of curves that we can use to easily estimate h_o given h_{ph} and θ. This is crude, and probably only works for red pine trees at this test site, but further refinements must await more simulations with the fractal model.

There are two ways of determining the height of the scattering phase center, h_{ph}, for use in height estimation. First, if the TOPSAR DEM is correct in an absolute sense then a simple subtraction of the known DEM of the area from the USGS data is sufficient. However, as seen previously, generating correct TOPSAR DEM data is laborious. An alternative is to use the good relative heights. In this scheme there MUST be a bare and flat area near the tree stand of interest in order to be able to have confidence that the subtraction gives meaningful results. Since we were able to find appropriate areas in the images, we used both methods. Table 4 shows the results of the phase center height estimation and the tree height estimation for several stands. Only two stands were used for several reasons: (1) limited to monoculture pine stands so could use model, (2) the stand must appear in both TOPSAR images in order to have data for two different incidence angles, and (3) an adjacent bare, flat surface at the same range for subtraction within the DEM while avoiding multipath errors. For each tree stand, we used the GPS data for the subtraction as well as the TOPSAR DEM. As you can see both methods yield similar results which compare well with the ground-based measurements of the tree height. The comparison with any independently-measured elevation still suffers due to the residual multipath errors, with an error as high as 2.65 meters, or 30% for stand 22. The worst-case error when using a nearby flat area for reference is 1 meter, or 11%. It is hoped that removal of the multipath errors will allow comparison with ground-based measurements to yield accurate tree height estimations.

4 Conclusions

While the data from the TOPSAR has problems with roll angle errors and multipath it appears that these can either be fixed, or judiciously avoided. A nicer method to deal with the roll angle error would not require a known DEM.

Tree height determination seems feasible, but we need more sophisticated models in order for it to work for a greater variety of trees. This work is in progress.

Another method of tree height determination could use more frequencies and polarizations so that a reference height is unneeded.

Acknowledgments

The authors appreciate the help of the JPL Radar Science group in providing the TOPSAR image data used in this study, and specially Dr. Y. Kim for corresponding with us related to this study.

References

[1] Askne, Jan I. H., Patrick B. G. Dammert, Lars M. H. Ulander, Gary Smith, " C-Band Repeat-Pass Interferometric SAR Observations of the Forest," *IEEE Trans. Geosci. Remote Sensing,* Vol. 35, No. 1, pp. 25–35, Jan. 1997.

[2] Bergen, K.M., Dobson, M.C., Sharik, T.L., Brodie, I., Structure, Composition, and Above-ground Biomass of SIR-C/X-SAR and ERS-1 Forest Test Stands 1991-1994, Raco Michigan Site, *University of Michigan, Report 026511-7-T,* Oct. 1995.

[3] Cloude, Shane R., Kostas P. Papathanassiou, "Polarimetric SAR Interferometry," *IEEE Trans. Geosci. Remote Sensing,* Vol. 36, No. 5, pp. 1551–1565, Sept. 1998.

[4] Dobson, M. Craig, Fawwaz T. Ulaby, and Leland Pierce, "Land-Cover Classification and Estimation of Terrain Attributes using Synthetic Aperture Radara," *Remote Sensing of Environment,* Vol. 51, No. 1, pp. 199–214, Jan. 1995.

[5] Dobson, M. Craig, Fawwaz T. Ulaby, Leland Pierce, Terry L. Sharik, Kathleen M. Bergen, Josef M. Kellndorfer, Jogn R. Kendra, Eric Li, Yi-Cheng Lin, Adib Nashashibi, Kamal Sarabandi and Paul Siqueira, "Estimation of Forest Biophysical Characteristics in Northern Michigan with SIR-C/X-SAR," *IEEE Trans. Geosci. Remote Sensing,* Vol. 33, No. 4, pp. 877–895, July 1995.

[6] Dobson, M. Craig, Leland E. Pierce, Fawwaz T. Ulaby, "Knowledge-Based Land-Cover Classification using ERS-1/JERS-1 SAR Composites," *IEEE Transactions on Geosciences and Remote Sensing,* Vol. 33, No. 1, pp. 83–99, Jan. 1996.

[7] Hagberg, Jan O., Lars M. H. Ulander, Jan I. H. Askne, "Repeat-Pass SAR Interferometry over Forested Terrain," *IEEE Trans. Geosci. Remote Sensing,* Vol. 33, No. 2, pp. 331–340, March 1995.

[8] Pierce, Leland E., Ulaby, Fawwaz T., Sarabandi, Kamal, Dobson, M. Craig, Knowledge-Based Classification of Polarimetric SAR Images, *IEEE Transactions on Geosciences and Remote Sensing*, Vol. 32, No. 5, pp. 1081-1086, Sept. 1994

[9] Schreier, G. (editor), SAR Geocoding: Data and Systems, Wichmann, Germany, 1993.

[10] Zebker, H.A., Madsen, S.N., Martin, J., Wheeler, K.B., Miller, T., Lou, Y., Alberti, G., Vetralls, S., and Cucci, A., The TOPSAR Interferometric Radar Topographic Mapping Instrument, *IEEE Transactions Geosciences and Remote Sensing*, Vol. 30, No. 5, pp. 933–940, 1992.

[11] Madsen, S.N., Zebker, H.A., and Martin, J., Topographic Mapping Using Radar Interferometry: Processing Techniques, *IEEE Trans. Geoscience and Remote Sensing*, Vol. 31, No. 1, pp. 246–256, 1993.

[12] Madsen, S.N., and Zebker, H.A., Automated Absolute Phase Retrieval in Across-track Interferometry, IGARSS '92: *Proceedings of the 1992 International Geosciences and Remote Sensing Symposium*, Houston, Texas, USA, Vol. 2, pp. 1582-1584.

[13] Y.J. Kim, Personal communication.

[14] Lin, Y.C., and Sarabandi, K., A., " Monte Carlo Coherent Scattering Model for Forest Canopies Using Fractal Generated Trees, " *IEEE Trans. Geoscience and Remote Sensing*, Vol. 37, No. 1, pp. 440–451, 1998.

[15] Sarabandi, K., and Lin, Y.C., Simulation of Interferometric SAR Response for Characterizing the Scattering Phase Center Statistics of Forest Canopies, *submitted to IEEE Transactions Geosciences and Remote Sensing*, (March 1997).

[16] Kim, Y., et al., NASA/JPL Airborne Three-Frequency Polarimetric/Interferometric SAR System, *1996 Intl. Geosci. and Remote Sensing Symp.,* pp. 1612–1614, 1996.

[17]Treuhaft, R. N. , S. N. Madsen, M. Moghaddam, and J. J. van Zyl, Inteferometric Remote Sensing of Vegetation and Surface Topography, *Radio Science,* vol. 31, pp. 1449-1485.

[18] Sarabandi,K., Δk-Radar equivalent of Interferometric SARs: A Theoretical Study for determination of vegetation height, *IEEE Trans. Geosci. Remote Sensing,* vol. 35, no. 5, Sept. 1997.

Table 1: TOPSAR interferometric parameters

Parameter	TOPSAR value
Baseline length(B)	2.58meter
Baseline angle(α)	62.77degree
Radar platform height(H)	around 7470meter
Wavelength of carrier frequency(λ)	5.67cm

Table 2: Description of test site and DEM data from the TOPSAR and USGS.

Michigan Forests Test Site(MFTS)	Located in the eastern part of Michigan's Upper Peninsula. The region is approximately 20 Km square. According to U.S.Geological Survey, the elevation difference in the whole area of MFTS is less than 60 m, which means MFTS is relatively flat area.
TOPSAR DEM	Both ground range and azimuth pixel spacing are 10 m. The following data are used. CCTID:TS0149(Acquired 26-April-1995) CCTID:TS0171(Acquired 26-April-1995) Some regions are covered by both of these two data, but are illuminated at different incidence angles.
USGS DEM	Original pixel spacing is 100 m in both North-South direction and East-West direction. It is interpolated into 10 m spacing. Elevation is based on NAD27 ellipsoid.

Table 3: Assessment of roll angle error compensation using GCPs. The compensation improves the agreement between the differential GPS measured data and TOPSAR DEM. Both the mean and standard deviation of height difference are improved.

(a) TOPSAR DEM(CCTID:TS0171, referenced DEM: USGS DEM)

GCP No.	$h_{TOPSAR} - h_{GPS}$ Before compensation	$h_{TOPSAR} - h_{GPS}$ After compensation
1	-54.3	-2.0
2	-43.7	2.2
3	-50.1	-2.7
4	-47.7	-1.8
5	-43.9	0.3
6	-58.7	-3.2
7	-44.8	1.7
8	-68.6	-6.3
Mean	-51.5	-1.5
Standard deviation	8.72	2.82

(b) TOPSAR DEM(CCTID:TS0149, referenced DEM: corrected TS0171 DEM)

GCP No.	$h_{TOPSAR} - h_{GPS}$ Before compensation	$h_{TOPSAR} - h_{GPS}$ After compensation
1	-46.7	-1.4
2	-44.5	-0.5
3	-44.9	-1.7
4	-48.0	-0.6
5	-44.0	-2.0
6	-36.4	-1.3
7	-41.9	-1.8
8	-44.0	-2.4
Mean	-43.8	-1.5
Standard deviation	3.5	0.64

Table 4: Results of extracted tree height from TOPSAR DEM. Height extracted by method (2) fits in the trend that the height of scattering phase center will increase as the incidence angle increases and it always appear below the canopy top, whereas height extracted by method (1) doesn't always fit this trend.

(a) Extracted by using DGPS data. (Method (1))

Stand No.	phase center height (CCTID:TS0149) [meters]	phase center height (CCTID:TS0171) [meters]	Modeled Tree ht [meters]	Actual tree height [meters]
22 (incidence angle)	3.8 (40°)	7.0 (53°)	9.0, 11.4	8.7
68 (incidence angle)	8.0 (49°)	5.5 (59°)	14.2, 8.0	13.8

(b) Extracted by using elevation difference between the forest stand and the nearby flat area. (Method (2))

Stand No.	phase center height (CCTID:TS0149) [meters]	phase center height (CCTID:TS0171) [meters]	Modeled Tree ht [meters]	Actual tree height [meters]
22 (incidence angle)	3.0 (40°)	6.0 (53°)	7.0, 9.7	8.7
68 (incidence angle)	7.7 (49°)	9.0 (59°)	13.6, 13.1	13.8

Remark:
1) Source of actual tree height and species are from [2].

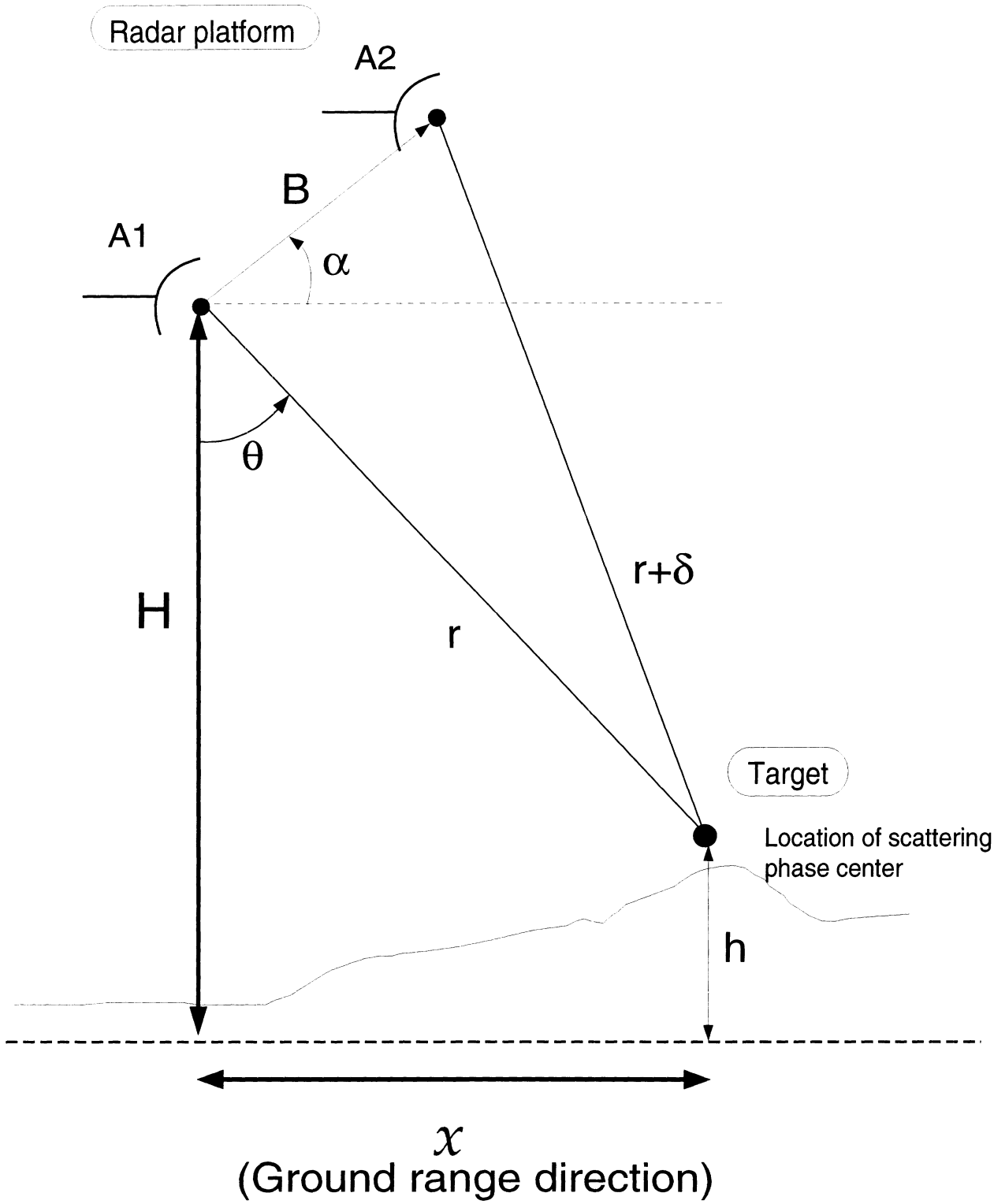

Figure 1: Geometry of single-pass interferometric SAR(INSAR)

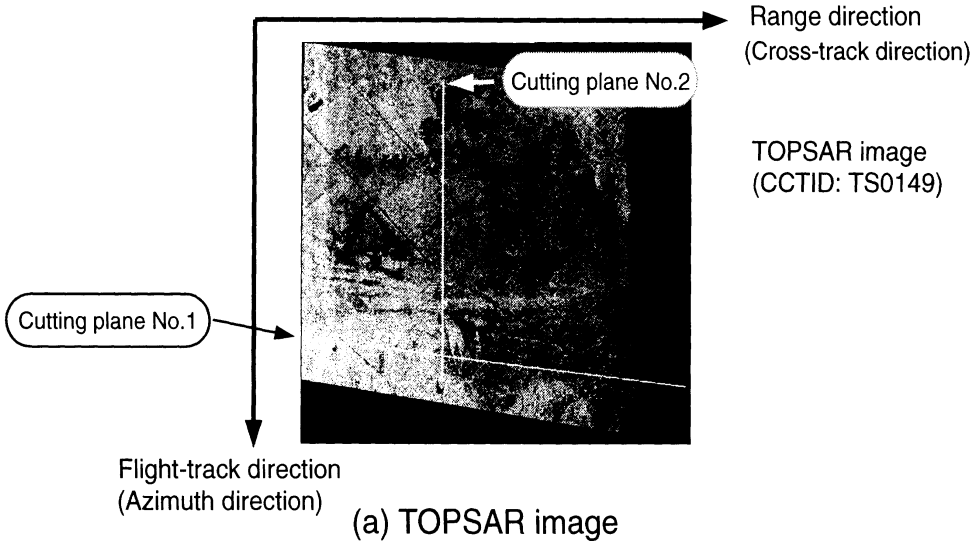

(a) TOPSAR image

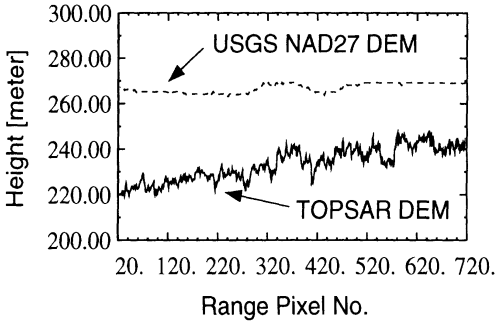

(b-1) Profile of TOPSAR DEM and USGS NAD27 DEM

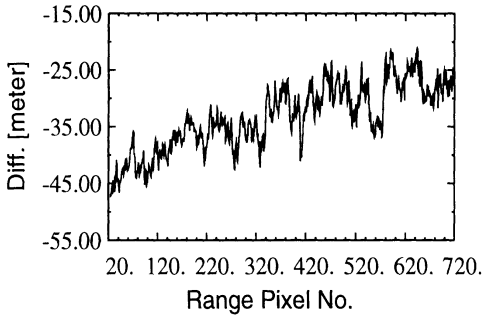

(b-2) Difference between TOPSAR and USGS NAD27 DEMs

(b) Profile by cutting plane No.1

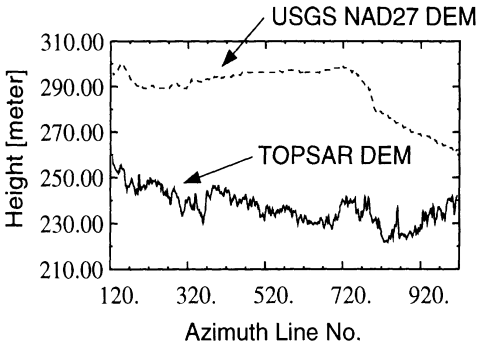

(c-1) Profile of TOPSAR DEM and USGS NAD27 DEM

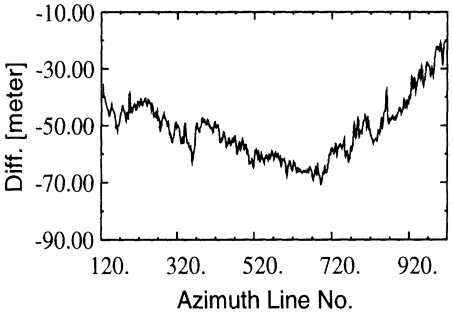

(c-2) Difference between TOPSAR and USGS NAD27 DEMs

(c) Profile by cutting plane No.2

Figure 2: Comparison between TOPSAR DEM and USGS NAD27 DEM

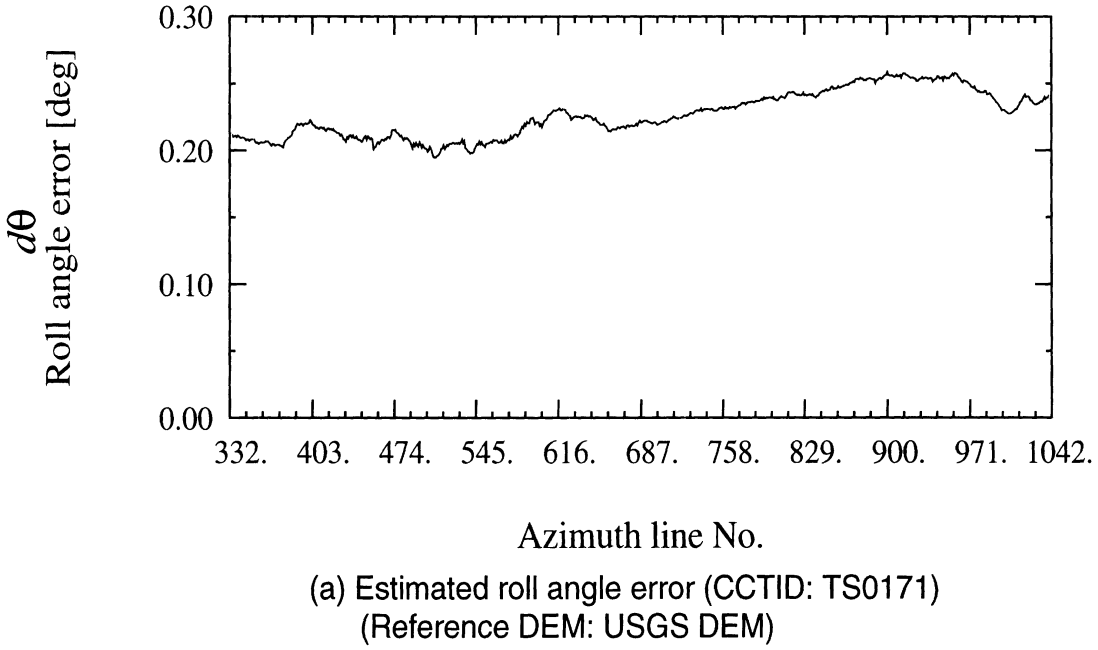

(a) Estimated roll angle error (CCTID: TS0171)
(Reference DEM: USGS DEM)

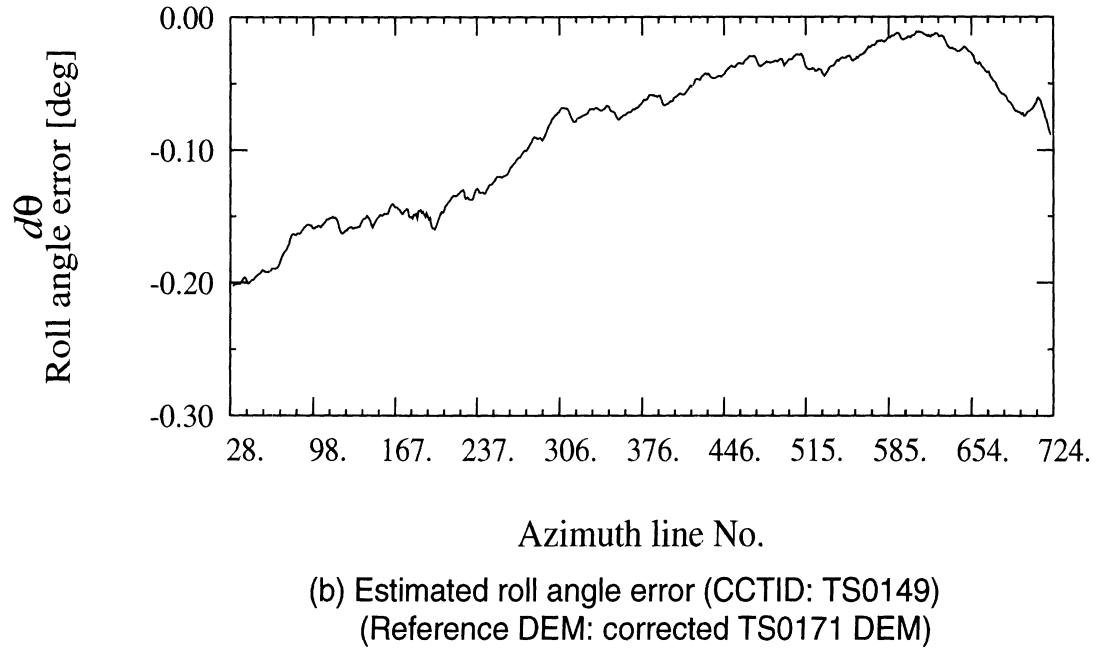

(b) Estimated roll angle error (CCTID: TS0149)
(Reference DEM: corrected TS0171 DEM)

Figure 3: Estimated roll angle error for two TOPSAR DEMs based on least-square minimization between TOPSAR and USGS data.

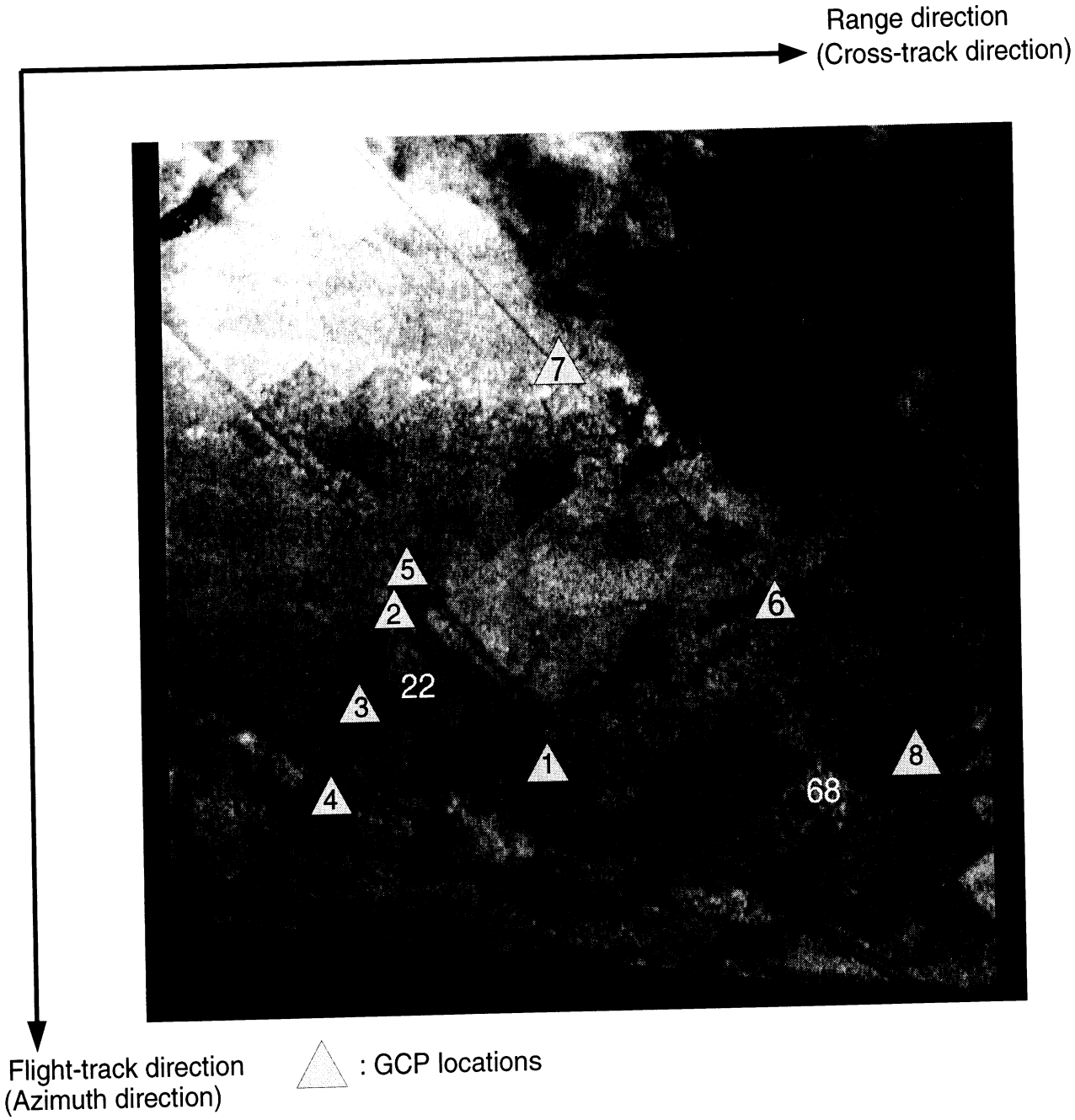

Figure 4: Corrected TOPSAR DEM(TS0171) showing both the location of the GCPs and the two test forest stands (22 and 68). The DEM image is shown in grey-scale such that low to high elevation is shown varying from black to white.

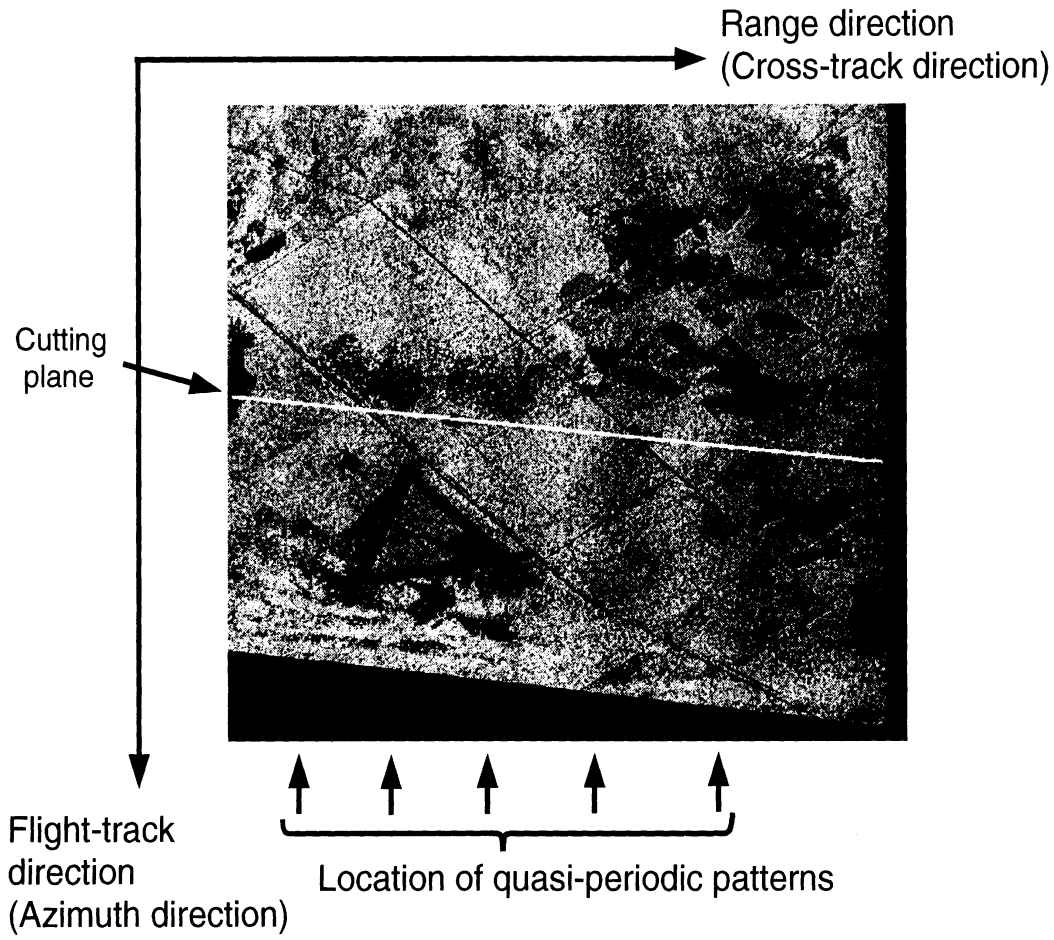

(a) Location of quasi-periodic patterns in TOPSAR DEM(CCTID:TS0171)

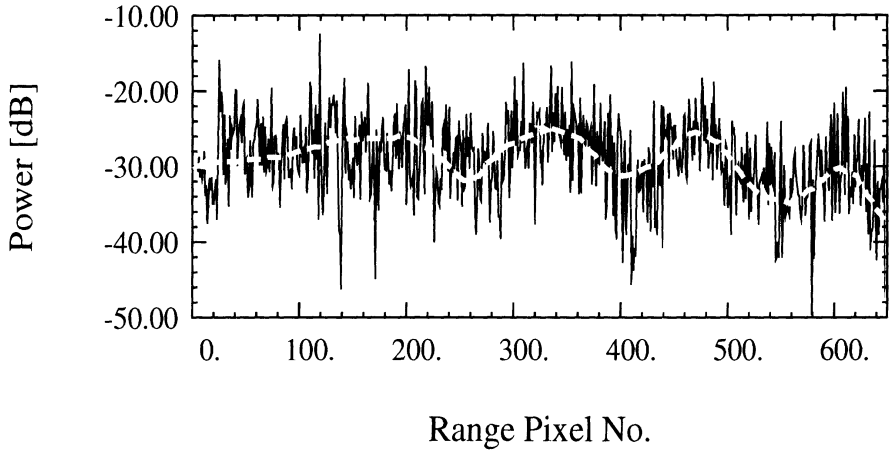

(b) Profile of TOPSAR power image
by cutting plane as shown in Figure 5(a)

Figure 5: Location of quasi-periodic patterns in TOPSAR power image

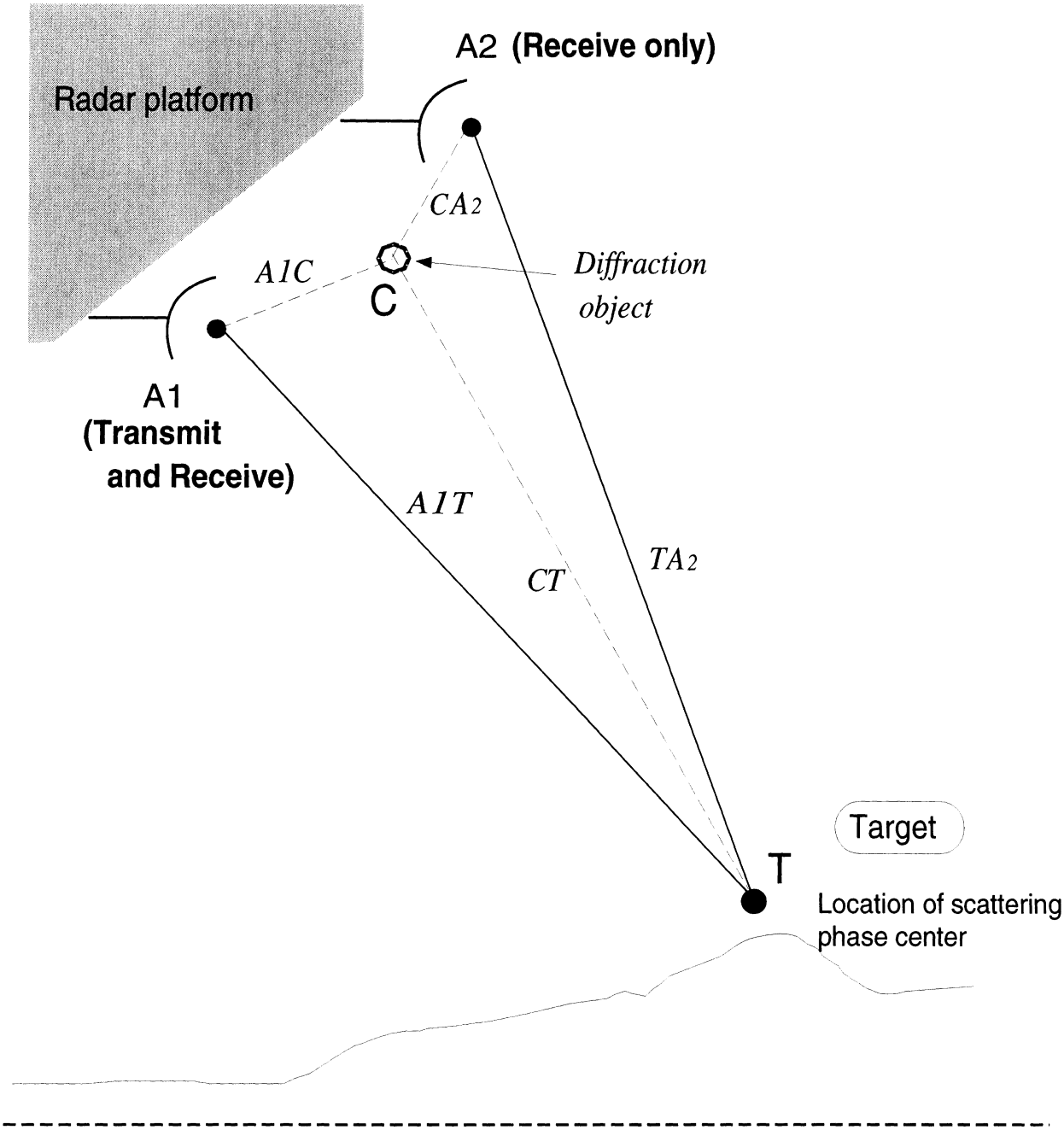

Figure 6: Multipath problem

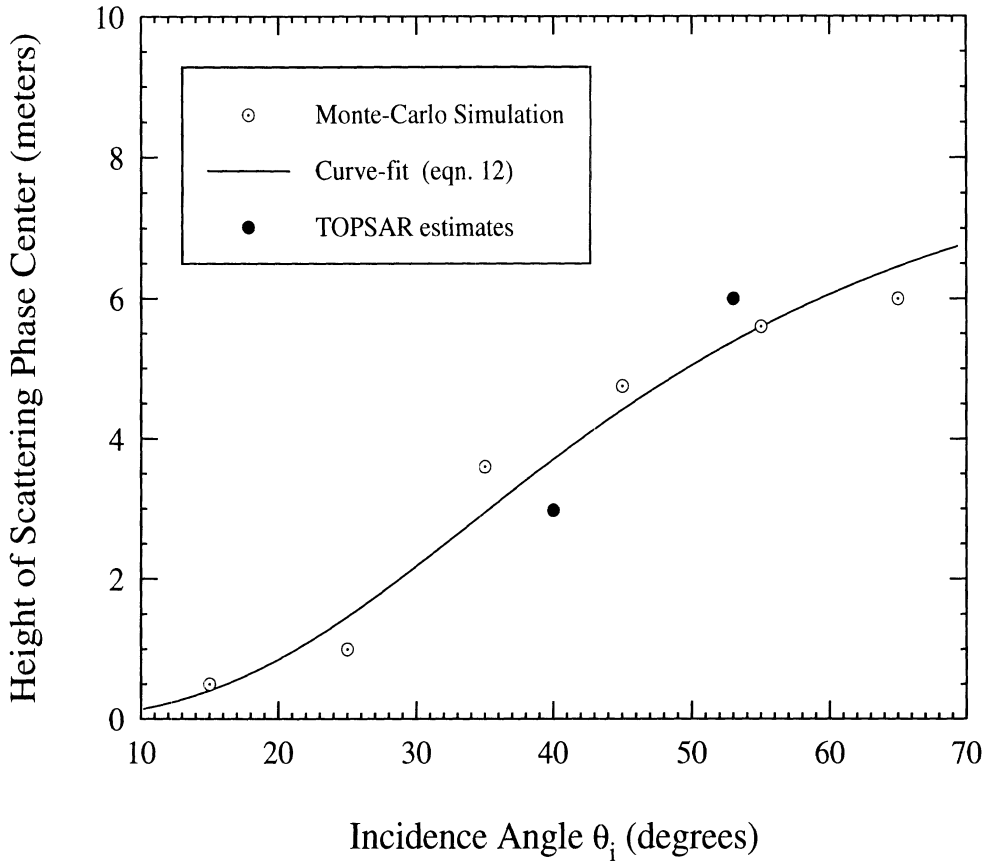

Figure 7: The estimated height of the scattering phase center of Stand 22, compared with the height extracted from two TOPSAR images of the same stand. This figure was adapted from a similar figure in [12].

Appendix VIII

GPS Measurements for SIR-C/X-SAR and TOPSAR Forest Test Stands at Raco, Michigan Site

RL-945

GPS Measurements for SIR-C/X-SAR and TOPSAR Forest Test Stands at Raco, Michigan Site

Yutaka Kobayashi
Kamal Sarabandi
M. Craig Dobson
Leland Pierce
Taeyeoul Yun

July 30, 1997

Table of Contents

1. Purpose 1
2. Methodology 1
2-1. Differential GPS
2-2. Application to Forest Environments
3. Equipment 4
4. Results 4

5. Appendices 5
A. Daily Log
B. Data of Each Stand
C. Description of Stands
D. Data of Ground Control Point(=GCP) Location
E. NGS Data Sheet

1. Purpose

This report presents the GPS measurement of ground level at SIR-C/X-SAR and TOPSAR forest test stands. In order to extract the trees' height information from images of SIR-C/X-SAR and TOPSAR, the ground level of each stands should be measured in high accuracy. To fulfill this purpose, differential GPS measurement has been done in May 18 - 24,1997.

At the same time, in order to create the Interferometric SAR(=IFSAR) images, the location of Ground Control Points(=GCPs) is needed in high accuracy for registeration of two images. To fulfill this purpose, differential GPS measurement has been done.

2. Methodology

2-1. Differential GPS

24 GPS satellites orbit the earth twice per day. GPS receivers on the ground calculate their positions by making distance measurement to four or more satellites.

If two GPS receivers are located within several miles and one of the their locations is the point whose coordinates are already known in high accuracy, differential GPS is applied for higher accurate measurement.

Figure 1 shows the concept of differential GPS. The GPS receiver A(known point) transmits the information of calculated location to GPS receiver B(unknown point) through radio link. This enables the GPS receiver B to calculate its own location in high accuracy. To calculate the location in high accuracy, the following things are required.

(a) The location of known point(GPS receiver A) should be known in high accuracy in advance.
(b) GPS receiver B analyzes the time it takes for radio signal to travel from GPS receiver A to GPS receiver B. So the farther the distance is, the more chances of multipath will occur. To avoid the multipath, the distance between the two GPS receivers should be within several miles.

To satisfy the condition (a), NGS data sheets of Benchmark are used in this measurement.(See Appendix E)

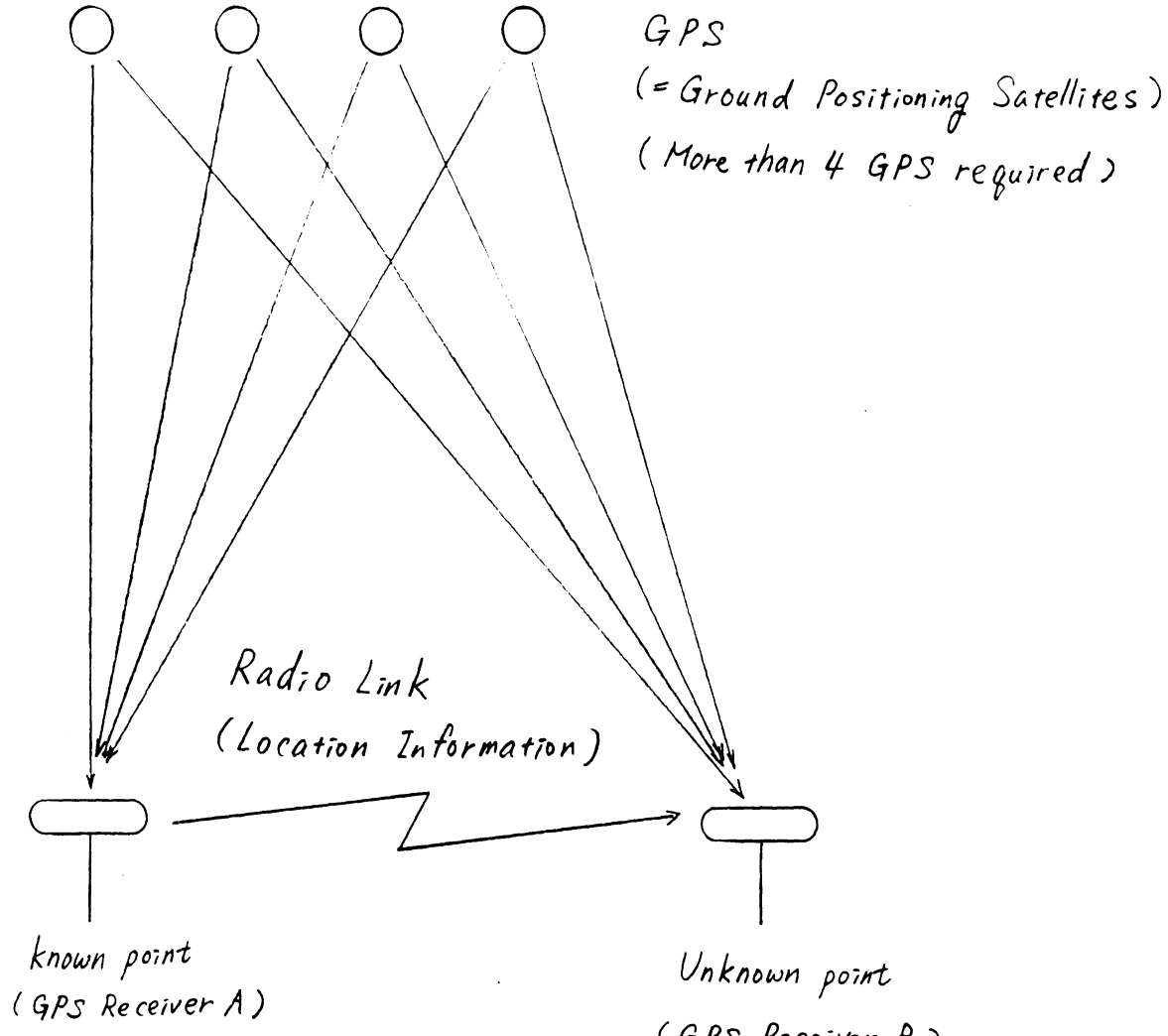

Figure 1 Differential GPS

2-2. Application to Forest Environments

To apply differential GPS to forest environments, 10-meter pole is used.

If the GPS antenna is installed at the top of the pole, GPS signal will be received even in the high forests. Figure 2 shows the installation.

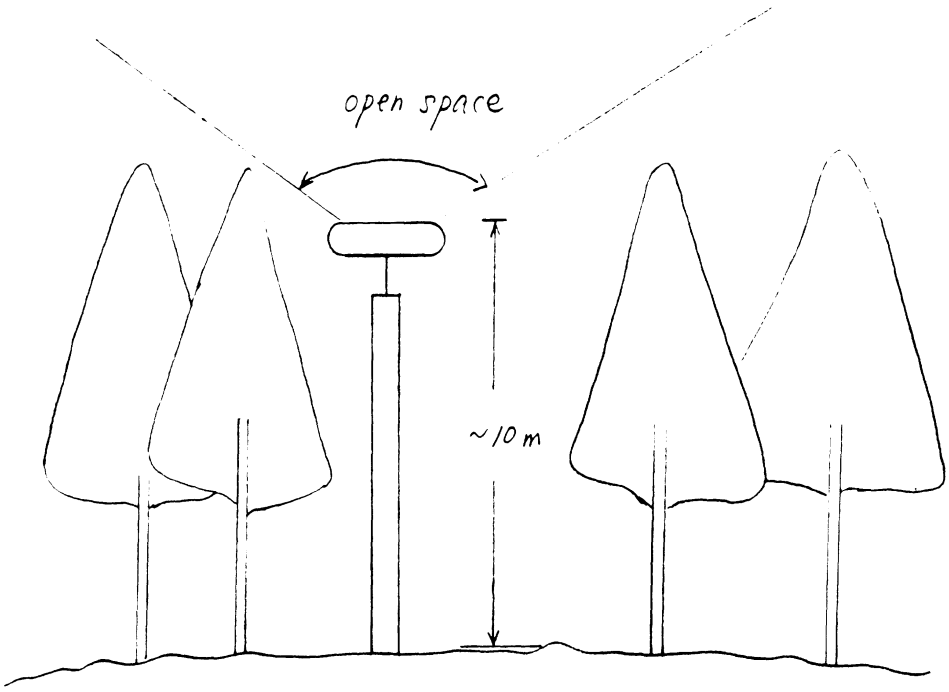

Figure 2 10-meter pole and GPS antenna

3. Equipment

Table 1 shows the equipment which were used in the measurement and its accuracy.

Table 1 Equipment used in the measurement

GPS Receiver	"Site Surveyor SSi 4000" [Trimble Navigation Co.]
Horizontal accuracy	+_(1cm +2ppm) +_(0.03ft.+2ppm*baseline length)
Vertical accuracy	+_(2cm +2ppm) +_(0.07ft.+2ppm*baseline length)

If the radio link is established, the calculation of location is done in realtime.This measurement is called "Realtime Kinematic(=RTK) mode".

In case that the radio link is unable to be established, postprocessing is possible by running the software at the personal computer. This measurement is called "Postprocess infill(=PP infill) mode".

4. Results

Table 2 shows the results of the measurement. The detail results are shown in the appendices.

Table 2 The results of the measurement

Number of measured stands	23
Number of points in measured stands	408
Number of locations of Ground Control Points(=GCPs)	29

Appendix A: Daily Log

Table A-1 shows the daily record. The measurement was done by two rovers(groups). The detail data record is shown afterwards.
All the data are expressed on WGS coordinate.
Including the cover sheet, **appendix A** is totally 20 pages.

Table A-1 GPS measurement daily record (1 of 2)

Day	Rover 1	Rover 2
May 18 (Sun)	[Leland,Dennis,Taeyeoul,Yutaka] **GCP in Rudyard area** 1000-1016(PP infill) valid points: 5 invalid points: 2	
May 19 (Mon)	[Leland,Yutaka] **Stand 67** 1001-1040(PP infill) valid points: 40 invalid points: 0	[Dennis,Taeyeoul] **Stand 22** 2002-2007(RTK) valid points: 5 invalid points: 1
May 20 (Tue)	[Leland,Dennis] **GCP in Raco area** **R14,R15,R16,R17,R8** 1000-1005(RTK) valid points: 6 invalid points: 0 **Stand 59** 1006-1045(RTK) valid points: 40 invalid points: 0 **Stand 56** 1047-1085(RTK) valid points: 39 invalid points: 0	[Taeyeoul,Yutaka] **GCP in Mc Nearney Lake area** **R22** 1000-1005(PP infill) valid points: 6 invalid points: 0 **Stand 58** 1009-1029(RTK) valid points: 21 invalid points: 0
May 21 (Wed)	[Leland,Dennis,Yi-Cheng] **GCP in Raco area** **R9???** 1000(RTK) valid points: 1 invalid points: 0 **Stand 54** 1001-1043(RTK) valid points: 43 invalid points: 0 **Stand 38** 1044-1085(RTK) valid points: 42 invalid points: 0 **Stand 80** 1086-1101(RTK) valid points: 16 invalid points: 0	[Kamal,Taeyeoul,Yutaka] **Stand 61** 2000-2012(RTK) valid points: 13 invalid points: 0 **Stand 68** 2014-2032(RTK) valid points: 19 invalid points: 0

RTK: Data are acquired by realtime kinematic mode.
PP infill: Data are acquired by postprocess infill mode

Table A-1 GPS measurement daily record (2 of 2)

Day	Rover 1	Rover 2
May 22 (Thu)	[Dennis,Yi-Cheng] **GCP in Raco area** **R8** 1000,1001(RTK) valid points: 2 invalid points: 0 **Stand 66** 1002-1029(RTK) valid points: 28 invalid points: 0 **Stand 55** 1030-1046(RTK) valid points: 17 invalid points: 0 **Stand 69** 1047-1053(PP infill) valid points: 3 invalid points: 4	[Kamal,Taeyeoul,Yutaka] **Stand 71** 2001-2012(RTK) valid points: 12 invalid points: 0 **Stand 72** 2013-2024(RTK) valid points: 12 invalid points: 0 **Stand 40** 2025-2039(RTK) valid points: 15 invalid points: 0 **GCP in Raco area** **R18,R19,R20** 2040-2064(PP infill) valid points: 25 invalid points: 15
May 23 (Fri)	[Dennis,Yi-Cheng] **Stand 45** 1000-1016(PP infill) valid points: 17 invalid points: 0 **Stand 34** 1017-1022(PP infill) valid points: 4 invalid points: 2	[Kamal,Taeyeoul,Yutaka] **Stand 31** 2000-2003(PP infill) valid points: 4 invalid points: 0 **Stand 49** 2004-2026(PP infill) valid points: 22 invalid points: 1
May 24 (Sat)	[Dennis,Yi-Cheng] **Stand 33** 1000-1006(RTK) valid points: 7 invalid points: 0 **Stand 85** 1007(PP infill) valid points: 1 invalid points: 0 **GCP in RACO area** **R18,R19,R20,R31** 1008-1019(PP infill) valid points: 12 invalid points: 0 **GCP in Rudyard area** **R33,R34** 1020-1027(RTK) valid points: 6 invalid points: 2	[Kamal,Taeyeoul,Yutaka] **Stand 50** 2000-2007(RTK) valid points: 8 invalid points: 0 **GCP in Mc Nearney Lake area** 2008-2018(PP infill) valid points: 10 invalid points: 1 **GCP in RACO area** 2019-2025(RTK) valid points: 7 invalid points: 0

RTK: Data are acquired by realtime kinematic mode.
PP infill: Data are acquired by postprocess infill mode

GCP measurement
May 18(Sunday) Rudyard area Day #1

The data are WGS coordinate.
Base Station
Pnt # Latitude Longitude Height Code
3001,46.1872884000,-84.5622481306,204.000,RJ1102 BM "RJ1102"

/*================= Rover No.1 ====================================*/
No RTK mode measurement was done.

PP infill mode
Pnt # Latitude Longitude Height Code
1000,46.1870756889,-84.5716812758,203.182,R5-1 GCP "R5" No.1
1001,46.1871502019,-84.5715828700,202.900,R5-2 GCP "R5" No.2
1002,46.1870113742,-84.5715860187,203.053,R5-3 GCP "R5" No.3
1003,46.1870087821,-84.5717947099,202.910,R5-4 GCP "R5" No.4
1004,46.1871423580,-84.5717901641,202.922,R5-5 GCP "R5" No.5
1005,46.2159930864,-84.5716630728,207.031,R2-1 GCP "R2" No.1
1006,46.2160548285,-84.5715898442,206.907,R2-2 GCP "R2" No.2
1007,46.2159567158,-84.5715958889,206.842,R2-3 GCP "R2" No.3
1008,46.2159595341,-84.5717193246,206.875,R2-4 GCP "R2" No.4
1009,46.2160450130,-84.5717210675,206.933,R2-5 GCP "R2" No.5
1010,46.2451467360,-84.5924850466,211.120,R4-1 GCP "R4" No.1
1011,46.2451885535,-84.5924081648,210.922,R4-2 GCP "R4" No.2
1012,46.2450965072,-84.5924086203,210.933,R4-3 GCP "R4" No.3
1013,46.2450922316,-84.5925334188,211.020,R4-4 GCP "R4" No.4
1014,46.2451822000,-84.5925362311,211.025,R4-5 GCP "R4" No.5
1015,46.2319067712,-84.5917093551,65.068,L4-13.4VBM Not Good. Memory is full.
1016,46.1725819811,-84.5719508663,214.580,L5-13.0VBM Not Good. Memory is full.

GCP measurement
May 19(Mon) Raco area Day #1

Base Station
Pnt # Latitude Longitude Height Code
3002,46.3589376000,-84.8456664300,280.746,RJ0241
2000,46.3563470300,-84.8038236900,274.367,AIR-001

/*================= Rover No.1 ====================================*/
RTK mode
Pnt # Latitude Longitude Height Code
1000 46.382342331 -84.801919850 276.485 R50 GCP "R50" See notebook.
PP infill mode
Pnt # Latitude Longitude Height Code
1001,46.3901153567,-84.8102929206,278.472,R67-122 Stand 67
1002,46.3903320207,-84.8102212677,279.217,R67-132
1003,46.3905563080,-84.8101885853,279.238,R67-142
1004,46.3907785626,-84.8102541785,279.241,R67-152
1005,46.3910944753,-84.8103553184,279.696,R67-162
1006,46.3913078929,-84.8104376751,279.095,R67-172
1007,46.3915762219,-84.8104398255,279.219,R67-182
1008,46.3917080041,-84.8099755002,280.514,R67-282
1009,46.3914887362,-84.8099043301,279.745,R67-272
1010,46.3912710794,-84.8098207622,279.936,R67-262
1011,46.3909702621,-84.8097178568,281.017,R67-252
1012,46.3905140327,-84.8098087827,279.603,R67-242
1013,46.3902935312,-84.8098721003,279.640,R67-232
1014,46.3900423730,-84.8098969017,279.033,R67-222
1015,46.3898230162,-84.8098215379,278.831,R67-212
1016,46.3897977728,-84.8093393276,278.973,R67-312
1017,46.3900217497,-84.8093710389,279.341,R67-322
1018,46.3902453046,-84.8093827462,279.783,R67-332
1019,46.3905503042,-84.8093388985,280.496,R67-342
1020,46.3907776197,-84.8092989739,280.324,R67-352
1021,46.3909922274,-84.8092192219,279.618,R67-362
1022,46.3912179216,-84.8091899876,279.160,R67-372
1023,46.3914723283,-84.8091766301,279.449,R67-382
1024,46.3914269833,-84.8086793304,279.182,R67-482
1025,46.3912050421,-84.8087161767,278.690,R67-472
1026,46.3909750806,-84.8087802228,279.071,R67-462
1027,46.3906693470,-84.8087550522,280.309,R67-452
1028,46.3903209758,-84.8087292940,280.636,R67-442
1029,46.3900917064,-84.8087105046,279.835,R67-432
1030,46.3898614454,-84.8086914054,280.072,R67-422
1031,46.3900171706,-84.8082189129,280.365,R67-512
1032,46.3901973896,-84.8082417540,280.423,R67-522
1033,46.3904010544,-84.8082495966,280.007,R67-532
1034,46.3905863191,-84.8082545052,279.435,R67-542
1035,46.3908177930,-84.8082667713,278.632,R67-552
1036,46.3910184144,-84.8082729834,278.514,R67-562
1037,46.3911883484,-84.8082880742,279.009,R67-572
1038,46.3914748533,-84.8082972707,279.624,R67-582
1039,46.3895566138,-84.8081602981,278.969,R67-ROAD-5
1040,46.3895728339,-84.8102629235,277.436,R67-ROAD-1

RTK mode

1041 46.358937606 -84.845666811 280.768 MORNING-BM just for checking

/*================= Rover No.2 ====================================*/
RTK mode

Pnt #	Latitude	Longitude	Height	Code	
2000	46.356347028	-84.803823692	274.367	AIR-001	
2001	46.357666139	-84.804970567	274.405	AIR-002	
2002	46.355478178	-84.822579681	275.804	S22B00	measurement failed(Taeyeoul)
2003	46.355351597	-84.822109336	276.011	S22-11	Stand 22
2004	46.354171394	-84.821035328	274.415	S22-51	
2005	46.353626133	-84.818556731	275.137	S22-58	
2006	46.354466206	-84.820438744	275.928	S22-35	
2007	46.354800464	-84.819968989	275.841	S22-18	
2008	46.357666106	-84.804970583	274.421	AIR002	just for checking

No PP infill mode measured by Rover No.2

GCP measurement
May 20(Tue) Raco area Day #2

The data are WGS coordinate.
Base Station
Pnt # Latitude Longitude Height Code
3005,46.3563470306,-84.8038237000,274.367,AIR-001

/*================= Rover No.1 ====================================*/
RTK mode

Pnt #	Latitude	Longitude	Height	Code	
1000	46.356880953	-84.804882997	274.760	R14	GCP at RACO airport runway
1001	46.356454694	-84.824510278	277.009	R15	GCP at RACO airport runway
1002	46.356454703	-84.824510278	277.005	R15-2	GCP at RACO airport runway
1003	46.350713006	-84.819791794	275.375	R16	GCP at RACO airport runway
1004	46.344839564	-84.814679747	275.618	R17	GCP at RACO airport runway
1005	46.375190372	-84.801734792	276.557	R8	GCP at road intersection of 3364&3018
1006	46.367859906	-84.805234450	275.974	R59TEST	Stand 59
1007	46.367592900	-84.805231686	276.150	R59-112	
1008	46.367382475	-84.805204844	275.971	R59-122	
1009	46.367132597	-84.805103519	276.226	R59-132	
1010	46.366978833	-84.804928961	275.749	R59-142	
1011	46.366830272	-84.804683567	275.561	R59-152	
1012	46.366711428	-84.804417706	275.486	R59-162	
1013	46.366592236	-84.804147569	275.362	R59-172	
1014	46.366569769	-84.803842072	275.480	R59-182	
1015	46.366266639	-84.804098531	275.320	R59-282	
1016	46.366438761	-84.804297275	275.381	R59-272	
1017	46.366399100	-84.804613814	275.425	R59-262	
1018	46.366451444	-84.804949319	275.555	R59-252	
1019	46.366455650	-84.805261608	275.679	R59-242	
1020	46.366452578	-84.805576981	276.019	R59-232	
1021	46.366460256	-84.805899608	275.934	R59-222	
1022	46.366428572	-84.806211783	276.098	R59-212	
1023	46.366591547	-84.806216175	276.075	R59-362	
1024	46.366652681	-84.806620786	276.082	R59-352	
1025	46.366637300	-84.806959483	276.326	R59-342	
1026	46.366679486	-84.807268811	276.459	R59-332	
1027	46.366727250	-84.807577419	276.299	R59-322	
1028	46.366768269	-84.807894933	276.352	R59-312	
1029	46.367554586	-84.807303108	273.035	R59-512	
1030	46.367380450	-84.806302281	275.736	R59-522	
1031	46.366949694	-84.806265497	276.068	R59-532	
1032	46.366742656	-84.806250047	275.976	R59-533	
1033	46.366595133	-84.806218267	276.117	R59-542	
1034	46.366392569	-84.806179744	276.069	R59-552	
1035	46.366227781	-84.806186386	276.253	R59-562	
1036	46.366012044	-84.806109253	276.195	R59-572	
1037	46.365798122	-84.806025161	276.012	R59-582	
1038	46.366019486	-84.804992633	275.695	R59-382	
1039	46.366252017	-84.805136383	275.791	R59-372	
1040	46.366452269	-84.805258064	275.652	R59-362	
1041	46.366642639	-84.805354239	275.639	R59-352	

```
1042 46.366894772  -84.805420578  275.465 R59-342
1043 46.367089233  -84.805370764  275.960 R59-332
1044 46.367307589  -84.805331878  275.841 R59-322
1045 46.367514544  -84.805241700  276.036 R59-312
1046 46.388173150  -84.803176031  278.957 BASE10    Base candidate
1047 46.381754772  -84.801591100  276.520 R56-112
1048 46.381727869  -84.801276542  275.765 R56-122
1049 46.381775167  -84.801019625  275.205 R56-132
1050 46.381774139  -84.800695314  275.319 R56-142
1051 46.381820583  -84.800283914  277.078 R56-152
1052 46.381824156  -84.799756797  277.343 R56-172
1053 46.381817558  -84.799516517  277.346 R56-182
1054 46.381453267  -84.799394472  277.438 R56-128
1055 46.381447494  -84.799661258  277.330 R56-272
1056 46.381444344  -84.799979831  277.041 R56-262
1057 46.381487336  -84.800279100  276.761 R56-252
1058 46.381418861  -84.800599967  276.757 R56-242
1059 46.381402597  -84.800885431  276.709 R56-232
1060 46.381390578  -84.801252661  277.066 R56-222
1061 46.381399756  -84.801471064  277.307 R56-212
1062 46.381040956  -84.801323078  276.899 R56-312
1063 46.381069522  -84.800996819  276.936 R56-322
1064 46.381117000  -84.800802831  276.956 R56-332
1065 46.381095117  -84.800336811  277.131 R56-342
1066 46.381101233  -84.800076058  277.140 R56-352
1067 46.381084858  -84.799773853  277.180 R56-362
1068 46.381106006  -84.799424650  277.357 R56-372
1069 46.381110975  -84.799053322  277.710 R56-382
1070 46.380703642  -84.799381139  277.522 R56-482
1071 46.380688039  -84.799826900  277.263 R56-472
1072 46.380718872  -84.800131686  277.267 R56-462
1073 46.380698569  -84.800529686  277.323 R56-452
1074 46.380678775  -84.800708064  277.558 R56-42
1075 46.380660481  -84.801010111  277.259 R56-422
1076 46.380692603  -84.801297406  277.173 R56-422
1077 46.380716006  -84.801567478  277.321 R56-412
1078 46.380301953  -84.801541378  277.242 R56-512
1079 46.380306083  -84.801314550  277.083 R56-522
1081 46.380284794  -84.800649306  277.248 R56-542
1082 46.380322958  -84.800381447  277.271 R56-552
1083 46.380300125  -84.800170539  277.420 R56-562
1084 46.380268908  -84.799888894  277.099 R56-572
1085 46.380265614  -84.799541300  277.264 R56-582

No PP infill mode measured by Rover No.1


/*================= Rover No.2 ====================================*/
RTK mode
Pnt # Latitude      Longitude     Height   Code
1007 46.356341622  -84.803834669  274.304 AIR001 Near1 just for checking
1009 46.373175500  -84.770793531  275.514 S58INIT POINTA Stand 58
1010 46.373175528  -84.770793528  275.495 S58INIT POINTB
1011 46.373207139  -84.771116314  275.252 S58-02
1012 46.373248633  -84.771399819  275.353 S58-03
1013 46.373656881  -84.770914731  275.952 S58-21
```

```
1014 46.373723114  -84.771218011  275.377 S58-22
1015 46.373811353  -84.771512831  275.507 S58-23
1016 46.373955225  -84.771633875  275.389 S58-24
1017 46.373891192  -84.771819656  275.171 S58-24
1018 46.374025064  -84.772070636  274.929 S58-25
1019 46.374125456  -84.772357878  274.152 S58-26
1020 46.374254747  -84.772626692  273.309 S58-27
1021 46.374341083  -84.770855900  275.193 S58-41
1022 46.374405289  -84.771090567  275.187 S58-42
1023 46.374537864  -84.771347869  274.912 S58-43
1024 46.374728978  -84.771534067  274.194 S58-44
1025 46.374911622  -84.771728556  273.218 S58-45
1026 46.375153150  -84.771707106  272.882 S58-R5
1027 46.375154547  -84.771377011  273.621 S58-R4
1028 46.375147022  -84.771048308  274.621 S58-R3
1029 46.375143825  -84.770715694  274.917 S58-R2

1030 46.375154703  -84.770503836  274.736 S58-CORNER1 GCP "R42" corner1
1031 46.375151878  -84.770375394  274.802 S58-CORNER2 GCP "R42" corner2
1032 46.375287639  -84.770373375  274.897 S58-CORNER3 GCP "R42" corner3
1033 46.375421111  -84.770367964  275.173 S58-CORNER4 GCP "R42" corner4
1034 46.375418719  -84.770498033  275.033 S58-CORNER5 GCP "R42" corner5
1035 46.375284444  -84.770503714  274.807 S58-CORNER6 GCP "R42" corner6
1036 46.375154783  -84.770503872  274.743 S58-CORNER7 GCP "R42" corner7

PP infill mode
Pnt # Latitude      Longitude     Height   Code
1000,46.4297625588,-84.9061364517,266.469,BM NEAR ST45 ----> GCP "R22" Corner_1
1001,46.4298219199,-84.9061780181,266.578,BM NEAR ST45 ---->BM N_2
1002,46.4297385741,-84.9059882138,266.574,ROAD CORN ST45 --> GCP "R22" Corner_2
1003,46.4295992170,-84.9059718765,266.597,ROAD CORN ST45 --> GCP "R22" Corner_3
1004,46.4296658391,-84.9061221572,266.561,ROAD CORN ST45 --> GCP "R22" Corner_4
1005,46.4296928091,-84.9060537808,266.666,ROAD CORN ST45 --> GCP "R22" Center
1006,46.3576660391,-84.8049707158,274.417,AIR002        just for checking
```

GCP measurement
May 21(Wed) Raco area Day #3

The data are WGS coordinate.
Base Station

Pnt #	Latitude	Longitude	Height	Code
3006	46.356347028	-84.803823703	274.367	AIR001

/*================= Rover No.1 ====================================*/
RTK mode

Pnt #	Latitude	Longitude	Height	Code
1000	46.365141342	-84.760581550	263.327	R8
1001	46.385504494	-84.801439514	278.623	R54-512 Stand 54
1002	46.385503156	-84.801135367	278.403	R54-522
1003	46.385483736	-84.800846850	278.283	R54-532
1004	46.385526697	-84.800592911	278.335	R54-542
1005	46.385560511	-84.800309789	278.485	R54-552
1006	46.385534781	-84.799935033	278.596	R54-562
1007	46.385575900	-84.799604081	277.816	R54-572
1008	46.385581953	-84.799320497	277.758	R54-582
1009	46.385997086	-84.799440678	277.891	R54-482
1010	46.386000525	-84.799716156	278.197	R54-472
1011	46.385976581	-84.799984422	278.171	R54-462
1012	46.385971439	-84.800298667	278.591	R54-452
1013	46.385934336	-84.800598531	278.632	R54-442
1014	46.385912131	-84.800856125	278.358	R54-432
1015	46.385869464	-84.801166189	278.731	R54-422
1016	46.385879886	-84.801516889	278.453	R54-412
1017	46.385150022	-84.801507142	278.407	R54-512
1018	46.385150239	-84.801249689	278.519	R54-522
1019	46.385162486	-84.800947769	278.182	R54-532
1020	46.385143875	-84.800654514	278.486	R54-542
1021	46.385132667	-84.800303267	278.728	R54-552
1022	46.385140600	-84.800032214	278.225	R54-562
1023	46.385147783	-84.799744192	278.376	R54-572
1024	46.385159828	-84.799412533	278.603	R54-582
1025	46.386210422	-84.801457542	278.818	R54-212
1026	46.386239714	-84.801160500	278.529	R54-222
1027	46.386231797	-84.800875278	278.539	R54-232
1028	46.386296067	-84.800557400	278.803	R54-242
1029	46.386335042	-84.800209319	278.276	R54-252
1030	46.386369461	-84.799964786	278.784	R54-262
1031	46.386380383	-84.799609989	278.452	R54-272
1032	46.386368272	-84.799263061	277.890	R54-282
1033	46.386697239	-84.799445269	278.516	R54-182
1034	46.386705694	-84.799765408	278.469	R54-172
1035	46.386682714	-84.800045892	278.264	R54-162
1036	46.386645822	-84.800314056	277.676	R54-152
1037	46.386656178	-84.800673644	277.277	R54-142
1038	46.386621808	-84.800960789	278.008	R54-132
1039	46.386511114	-84.801369583	277.762	R54-122
1040	46.386552322	-84.801523122	277.776	R54-112
1041	46.386618967	-84.801911567	277.683	R54-BL0
1042	46.384820889	-84.801858075	278.342	R54-BL1
1043	46.384820964	-84.801858122	277.836	R54-BL1

1044	46.389788078	-84.796109789	278.896	R38-112	Stand 38
1045	46.390036983	-84.796109189	279.268	R38-122	
1046	46.390183119	-84.795913369	279.074	R38-132	
1047	46.390329922	-84.795816925	278.758	R38-142	
1048	46.390522706	-84.795733733	278.202	R38-152	
1049	46.390733875	-84.795668756	278.271	R38-162	
1050	46.391069258	-84.795546231	277.347	R38-172	
1051	46.391287794	-84.795465983	277.334	R38-182	
1052	46.391128256	-84.794847697	277.404	R38-272	
1053	46.391361900	-84.794786933	277.260	R38-282	
1054	46.390920581	-84.794960822	277.553	R38-262	
1055	46.390713097	-84.795088717	277.870	R38-252	
1056	46.390516894	-84.795221828	277.924	R38-242	
1057	46.390290008	-84.795272328	278.026	R38-232	
1058	46.390077350	-84.795438981	278.482	R38-222	
1059	46.389861364	-84.795520647	277.850	R38-212	
1060	46.389812314	-84.795140675	278.035	R38-312	
1061	46.390006033	-84.795022558	278.066	R38-322	
1062	46.390254894	-84.794928458	277.885	R38-332	
1063	46.390464608	-84.794827725	277.689	R38-342	
1064	46.390685453	-84.794720667	277.516	R38-352	
1065	46.390851478	-84.794634239	277.585	R38-362	
1066	46.391086333	-84.794524806	277.147	R38-372	
1067	46.391277142	-84.794463422	277.210	R38-382	
1068	46.391362403	-84.793874522	277.170	R38-482	
1069	46.391135822	-84.793959447	277.271	R38-472	
1070	46.390932669	-84.794045286	277.370	R38-462	
1071	46.390706269	-84.794187758	277.540	R38-452	
1072	46.390521025	-84.794271525	276.900	R38-442	
1073	46.390293514	-84.794358097	277.087	R38-432	
1074	46.390076908	-84.794472142	277.417	R38-422	
1075	46.389862158	-84.794580181	277.718	R38-412	
1076	46.389802475	-84.794059039	277.326	R38-512	
1077	46.390001525	-84.793913897	277.609	R38-522	
1078	46.390213992	-84.793801447	277.363	R38-532	
1079	46.390409206	-84.793743683	276.543	R38-542	
1080	46.390643928	-84.793591692	277.570	R38-552	
1081	46.390850350	-84.793438794	277.390	R38-562	
1082	46.391071264	-84.793350325	277.333	R38-572	
1083	46.391262450	-84.793248003	277.565	R38-582	
1084	46.389658639	-84.793659053	276.843	R38-bl0	
1085	46.389653581	-84.796257856	279.639	R38-bl1	
1086	46.340864353	-84.905768011	278.491	R80-11	Stand 80
1087	46.340898856	-84.906358378	277.688	R80-12	
1088	46.340901892	-84.906962819	277.804	R80-13	
1089	46.340962608	-84.907612953	277.756	R80-14	
1090	46.340600489	-84.907754861	278.331	R80-24	
1091	46.340570142	-84.907307519	278.925	R80-23	
1092	46.340560278	-84.906891783	278.904	R80-22	
1093	46.340523606	-84.906372950	279.138	R80-21	
1094	46.340255472	-84.906200339	279.267	R80-31	
1095	46.340279442	-84.906699783	279.324	R80-32	
1096	46.340322158	-84.907171717	279.122	R80-33	
1097	46.340348314	-84.907703256	278.778	R80-34	
1098	46.339919667	-84.907718475	279.028	R80-44	

```
1099 46.339957861  -84.907255611  279.110 R80-43
1100 46.340021633  -84.906807128  279.471 R80-42
1101 46.340051022  -84.906184628  279.336 R80-41

No PP infill mode measured by Rover No.1

/*================= Rover No.2 ======================================*/
RTK mode
Pnt # Latitude      Longitude     Height   Code
2000 46.367813819  -84.812976461  276.940 S61-R1   Stand 61
2001 46.367538775  -84.813256864  277.033 S61-T11
2003 46.366957700  -84.813403606  277.028 S61-T13
2004 46.366959606  -84.813406689  277.034 S61-T13
2005 46.366164253  -84.813711631  277.565 S61-T15
2006 46.366169942  -84.814388119  277.213 S61-T15
2007 46.367847589  -84.813896900  277.483 S61-R2
2008 46.367845217  -84.814411350  277.629 S61-R3
2009 46.367859342  -84.814802392  277.833 S61-R4
2010 46.367850494  -84.815340022  278.125 S61-R5
2011 46.367411161  -84.815059242  277.611 S61-T42
2012 46.367157322  -84.815114481  277.333 S61-T52

2014 46.367783572  -84.786611078  273.305 S68-R1   Stand 68
2015 46.367791731  -84.786089939  273.340 S68-R2
2016 46.367798503  -84.785581544  273.161 S68-R3
2017 46.367803117  -84.785068611  273.929 S68-R4
2018 46.367798425  -84.784539567  273.677 S68-R5
2019 46.368418719  -84.784632419  274.303 S68-T51
2020 46.368414850  -84.784629156  273.282 S68-T51
2021 46.369071008  -84.784691983  273.143 S68-T52
2022 46.369512683  -84.784717133  274.117 S68-T53
2023 46.369277558  -84.784869981  272.761 S68-T54
2025 46.369436500  -84.786126814  273.654 S68-T45
2026 46.369444392  -84.786620183  273.580 S68-T35
2027 46.369376408  -84.787182458  274.931 S68-T25
2028 46.368768047  -84.787050372  275.052 S68-T32
2029 46.368676894  -84.786991508  272.730 S68-T31
2030 46.368651675  -84.786410053  273.519 S68-T21
2031 46.368747019  -84.785859956  272.979 S68-T22
2032 46.368739253  -84.785120672  273.047 S68-T23
2033 46.356350897  -84.803821389  274.302 AIR-001 just for checking

No PP infill mode measured by Rover No.2
```

GCP measurement
May 22(Thursday) Raco area Day #4

The data are WGS coordinate.
Base Station
Pnt # Latitude Longitude Height Code
3002,46.3881731700,-84.8031762400,278.946,BASE10A

/*================= Rover No.1 ====================================*/
RTK mode

Pnt #	Latitude	Longitude	Height	Code	
1000	46.388173172	-84.803176236	278.946	R8	
1001	46.388166236	-84.803181056	278.938	R8-CHECK	
1002	46.382977881	-84.807120883	273.131	R66-11	Stand 66
1003	46.382977933	-84.807120892	273.635	R66-112	
1004	46.383351053	-84.807208094	274.095	R66-12	
1005	46.383802664	-84.807285931	273.528	R66-13	
1006	46.384324011	-84.807254783	273.886	R66-14	
1007	46.384126281	-84.807694833	273.190	R66-24	
1008	46.383911286	-84.807682567	272.555	R66-23	
1009	46.383667886	-84.807757156	272.101	R66-22.9	
1010	46.383421642	-84.807834303	272.387	R66-22.3	
1011	46.383188706	-84.807929464	272.695	R66-25	
1012	46.382978575	-84.807938097	273.046	R66-26	
1013	46.382792661	-84.807895261	272.503	R66-27	
1014	46.382948294	-84.808358242	272.113	R66-41	
1015	46.383137072	-84.808178281	272.584	R66-42	
1016	46.383347686	-84.808017217	272.193	R66-43	
1017	46.383554844	-84.807833181	272.358	R66-44	
1018	46.383751947	-84.807661597	272.549	R66-45	
1019	46.383922425	-84.807499028	273.542	R66-46	
1020	46.384081192	-84.807387072	274.037	R66-47	
1021	46.384262981	-84.807244036	273.978	R66-48	
1022	46.384116369	-84.806909236	274.901	R66-38	
1023	46.383932647	-84.807043806	274.192	R66-37	
1024	46.383778628	-84.807175783	273.538	R66-36	
1025	46.383595239	-84.807294456	273.327	R66-35	
1026	46.383386392	-84.807483767	273.329	R66-34	
1027	46.383195089	-84.807615903	273.154	R66-33	
1028	46.383026636	-84.807744708	272.986	R66-32	
1029	46.382845403	-84.807836383	272.552	R66-31	
1030	46.398455031	-84.795589928	281.691	R55-11	Stand 55
1031	46.398676514	-84.795176511	281.377	R55-12	
1032	46.398904494	-84.794775864	281.526	R55-13	
1033	46.399215561	-84.794534700	280.996	R55-14	
1034	46.399607292	-84.794845378	280.100	R55-24	
1035	46.399377392	-84.795316981	280.923	R55-23	
1036	46.399239753	-84.795645567	281.301	R55-22	
1037	46.399109081	-84.796099161	281.420	R55-21	
1038	46.399294797	-84.796416011	281.740	R55-31	
1039	46.399468872	-84.796112136	281.217	R55-32	
1040	46.399741500	-84.795581458	281.090	R55-33	
1041	46.399909403	-84.795213953	279.879	R55-34	
1042	46.400113900	-84.795537344	280.331	R55-44	

```
1043 46.399919100  -84.795876806  281.364 R55-43
1044 46.399730617  -84.796282606  281.571 R55-42
1045 46.399546383  -84.796595486  281.639 R55-41
1046 46.399702561  -84.796989983  281.992 R55-51

PP infill mode
Pnt #  Latitude       Longitude   Height  Code
1047,46.4048937315,-84.7386432491,271.272,R69-11 Stand 69
1048,46.4049365707,-84.7383223638,271.287,R69-12
1049,46.4047676075,-84.7379993578,271.927,R69-13
1050,46.4055185944,-84.7382674861,178.112,R69-14 Not Good. Memory was full
1051,46.4049030472,-84.7384378667,227.756,R69-15 Not Good. Memory was full
1052,46.4054099000,-84.7384945694,341.713,R69-17 Not Good. Memory was full
1053,46.4057799194,-84.7381197528,249.478,R69-18 Not Good. Memory was full


/*================= Rover No.2 ====================================*/
RTK mode
Pnt #  Latitude       Longitude   Height  Code
2000 46.356348533  -84.803822056  274.356 AIR001 just for checking
2001 46.390223167  -84.765548475  274.429 S71-T11 Stand 71
2002 46.390194797  -84.765147622  272.827 S71-T21
2003 46.390215258  -84.764702297  272.162 S71-T31
2004 46.390183361  -84.763911497  272.069 S71-T41
2005 46.390283386  -84.763241019  273.058 S71-T51
2007 46.390746569  -84.763620067  272.409 S71-T52
2008 46.390911217  -84.765158344  272.135 S71-T22
2009 46.390762506  -84.766047581  275.468 S71-T12
2010 46.391341567  -84.766071275  274.738 S71-T13
2011 46.391439022  -84.765572256  272.299 S71-T23
2012 46.391597147  -84.763916400  272.245 S71-T53

2013 46.389923261  -84.762884100  273.479 S72-T11 Stand 72
2014 46.389964342  -84.762104206  273.053 S72-T31
2015 46.389974114  -84.761145825  272.680 S72-T51
2016 46.390406753  -84.761218017  275.077 S72-T52
2017 46.390316242  -84.762203517  274.749 S72-T22
2018 46.390694903  -84.762436144  274.913 S72-T23
2019 46.391101447  -84.762864014  272.734 S72-T24
2020 46.391200369  -84.761974664  272.160 S72-T34
2021 46.391426872  -84.760631175  273.924 S72-T44
2022 46.391803644  -84.760716350  271.040 S72-T45
2023 46.392210481  -84.760845792  272.423 S72-T46
2024 46.392194483  -84.761957697  272.435 S72-T26

2025 46.391111836  -84.755114625  274.096 S40-T11 Stand 40
2026 46.390988736  -84.754577050  274.374 S40-T21
2027 46.391564658  -84.754977950  272.450 S40-T23
2028 46.391555519  -84.754448842  272.871 S40-T33
2029 46.391556806  -84.753937856  272.918 S40-T43
2030 46.391549497  -84.753373394  272.982 S40-T53
2031 46.391648186  -84.752932339  273.744 S40-T63
2032 46.391752728  -84.752380517  274.171 S40-T73
2033 46.391781081  -84.751774747  274.685 S40-T83
2034 46.391238889  -84.751523853  274.721 S40-T82
2035 46.390324272  -84.751265589  274.390 S40-T81
```

2036 46.390388747 -84.751728369 273.930 S40-T71
2037 46.390575847 -84.752711903 273.748 S40-T61
2038 46.390791981 -84.753706117 274.284 S40-T51
2039 46.390976528 -84.754567169 274.471 S40-T41

PP infill mode
Pnt # Latitude Longitude Height Code
2040,46.4042942552,-84.7392223628,272.399,R21A GCP "R21" No.1
2041,46.4044018162,-84.7392304077,272.365,R21B GCP "R21" No.2
2042,46.4043883303,-84.7391176508,272.431,R21C GCP "R21" No.3
2043,46.4042878505,-84.7391207019,272.440,R21D GCP "R21" No.4
2044,46.4041332027,-84.7391172883,272.454,R21E GCP "R21" No.5
2045,46.4040676061,-84.7391176308,272.468,R21F GCP "R21" No.6
2046,46.4040730130,-84.7392110507,272.476,R21G GCP "R21" No.7
2047,46.4041331362,-84.7392097999,272.479,R21H GCP "R21" No.8
2048,46.4040949452,-84.7391640552,272.561,R21I GCP "R21" No.9
2049,46.4043478102,-84.7391624788,272.504,R21J GCP "R21" No.10
2050,46.3696386596,-84.7392186814,202.125,R18A Not Good. Memory was full
2051,46.3692960958,-84.7388804146,199.837,R18B Not Good. Memory was full
2052,46.3692526867,-84.7388282896,154.804,R18C Not Good. Memory was full
2053,46.3692066236,-84.7391163874,174.292,R18D Not Good. Memory was full
2054,46.3753719534,-84.7389104231,204.387,R19A Not Good. Memory was full
2055,46.3750873072,-84.7388523601,196.343,R19E Not Good. Memory was full
2056,46.3751883760,-84.7387607832,197.745,R19B Not Good. Memory was full
2057,46.3751714324,-84.7390817597,268.893,R19C Not Good. Memory was full
2058,46.3750818698,-84.7387220582,212.382,R19D Not Good. Memory was full
2059,46.3896185989,-84.7391013943,263.278,R20E Not Good. Memory was full
2060,46.3898563539,-84.7392369441,243.927,R20A Not Good. Memory was full
2061,46.3898819871,-84.7391537674,277.634,R20B Not Good. Memory was full
2062,46.3897391906,-84.7391128107,291.512,R20C Not Good. Memory was full
2063,46.3896612350,-84.7391497828,276.082,R20D Not Good. Memory was full
2064,46.3897006541,-84.7390836882,242.232,R20D Not Good. Memory was full

GCP measurement
May 23(Friday) Raco area Day #5

The data are WGS coordinate.
Base Station
Pnt # North East Height Code
3001,46.3563470300,-84.8038237000,274.367,AIR001

/*================= Rover No.1 ====================================*/
No RTK mode measurement was done by Rover No.2

PP infill mode
Pnt # Latitude Longitude Height Code
1000,46.4365839577,-84.9187931110,255.337,R45-11 Stand 45
1001,46.4366218777,-84.9184608646,255.601,R45-12
1002,46.4374355212,-84.9176143379,255.150,R45-13
1003,46.4372892501,-84.9174154600,254.983,R45-23
1004,46.4372894440,-84.9174157271,255.543,R45-23
1005,46.4369403120,-84.9171518857,255.732,R45-33
1006,46.4365483460,-84.9170620612,255.869,R45-32
1007,46.4365480911,-84.9175889154,255.826,R45-33
1008,46.4365978184,-84.9180329024,255.833,R45-34
1009,46.4366627572,-84.9183520006,255.699,R45-35
1010,46.4362817201,-84.9184352662,255.268,R45-41
1011,46.4360954328,-84.9180471209,255.561,R45-42
1012,46.4362133052,-84.9175049734,255.493,R45-43
1013,46.4362134354,-84.9175049825,255.487,R45-43
1014,46.4362293337,-84.9169745528,255.944,R45-44
1015,46.4360253642,-84.9170291355,255.799,R45-54
1016,46.4358002985,-84.9173617144,256.713,R45-53

1017,46.4297585419,-84.9076556245,276.400,S34-11 Stand 34
1018,46.4297583075,-84.9076557435,268.706,S34-11
1019,46.4283677891,-84.9085358781,270.109,S34-18
1020,46.4300459221,-84.9096448955,269.077,S34-3
1021,46.4295527084,-84.9100049274,197.634,S34-54 Not Good. Memory was full
1022,46.4291308060,-84.9102622806,242.284,S34-54 Not Good. Memory was full

/*================= Rover No.2 ====================================*/
No RTK mode measurement was done by Rover No.2

PP infill mode
Pnt # Latitude Longitude Height Code
2000,46.4339206424,-84.9060179304,256.163,S31-R1 Stand 31
2001,46.4339082715,-84.9050283954,256.342,S31-T1
2002,46.4327372279,-84.9046723278,256.645,S31-T2
2003,46.4324554032,-84.9060329670,257.515,S31-R5

2004,46.4309067575,-84.9012592083,257.559,S49-BASE1 Stand 49
2005,46.4303569257,-84.9017260754,259.287,S49-BASE2
2006,46.4305381461,-84.9011065354,259.541,S49-T11
2007,46.4303660329,-84.9010633171,258.197,S49-T12
2008,46.4302623675,-84.9005200489,205.246,S49-T13
2009,46.4300308731,-84.9009847520,259.731,S49-T23

2010,46.4298352713,-84.9011805030,261.339,S49-T24
2011,46.4297100957,-84.9011904800,262.448,S49-T25
2012,46.4296476971,-84.9012287543,263.229,S49-T35
2013,46.4295384146,-84.9013181699,263.618,S49-T45
2014,46.4296505475,-84.9014200266,263.711,S49-T46
2015,46.4297327994,-84.9013710273,262.966,S49-T35
2016,46.4297933404,-84.9014471757,262.133,S49-T36
2017,46.4299891044,-84.9016304519,261.663,S49-T34
2018,46.4300136680,-84.9017078434,261.811,S49-T33
2019,46.4300791292,-84.9017117465,260.945,S49-T32
2020,46.4301459191,-84.9017549974,260.450,S49-T331
2021,46.4302067742,-84.9017837576,260.139,S49-T31
2022,46.4300712672,-84.9020575414,261.314,S49-T3ROAD
2023,46.4297600451,-84.9022895670,263.478,S49-T41
2024,46.4296037331,-84.9022320765,263.931,S49-T42
2025,46.4296432952,-84.9019489311,263.854,S49-T43
2026,46.4295179658,-84.9017728642,263.967,S49-T44

GCP measurement
May 24(Saturday) Raco area Day #6

The data are WGS coordinate.
Base Station

Pnt #	Latitude	Longitude	Height	Code	
3001	46.429762561	-84.906136458	266.469	R22-AT-CORNER	located at Mc Nearney Lake
5001	46.358937600	-84.845666433	280.746	RJ0241	located at Raco
6001	46.187288400	-84.562248133	204.000	RJ1102	located at Rudyard

/*================= Rover No.1 ====================================*/
RTK mode

Pnt #	Latitude	Longitude	Height	Code	
1000	46.431094403	-84.910565575	268.339	R33-11	Stand 33
1001	46.431391442	-84.911817011	269.639	R33-31	
1002	46.431715600	-84.912801706	269.574	R33-51	
1003	46.431896214	-84.912336172	269.344	R33-53	
1004	46.432338517	-84.912333939	269.554	R33-58	
1005	46.431849892	-84.911089378	268.382	R33-34	
1006	46.431998686	-84.910379150	267.223	R33-18	

1020	46.230411150	84.571541517	210.555	IT33-1	GCP "R33" No.1 (Rudyard area)
1021	46.230394158	84.571827400	210.142	IT33-2	Not Good. (by Yi-Cheng)
1022	46.230559117	84.571815422	210.235	IT33-3	Not Good. (by Yi-Cheng)
1023	46.230559069	84.571815319	210.620	IT33-32	GCP "R33" No.2 (Rudyard area)
1024	46.230559042	84.571612122	210.558	IT33-42	GCP "R33" No.3 (Rudyard area)
1025	46.230471825	84.550923908	209.141	IT34-1	GCP "R34" No.1 (Rudyard area)
1026	46.230474958	84.550780092	209.158	IT34-2	GCP "R34" No.2 (Rudyard area)
1027	46.230584964	84.550770667	209.170	IT34-3	GCP "R34" No.3 (Rudyard area)

PP infill mode

Pnt #	Latitude	Longitude	Height	Code	
1007,	46.3942790996,	-84.9706821837,	278.604,	R85-1	Stand 85
1008,	46.3694893633,	-84.7388115976,	259.044,	IT-1	GCP "R18" No.1
1009,	46.3694390760,	-84.7390001988,	259.091,	IT-2	GCP "R18" No.2
1010,	46.3693180115,	-84.7388104672,	258.946,	IT-3	GCP "R18" No.3
1011,	46.3732296627,	-84.7390470582,	259.416,	IT19-1	GCP "R19" No.1
1012,	46.3733355559,	-84.7390545540,	259.473,	IT19-2	GCP "R19" No.2
1013,	46.3733039973,	-84.7389944168,	259.513,	IT19-3	GCP "R19" No.3
1014,	46.3896860152,	-84.7390268249,	266.384,	IT20-1	GCP "R20" No.1
1015,	46.3896005033,	-84.7390261682,	266.409,	IT20-2	GCP "R20" No.2
1016,	46.3895905163,	-84.7391350773,	266.300,	IT20-3	GCP "R20" No.3
1017,	46.3751789172,	-84.7809876803,	275.045,	IT31-1	GCP "R31" No.1
1018,	46.3751902311,	-84.7808610433,	274.628,	IT31-2	GCP "R31" No.2
1019,	46.3752989637,	-84.7808818752,	274.445,	IT31-3	GCP "R31" No.3

/*================= Rover No.2 ====================================*/
RTK mode

Pnt #	Latitude	Longitude	Height	Code	
2000	46.426453714	-84.900390139	268.155	S50-T1	Stand 50
2001	46.426775761	-84.899897294	266.754	S50-T12	
2002	46.427709986	-84.898846422	264.892	S50-T13	

```
2003 46.427754147  -84.898418281  264.534 S50-T23
2004 46.425699444  -84.898554119  268.047 S50-R4
2005 46.425727914  -84.899038236  268.416 S50-R4A
2006 46.425772539  -84.899008414  268.635 S50-R4B
2007 46.425977581  -84.899728903  267.909 S50-R3
2019 46.358734100  -84.829831186  278.615 R10NEAR  GCP "R10Near"
2020 46.375215489  -84.833054431  283.468 R10E     Center of intersection "R10"
2021 46.356631278  -84.893252253  282.384 R30      GCP "R30"
2022 46.358503917  -84.893683442  281.662 R6       GCP "R6"
2023 46.367233003  -84.893898458  277.844 R78      GCP "R7" No.1
2024 46.367112186  -84.893884428  276.955 R78E     GCP "R7" No.2
2025 46.351503847  -84.905825956  275.119 R24      GCP "R24"

PP infill mode
Pnt #  Latitude       Longitude   Height  Code
2008,46.4549477881,-84.9058569749,205.738,R11F          GCP "R11" No.1
2009,46.4549553575,-84.9059144442,205.665,R11E          GCP "R11" No.2 (Center)
2010,46.4555509192,-84.9059012910,204.829,R11NEAR1      Near "R11"
2011,46.4569101202,-84.9058848591,205.425,R11NEAR-HILL1 Near "R11"
2012,46.4586133798,-84.9058626065,205.821,CRYDERMAN1    GCP "R40"
2013,46.4649589117,-84.9058862222,185.549,CORNER-LAKE   GCP "R41"
2014,46.4730625042,-84.9573431082,213.650,R12A          GCP "R12" No.1
2015,46.4731295504,-84.9569849900,214.061,R12B          GCP "R12" No.2
2016,46.4729805411,-84.9566907434,214.475,R12C          GCP "R12" No.3
2017,46.4865157492,-85.0394154128,211.261,R13A          GCP "R13" No.1
2018,46.4865525296,-85.0393407835,206.746,R13B       Not Good. (by Yutaka)
```

Appendix B: Data of Each Stand

Table B-1 shows the information on measured stands.
Figure B-1 shows location of each stand .
The detail data record is shown afterwards.
All the data are expressed on WGS coordinate.
Including the cover sheet, **appendix B** is totally 28 pages.

Table B-1 GPS measurement results at each stand (1 of 2)

Raco Area

Stand No.	Tree description 1)	Tree Mean Height (m) 1)	Mode	Measured Date	Valid point	In-valid point	GPS measured Height Average (m)	Minimun (m)	Maximum (m)	Std.dev. (m)
22	Red Pine (sa) 2)	8.74 (1994)	RTK 3)	5/19 (Mon)	5	1	275.466	274.415	276.011	0.683
38	Jack Pine(sa)	5	RTK	5/21 (Wed)	42	0	277.722	276.543	279.639	0.658
40	Red Pine (seedling)	2-3	RTK	5/22 (Thu)	15	0	273.856	272.450	274.721	0.723
54	Jack Pine(sa)	5	RTK	5/21 (Wed)	43	0	278.292	277.277	278.818	0.364
55	Jack Pine(sa)	5	RTK	5/22 (Thu)	17	0	281.186	279.879	281.992	0.589
56	Jack 2) Pine(ma)	11	RTK	5/20 (Mon)	39	0	277.042	275.205	277.710	0.540
58	Jack Pine(sa)	3	RTK	5/20 (Mon)	21	0	274.769	272.882	275.952	0.869
59	Jack Pine(sa)	6	RTK	5/20 (Mon)	40	0	275.884	275.320	276.459	0.311
61	Jack Pine(ma)	13	RTK	5/21 (Wed)	13	0	277.402	276.940	278.125	0.370
66	Jack Pine (seedling)		RTK	5/22 (Thu)	28	0	273.146	272.101	274.901	0.724
67	Jack Pine(ma)	15	Infill 3)	5/19 (Mon)	40	0	279.496	277.436	281.017	0.711
68	Red Pine (pole)	11	RTK	5/21 (Wed)	19	0	273.584	272.730	275.052	0.667
69	Aspen (sa)	6	Infill	5/22 (Thu)	3	4	271.495	271.272	271.927	0.374
71	Red Pine (pole)	11	RTK	5/22 (Thu)	12	0	273.076	272.069	275.468	1.219
72	Red Pine (pole)	14	RTK	5/22 (Thu)	12	0	273.222	271.040	275.077	1.239
80	Red Pine (seedling)	2-3	RTK	5/21 (Wed)	16	0	278.780	277.688	279.471	0.592

Remark 1) Tree description and tree mean height information are acquired from the following reference.
"Structure, Composition, and Above-ground Biomass of SIR-C/X- SAR and ERS-1 Forest Test Stands 1991-1994, Raco Michigan Site"
Kathleen M.Bergen, M.Craig Dobson, Terry L.Sharik, Ian Brodie
October 30,1995 , Report 026511-7-T

Remark 2) The meanings of abbreviation are shown below.
(ma): mature
(sa): sapling

Remark 3) The meanings of abbreviation are shown below.
(RTK): realtime kinematic mode
(Infill): postprocessing infill mode

Table B-1 GPS measurement results at each stand (2 of 2)

Mc Nearney Lake area

Stand No.	Tree description 1)	Tree Mean Height (m) 1)	Mode	Measured Date	Valid point	Invalid point	GPS measured Height Average (m)	Minimum (m)	Maximum (m)	Std.dev
31	Hardwood (ma) 2)	18	Infill 3)	5/23 (Fri)	4	0	256.666	256.163	257.515	0.600
33	Aspen(sa) 2)	12	3)RTK	5/24 (Sat)	7	0	268.865	267.223	269.639	0.914
34	Hardwood (ma)	20	Infill	5/23 (Fri)	4	2	271.073	268.706	276.400	3.601
45	Aspen(sa)	3	Infill	5/23 (Fri)	17	0	255.638	254.983	256.713	0.385
49	Aspen(sa)	6	Infill	5/23 (Fri)	22	1	261.605	257.559	263.967	1.937
50	Red Pine (ma)	16	RTK	5/24 (Sat)	8	0	267.168	264.534	268.635	1.617
85	Hardwood (ma)	15	Infill	5/24 (Sat)	1	0	278.604	278.604	278.604	0.000

Remark 1) Tree description and tree mean height information are acquired from the following reference.
"Structure, Composition, and Above-ground Biomass of SIR-C/X- SAR and ERS-1 Forest Test Stands 1991-1994, Raco Michigan Site"
Kathleen M.Bergen, M.Craig Dobson, Terry L.Sharik, Ian Brodie
October 30,1995 , Report 026511-7-T

Remark 2) The meanings of abbreviation are shown below.
(ma): mature
(sa): sapling

Remark 3) The meanings of abbreviation are shown below.
(RTK): realtime kinematic mode
(Infill): postprocessing infill mode

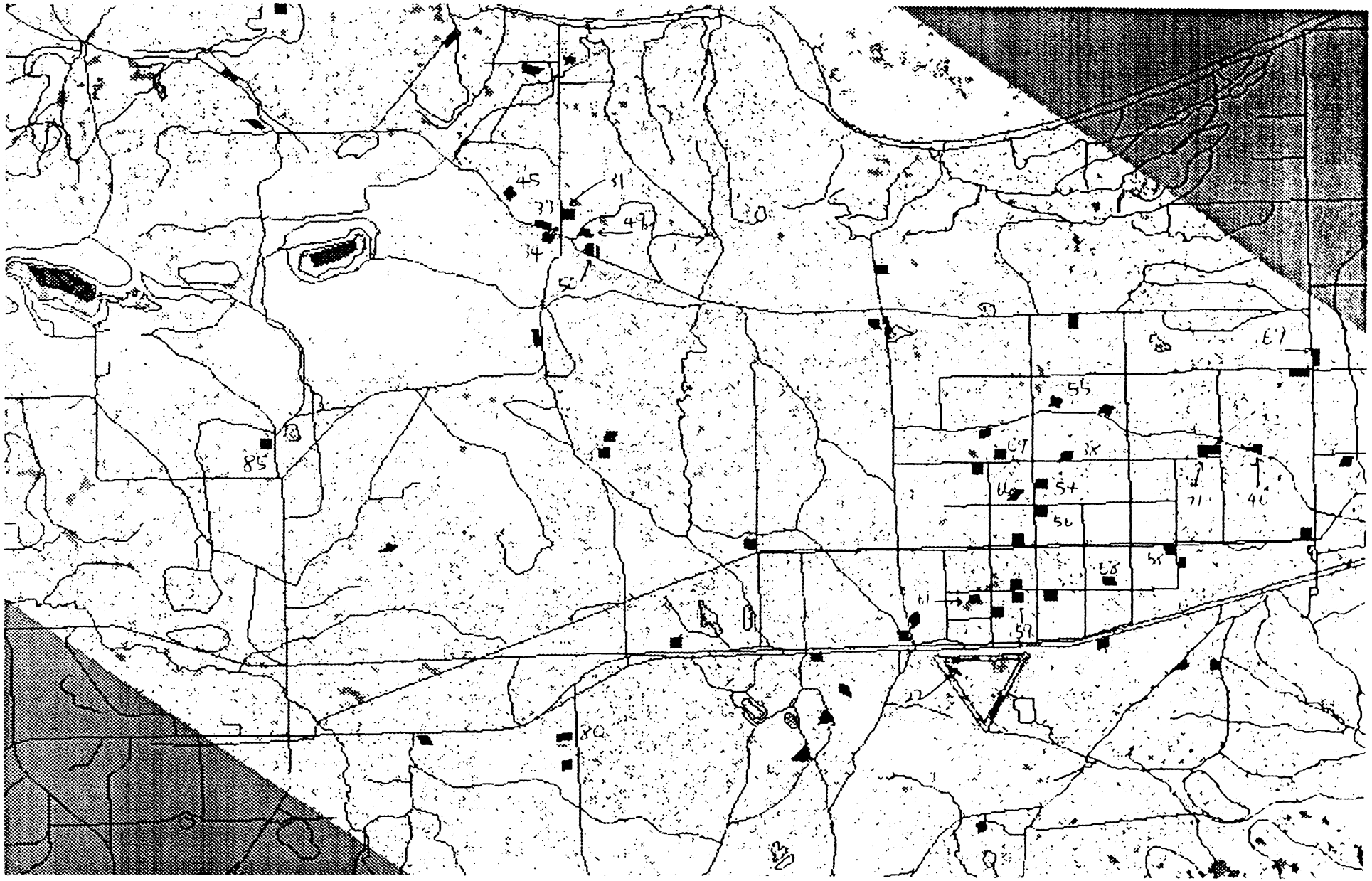

Figure B-1 Stand Location (Totally 23 stands)

GCP measurement at Stand 22
May 19(Mon) Raco area Day #1

Pnt #	Latitude	Longitude	Height	Code
2003	46.355351597	-84.822109336	276.011	S22-11
2004	46.354171394	-84.821035328	274.415	S22-51
2005	46.353626133	-84.818556731	275.137	S22-58
2006	46.354466206	-84.820438744	275.928	S22-35
2007	46.354800464	-84.819968989	275.841	S22-18

GCP measurement at Stand 31
May 23(Friday) Raco area Day #5

Pnt #	Latitude	Longitude	Height	Code
2000	46.4339206424	-84.9060179304	256.163	S31-R1
2001	46.4339082715	-84.9050283954	256.342	S31-T1
2002	46.4327372279	-84.9046723278	256.645	S31-T2
2003	46.4324554032	-84.9060329670	257.515	S31-R5

GCP measurement at Stand 33
May 24(Saturday) Raco area Day #6

Pnt #	Latitude	Longitude	Height	Code
1000	46.431094403	-84.910565575	268.339	R33-11
1001	46.431391442	-84.911817011	269.639	R33-31
1002	46.431715600	-84.912801706	269.574	R33-51
1003	46.431896214	-84.912336172	269.344	R33-53
1004	46.432338517	-84.912333939	269.554	R33-58
1005	46.431849892	-84.911089378	268.382	R33-34
1006	46.431998686	-84.910379150	267.223	R33-18

GCP measurement at Stand 34
May 23(Friday) Raco area Day #5

Pnt #	Latitude	Longitude	Height	Code
1017	46.4297585419	-84.9076556245	276.400	S34-11
1018	46.4297583075	-84.9076557435	268.706	S34-11
1019	46.4283677891	-84.9085358781	270.109	S34-18
1020	46.4300459221	-84.9096448955	269.077	S34-3

GCP measurement at Stand 38
May 21(Wed) Raco area Day #3

Pnt #	Latitude	Longitude	Height	Code
1044	46.389788078	-84.796109789	278.896	R38-112
1045	46.390036983	-84.796109189	279.268	R38-122
1046	46.390183119	-84.795913369	279.074	R38-132
1047	46.390329922	-84.795816925	278.758	R38-142
1048	46.390522706	-84.795733733	278.202	R38-152
1049	46.390733875	-84.795668756	278.271	R38-162
1050	46.391069258	-84.795546231	277.347	R38-172
1051	46.391287794	-84.795465983	277.334	R38-182
1052	46.391128256	-84.794847697	277.404	R38-272
1053	46.391361900	-84.794786933	277.260	R38-282
1054	46.390920581	-84.794960822	277.553	R38-262
1055	46.390713097	-84.795088717	277.870	R38-252
1056	46.390516894	-84.795221828	277.924	R38-242
1057	46.390290008	-84.795272328	278.026	R38-232
1058	46.390077350	-84.795438981	278.482	R38-222
1059	46.389861364	-84.795520647	277.850	R38-212
1060	46.389812314	-84.795140675	278.035	R38-312
1061	46.390006033	-84.795022558	278.066	R38-322
1062	46.390254894	-84.794928458	277.885	R38-332
1063	46.390464608	-84.794827725	277.689	R38-342
1064	46.390685453	-84.794720667	277.516	R38-352
1065	46.390851478	-84.794634239	277.585	R38-362
1066	46.391086333	-84.794524806	277.147	R38-372
1067	46.391277142	-84.794463422	277.210	R38-382
1068	46.391362403	-84.793874522	277.170	R38-482
1069	46.391135822	-84.793959447	277.271	R38-472
1070	46.390932669	-84.794045286	277.370	R38-462
1071	46.390706269	-84.794187758	277.540	R38-452
1072	46.390521025	-84.794271525	276.900	R38-442
1073	46.390293514	-84.794358097	277.087	R38-432
1074	46.390076908	-84.794472142	277.417	R38-422
1075	46.389862158	-84.794580181	277.718	R38-412
1076	46.389802475	-84.794059039	277.326	R38-512
1077	46.390001525	-84.793913897	277.609	R38-522
1078	46.390213992	-84.793801447	277.363	R38-532
1079	46.390409206	-84.793743683	276.543	R38-542
1080	46.390643928	-84.793591692	277.570	R38-552
1081	46.390850350	-84.793438794	277.390	R38-562
1082	46.391071264	-84.793350325	277.333	R38-572
1083	46.391262450	-84.793248003	277.565	R38-582
1084	46.389658639	-84.793659053	276.843	R38-bl0
1085	46.389653581	-84.796257856	279.639	R38-bl1

GCP measurement at Stand 40
May 22(Thursday) Raco area Day #4

Pnt #	Latitude	Longitude	Height	Code	
2025	46.391111836	-84.755114625	274.096	S40-T11	Stand 40
2026	46.390988736	-84.754577050	274.374	S40-T21	
2027	46.391564658	-84.754977950	272.450	S40-T23	
2028	46.391555519	-84.754448842	272.871	S40-T33	
2029	46.391556806	-84.753937856	272.918	S40-T43	
2030	46.391549497	-84.753373394	272.982	S40-T53	
2031	46.391648186	-84.752932339	273.744	S40-T63	
2032	46.391752728	-84.752380517	274.171	S40-T73	
2033	46.391781081	-84.751774747	274.685	S40-T83	
2034	46.391238889	-84.751523853	274.721	S40-T82	
2035	46.390324272	-84.751265589	274.390	S40-T81	
2036	46.390388747	-84.751728369	273.930	S40-T71	
2037	46.390575847	-84.752711903	273.748	S40-T61	
2038	46.390791981	-84.753706117	274.284	S40-T51	
2039	46.390976528	-84.754567169	274.471	S40-T41	

GCP measurement at Stand 45
May 23(Friday) Raco area Day #5

Pnt #	Latitude	Longitude	Height	Code
1000	46.4365839577	-84.9187931110	255.337	R45-11
1001	46.4366218777	-84.9184608646	255.601	R45-12
1002	46.4374355212	-84.9176143379	255.150	R45-13
1003	46.4372892501	-84.9174154600	254.983	R45-23
1004	46.4372894440	-84.9174157271	255.543	R45-23
1005	46.4369403120	-84.9171518857	255.732	R45-33
1006	46.4365483460	-84.9170620612	255.869	R45-32
1007	46.4365480911	-84.9175889154	255.826	R45-33
1008	46.4365978184	-84.9180329024	255.833	R45-34
1009	46.4366627572	-84.9183520006	255.699	R45-35
1010	46.4362817201	-84.9184352662	255.268	R45-41
1011	46.4360954328	-84.9180471209	255.561	R45-42
1012	46.4362133052	-84.9175049734	255.493	R45-43
1013	46.4362134354	-84.9175049825	255.487	R45-43
1014	46.4362293337	-84.9169745528	255.944	R45-44
1015	46.4360253642	-84.9170291355	255.799	R45-54
1016	46.4358002985	-84.9173617144	256.713	R45-53

GCP measurement at Stand 49
May 23(Friday) Raco area Day #5

Pnt #	Latitude	Longitude	Height	Code
2004	46.4309067575	-84.9012592083	257.559	S49-BASE1
2005	46.4303569257	-84.9017260754	259.287	S49-BASE2
2006	46.4305381461	-84.9011065354	259.541	S49-T11
2007	46.4303660329	-84.9010633171	258.197	S49-T12
2009	46.4300308731	-84.9009847520	259.731	S49-T23
2010	46.4298352713	-84.9011805030	261.339	S49-T24
2011	46.4297100957	-84.9011904800	262.448	S49-T25
2012	46.4296476971	-84.9012287543	263.229	S49-T35
2013	46.4295384146	-84.9013181699	263.618	S49-T45
2014	46.4296505475	-84.9014200266	263.711	S49-T46
2015	46.4297327994	-84.9013710273	262.966	S49-T35
2016	46.4297933404	-84.9014471757	262.133	S49-T36
2017	46.4299891044	-84.9016304519	261.663	S49-T34
2018	46.4300136680	-84.9017078434	261.811	S49-T33
2019	46.4300791292	-84.9017117465	260.945	S49-T32
2020	46.4301459191	-84.9017549974	260.450	S49-T331
2021	46.4302067742	-84.9017837576	260.139	S49-T31
2022	46.4300712672	-84.9020575414	261.314	S49-T3ROAD
2023	46.4297600451	-84.9022895670	263.478	S49-T41
2024	46.4296037331	-84.9022320765	263.931	S49-T42
2025	46.4296432952	-84.9019489311	263.854	S49-T43
2026	46.4295179658	-84.9017728642	263.967	S49-T44

Remark) Point #2008 is excluded because of incorrect measurement.

GCP measurement at Stand 50
May 24(Saturday) Raco area Day #6

Pnt #	Latitude	Longitude	Height	Code	
2000	46.426453714	-84.900390139	268.155	S50-T1	Stand 50
2001	46.426775761	-84.899897294	266.754	S50-T12	
2002	46.427709986	-84.898846422	264.892	S50-T13	
2003	46.427754147	-84.898418281	264.534	S50-T23	
2004	46.425699444	-84.898554119	268.047	S50-R4	
2005	46.425727914	-84.899038236	268.416	S50-R4A	
2006	46.425772539	-84.899008414	268.635	S50-R4B	
2007	46.425977581	-84.899728903	267.909	S50-R3	

GCP measurement at Stand 54
May 21(Wed) Raco area Day #3

Pnt #	Latitude	Longitude	Height	Code
1001	46.385504494	-84.801439514	278.623	R54-512
1002	46.385503156	-84.801135367	278.403	R54-522
1003	46.385483736	-84.800846850	278.283	R54-532
1004	46.385526697	-84.800592911	278.335	R54-542
1005	46.385560511	-84.800309789	278.485	R54-552
1006	46.385534781	-84.799935033	278.596	R54-562
1007	46.385575900	-84.799604081	277.816	R54-572
1008	46.385581953	-84.799320497	277.758	R54-582
1009	46.385997086	-84.799440678	277.891	R54-482
1010	46.386000525	-84.799716156	278.197	R54-472
1011	46.385976581	-84.799984422	278.171	R54-462
1012	46.385971439	-84.800298667	278.591	R54-452
1013	46.385934336	-84.800598531	278.632	R54-442
1014	46.385912131	-84.800856125	278.358	R54-432
1015	46.385869464	-84.801166189	278.731	R54-422
1016	46.385879886	-84.801516889	278.453	R54-412
1017	46.385150022	-84.801507142	278.407	R54-512
1018	46.385150239	-84.801249689	278.519	R54-522
1019	46.385162486	-84.800947769	278.182	R54-532
1020	46.385143875	-84.800654514	278.486	R54-542
1021	46.385132667	-84.800303267	278.728	R54-552
1022	46.385140600	-84.800032214	278.225	R54-562
1023	46.385147783	-84.799744192	278.376	R54-572
1024	46.385159828	-84.799412533	278.603	R54-582
1025	46.386210422	-84.801457542	278.818	R54-212
1026	46.386239714	-84.801160500	278.529	R54-222
1027	46.386231797	-84.800875278	278.539	R54-232
1028	46.386296067	-84.800557400	278.803	R54-242
1029	46.386335042	-84.800209319	278.276	R54-252
1030	46.386369461	-84.799964786	278.784	R54-262
1031	46.386380383	-84.799609989	278.452	R54-272
1032	46.386368272	-84.799263061	277.890	R54-282
1033	46.386697239	-84.799445269	278.516	R54-182
1034	46.386705694	-84.799765408	278.469	R54-172
1035	46.386682714	-84.800045892	278.264	R54-162
1036	46.386645822	-84.800314056	277.676	R54-152
1037	46.386656178	-84.800673644	277.277	R54-142
1038	46.386621808	-84.800960789	278.008	R54-132
1039	46.386511114	-84.801369583	277.762	R54-122
1040	46.386552322	-84.801523122	277.776	R54-112
1041	46.386618967	-84.801911567	277.683	R54-BL0
1042	46.384820889	-84.801858075	278.342	R54-BL1
1043	46.384820964	-84.801858122	277.836	R54-BL1

GCP measurement at Stand 55
May 22(Thursday) Raco area Day #4

Pnt #	Latitude	Longitude	Height	Code
1030	46.398455031	-84.795589928	281.691	R55-11
1031	46.398676514	-84.795176511	281.377	R55-12
1032	46.398904494	-84.794775864	281.526	R55-13
1033	46.399215561	-84.794534700	280.996	R55-14
1034	46.399607292	-84.794845378	280.100	R55-24
1035	46.399377392	-84.795316981	280.923	R55-23
1036	46.399239753	-84.795645567	281.301	R55-22
1037	46.399109081	-84.796099161	281.420	R55-21
1038	46.399294797	-84.796416011	281.740	R55-31
1039	46.399468872	-84.796112136	281.217	R55-32
1040	46.399741500	-84.795581458	281.090	R55-33
1041	46.399909403	-84.795213953	279.879	R55-34
1042	46.400113900	-84.795537344	280.331	R55-44
1043	46.399919100	-84.795876806	281.364	R55-43
1044	46.399730617	-84.796282606	281.571	R55-42
1045	46.399546383	-84.796595486	281.639	R55-41
1046	46.399702561	-84.796989983	281.992	R55-51

GCP measurement at Stand 56
May 20(Tue) Raco area Day #2

Pnt #	Latitude	Longitude	Height	Code
1047	46.381754772	-84.801591100	276.520	R56-112
1048	46.381727869	-84.801276542	275.765	R56-122
1049	46.381775167	-84.801019625	275.205	R56-132
1050	46.381774139	-84.800695314	275.319	R56-142
1051	46.381820583	-84.800283914	277.078	R56-152
1052	46.381824156	-84.799756797	277.343	R56-172
1053	46.381817558	-84.799516517	277.346	R56-182
1054	46.381453267	-84.799394472	277.438	R56-128
1055	46.381447494	-84.799661258	277.330	R56-272
1056	46.381444344	-84.799979831	277.041	R56-262
1057	46.381487336	-84.800279100	276.761	R56-252
1058	46.381418861	-84.800599967	276.757	R56-242
1059	46.381402597	-84.800885431	276.709	R56-232
1060	46.381390578	-84.801252661	277.066	R56-222
1061	46.381399756	-84.801471064	277.307	R56-212
1062	46.381040956	-84.801323078	276.899	R56-312
1063	46.381069522	-84.800996819	276.936	R56-322
1064	46.381117000	-84.800802831	276.956	R56-332
1065	46.381095117	-84.800336811	277.131	R56-342
1066	46.381101233	-84.800076058	277.140	R56-352
1067	46.381084858	-84.799773853	277.180	R56-362
1068	46.381106006	-84.799424650	277.357	R56-372
1069	46.381110975	-84.799053322	277.710	R56-382
1070	46.380703642	-84.799381139	277.522	R56-482
1071	46.380688039	-84.799826900	277.263	R56-472
1072	46.380718872	-84.800131686	277.267	R56-462
1073	46.380698569	-84.800529686	277.323	R56-452
1074	46.380678775	-84.800708064	277.558	R56-42
1075	46.380660481	-84.801010111	277.259	R56-422
1076	46.380692603	-84.801297406	277.173	R56-422
1077	46.380716006	-84.801567478	277.321	R56-412
1078	46.380301953	-84.801541378	277.242	R56-512
1079	46.380306083	-84.801314550	277.083	R56-522
1081	46.380284794	-84.800649306	277.248	R56-542
1082	46.380322958	-84.800381447	277.271	R56-552
1083	46.380300125	-84.800170539	277.420	R56-562
1084	46.380268908	-84.799888894	277.099	R56-572
1085	46.380265614	-84.799541300	277.264	R56-582

GCP measurement at Stand 58
May 20(Tue) Raco area Day #2

Pnt #	Latitude	Longitude	Height	Code
1009	46.373175500	-84.770793531	275.514	S58INIT POINTA
1010	46.373175528	-84.770793528	275.495	S58INIT POINTB
1011	46.373207139	-84.771116314	275.252	S58-02
1012	46.373248633	-84.771399819	275.353	S58-03
1013	46.373656881	-84.770914731	275.952	S58-21
1014	46.373723114	-84.771218011	275.377	S58-22
1015	46.373811353	-84.771512831	275.507	S58-23
1016	46.373955225	-84.771633875	275.389	S58-24
1017	46.373891192	-84.771819656	275.171	S58-24
1018	46.374025064	-84.772070636	274.929	S58-25
1019	46.374125456	-84.772357878	274.152	S58-26
1020	46.374254747	-84.772626692	273.309	S58-27
1021	46.374341083	-84.770855900	275.193	S58-41
1022	46.374405289	-84.771090567	275.187	S58-42
1023	46.374537864	-84.771347869	274.912	S58-43
1024	46.374728978	-84.771534067	274.194	S58-44
1025	46.374911622	-84.771728556	273.218	S58-45
1026	46.375153150	-84.771707106	272.882	S58-R5
1027	46.375154547	-84.771377011	273.621	S58-R4
1028	46.375147022	-84.771048308	274.621	S58-R3
1029	46.375143825	-84.770715694	274.917	S58-R2

GCP measurement at Stand 59
May 20(Tue) Raco area Day #2

Pnt #	Latitude	Longitude	Height	Code
1006	46.367859906	-84.805234450	275.974	R59TEST
1007	46.367592900	-84.805231686	276.150	R59-112
1008	46.367382475	-84.805204844	275.971	R59-122
1009	46.367132597	-84.805103519	276.226	R59-132
1010	46.366978833	-84.804928961	275.749	R59-142
1011	46.366830272	-84.804683567	275.561	R59-152
1012	46.366711428	-84.804417706	275.486	R59-162
1013	46.366592236	-84.804147569	275.362	R59-172
1014	46.366569769	-84.803842072	275.480	R59-182
1015	46.366266639	-84.804098531	275.320	R59-282
1016	46.366438761	-84.804297275	275.381	R59-272
1017	46.366399100	-84.804613814	275.425	R59-262
1018	46.366451444	-84.804949319	275.555	R59-252
1019	46.366455650	-84.805261608	275.679	R59-242
1020	46.366452578	-84.805576981	276.019	R59-232
1021	46.366460256	-84.805899608	275.934	R59-222
1022	46.366428572	-84.806211783	276.098	R59-212
1023	46.366591547	-84.806216175	276.075	R59-362
1024	46.366652681	-84.806620786	276.082	R59-352
1025	46.366637300	-84.806959483	276.326	R59-342
1026	46.366679486	-84.807268811	276.459	R59-332
1027	46.366727250	-84.807577419	276.299	R59-322
1028	46.366768269	-84.807894933	276.352	R59-312
1029	46.367554586	-84.807303108	273.035	R59-512
1030	46.367380450	-84.806302281	275.736	R59-522
1031	46.366949694	-84.806265497	276.068	R59-532
1032	46.366742656	-84.806250047	275.976	R59-533
1033	46.366595133	-84.806218267	276.117	R59-542
1034	46.366392569	-84.806179744	276.069	R59-552
1035	46.366227781	-84.806186386	276.253	R59-562
1036	46.366012044	-84.806109253	276.195	R59-572
1037	46.365798122	-84.806025161	276.012	R59-582
1038	46.366019486	-84.804992633	275.695	R59-382
1039	46.366252017	-84.805136383	275.791	R59-372
1040	46.366452269	-84.805258064	275.652	R59-362
1041	46.366642639	-84.805354239	275.639	R59-352
1042	46.366894772	-84.805420578	275.465	R59-342
1043	46.367089233	-84.805370764	275.960	R59-332
1044	46.367307589	-84.805331878	275.841	R59-322
1045	46.367514544	-84.805241700	276.036	R59-312

GCP measurement at Stand 61
May 21(Wed) Raco area Day #3

Pnt #	Latitude	Longitude	Height	Code
2000	46.367813819	-84.812976461	276.940	S61-R1
2001	46.367538775	-84.813256864	277.033	S61-T11
2003	46.366957700	-84.813403606	277.028	S61-T13
2004	46.366959606	-84.813406689	277.034	S61-T13
2005	46.366164253	-84.813711631	277.565	S61-T15
2006	46.366169942	-84.814388119	277.213	S61-T15
2007	46.367847589	-84.813896900	277.483	S61-R2
2008	46.367845217	-84.814411350	277.629	S61-R3
2009	46.367859342	-84.814802392	277.833	S61-R4
2010	46.367850494	-84.815340022	278.125	S61-R5
2011	46.367411161	-84.815059242	277.611	S61-T42
2012	46.367157322	-84.815114481	277.333	S61-T52

GCP measurement at Stand 66
May 22(Thursday) Raco area Day #4

Pnt #	Latitude	Longitude	Height	Code
1002	46.382977881	-84.807120883	273.131	R66-11
1003	46.382977933	-84.807120892	273.635	R66-112
1004	46.383351053	-84.807208094	274.095	R66-12
1005	46.383802664	-84.807285931	273.528	R66-13
1006	46.384324011	-84.807254783	273.886	R66-14
1007	46.384126281	-84.807694833	273.190	R66-24
1008	46.383911286	-84.807682567	272.555	R66-23
1009	46.383667886	-84.807757156	272.101	R66-22.9
1010	46.383421642	-84.807834303	272.387	R66-22.3
1011	46.383188706	-84.807929464	272.695	R66-25
1012	46.382978575	-84.807938097	273.046	R66-26
1013	46.382792661	-84.807895261	272.503	R66-27
1014	46.382948294	-84.808358242	272.113	R66-41
1015	46.383137072	-84.808178281	272.584	R66-42
1016	46.383347686	-84.808017217	272.193	R66-43
1017	46.383554844	-84.807833181	272.358	R66-44
1018	46.383751947	-84.807661597	272.549	R66-45
1019	46.383922425	-84.807499028	273.542	R66-46
1020	46.384081192	-84.807387072	274.037	R66-47
1021	46.384262981	-84.807244036	273.978	R66-48
1022	46.384116369	-84.806909236	274.901	R66-38
1023	46.383932647	-84.807043806	274.192	R66-37
1024	46.383778628	-84.807175783	273.538	R66-36
1025	46.383595239	-84.807294456	273.327	R66-35
1026	46.383386392	-84.807483767	273.329	R66-34
1027	46.383195089	-84.807615903	273.154	R66-33
1028	46.383026636	-84.807744708	272.986	R66-32
1029	46.382845403	-84.807836383	272.552	R66-31

GCP measurement at Stand 67
May 19(Mon) Raco area Day #1

Pnt #	Latitude	Longitude	Height	Code
1001	46.3901153567	-84.8102929206	278.472	R67-122
1002	46.3903320207	-84.8102212677	279.217	R67-132
1003	46.3905563080	-84.8101885853	279.238	R67-142
1004	46.3907785626	-84.8102541785	279.241	R67-152
1005	46.3910944753	-84.8103553184	279.696	R67-162
1006	46.3913078929	-84.8104376751	279.095	R67-172
1007	46.3915762219	-84.8104398255	279.219	R67-182
1008	46.3917080041	-84.8099755002	280.514	R67-282
1009	46.3914887362	-84.8099043301	279.745	R67-272
1010	46.3912710794	-84.8098207622	279.936	R67-262
1011	46.3909702621	-84.8097178568	281.017	R67-252
1012	46.3905140327	-84.8098087827	279.603	R67-242
1013	46.3902935312	-84.8098721003	279.640	R67-232
1014	46.3900423730	-84.8098969017	279.033	R67-222
1015	46.3898230162	-84.8098215379	278.831	R67-212
1016	46.3897977728	-84.8093393276	278.973	R67-312
1017	46.3900217497	-84.8093710389	279.341	R67-322
1018	46.3902453046	-84.8093827462	279.783	R67-332
1019	46.3905503042	-84.8093388985	280.496	R67-342
1020	46.3907776197	-84.8092989739	280.324	R67-352
1021	46.3909922274	-84.8092192219	279.618	R67-362
1022	46.3912179216	-84.8091899876	279.160	R67-372
1023	46.3914723283	-84.8091766301	279.449	R67-382
1024	46.3914269833	-84.8086793304	279.182	R67-482
1025	46.3912050421	-84.8087161767	278.690	R67-472
1026	46.3909750806	-84.8087802228	279.071	R67-462
1027	46.3906693470	-84.8087550522	280.309	R67-452
1028	46.3903209758	-84.8087292940	280.636	R67-442
1029	46.3900917064	-84.8087105046	279.835	R67-432
1030	46.3898614454	-84.8086914054	280.072	R67-422
1031	46.3900171706	-84.8082189129	280.365	R67-512
1032	46.3901973896	-84.8082417540	280.423	R67-522
1033	46.3904010544	-84.8082495966	280.007	R67-532
1034	46.3905863191	-84.8082545052	279.435	R67-542
1035	46.3908177930	-84.8082667713	278.632	R67-552
1036	46.3910184144	-84.8082729834	278.514	R67-562
1037	46.3911883484	-84.8082880742	279.009	R67-572
1038	46.3914748533	-84.8082972707	279.624	R67-582
1039	46.3895566138	-84.8081602981	278.969	R67-ROAD-5
1040	46.3895728339	-84.8102629235	277.436	R67-ROAD-1

GCP measurement at Stand 68
May 21(Wed) Raco area Day #3

Pnt #	Latitude	Longitude	Height	Code
2014	46.367783572	-84.786611078	273.305	S68-R1
2015	46.367791731	-84.786089939	273.340	S68-R2
2016	46.367798503	-84.785581544	273.161	S68-R3
2017	46.367803117	-84.785068611	273.929	S68-R4
2018	46.367798425	-84.784539567	273.677	S68-R5
2019	46.368418719	-84.784632419	274.303	S68-T51
2020	46.368414850	-84.784629156	273.282	S68-T51
2021	46.369071008	-84.784691983	273.143	S68-T52
2022	46.369512683	-84.784717133	274.117	S68-T53
2023	46.369277558	-84.784869981	272.761	S68-T54
2025	46.369436500	-84.786126814	273.654	S68-T45
2026	46.369444392	-84.786620183	273.580	S68-T35
2027	46.369376408	-84.787182458	274.931	S68-T25
2028	46.368768047	-84.787050372	275.052	S68-T32
2029	46.368676894	-84.786991508	272.730	S68-T31
2030	46.368651675	-84.786410053	273.519	S68-T21
2031	46.368747019	-84.785859956	272.979	S68-T22
2032	46.368739253	-84.785120672	273.047	S68-T23

GCP measurement at Stand 69
May 22(Thursday) Raco area Day #4

Pnt #	Latitude	Longitude	Height	Code
1047	46.4048937315	-84.7386432491	271.272	R69-11
1048	46.4049365707	-84.7383223638	271.287	R69-12
1049	46.4047676075	-84.7379993578	271.927	R69-13

GCP measurement at Stand 71
May 22(Thursday) Raco area Day #4

Pnt #	Latitude	Longitude	Height	Code
2001	46.390223167	-84.765548475	274.429	S71-T11
2002	46.390194797	-84.765147622	272.827	S71-T21
2003	46.390215258	-84.764702297	272.162	S71-T31
2004	46.390183361	-84.763911497	272.069	S71-T41
2005	46.390283386	-84.763241019	273.058	S71-T51
2007	46.390746569	-84.763620067	272.409	S71-T52
2008	46.390911217	-84.765158344	272.135	S71-T22
2009	46.390762506	-84.766047581	275.468	S71-T12
2010	46.391341567	-84.766071275	274.738	S71-T13
2011	46.391439022	-84.765572256	272.299	S71-T23
2012	46.391597147	-84.763916400	272.245	S71-T53

GCP measurement at Stand 72
May 22(Thursday) Raco area Day #4

Pnt #	Latitude	Longitude	Height	Code
2013	46.389923261	-84.762884100	273.479	S72-T11
2014	46.389964342	-84.762104206	273.053	S72-T31
2015	46.389974114	-84.761145825	272.680	S72-T51
2016	46.390406753	-84.761218017	275.077	S72-T52
2017	46.390316242	-84.762203517	274.749	S72-T22
2018	46.390694903	-84.762436144	274.913	S72-T23
2019	46.391101447	-84.762864014	272.734	S72-T24
2020	46.391200369	-84.761974664	272.160	S72-T34
2021	46.391426872	-84.760631175	273.924	S72-T44
2022	46.391803644	-84.760716350	271.040	S72-T45
2023	46.392210481	-84.760845792	272.423	S72-T46
2024	46.392194483	-84.761957697	272.435	S72-T26

GCP measurement at Stand 80
May 21(Wed) Raco area Day #3

Pnt #	Latitude	Longitude	Height	Code
1086	46.340864353	-84.905768011	278.491	R80-11
1087	46.340898856	-84.906358378	277.688	R80-12
1088	46.340901892	-84.906962819	277.804	R80-13
1089	46.340962608	-84.907612953	277.756	R80-14
1090	46.340600489	-84.907754861	278.331	R80-24
1091	46.340570142	-84.907307519	278.925	R80-23
1092	46.340560278	-84.906891783	278.904	R80-22
1093	46.340523606	-84.906372950	279.138	R80-21
1094	46.340255472	-84.906200339	279.267	R80-31
1095	46.340279442	-84.906699783	279.324	R80-32
1096	46.340322158	-84.907171717	279.122	R80-33
1097	46.340348314	-84.907703256	278.778	R80-34
1098	46.339919667	-84.907718475	279.028	R80-44
1099	46.339957861	-84.907255611	279.110	R80-43
1100	46.340021633	-84.906807128	279.471	R80-42
1101	46.340051022	-84.906184628	279.336	R80-41

GCP measurement at Stand 85
May 24(Saturday) Raco area Day #6
Pnt # Latitude Longitude Height Code
1007,46.3942790996,-84.9706821837,278.604,R85-1

Appendix C: Brief Description of Stands

Appendix C consists of three parts.

(1) The location and description of each stand ..... Page C-3 – C-7
The information is based on the following reference.

Reference)
"Structure, Composition, and Above-ground Biomass of SIR-C/X-SAR and ERS-1 Forest Test Stands 1991-1994, Raco Michigan Site"
Kathleen M.Bergen, M.Craig Dobson, Terry L.Sharik, Ian Brodie
October 30,1995
Report 026511-7-T

(2) 3 dimensional plots of each stand .....Page C-8 – C-30
Each measured datum is plotted three dimensionally.

(3) The brief sketches of some stands .....Page C-31 – C-39
During the measurement, sketches were made in some stands, not all of the stands.

Stand 22 (D)--Red pine--sapling (C55-S35)

Raco Airfield, NW corner. Entrance to airport is south off M-28, 0.1 mi. west of Rt. 3157. Baseline starts 30 m. down from NW corner of airfield and runs along stand edge on azimuth of 155 deg. Transect #1 begins at m. 30 on the baseline and runs on 110 deg. azimuth. Sample points begin a minimum of 20 m. from the baseline (plantation edge), except for transect #5 where the minimum was 30 m. Location of the first sample point on the transects is 19, 23, 4, 6, and 9 m. beyond the minimum distance, respectively.

Stand 31 (Q)--Northern hardwoods--pole (C20-S8)

W side of Rt. 3159, 0.2 mi. N of Rt. 3156. Baseline runs along stand edge on az of 180 deg. Transect #1 starts at m. 19 along the baseline and runs on az of 90 deg, with first sample point a min. of 30 m. from the edge. Location of the first sample point on the transects is 1, 24, 3, 22, and 21 m. beyond the minimum distance, respectively.

Stand 33 (S)--Aspen--sapling (C20-S10)**

On Rt. 3156, 0.15 mi. W of intersection with Rt. 3159. Original baseline ran along stand edge on az. of 115 deg for a distance of 320 m. Transect #1 started at m. 14 along baseline on an az. of 0 deg.; first sample point was a min. of 20 m. from the edge. There were 8 transects with 5 sample points per transect. Due to stand irregularities, transects 9 and 10 were added (with 4 points per transect) to the west of transect #1 to compensate for missing plots on Transects 6, 7, and 8, which now contain 1, 2, and 4 points, respectively. Transect #9 starts 33 m. W of a logging trail which runs on an az of 20 deg. Location of the first sample point is 22, 15, 18, 13, 20, 19, 10, 16, 17, and 1 m. beyond the minimum distance for transects 1-10 respectively.

Stand 34 (T)--Aspen--mature (C19-S24)**

On N side of Rd. opposite Stand S, starting 75 m. W of intersection with Rt. 3161. Baseline runs along stand edge on az. of 295 deg. Transect #1 starts at m. 39 on the baseline and runs on an az of 205 deg; first sample point is a minimum of 30 m. from the edge. Transect #5 has only 5 points because of space constraints. Location of the first sample point on the transects is 7, 13, 8, 16, and 6 m. beyond the minimum distance, respectively.

Stand 38 (X)--Jack pine--sapling (C31-S50)

On Rt. 3036, 0.25 mi. E of junction with Rt. 3018. Baseline runs along the N side of Rt. 3036, on az. of 90 deg.; m. 200 on the baseline is 61.8 m. W of the E edge of the stand. Transect #1 starts at m. 5 along the baseline and runs on an az. of 20 deg.; first sample point is min. of 10 m. from the baseline. Location of first sample point on the transects is 5, 16, 3, 13, and 7 m. beyond the minimum distance, respectively.

Stand 40 (Z)--Red pine--sapling (C29-R18)**

On Rt. 3366, 0.25 mi. E of junction with Rt. 3041. Baseline runs along the N side of Rt. 3366 for a distance of 440 m, on az. of 120 deg.; baseline starts 38 m. E of W edge of stand, while m. 440 on baseline is 42 m. W of E end of stand. There are 9 transects along the baseline, with a variable number of sample points per transect to accommodate the irregular shape of the stand. The number of points are 3, 2, 3, 3, 6, 7, 7, 6, and 3 respectively. Transect #1 starts at m. 38 along the baseline and runs on an az. of 30 deg.; first sample point is a min. of 10 m. from the baseline. Location of first sample point on the transects is 22, 11, 10, 21, 23, 1, 23, 6, 22, 9, and 22 m. beyond the minimum distance, respectively.

Stand 45 (EE)--Aspen--sapling (C20-R30)

Take Rt. 3156 0.9 mi. NW of junction with Rt. 3159, turn right (NE) onto spur road for 75 m. to W-central edge of stand. Baseline starts 20 m. in from spur road and runs along the edge of the stand on an az. of 152 deg. Transect #1 begins at m. 9 on the baseline and runs on an az. of 36 deg.; first sample point is a minimum of 30 m. from the baseline. Location of first sample point on the transects is 15, 8, 7, 10, and 17 m. beyond the minimum distance, respectively. Wire flags marking sample points are reversed, with yellow at the upper stratum plot center and red at the middle stratum plot centers. Rebars may be absent at the ends of the baseline. There are scattered individuals in the overstory which have not been removed as of 10-19-92 (ditto for 7/94).

Stand 49 (JJ)--Aspen--sapling (C21-S9 & 10)**

On Rt 3640, 0.3 mi. NE of junction with Rt. 3156. Baseline starts 40 m. from the NE corner of the stand and runs on an az. of approx. 230 deg. along the NW edge of the stand. Transect #1 begins at m. 36 on the baseline and runs on an az. of 100 deg.; first sample point is a minimum of 20 m. from the baseline. Due to size limitations, only 38 sample points were established along 5 transects, with 5, 6, 8, 10, and 9 sample points, respectively. Location of first sample point of the transects is 10, 4, 7 (17?), 3, and 9 m. beyond the minimum distance, respectively. On transect #5 a truck trail passes between sample points 3 and 4, thus moved point #4 20 m. down the transect.

Stand 50 (KK)--Red pine--mature (C21-S8)**

On Rt. 3156, 0.33 mi. SE of junction with Rt. 3159. Baseline starts 40 m. from W edge of stand and runs along N side of Rt. 3156, on an az. of 118 deg. Transect #1 begins at m. 9 on the baseline and runs on an az. of 360 deg.; first sample point is a min. of 20 m. from the baseline. Because of stand irregularities, transect #5 was skipped and a sixth transect added. The number of sample points per transect is 6, 8, 8, 9, and 9, respectively. Location of first sample point on the transects is 11, 1, 12, 16, and 3, respectively.

Stand 54--Jack pine--sapling (C31-S38)

On FS 3018, m. 0.0 is 0.3 mi. south of junction with FS 3036. Baseline runs along the east side of 3018, on an az. of 180 deg. Transect #1 begins at m. 7 on the baseline and runs on an az. of 87 deg. First sample point is a minimum of 20 m. from the baseline. Location of first sample point on the transects is 9, 15, 12, 15, and 6 m. beyond the minimum distance, respectively.

Stand 55--Jack pine--sapling (C31-S52)

On north side of FS 3366, a reference point is 0.3 mi. east of junction with FS 3018. From reference point, baseline m. 0.0 is 62.5 m. into the forest at an az. of 18 deg. Transect #1 begins at m. 36 on the baseline and runs on an az. of 288 deg. First sample point is a minimum of 0 m. from the baseline. Location of first sample point on the transects is 6, 25, 11, 3, and 5 m, respectively.

Stand 56--Jack Pine--pole (C31-S62)

On FS 3018, m. 0.0 is 40 m. south of junction with FS 3037. Baseline runs along the east side of FS 3018, on and az. of 180 deg. Transect #1 begins at m. 18 on the baseline and runs on an az. of 90 deg. First sample point is a minimum of 20 m. from the baseline. Location of first sample point on the transects is 3, 6, 22, 2, and 6 m. beyond the minimum distance, respectively.

Stand 58--Jack pine--sapling (C49-S33)

On FS 3040, m. 200 is 20 m. south of junction with FS 3364. Baseline runs along the west side of FS 3040, on an az. of 0 deg. Transect #1 begins at m. 11 on the baseline and runs on an az. of 270 deg. First sample point is a minimum of 20 m. from the baseline. Location of first sample point on the transects is 19, 24, 18, 9, and 18 m. beyond the minimum distance, respectively.

Stand 59--Jack pine--sapling (C48-S5)

On FS 3040, m. 200 is 0.2 mi. west of junction with FS 3018. Baseline runs along the south side of FS 3040, on an az. of 269 deg. Transect #1 begins at m. 30 on the baseline and runs on an az. of 180 deg. First sample point is a minimum of 20 m. from the baseline. Location of first sample point on the transects is 6, 20, 6, 17, and 22 m. beyond the minimum distance, respectively.

Stand 61--Jack pine--mature (C48-S13)

On FS 3040, m. 0.0 is 50 m. west of junction with FS 3039. Baseline runs along the south side of FS 3040, on an az. of 88 deg. Transect #1 begins at m. 24 on the baseline and runs on an az. of 180 deg. First sample point is a minimum of 30 m. from the baseline. Location of first sample point on the transects is 15, 6, 6, 22, and 2 m. beyond the minimum distance, respectively.

Stand 66--Jack pine--seedling (C32-S21)

On FS 3037, m. 160 is 0.2 mi. west of junction with FS 3018. Baseline runs along the north side of FS 3037, on an az. of 270 deg. Transect #1 begins at m. 29 on the baseline and runs on an az. of 36 deg. (Road crosses baseline at 50 m. mark.) First sample point is a minimum of 80 m. from the baseline. Location of first sample point on the transects is 13, 14, 2, and 25 m. beyond the minimum distance, respectively. The stand shape is irregular with 4 transects having 10 plots each.

Stand 67--Jack pine--mature (C32-S22)

On FS 3036, m. 200 is 0.3 mi. west of junction with FS 3018. Baseline runs along the north side of FS 3036, on an az. of 90 deg. Transect #1 begins at m. 24 on the baseline and runs on an az. of 0 deg. First sample point is a minimum of 30 m. from the baseline. Location of first sample point on the transects is 4, 8, 14, 8, and 22 m. beyond the minimum distance, respectively.

Stand 68--Red pine--pole (C49-S9)

On FS 3040, m. 0.0 is 0.8 mi. east of junction with FS 3018. Baseline runs along the north side of FS 3040, on an az. of 90 deg. Transect #1 begins at m. 29 on the baseline and runs on an az. of 355 deg. First sample point is a minimum of 50 m. from the baseline. Location of first sample point on the transects is 19, 14, 17, 15, and 22 m. beyond the minimum distance, respectively. A jack pine inclusion occurs at 125 m. on the baseline and goes in approx. 60 m.

Stand 69--Aspen (upland)--sapling (C23-S23)

On FS 3154, m. 200 is 0.1 mi. north of junction with FS 3622. Baseline runs along the east side of FS 3154, on an az. of 180 deg. Transect #1 begins at m. 23 on the baseline and runs on an az. of 90 deg. First sample point is a minimum of 20 m. from the baseline. Location of first sample point on the transects is 18, 11, 21, 5, and 12 m. beyond the minimum distance, respectively. 15 plots were measured in 1993. (T1 plots 1-5, T2 plots 1-4, T3 plots 1-3, T4 plots 4 & 6, T5 plot 5). Later reconfigured for GPS survey to be 8 transects (320 m.) by 5 plots ea. deep.

Stand 71--Red pine--pole (C30-S52)

On FS 3036, m. 200 is 220 m. west of junction with FS 3041. Baseline runs along the north side of FS 3036, on an az. of 90 deg. Transect #1 begins at m. 3 on the baseline and runs on an az. of 0 deg. First sample point is a minimum of 30 m. from the baseline. Location of first sample point on the transects is 12, 21, 9, 19, and 11 m. beyond the minimum distance, respectively.

Stand 72--Red pine--pole (C30-S52)

On FS 3036, m. 200 is 17.5 m. west of junction with FS 3041. Baseline runs along the north side of FS 3036, on an az. of 90 deg. Transect #1 begins at m. 9 on the baseline and runs on an az. of 0 deg. First sample point is a minimum of 30 m. from the baseline. Location of first sample point on the transects is 13, 15, 30, 4, and 2 m. beyond the minimum distance, respectively.

Stand 80--Red pine--seedling (C58-S39)

On FS 3139, m. 160 is 0.4 mi. south of junction with M-28. Baseline runs along the west side of FS 3139, on an az. of 0 deg. Transect #1 begins at m. 28 on the baseline and runs on an az. of 260 deg. First sample point is a minimum of 65 m. from the baseline. Location of first sample point on the transects is 3, 25, 24, and 5 m. beyond the minimum distance, respectively. The stand shape is irregular having 4 transects with 10 plots each.

Stand 85--Northern hardwoods--pole (C44-S19)

On trail to Peck and Rye Lake, m. 0.0 is 0.3 mi. north of junction with FS 3162. Baseline runs along the west side of the trail to Peck and Rye lake, on an az. of 360 deg. Transect #1 begins at m. 31 on the baseline and runs on an az. of 270 deg. First sample point is a minimum of 20 m. from the baseline. Location of first sample point on the transects is 14, 5, 12, 1, and 8 m. beyond the minimum distance, respectively.

---

*All baselines are 200 m. long with 5 transects situated along them and with 8 sample points per transect, unless otherwise indicated. Sample points on a transect are at intervals of 25 m, with the first point located at a random distance of 1-25 m. from the baseline or from the "minimum distance from the baseline", depending on the stand. White wire flags mark locations of transects on the baseline, while red and yellow flags mark the centers of the upper- and middle-stratum plot centers, respectively , unless otherwise noted. Magnetic declination is 5 deg. W.

**Some irregularities in plot layout or homogeneity of vegetation, topography, and/or soil conditions

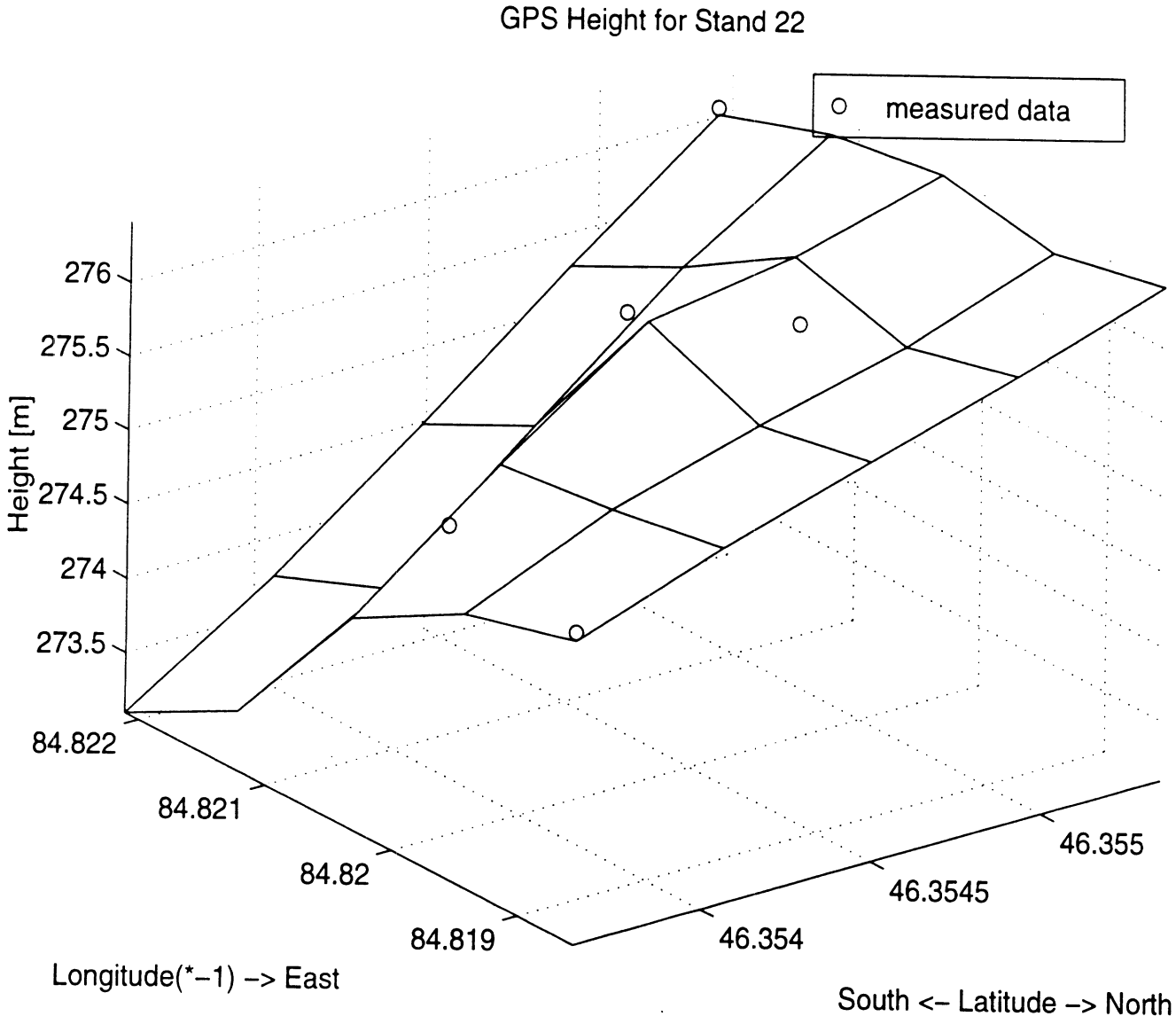
GPS Height for Stand 22
measured data
Height [m]
276
275.5
275
274.5
274
273.5
84.822
84.821
84.82
84.819
Longitude(*−1) -> East
46.355
46.3545
46.354
South <- Latitude -> North

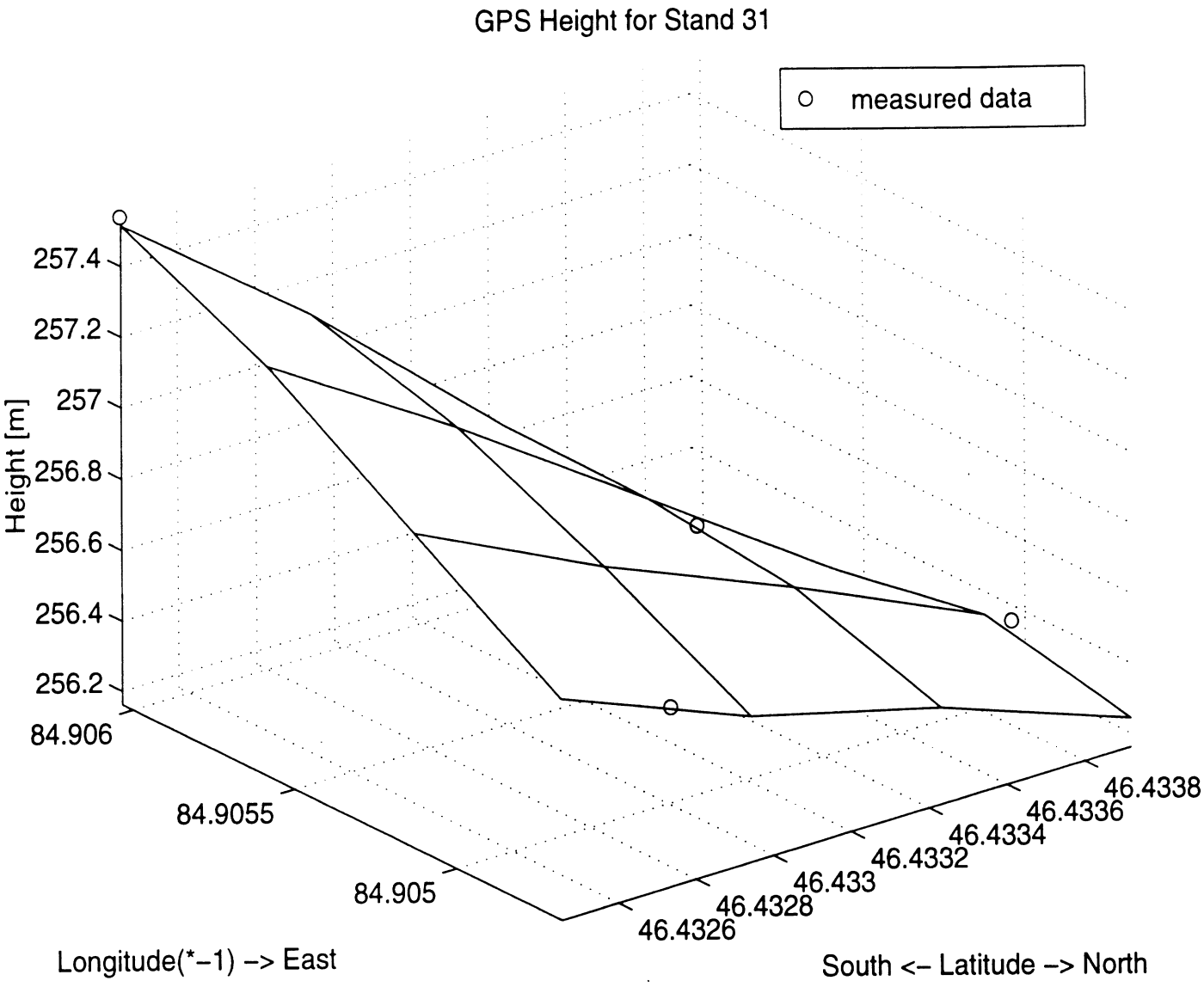
GPS Height for Stand 31
measured data
257.4
257.2
257
256.8
256.6
256.4
256.2
Height [m]
84.906
84.9055
84.905
Longitude(*−1) -> East
46.4326
46.4328
46.433
46.4332
46.4334
46.4336
46.4338
South <- Latitude -> North

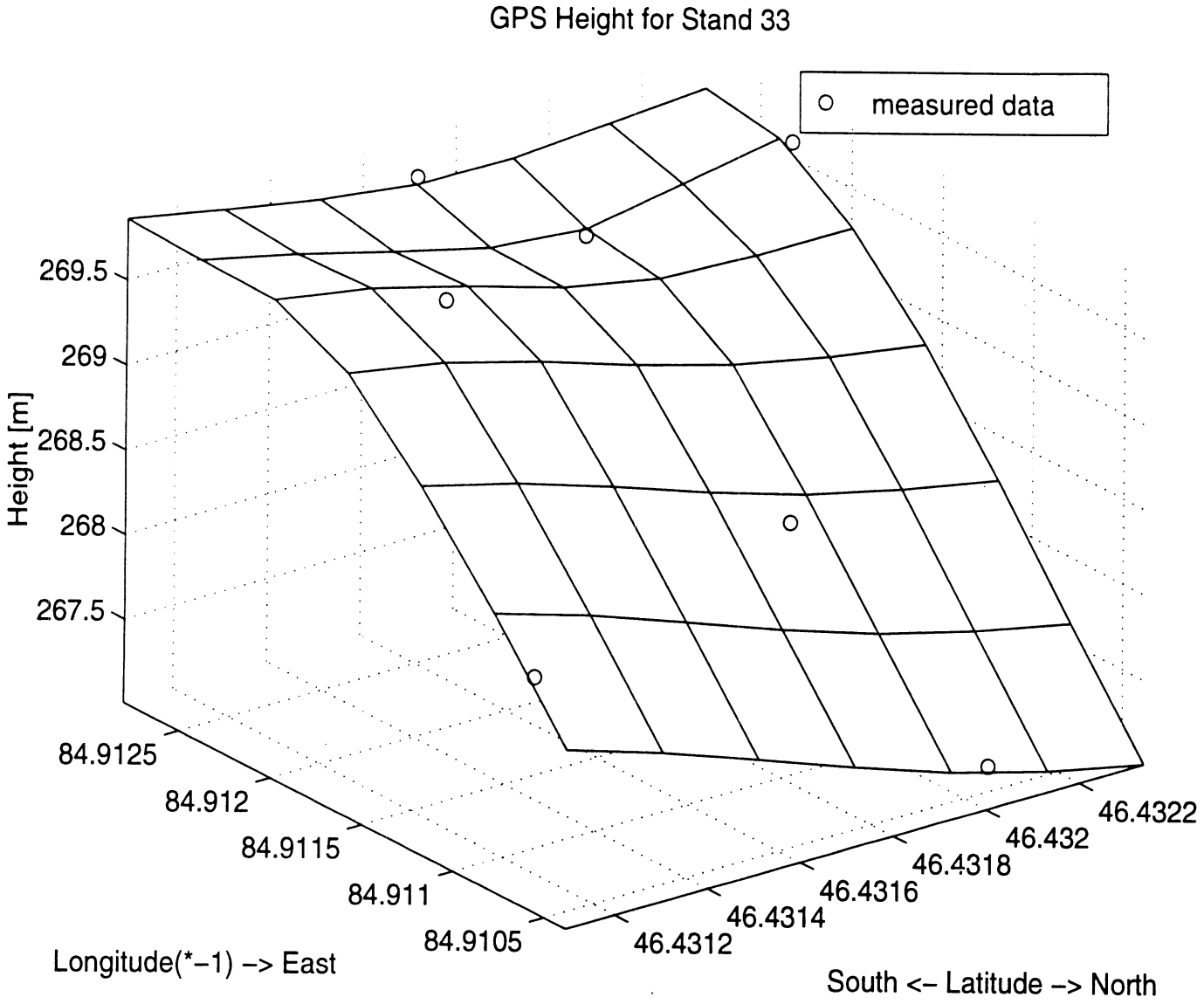
GPS Height for Stand 33
measured data
Height [m]
269.5
269
268.5
268
267.5
84.9125
84.912
84.9115
84.911
84.9105
Longitude(*−1) -> East
46.4312
46.4314
46.4316
46.4318
46.432
46.4322
South <- Latitude -> North

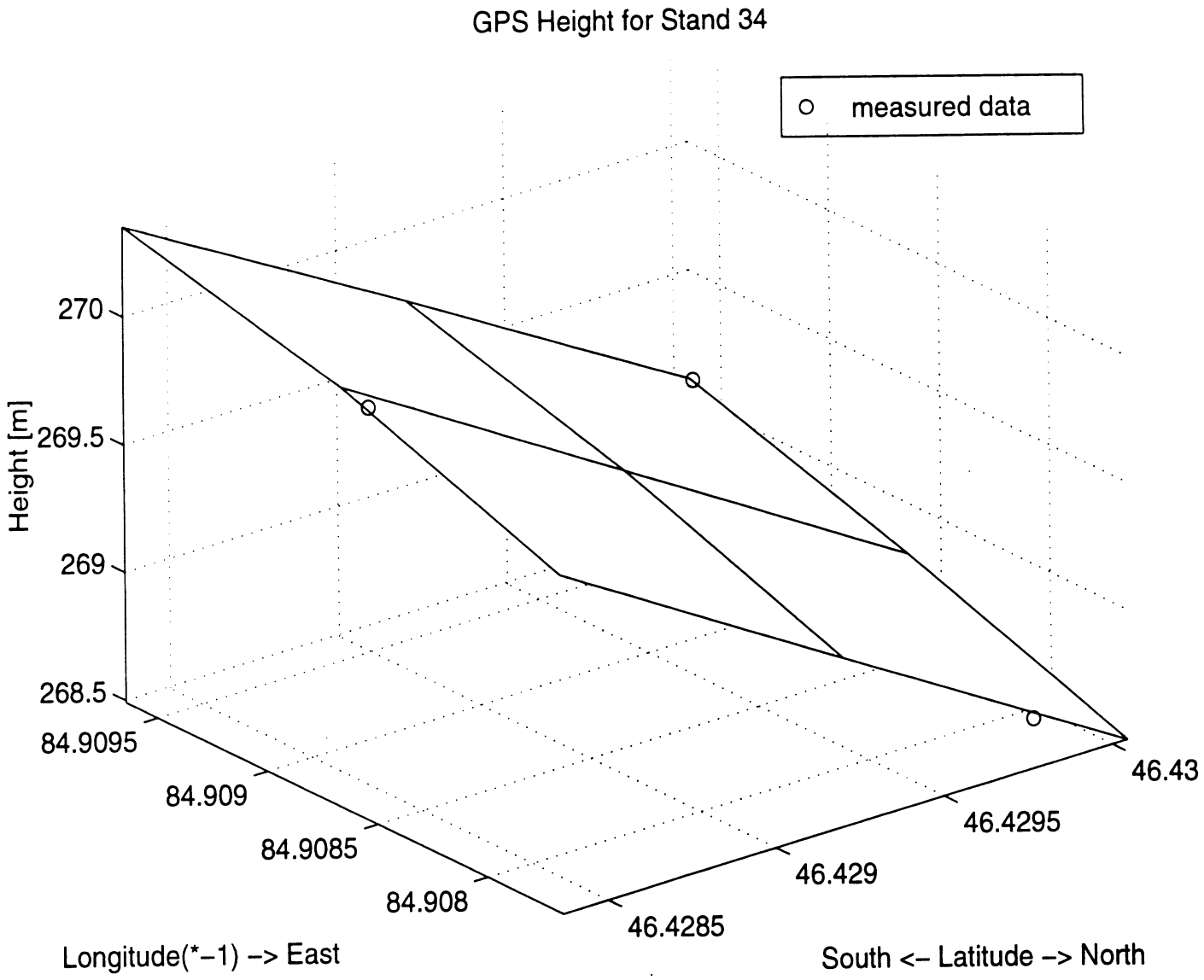
GPS Height for Stand 34
measured data
Height [m]
270
269.5
269
268.5
84.9095
84.909
84.9085
84.908
Longitude(*−1) -> East
46.4285
46.429
46.4295
46.43
South <- Latitude -> North

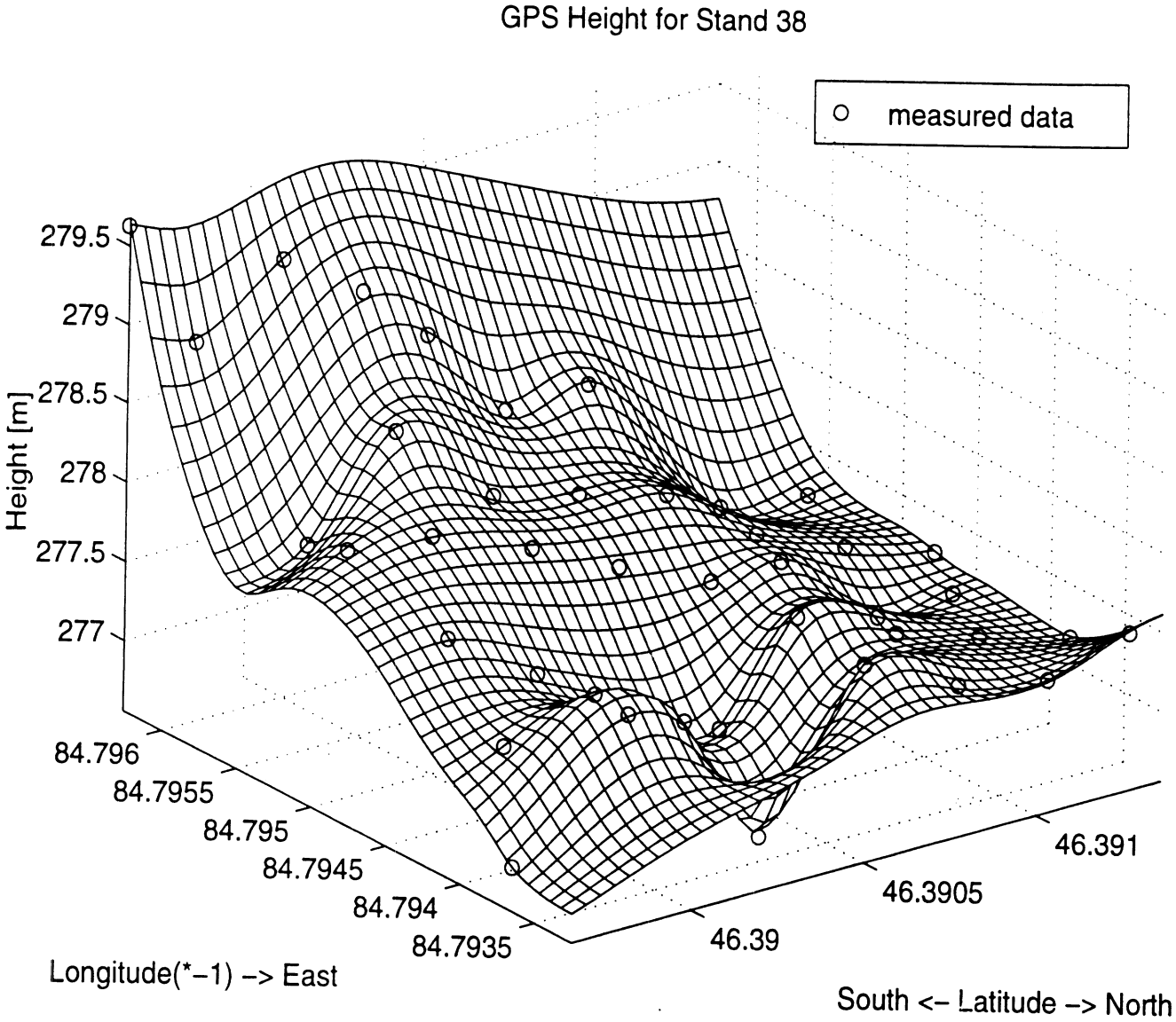
GPS Height for Stand 38
measured data
279.5
279
278.5
278
277.5
277
Height [m]
84.796
84.7955
84.795
84.7945
84.794
84.7935
Longitude(*-1) -> East
46.39
46.3905
46.391
South <- Latitude -> North

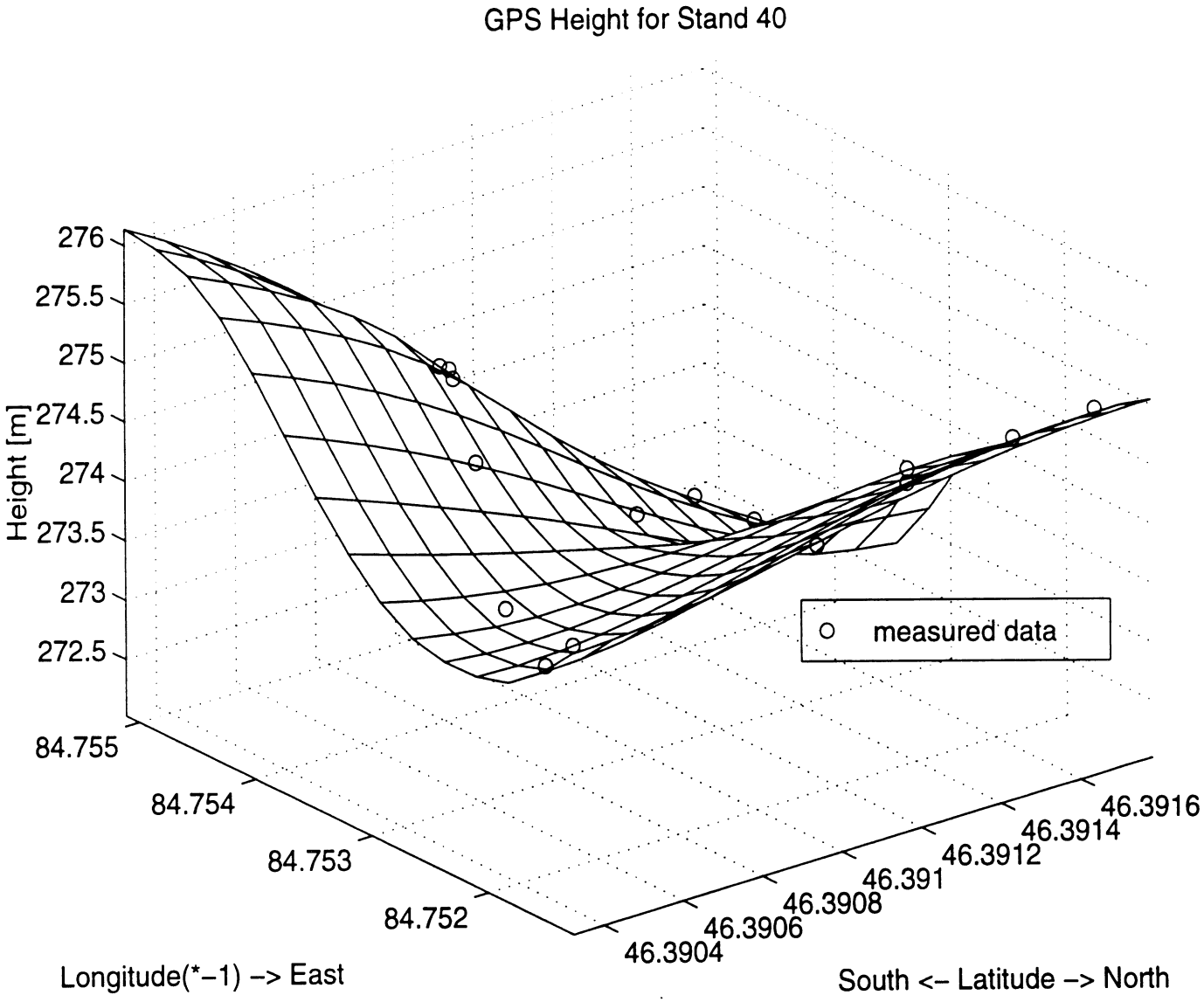
GPS Height for Stand 40
Height [m]
276
275.5
275
274.5
274
273.5
273
272.5
84.755
84.754
84.753
84.752
Longitude(*−1) -> East
46.3904
46.3906
46.3908
46.391
46.3912
46.3914
46.3916
South <- Latitude -> North
measured data

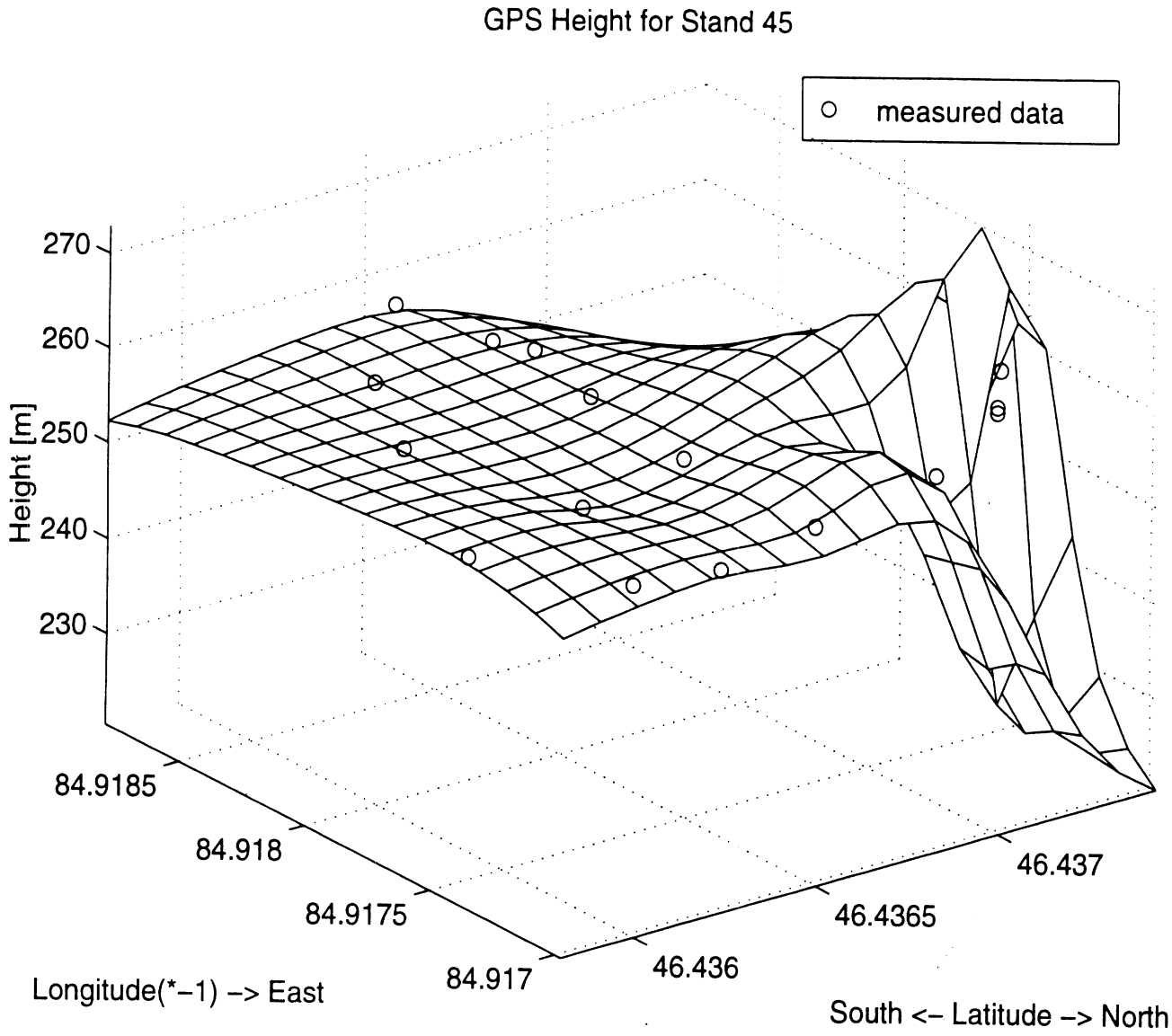
GPS Height for Stand 45
measured data
270
260
250
240
230
Height [m]
84.9185
84.918
84.9175
84.917
Longitude(*−1) -> East
46.436
46.4365
46.437
South <- Latitude -> North

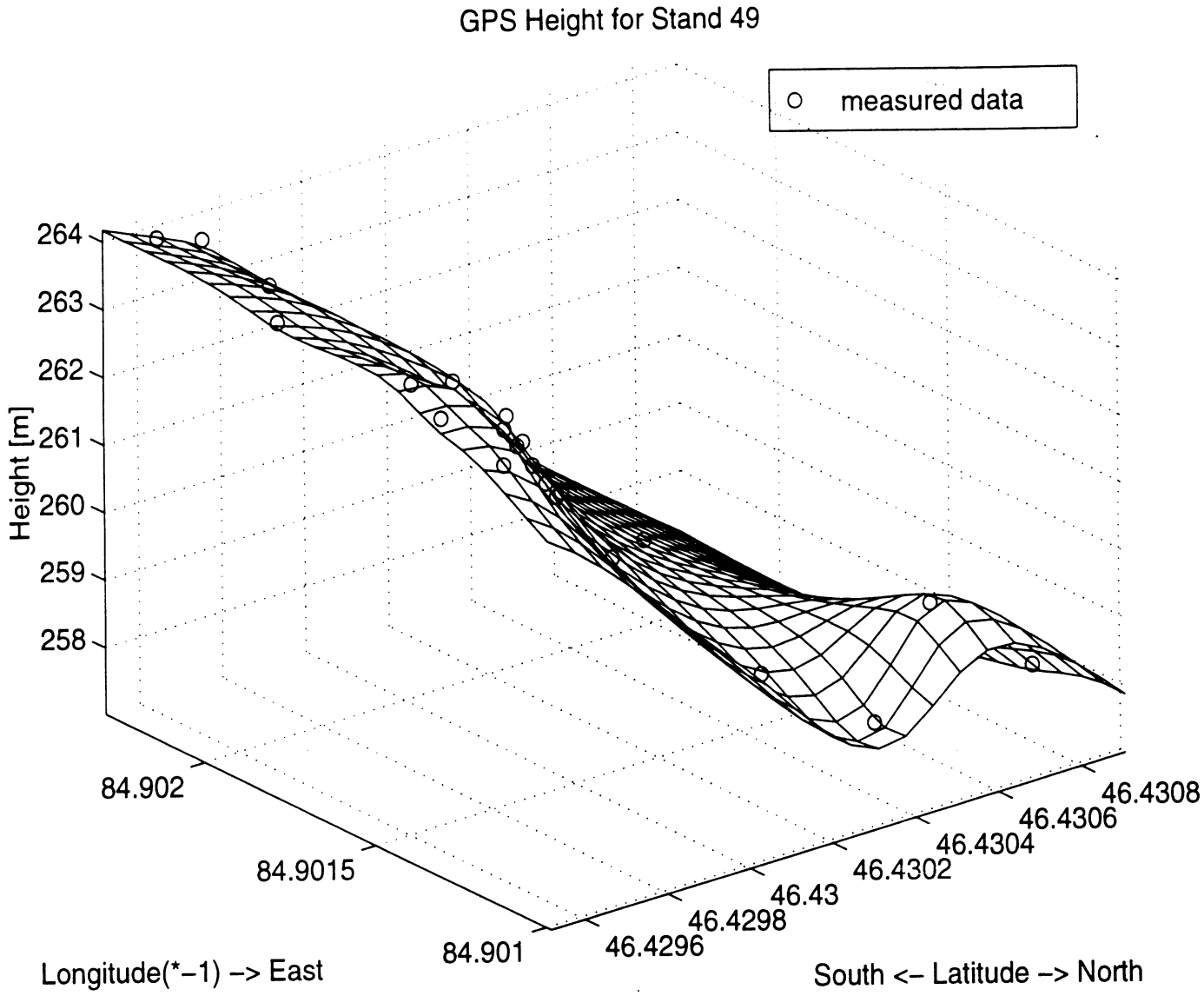
GPS Height for Stand 49
measured data
Height [m]
264
263
262
261
260
259
258
84.902
84.9015
84.901
Longitude(*−1) -> East
46.4296
46.4298
46.43
46.4302
46.4304
46.4306
46.4308
South <- Latitude -> North

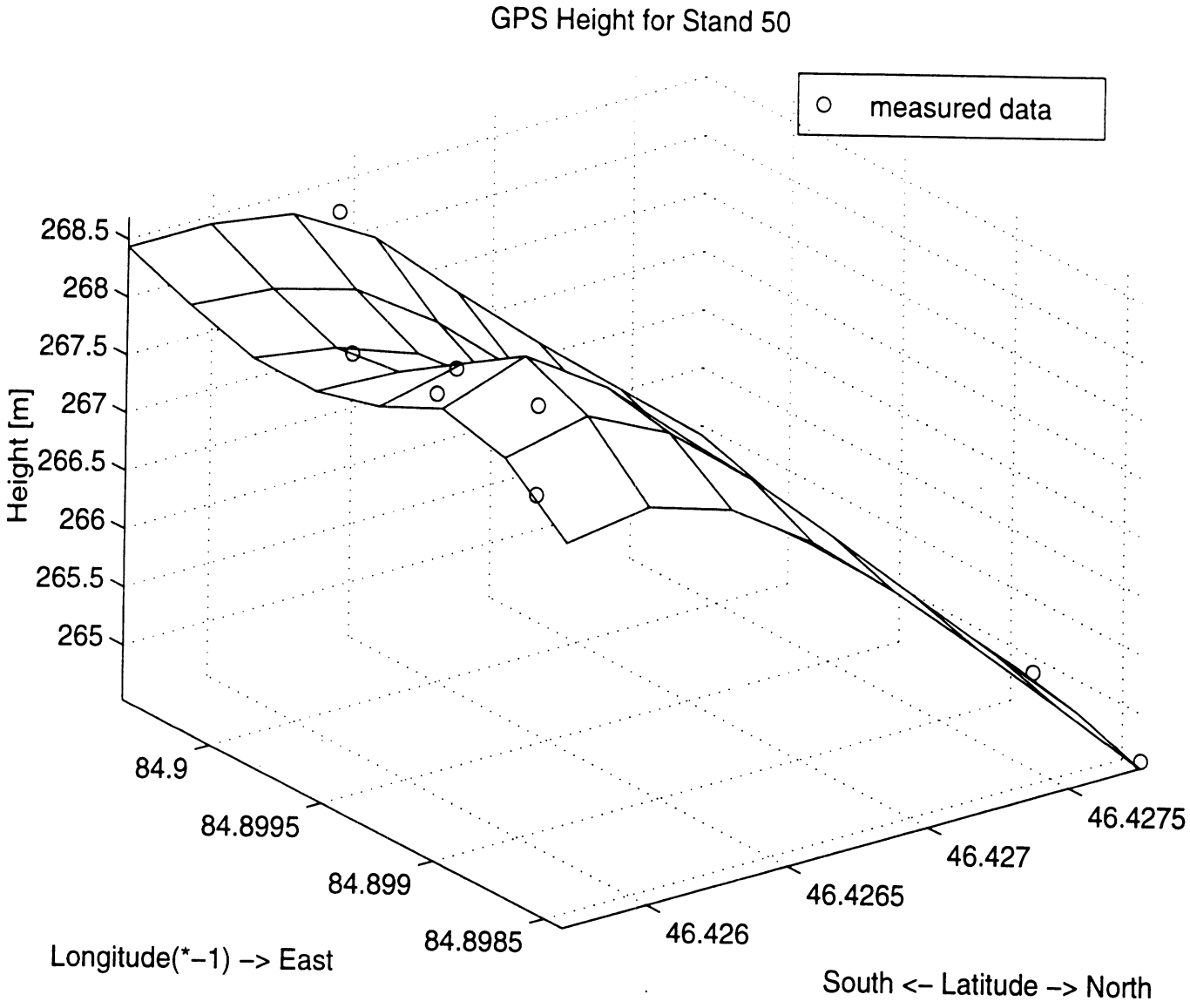
GPS Height for Stand 50
measured data
Height [m]
268.5
268
267.5
267
266.5
266
265.5
265
84.9
84.8995
84.899
84.8985
Longitude(*−1) -> East
46.426
46.4265
46.427
46.4275
South <- Latitude -> North

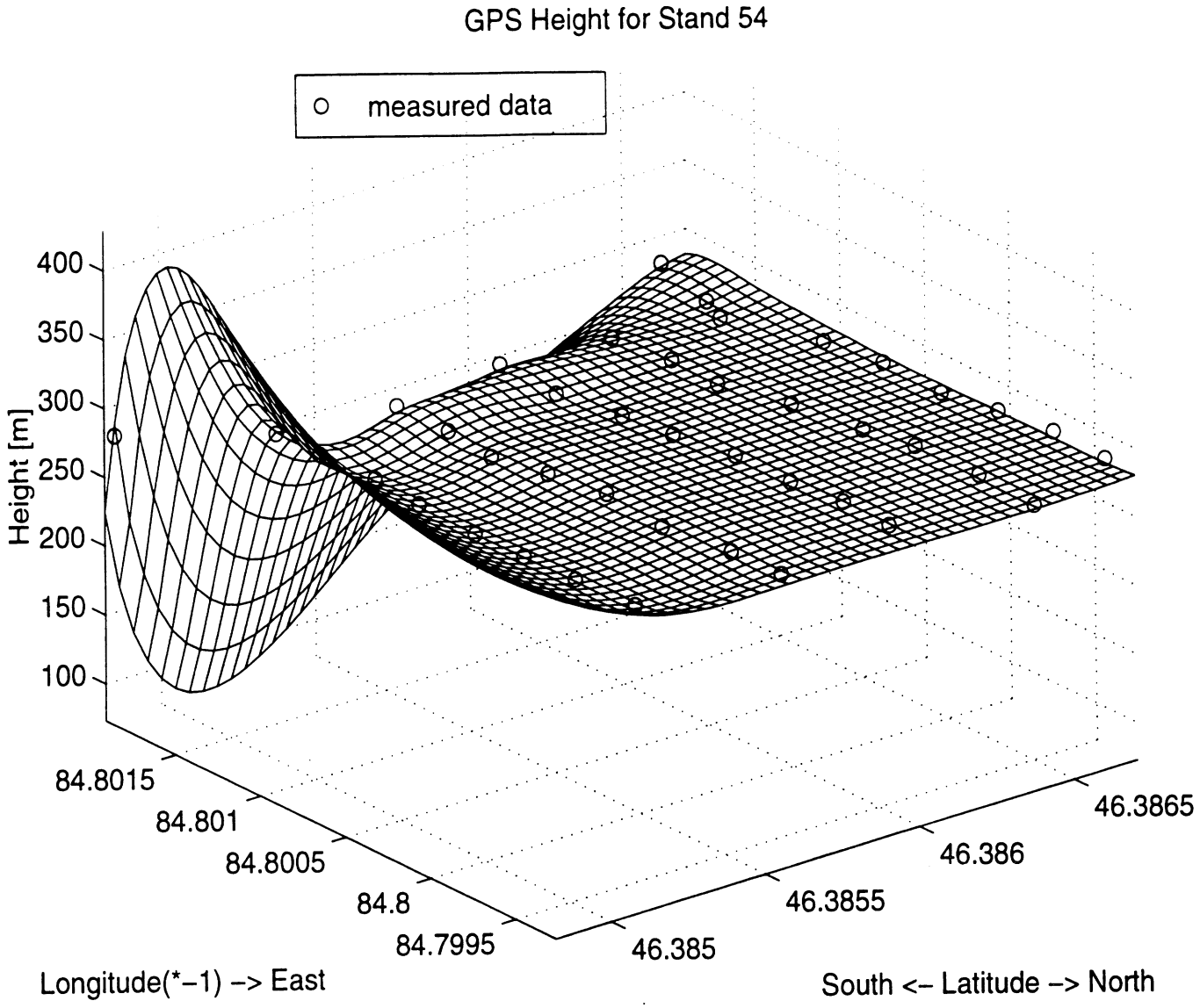
GPS Height for Stand 54
measured data
Height [m]
400
350
300
250
200
150
100
84.8015
84.801
84.8005
84.8
84.7995
Longitude(*−1) -> East
46.385
46.3855
46.386
46.3865
South <- Latitude -> North

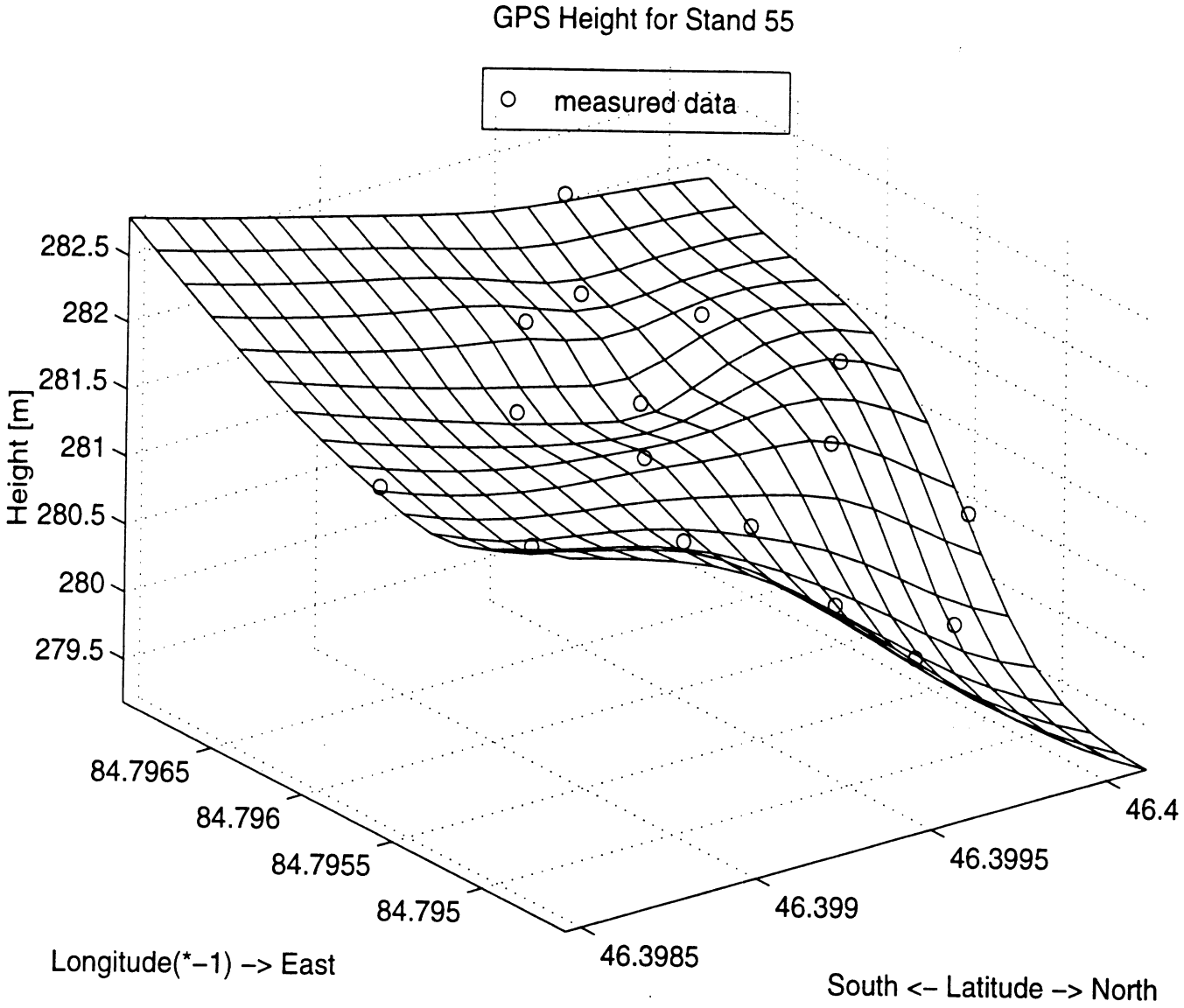
GPS Height for Stand 55
measured data
282.5
282
281.5
281
280.5
280
279.5
Height [m]
84.7965
84.796
84.7955
84.795
Longitude(*−1) -> East
46.3985
46.399
46.3995
46.4
South <- Latitude -> North

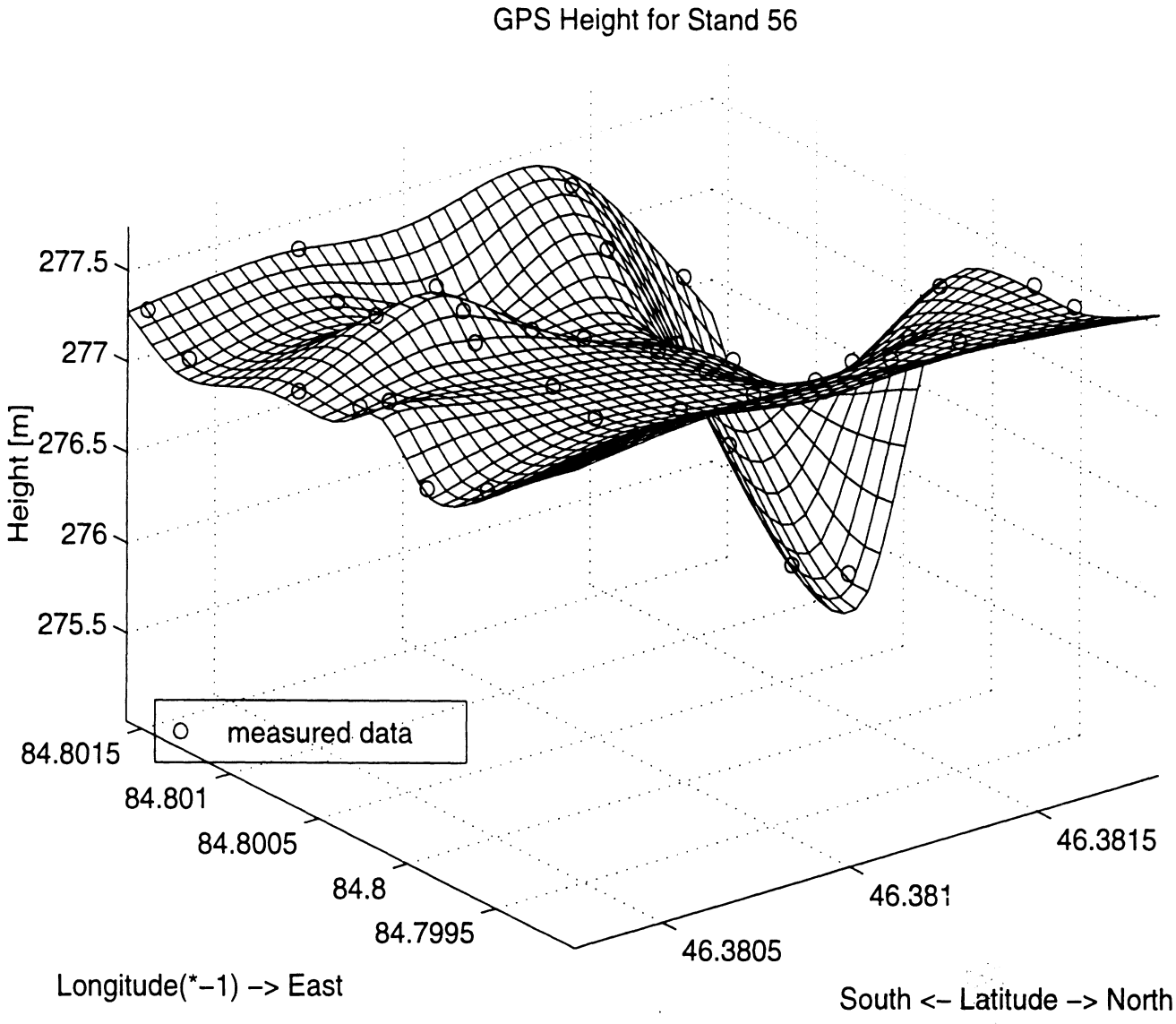
GPS Height for Stand 56
277.5
277
276.5
276
275.5
Height [m]
measured data
84.8015
84.801
84.8005
84.8
84.7995
Longitude(*−1) -> East
46.3805
46.381
46.3815
South <- Latitude -> North

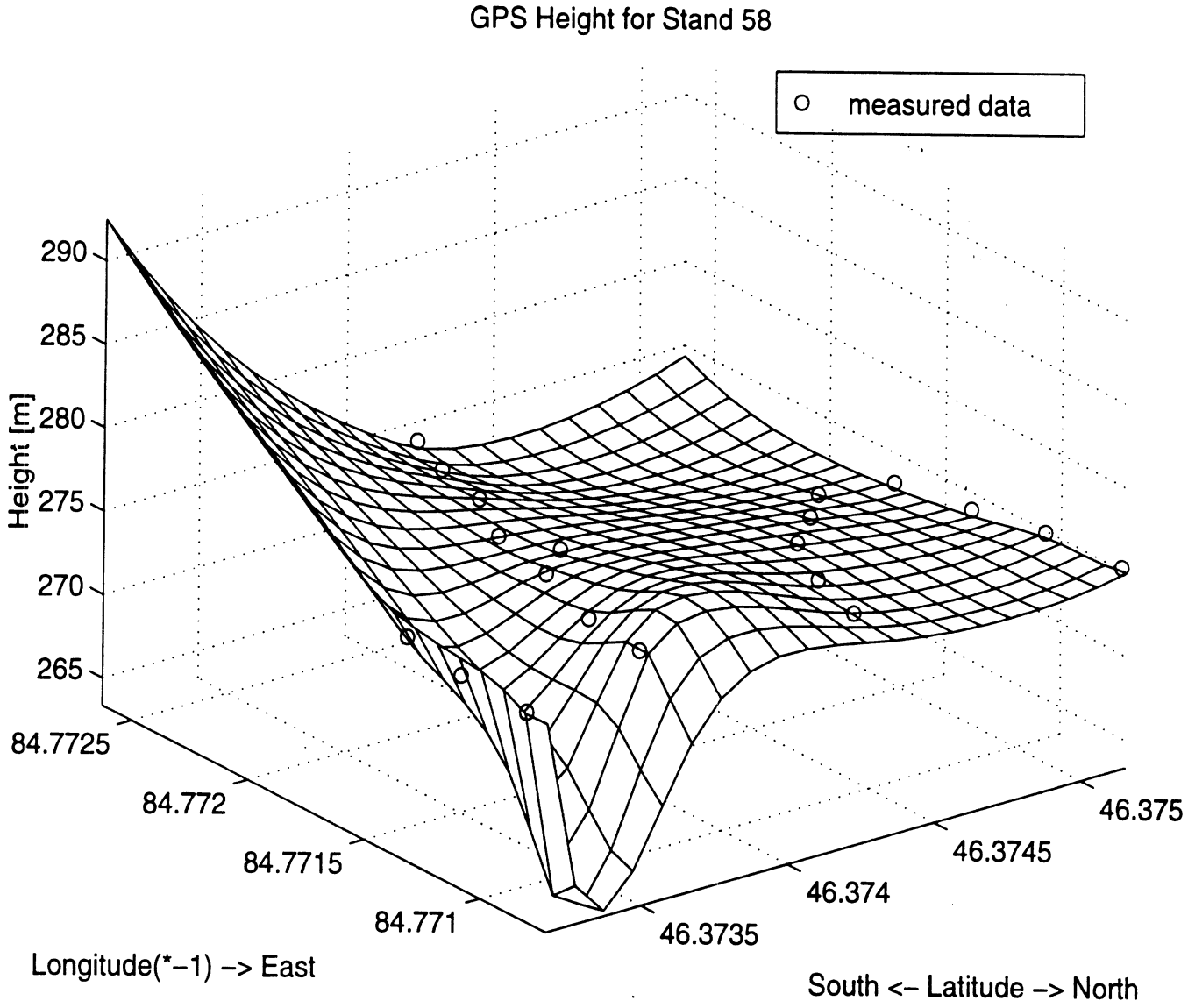
GPS Height for Stand 58
measured data
290
285
280
275
270
265
Height [m]
84.7725
84.772
84.7715
84.771
Longitude(*-1) -> East
46.375
46.3745
46.374
46.3735
South <- Latitude -> North

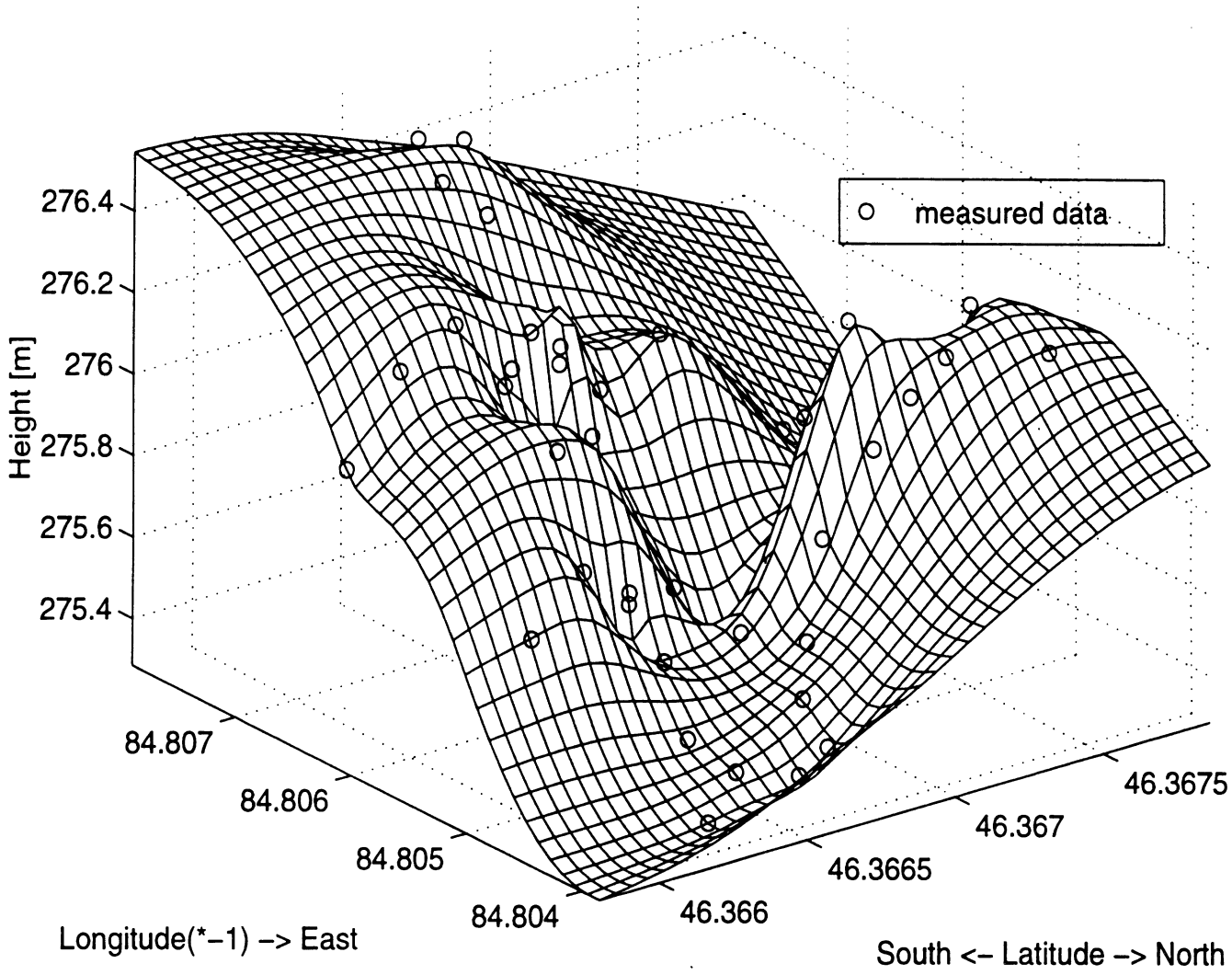
GPS Height for Stand 59
measured data
Height [m]
276.4
276.2
276
275.8
275.6
275.4
84.807
84.806
84.805
84.804
Longitude(*−1) -> East
46.366
46.3665
46.367
46.3675
South <- Latitude -> North

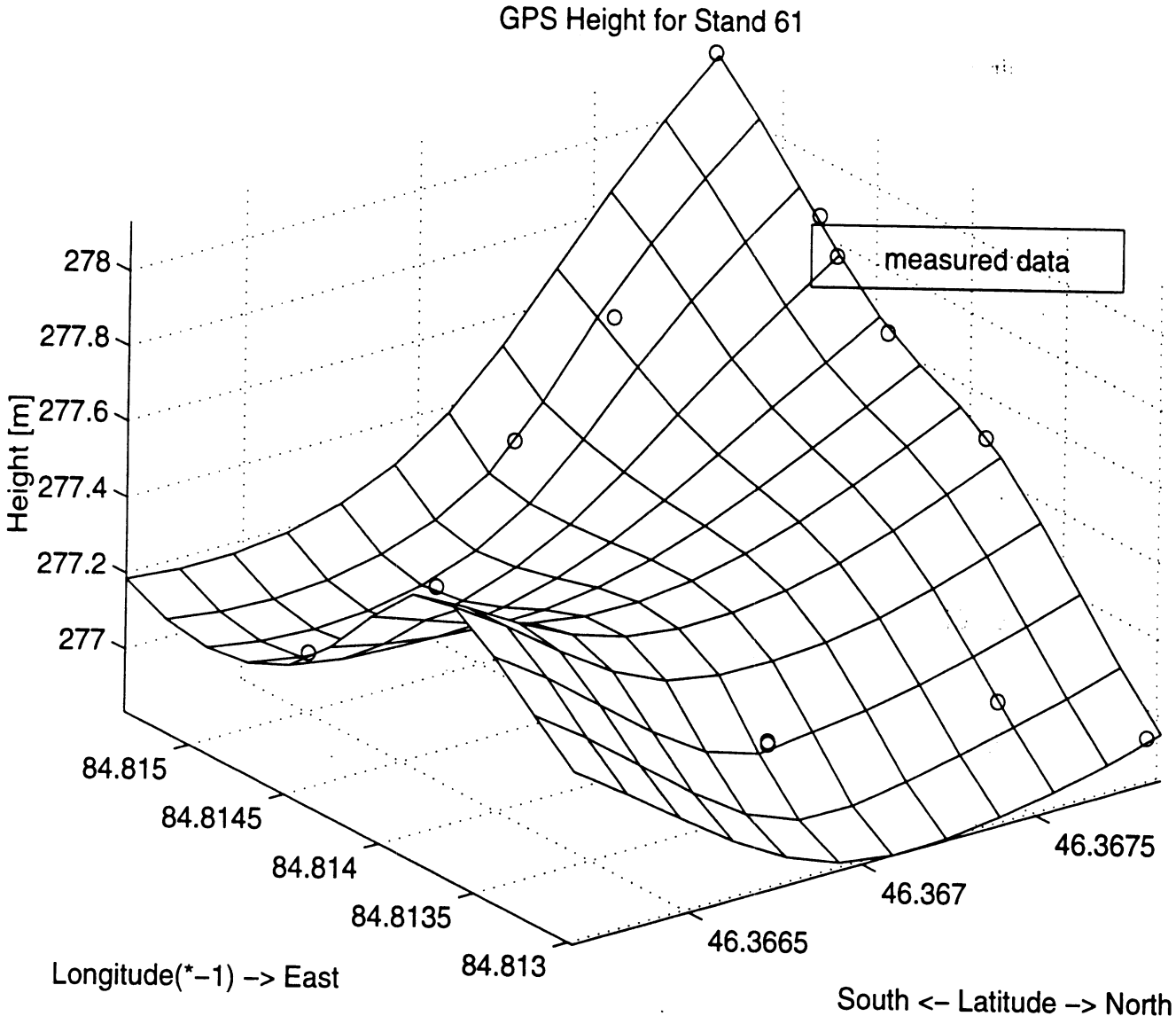
GPS Height for Stand 61
measured data
Height [m]
278
277.8
277.6
277.4
277.2
277
84.815
84.8145
84.814
84.8135
84.813
Longitude(*−1) -> East
46.3665
46.367
46.3675
South <- Latitude -> North

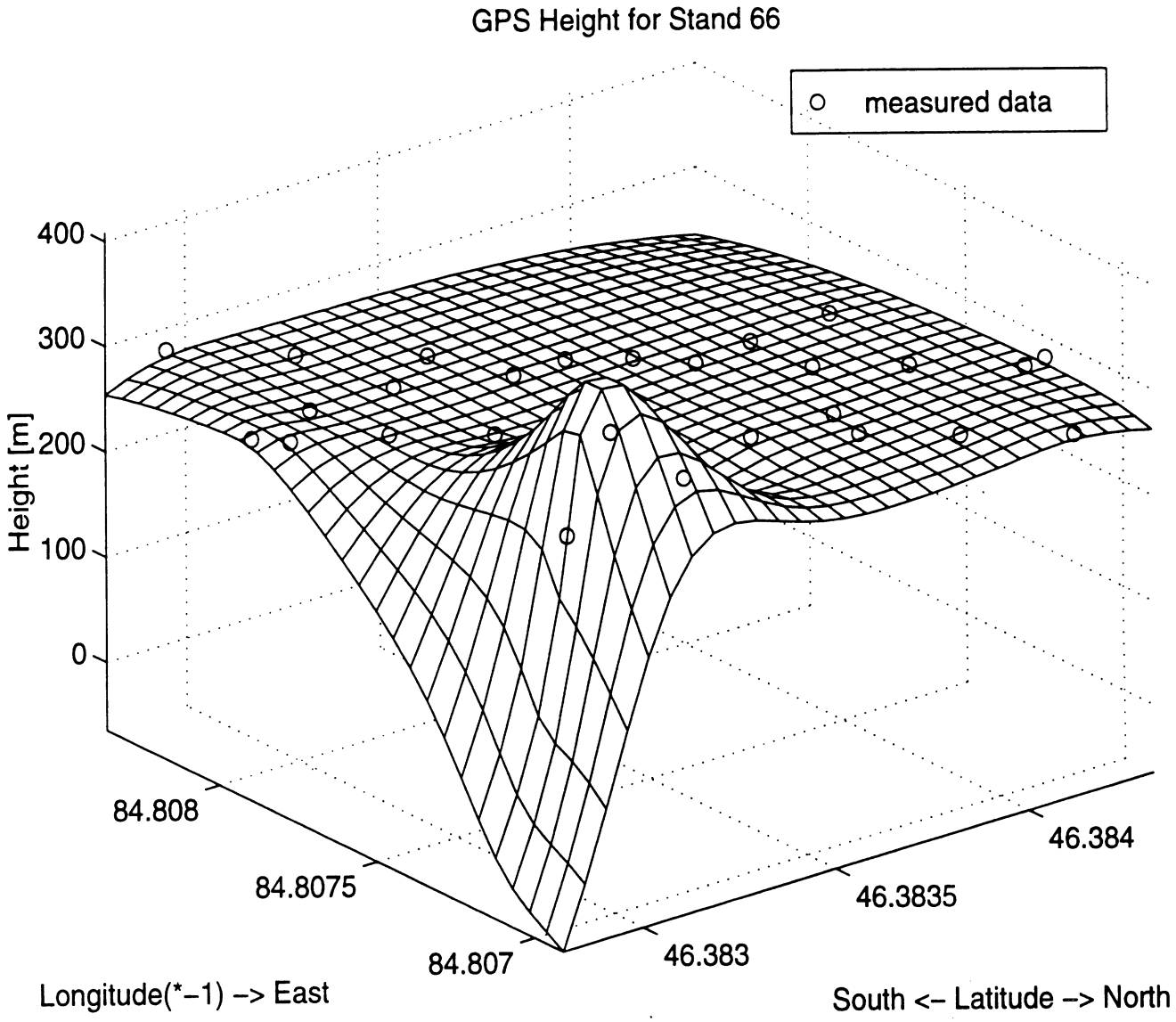
GPS Height for Stand 66
measured data
400
300
200
100
0
Height [m]
84.808
84.8075
84.807
46.383
46.3835
46.384
Longitude(*-1) -> East
South <- Latitude -> North

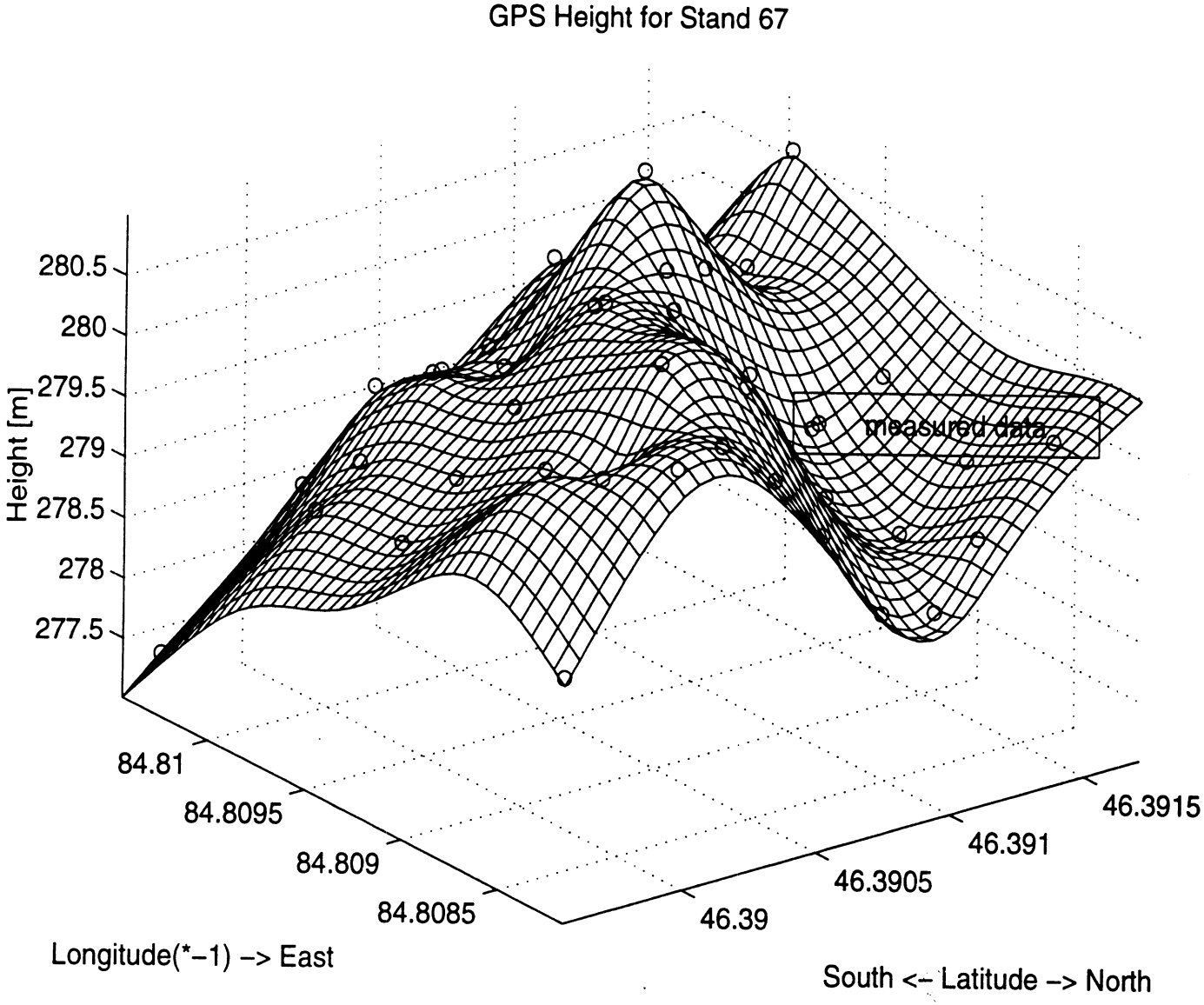
GPS Height for Stand 67
Height [m]
280.5
280
279.5
279
278.5
278
277.5
measured data
84.81
84.8095
84.809
84.8085
Longitude(*-1) -> East
46.39
46.3905
46.391
46.3915
South <- Latitude -> North

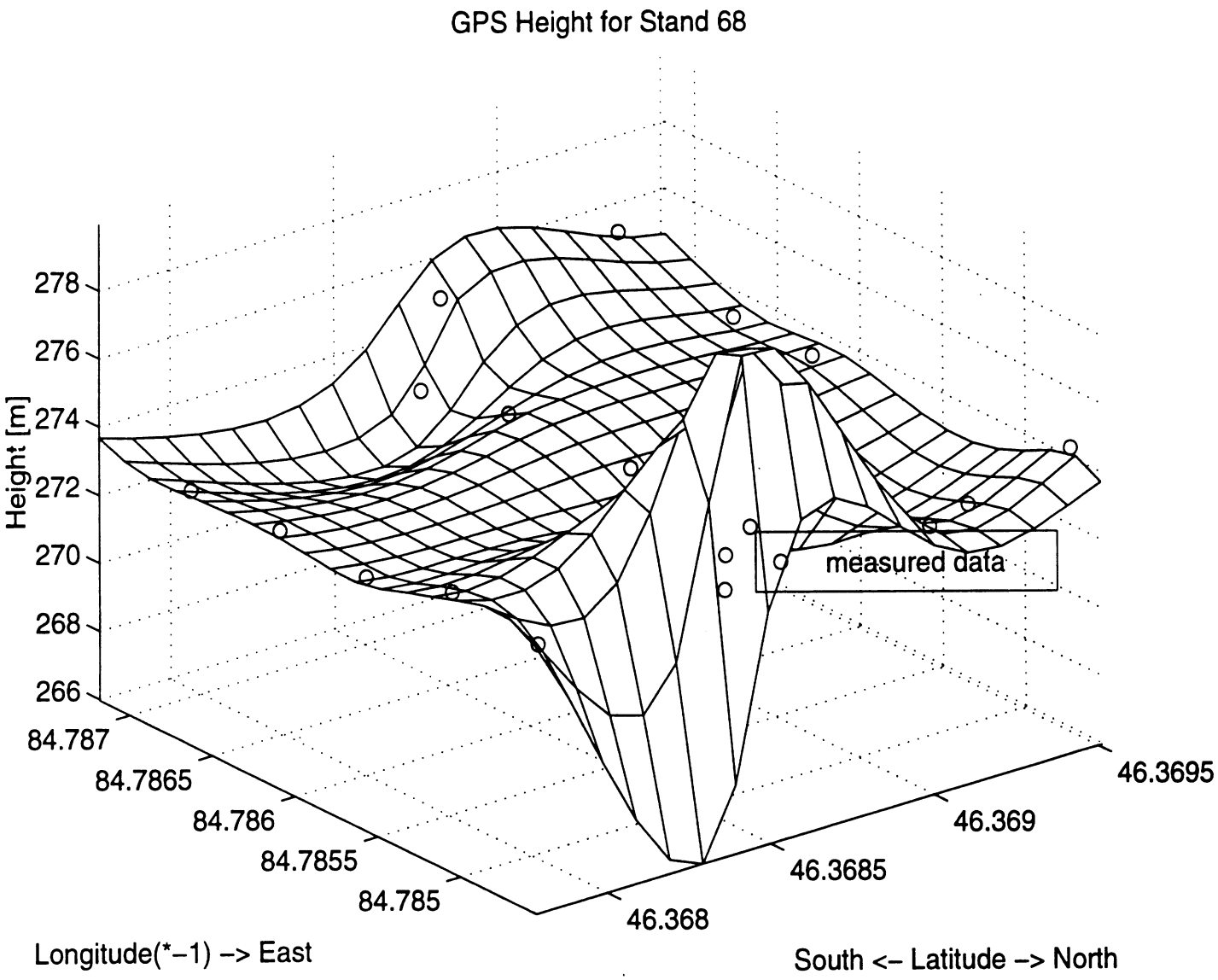
GPS Height for Stand 68
Height [m]
278
276
274
272
270
268
266
84.787
84.7865
84.786
84.7855
84.785
Longitude(*-1) -> East
46.368
46.3685
46.369
46.3695
South <- Latitude -> North
measured data

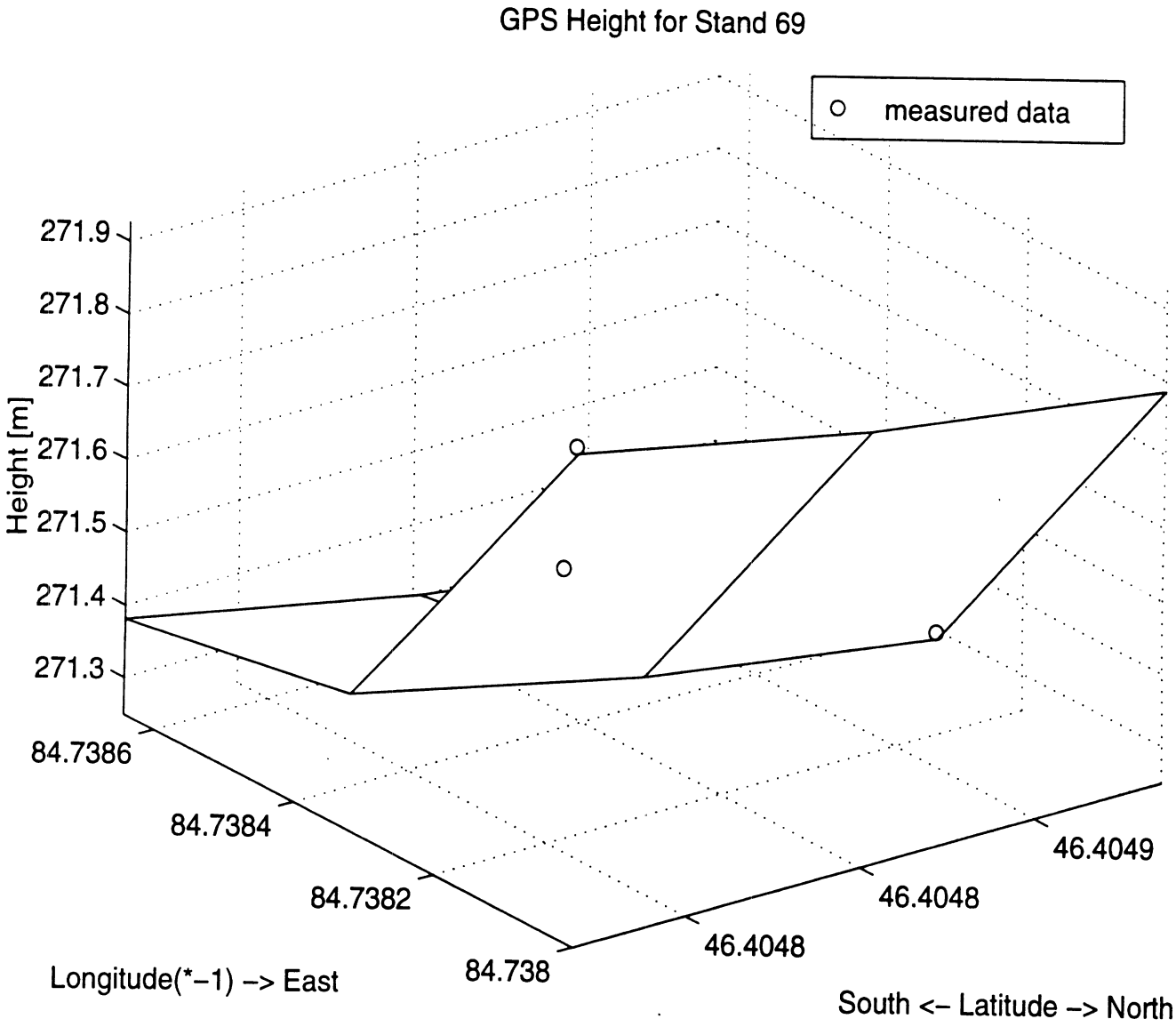
GPS Height for Stand 69
measured data
271.9
271.8
271.7
271.6
271.5
271.4
271.3
Height [m]
84.7386
84.7384
84.7382
84.738
Longitude(*-1) -> East
46.4049
46.4048
46.4048
South <- Latitude -> North

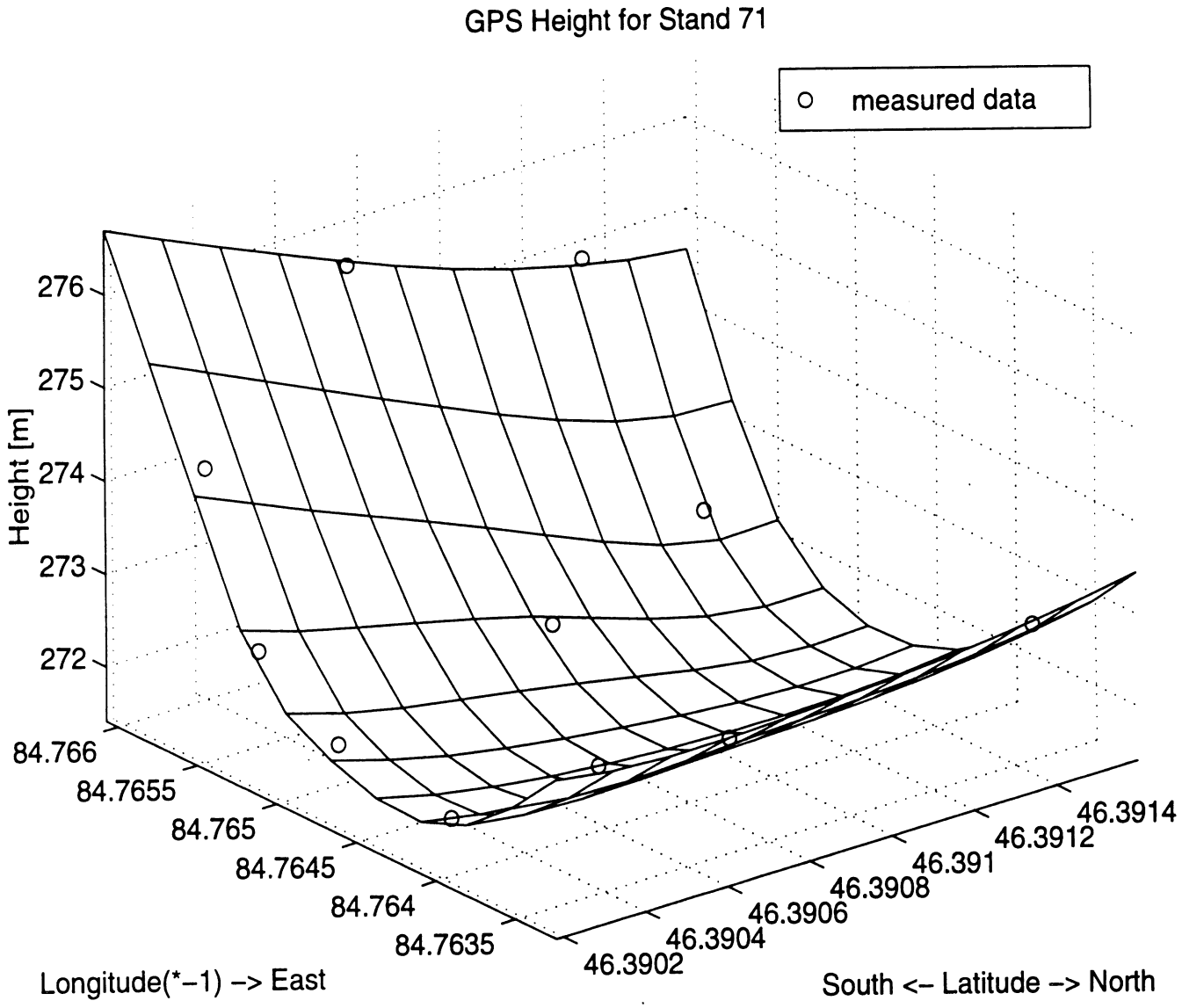
GPS Height for Stand 71
measured data
Height [m]
276
275
274
273
272
84.766
84.7655
84.765
84.7645
84.764
84.7635
Longitude(*−1) -> East
46.3902
46.3904
46.3906
46.3908
46.391
46.3912
46.3914
South <- Latitude -> North

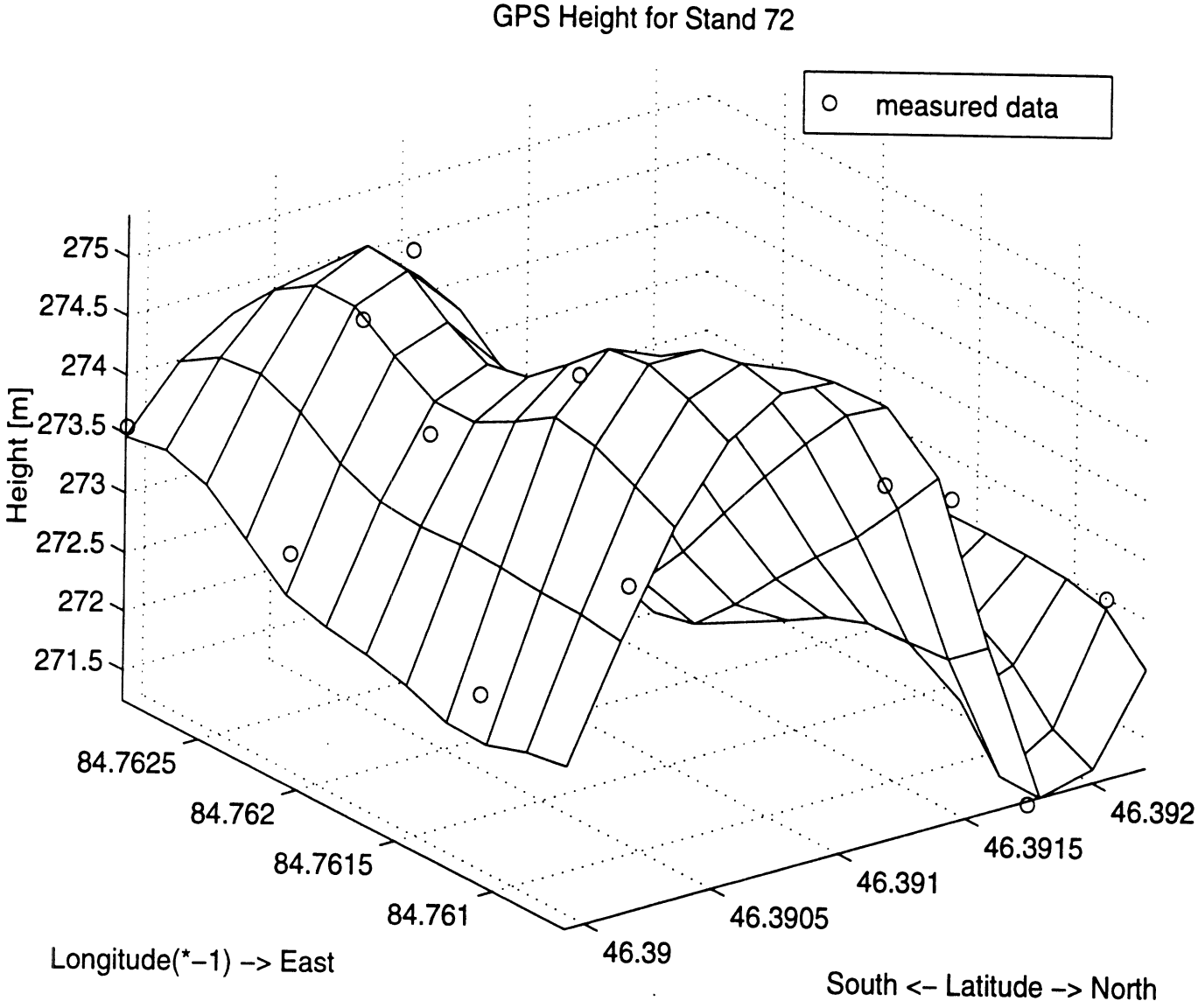
GPS Height for Stand 72
measured data
Height [m]
275
274.5
274
273.5
273
272.5
272
271.5
84.7625
84.762
84.7615
84.761
46.39
46.3905
46.391
46.3915
46.392
Longitude(*−1) -> East
South <- Latitude -> North

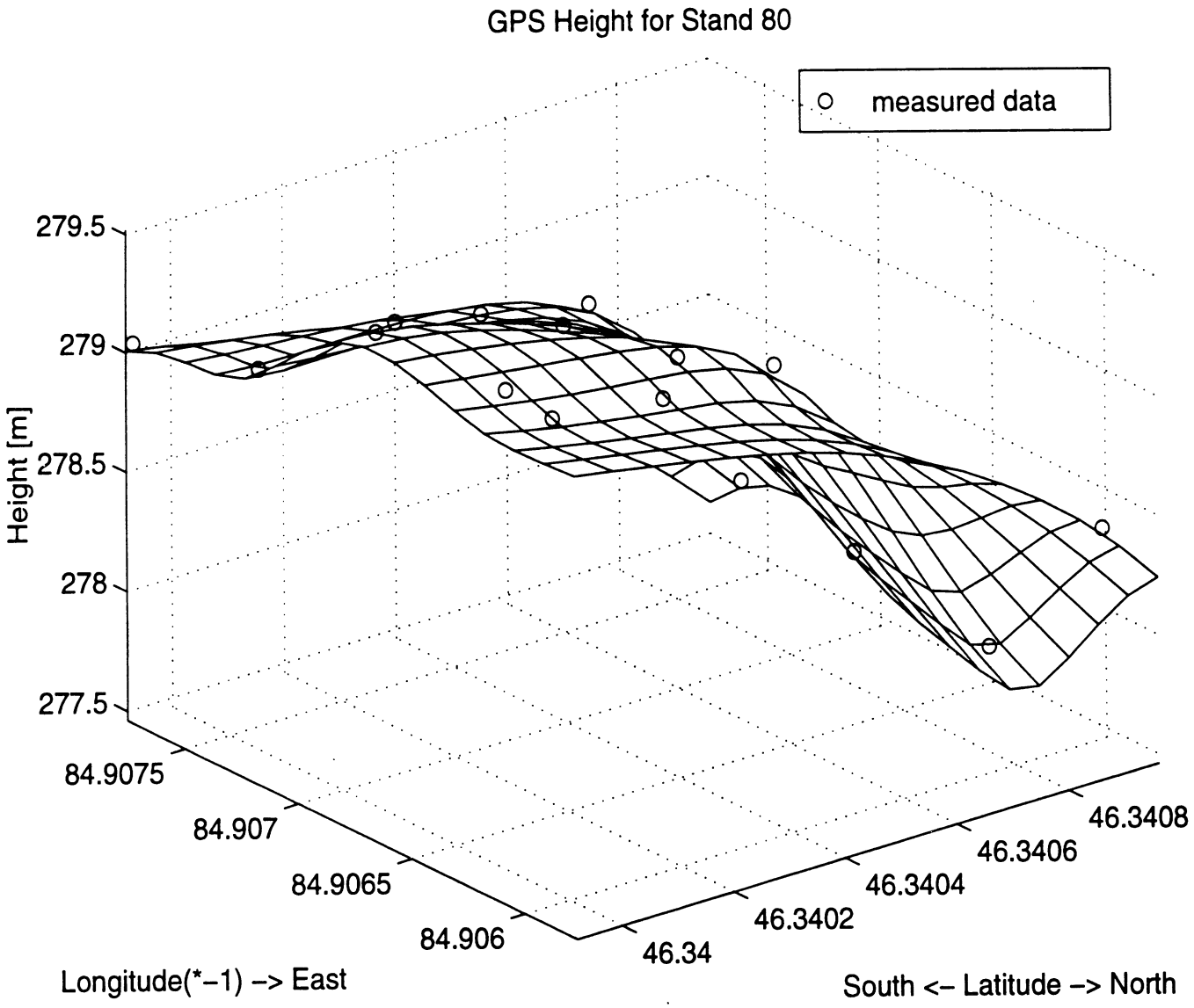
GPS Height for Stand 80
measured data
279.5
279
278.5
278
277.5
Height [m]
84.9075
84.907
84.9065
84.906
Longitude(*-1) -> East
46.34
46.3402
46.3404
46.3406
46.3408
South <- Latitude -> North

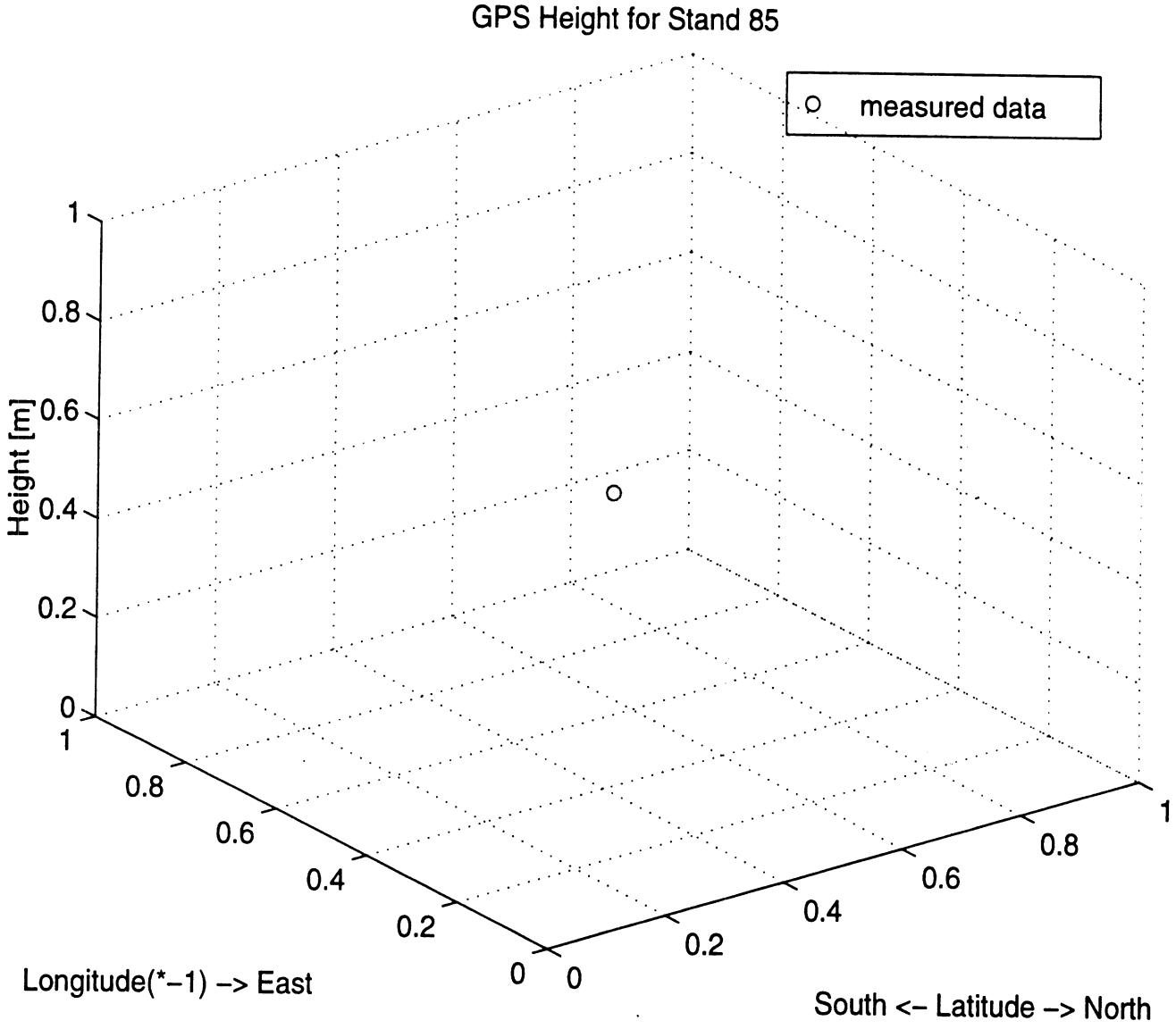
GPS Height for Stand 85
measured data
Height [m]
1
0.8
0.6
0.4
0.2
0
Longitude(*−1) -> East
South <- Latitude -> North

Stand 22 - Red pine - not sapling(~10 m)

Measured by Dennis Taeyeoul on May 19(Mon.).

Species ; All trees are red pine(99.9%).

Tree height ; ~10m

Ground surface ; very flat

Tree density ; Red pines were regularly planted following East-West direction(see below figure)

Weather ; a little rain, very windy, ~8 ^{o}C, not good condition to get data.

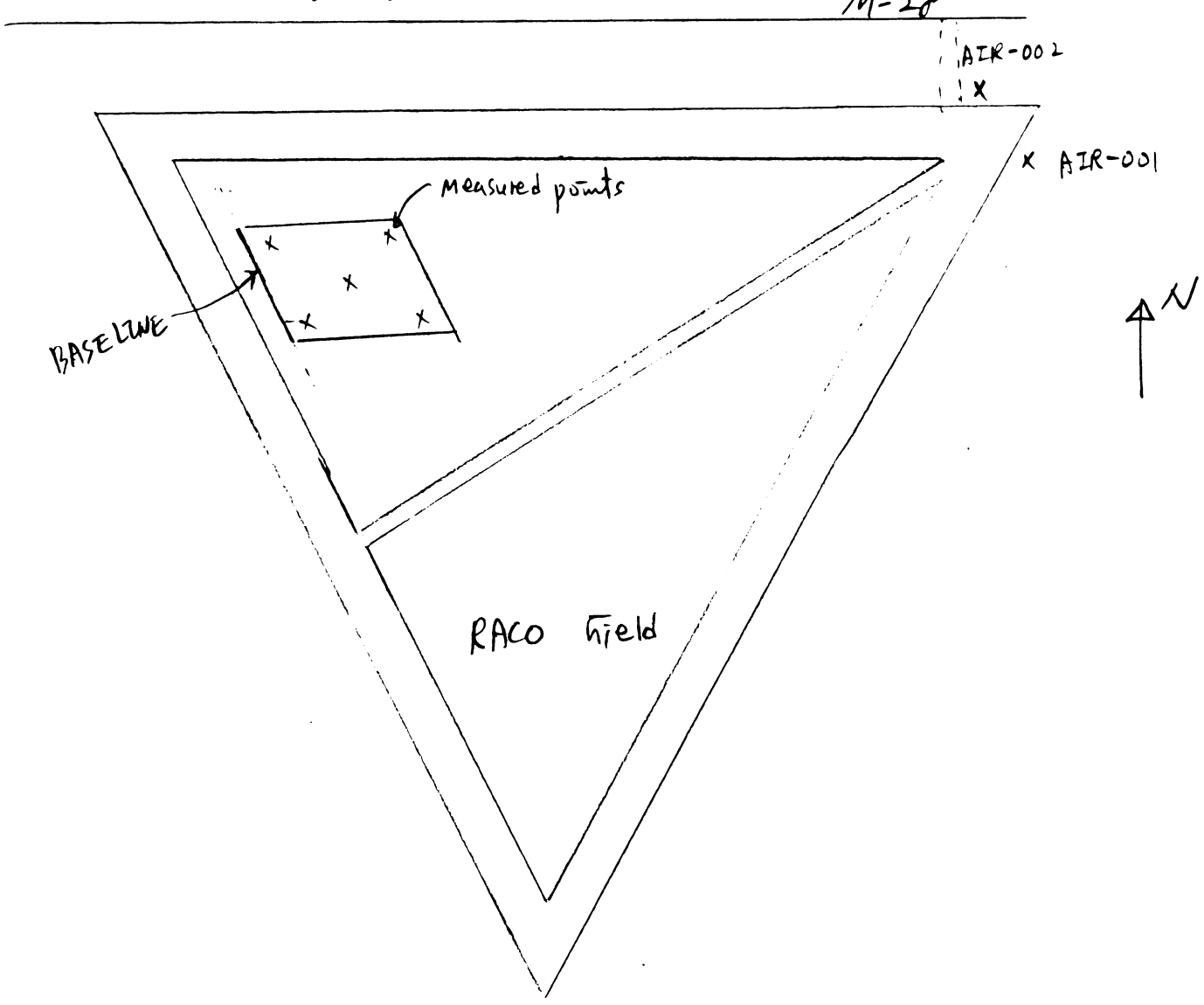

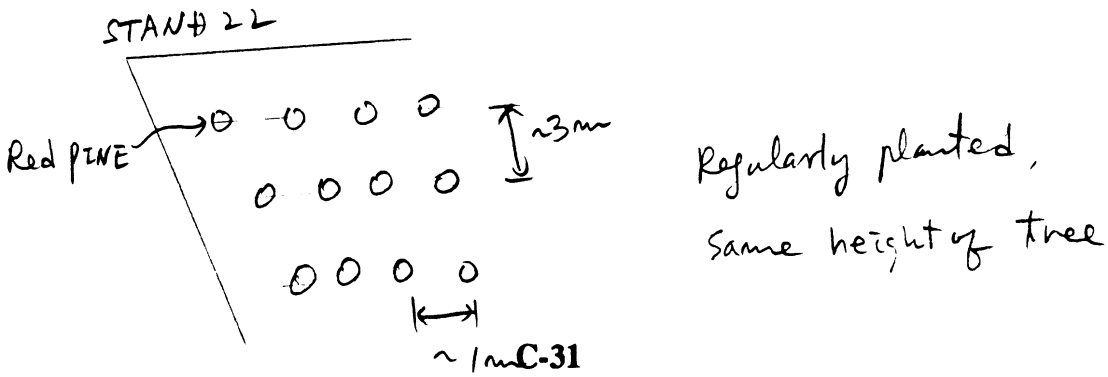

Stand 31 - Maple - pole

Measured by Kamal, Yutaka, Taeyeoul on May 23(Fri.).

Species ; Almost of all trees are Maples(> 90%).

Tree height ; greater than 15m

Ground surface ; flat

Tree density ; not dense, 1 tree/2m*2m

Weather ; no rain, very small wind, ~15 ^{o}C, very good condition to get data.

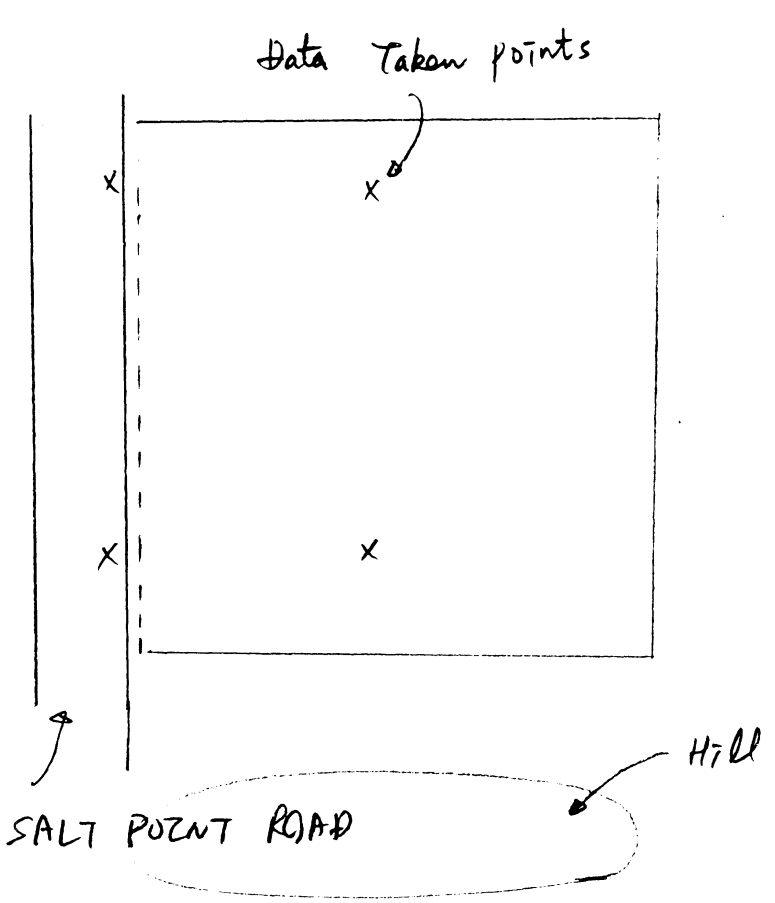

Almost flat / SALT POINT ROAD's SLOPE IS Increasing after T5 (or End of Base Line) to Southern direction

Stand 40 - Red Pine - sapling

Measured by Kamal, Yutaka, Taeyeoul on May 22(Thu.).

Species ; Almost of all red pine trees are regularly planted(> 90%). randomly growing jack pine.

Tree height ; greater than ~ 2m

Ground surface ; flat

Tree density ; spacing of 2m by 1m.

Weather ; no rain, no wind, ~15 ^{o}C, very good condition to get data.

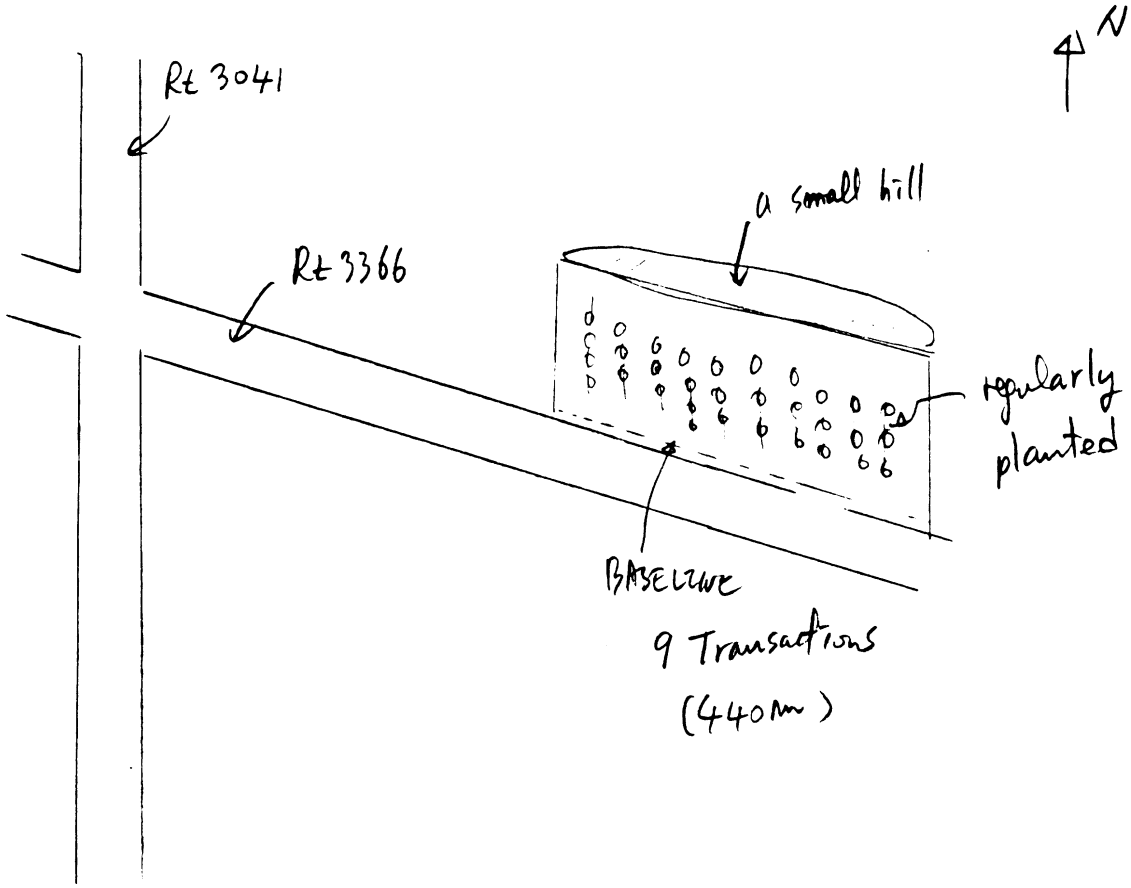

Stand 49 - Aspen - sapling

Measured by Kamal, Yutaka, Taeyeoul on May 23(Fri.).

Species ; Almost of all trees are aspen(> 90%).

Tree height ; 3 ~ 5m

Ground surface ; Ground level is linearly slanted, i.e. increasing from T1 to T5.

Tree density ; very dense, hard to move

Weather ; no rain, very small wind, ~15 ^{o}C, very good condition to get data.

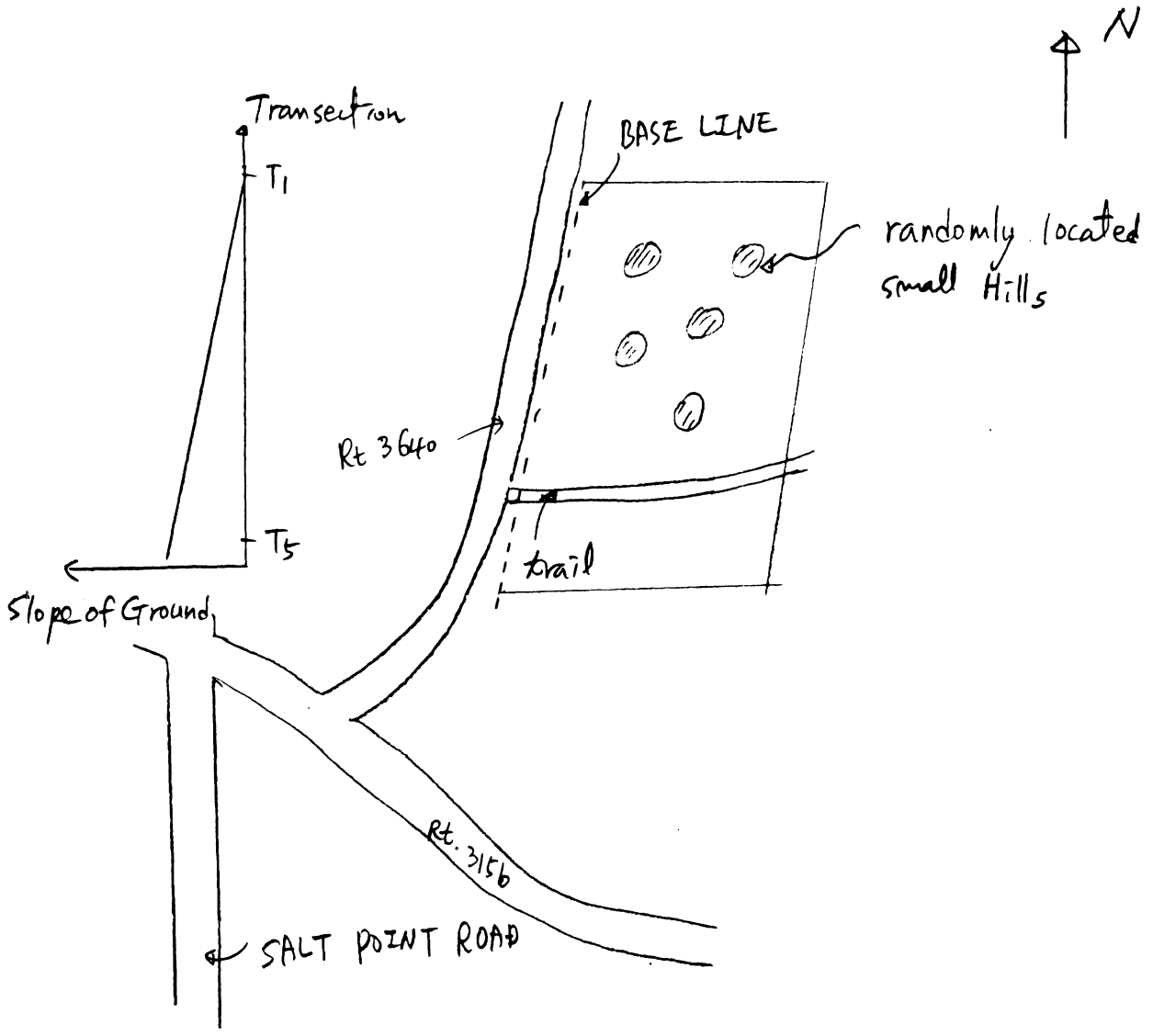

Stand 50 - Red Pine - mature

Measured by Kamal, Yutaka, Taeyeoul on May 24(Sat.).

Species ; All tall trees are Maples(> 90%).

Tree height ; ~ 20m, branches come out from height of ~10m.

Ground surface ; flat

Tree density ; not dense, 1 tree/2m*2m

Weather ; no rain, very small wind, ~15 ^{o}C, very good condition to get data.

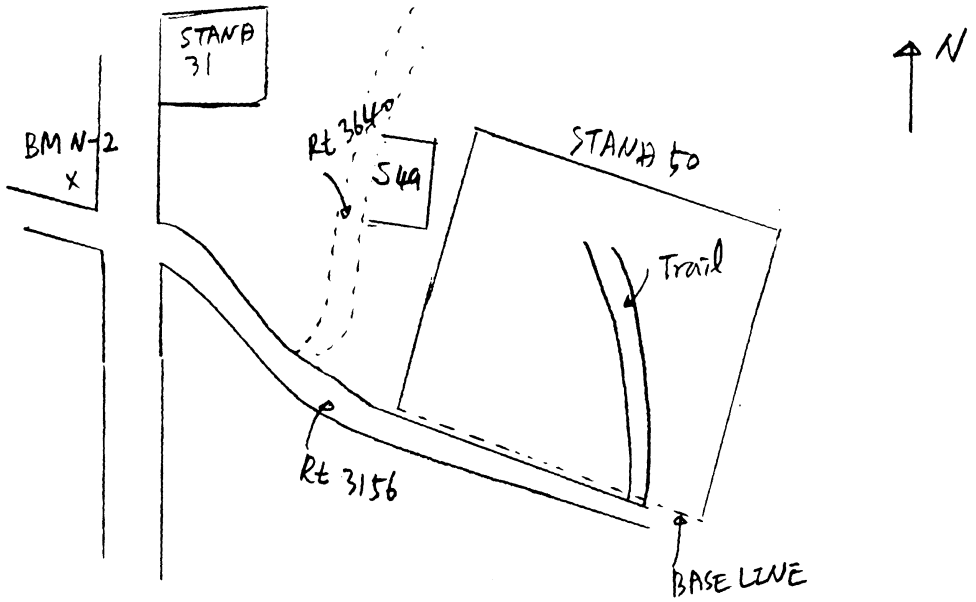

Ground of Road Rt 3156 is higher than S50's Ground, about 40 cm.

Stand 58 - Jack Pine - sapling

Measured by Yutaka, Taeyeoul on May 20(Tue.).

Species ; Almost of all trees are Jack pine(> 99.9%).

Tree height ; ~ 2m

Ground surface ; flat

Tree density ; Tree spacing is aoubt 2.5m by 2.5m, irregularly.

Weather ; no rain, very small wind, ~10 ^{o}C, very good condition to get data.

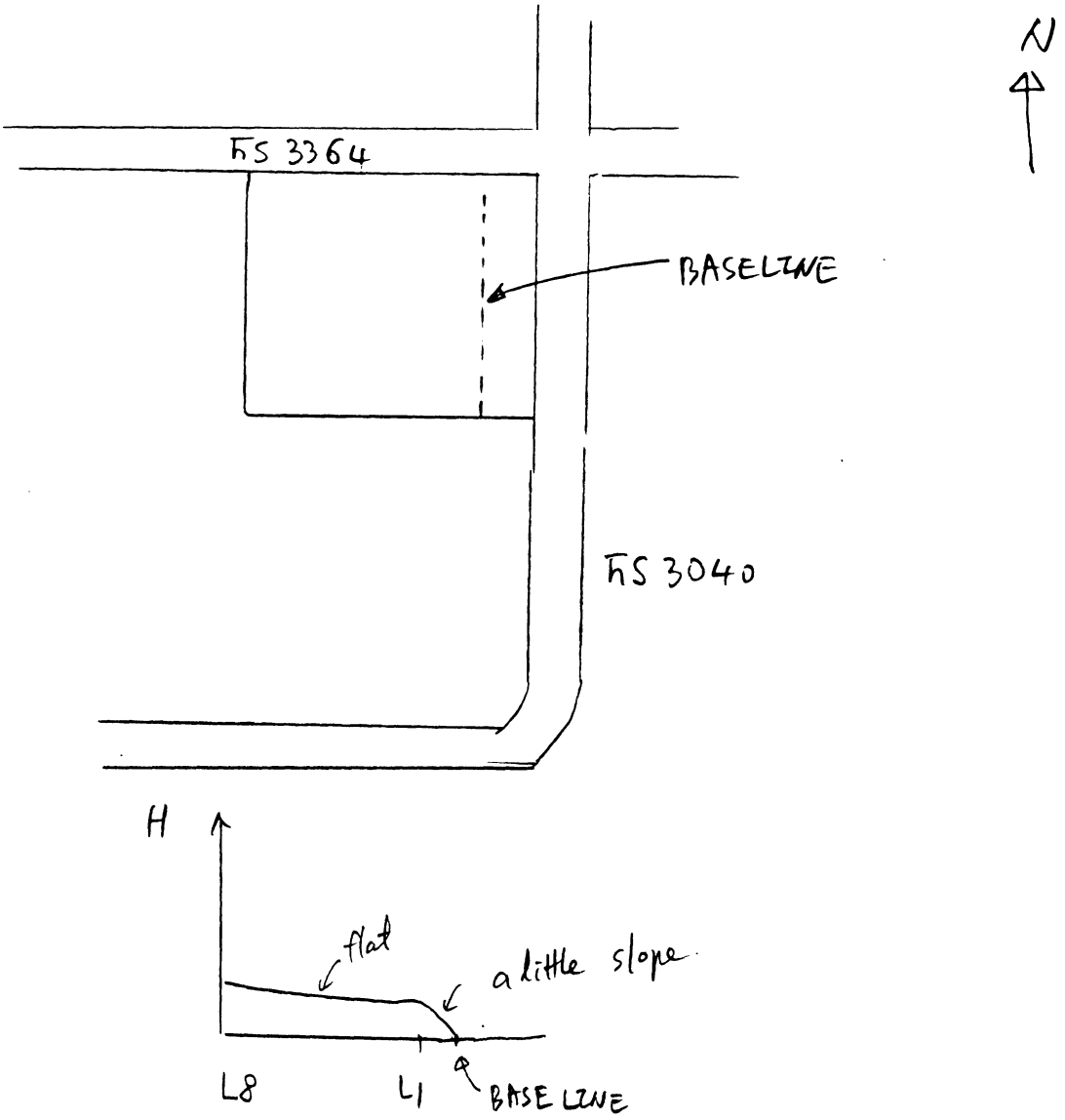

Stand 61 - Jack Pine - mature

Measured by Yutaka, Taeyeoul on May 21(Wed.).

Species ; All trees are Jack pine(> 99.9%).

Tree height ; ~ 15m

Ground surface ; flat

Tree density ; randomly located, tree spacing is 2.5m by 2.5m.

Weather ; no rain, very small wind, ~15 ^{o}C, very good condition to get data.

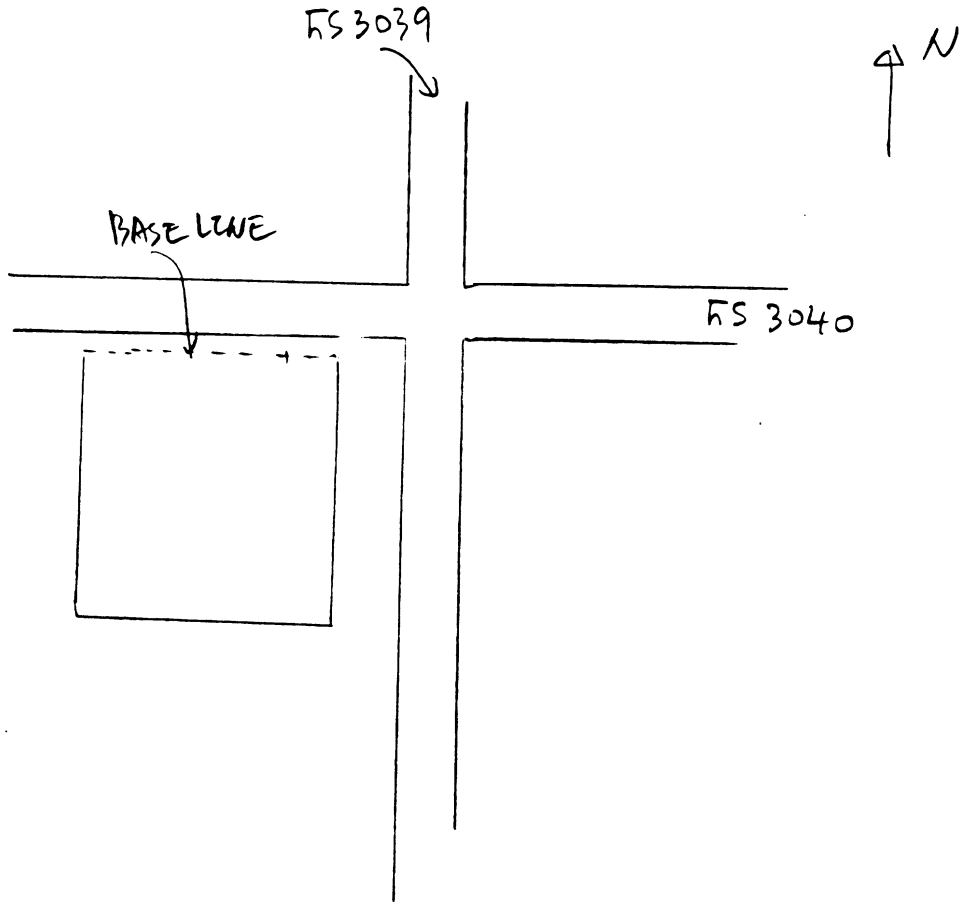

Stand 68 - Red Pine - mature

Measured by Kamal, Yutaka, Taeyeoul on May 21(Wed.).

Species ; All trees are Jack pine(> 99.9%).

Tree height ; greater than ~ 15m

Ground surface ; some locations are higher, generally flat.

Tree density ; regularly planted, tree spacing is 2.5m by 2.5m.

Weather ; no rain, no wind, ~15 ^{o}C, very good condition to get data.

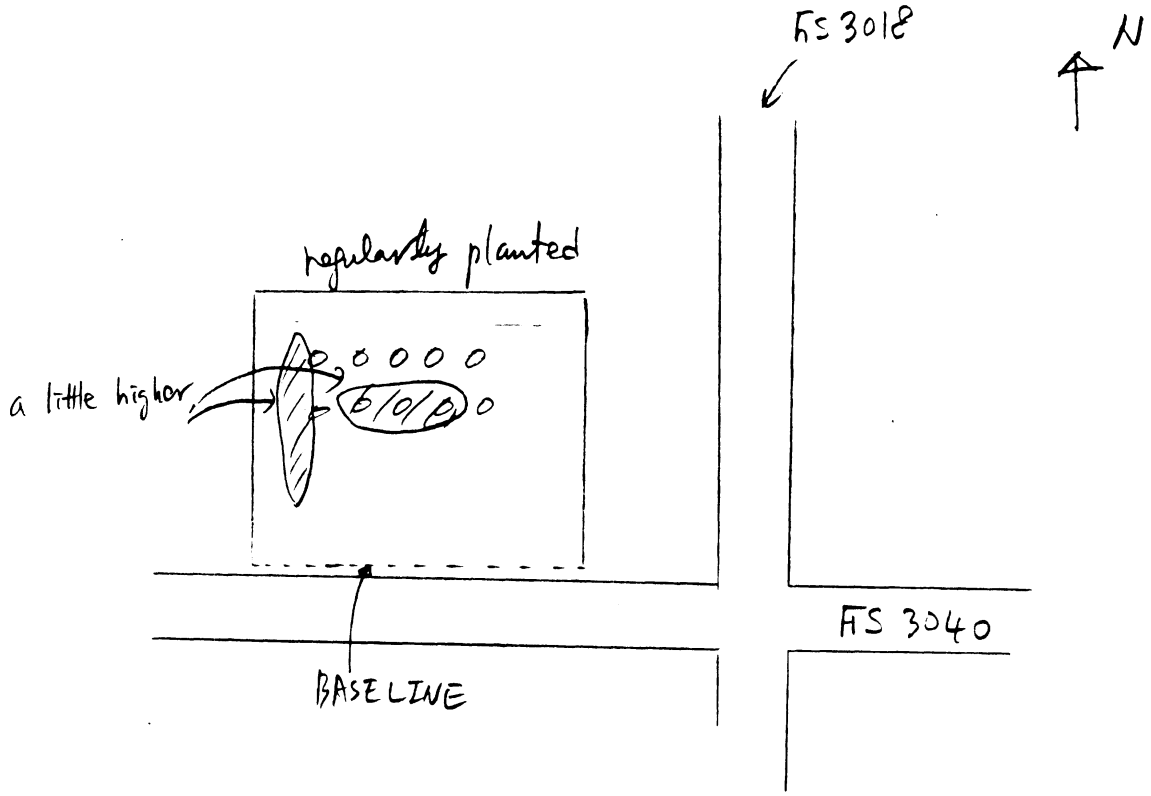

Stand 71 and 72 - Red Pine - pole

Measured by Kamal, Yutaka, Taeyeoul on May 22(Thu.).

Species ; All trees are Red pine(> 99.9%).

Tree height ; 10 ~ 15m

Ground surface ; flat and 2 ~3 hills

Tree density ; Almost of all red pine was already logged. There are several trees near hills.

Weather ; no rain, no wind, ~15 ^{o}C, very good condition to get data.

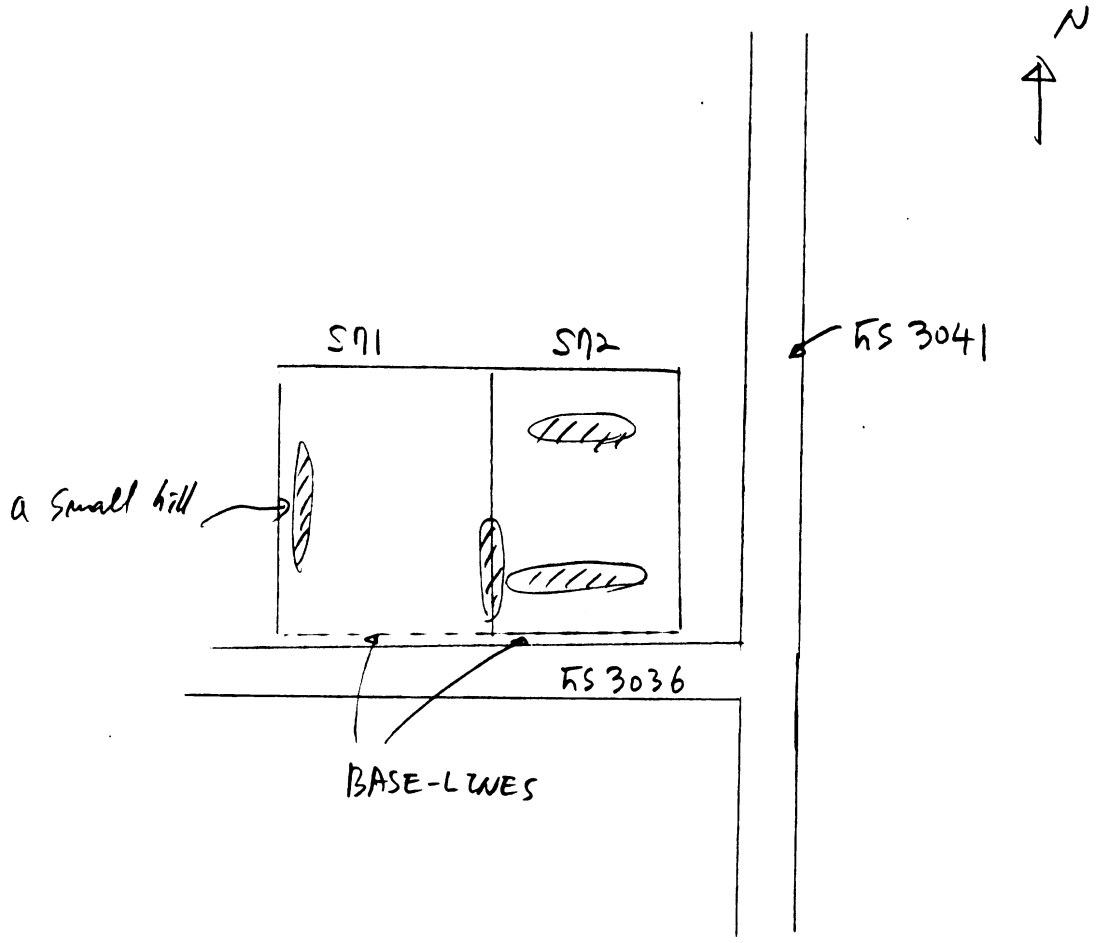

Appendix D:
Data of Ground Control Point(=GCP) Location

Table D-1 shows the information on GCPs.
Figure D-1 shows location of each GCP.
The detail data record is shown afterwards.
All the data are expressed on WGS coordinate.

Including the cover sheet, **appendix D** is totally 7 pages.

Table D-1 Ground Control Point(GCP) description (1 of 2)

GCP NO.	Description	Area	Measured by	Measured date
R2	Road intersection of Centerline Road & 20 Mile Road.	Rudyard	Leland,Dennis, Taeyeoul, Yutaka	May 18
R4	Road intersection of Tilson Road & 18 Mile Road. At the northwestern corner, there is "Christian Reformed Church".	Rudyard	the same as above	May 18
R5	Road intersection of Centerline Road & M48.	Rudyard	the same as above	May 18
R6	Road intersection of USFS3161(Flatfoot Road) & 3367(snow mobile trail)	Raco	kamal, Taeyeoul, Yutaka	May 24
R7	Cross point of USFS3161(Flatfoot Road) & Power line The power line is the same power line which is extending along USFS3364.	Raco	the same as above	May 24
R8	Road intersection of USFS3364 & USFS3018. USFS3364 is running from East to West and there is power line along USFS3364.	Raco	Leland, Dennis	May 20
R9	Road intersection of M28 & USFS3131(Sullivan Creek T.T.)	Raco	the same as above	May 2
R10NEAR	Road intersection of M28 & USFS3157(Rexford Road)	Raco	Kamal, Taeyeoul,Yutaka	May 24
R10	Road intersection of USFS3364 & USFS3157(Rexford Road)	Raco	the same as above	May 24
R11	Road intersection of USFS3159(Salt Point Road) & Wyckoff Road. This GCP is located 620 meter south of the lakeshore of Lake Superior. Wyckoff Road is not shown in the map.	Mc Nearney	the same as above	May 24
R12	Located West of Naomikong Point. This GCP is along the FH42(Curley Lewis Road) and is located at the cross point of FH42 & Road to Naomikong pond(ball field).	Mc Nearney	the same as above	May 24
R13	Located 4miles West of Naomikong Point. This GCP is along the FH42(Curley Lewis Road) and is located at the cross point of FH42 & North Country Trail.	Mc Nearney	the same as above	May 24
R14	The Northeast corner of Raco airfield runway.	Raco	Leland, Dennis	May 20
R15	The Northwest corner of Raco airfield runway.	Raco	the same as above	May 20

Table D-1 Ground Control Point(GCP) description (2 of 2)

GCP NO.	Description	Area	Measured by	Measured date
R16	The middle point between R15 and R17. (Raco airfield runway.)	Raco	Leland, Dennis	May 20
R17	The South corner of Raco airfield runway.	Raco	the same as above	May 20
R18	Road intersection of M28 & USFS3154(Ranger Road)	Raco	Dennis, Yi-Cheng	May 24
R19	Road intersection of USFS3364 & USFS3154(Ranger Road)	Raco	the same as above	May 24
R20	Road intersection of USFS3581 & USFS3154(Ranger Road)	Raco	the same as above	May 24
R21	Road intersection of USFS3622 & USFS3154(Ranger Road)	Raco	Taeyeoul, Yutaka	May 22
R22	Road intersection of USFS3159(Salt Point Road) & USFS3156(Richardson Avery Grade)	Mc Nearney	Taeyeoul, Yutaka	May 20
R24	Road intersection of M28 & USFS3139(Dick Road)	Raco	Kamal, Taeyeoul, Yutaka	May 24
R30	Road intersection of M28 & USFS3161(Flatfoot Road)	Raco	the same as above	May 24
R31	Road intersection of USFS3605 & USFS3364	Raco	Dennis, Yi-Cheng	May 24
R33	Road intersection of Centerline Road & M48.	Rudyard	the same as above	May 24
R34	Road intersection of Kallio Road & 19 Mile Road.	Rudyard	the same as above	May 24
R40	This GCP is located at the entrance of Cryderman hill. This point is along USFS3159 (Salt Point Road) . This GCP is located 410 meter south of the lakeshore of Lake Superior.	Mc Nearney	Kamal, Taeyeoul, Yutaka	May 24
R41	Road intersection of USFS3159 (Salt Point Road) & USFS3150(Curley Lewis Road).	Mc Nearney	Kamal, Taeyeoul, Yutaka	May 24
R42	Road intersection of USFS3364 & USFS3040. This GCP is located northeastern corner of Stand 58.	Raco	Taeyeoul,Yutaka	May 20

Remark)

1. The map shown below is very helpful to know the exact location of the GCPs.
   "Eastern Upper Peninsula of Michigan" $3.95 ISBN 1-56464-354-9
   Distributed by Universal Map, Inc. P.O. Box 15 795 Progress Court Williamston, MI. 48895 Phone (517)-655-5641
   Stock No. MI206

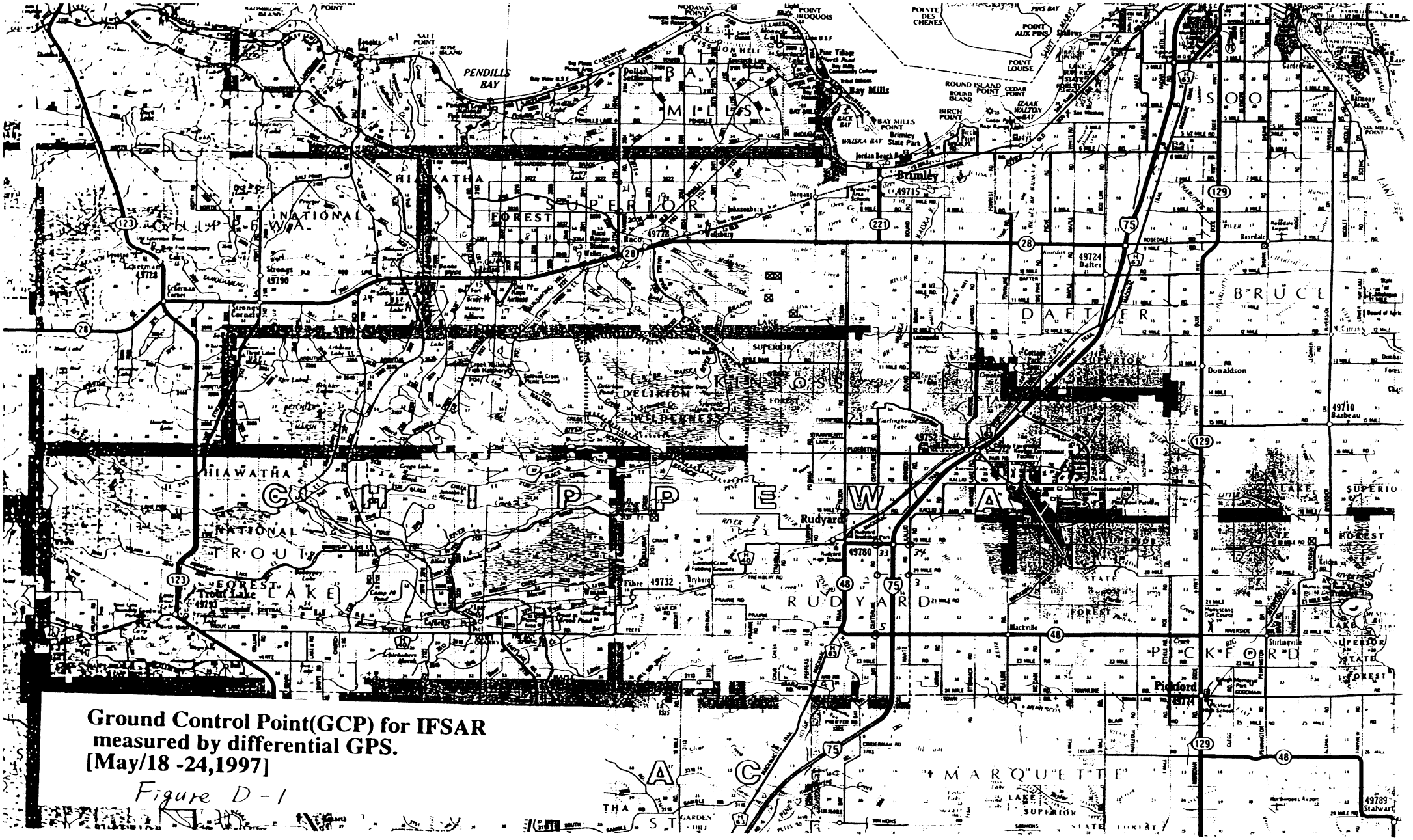

Ground Control Point(GCP) for IFSAR measured by differential GPS. [May/18 -24,1997]

Figure D-1

GCP measurement of Ground Control Points(=GCPs)

Pnt #	Latitude	Longitude	Height	Code	
1005,	46.2159930864,	-84.5716630728,	207.031,	R2-1	GCP "R2" No.1
1006,	46.2160548285,	-84.5715898442,	206.907,	R2-2	GCP "R2" No.2
1007,	46.2159567158,	-84.5715958889,	206.842,	R2-3	GCP "R2" No.3
1008,	46.2159595341,	-84.5717193246,	206.875,	R2-4	GCP "R2" No.4
1009,	46.2160450130,	-84.5717210675,	206.933,	R2-5	GCP "R2" No.5
1010,	46.2451467360,	-84.5924850466,	211.120,	R4-1	GCP "R4" No.1
1011,	46.2451885535,	-84.5924081648,	210.922,	R4-2	GCP "R4" No.2
1012,	46.2450965072,	-84.5924086203,	210.933,	R4-3	GCP "R4" No.3
1013,	46.2450922316,	-84.5925334188,	211.020,	R4-4	GCP "R4" No.4
1014,	46.2451822000,	-84.5925362311,	211.025,	R4-5	GCP "R4" No.5
1000,	46.1870756889,	-84.5716812758,	203.182,	R5-1	GCP "R5" No.1
1001,	46.1871502019,	-84.5715828700,	202.900,	R5-2	GCP "R5" No.2
1002,	46.1870113742,	-84.5715860187,	203.053,	R5-3	GCP "R5" No.3
1003,	46.1870087821,	-84.5717947099,	202.910,	R5-4	GCP "R5" No.4
1004,	46.1871423580,	-84.5717901641,	202.922,	R5-5	GCP "R5" No.5
2022	46.358503917	-84.893683442	281.662	R6	GCP "R6"
2023	46.367233003	-84.893898458	277.844	R78	GCP "R7" No.1
2024	46.367112186	-84.893884428	276.955	R78E	GCP "R7" No.2
1005	46.375190372	-84.801734792	276.557	R8	GCP at road intersection of 3364&3018
1000	46.388173172	-84.803176236	278.946	R8	Maybe wrong
1001	46.388166236	-84.803181056	278.938	R8-CHECK	Maybe wrong
1000	46.365141342	-84.760581550	263.327	R8	Maybe GCP "R9"
2020	46.375215489	-84.833054431	283.468	R10E	GCP "R10" (Center)
2019	46.358734100	-84.829831186	278.615	R10NEAR	GCP "R10Near"
2008,	46.4549477881,	-84.9058569749,	205.738,	R11F	GCP "R11" No.1
2009,	46.4549553575,	-84.9059144442,	205.665,	R11E	GCP "R11" No.2 (Center)
2014,	46.4730625042,	-84.9573431082,	213.650,	R12A	GCP "R12" No.1
2015,	46.4731295504,	-84.9569849900,	214.061,	R12B	GCP "R12" No.2
2016,	46.4729805411,	-84.9566907434,	214.475,	R12C	GCP "R12" No.3
2017,	46.4865157492,	-85.0394154128,	211.261,	R13A	GCP "R13" No.1
1000	46.356880953	-84.804882997	274.760	R14	GCP "R14"
1001	46.356454694	-84.824510278	277.009	R15	GCP "R15"
1002	46.356454703	-84.824510278	277.005	R15-2	GCP "R15"
1003	46.350713006	-84.819791794	275.375	R16	GCP "R16"
1004	46.344839564	-84.814679747	275.618	R17	GCP "R17"
1008,	46.3694893633,	-84.7388115976,	259.044,	IT-1	GCP "R18" No.1
1009,	46.3694390760,	-84.7390001988,	259.091,	IT-2	GCP "R18" No.2
1010,	46.3693180115,	-84.7388104672,	258.946,	IT-3	GCP "R18" No.3
1011,	46.3732296627,	-84.7390470582,	259.416,	IT19-1	GCP "R19" No.1
1012,	46.3733355559,	-84.7390545540,	259.473,	IT19-2	GCP "R19" No.2
1013,	46.3733039973,	-84.7389944168,	259.513,	IT19-3	GCP "R19" No.3

```
1014,46.3896860152,-84.7390268249,266.384,IT20-1     GCP "R20" No.1
1015,46.3896005033,-84.7390261682,266.409,IT20-2     GCP "R20" No.2
1016,46.3895905163,-84.7391350773,266.300,IT20-3     GCP "R20" No.3

2040,46.4042942552,-84.7392223628,272.399,R21A       GCP "R21" No.1
2041,46.4044018162,-84.7392304077,272.365,R21B       GCP "R21" No.2
2042,46.4043883303,-84.7391176508,272.431,R21C       GCP "R21" No.3
2043,46.4042878505,-84.7391207019,272.440,R21D       GCP "R21" No.4
2044,46.4041332027,-84.7391172883,272.454,R21E       GCP "R21" No.5
2045,46.4040676061,-84.7391176308,272.468,R21F       GCP "R21" No.6
2046,46.4040730130,-84.7392110507,272.476,R21G       GCP "R21" No.7
2047,46.4041331362,-84.7392097999,272.479,R21H       GCP "R21" No.8
2048,46.4040949452,-84.7391640552,272.561,R21I       GCP "R21" No.9
2049,46.4043478102,-84.7391624788,272.504,R21J       GCP "R21" No.10

1000,46.4297625588,-84.9061364517,266.469,BM NEAR ST45 --->GCP "R22" Corner_1
1002,46.4297385741,-84.9059882138,266.574,ROAD CORN ST45 ->GCP "R22" Corner_2
1003,46.4295992170,-84.9059718765,266.597,ROAD CORN ST45 ->GCP "R22" Corner_3
1004,46.4296658391,-84.9061221572,266.561,ROAD CORN ST45 ->GCP "R22" Corner_4
1005,46.4296928091,-84.9060537808,266.666,ROAD CORN ST45 ->GCP "R22" Center

2025 46.351503847  -84.905825956  275.119 R24        GCP "R24"

2021 46.356631278  -84.893252253  282.384 R30        GCP "R30"

1017,46.3751789172,-84.7809876803,275.045,IT31-1     GCP "R31" No.1
1018,46.3751902311,-84.7808610433,274.628,IT31-2     GCP "R31" No.2
1019,46.3752989637,-84.7808818752,274.445,IT31-3     GCP "R31" No.3

1020 46.230411150  -84.571541517  210.555 IT33-1        GCP "R33" No.1
1023 46.230559069  -84.571815319  210.620 IT33-32       GCP "R33" No.2
1024 46.230559042  -84.571612122  210.558 IT33-42       GCP "R33" No.3

1025 46.230471825  -84.550923908  209.141 IT34-1        GCP "R34" No.1
1026 46.230474958  -84.550780092  209.158 IT34-2        GCP "R34" No.2
1027 46.230584964  -84.550770667  209.170 IT34-3        GCP "R34" No.3

2012,46.4586133798,-84.9058626065,205.821,CRYDERMAN1    GCP "R40"
2013,46.4649589117,-84.9058862222,185.549,CORNER-LAKE   GCP "R41"

1030 46.375154703  -84.770503836  274.736 S58-CORNER1 GCP "R42" corner1
1031 46.375151878  -84.770375394  274.802 S58-CORNER2 GCP "R42" corner2
1032 46.375287639  -84.770373375  274.897 S58-CORNER3 GCP "R42" corner3
1033 46.375421111  -84.770367964  275.173 S58-CORNER4 GCP "R42" corner4
1034 46.375418719  -84.770498033  275.033 S58-CORNER5 GCP "R42" corner5
1035 46.375284444  -84.770503714  274.807 S58-CORNER6 GCP "R42" corner6
1036 46.375154783  -84.770503872  274.743 S58-CORNER7 GCP "R42" corner7
```

Appendix E: NGS Data Sheet

Two benchmarks are used in this measurement. Here are the orignal sources of these two benchmarks.
Including the cover sheet, appendix E is totally 6 pages.

The NGS Data Sheet

```
DATABASE = Sybase ,PROGRAM = datasheet, VERSION = 5.21
       Retrieval Date = MAY  8, 1997          Version = 5.21
Starting Datasheet Retrieval...
1        National Geodetic Survey,   Retrieval Date = MAY  8, 1997
 RJ1102 ***********************************************************************
 RJ1102  DESIGNATION -  OVERPASS
 RJ1102  PID         -  RJ1102
 RJ1102  STATE/COUNTY-  MI/CHIPPEWA
 RJ1102  USGS QUAD   -  RUDYARD (1977)
 RJ1102
 RJ1102                         *CURRENT SURVEY CONTROL
 RJ1102  ______________________________________________________________________
 RJ1102* NAD 83(1994)-  46 11 14.23823(N)    084 33 44.09326(W)      ADJUSTED
 RJ1102* NAVD 88     -       204.      (meters)      669.      (feet)  SCALED
 RJ1102  ______________________________________________________________________
 RJ1102  LAPLACE CORR-          -3.49  (seconds)                      DEFLEC96
 RJ1102  GEOID HEIGHT-         -36.07  (meters)                       GEOID96
 RJ1102
 RJ1102  HORZ ORDER  -  THIRD
 RJ1102
 RJ1102
 RJ1102
 RJ1102.The horizontal coordinates were established by classical geodetic methods
 RJ1102.and adjusted by the National Geodetic Survey in February 1997.
 RJ1102
 RJ1102.The orthometric height was scaled from a topographic map.
 RJ1102
 RJ1102.The Laplace correction was computed from DEFLEC96 derived deflections
 RJ1102
 RJ1102.The geoid height was determined by GEOID96.
 RJ1102
 RJ1102;                    North          East      Units   Scale      Converg.
 RJ1102;SPC MI N      -   158,934.365 8,188,150.489   MT  0.99990429 +1 45 43.1
 RJ1102;UTM  16       - 5,117,745.562   688,120.601   MT  1.00003505 +1 45 34.6
 RJ1102
 RJ1102:                Primary Azimuth Mark                     Grid Az
 RJ1102:SPC MI N      -  OVERPASS AZ MK                          265 03 18.2
 RJ1102:UTM  16       -  OVERPASS AZ MK                          265 03 26.7
 RJ1102
 RJ1102|-----------------------------------------------------------------------|
 RJ1102| PID    Reference Object                    Distance      Geod. Az     |
 RJ1102|                                                          dddmmss.s    |
 RJ1102|        OVERPASS RM 1                       29.329 METERS 12119        |
 RJ1102|        OVERPASS RM 2                       16.923 METERS 20456        |
 RJ1102| RJ1112 MAPLE HILL MICROWAVE MAST          APPROX.17.4 KM 2584451.2    |
 RJ1102|        OVERPASS AZ MK                                    2664901.3    |
 RJ1102| RJ1101 RUDYARD BELL TEL CO MICROWAVE      APPROX. 6.1 KM 3483321.4    |
 RJ1102|-----------------------------------------------------------------------|
 RJ1102
 RJ1102                          SUPERSEDED SURVEY CONTROL
 RJ1102
 RJ1102  NAD 83(1986)-  46 11 14.23079(N)    084 33 44.09122(W)      ADJUSTED
 RJ1102  NAD 27      -  46 11 14.16536(N)    084 33 43.92730(W)      ADJUSTED
 RJ1102
 RJ1102.Superseded values are not recommended for survey control.
 RJ1102.NGS no longer adjusts projects to the NAD 27 or NGVD 29 datums.
 RJ1102.See file format.dat to determine how the superseded data were derived.
 RJ1102
```

```
RJ1102  HISTORY      - Date      Condition        Recov. By
RJ1102  HISTORY      - 1965      MONUMENTED       CGS
RJ1102
RJ1102                            STATION DESCRIPTION
RJ1102
RJ1102'DESCRIBED BY COAST AND GEODETIC SURVEY 1965 (LMC)
RJ1102'THE STATION IS LOCATED NEAR THE NORTHWEST CORNER OF A BRIDGE, WHERE
RJ1102'STATE HIGHWAY 48
RJ1102'CROSSES OVER INTERSTATE HIGHWAY 75, ABOUT 3-1/2 MILES
RJ1102'SOUTHEAST OF RUDYARD, 6-1/2 MILES
RJ1102'WEST-SOUTHWEST OF KINROSS, AND ON
RJ1102'STATE OWNED PROPERTY.
RJ1102'
RJ1102'TO REACH THE STATION FROM THE POST OFFICE IN RUDYARD, GO EAST ON
RJ1102'MAIN STREET FOR
RJ1102'0.4 MILE TO A CROSSROAD.  TURN RIGHT AND GO SOUTH ON
RJ1102'MACKINAC TRAIL AND STATE HIGHWAY
RJ1102'48 FOR 3 MILES TO A SIDE ROAD LEFT.
RJ1102'TURN LEFT AND GO EAST ON HIGHWAY 48 FOR 1.5 MILES
RJ1102'TO A CROSSROAD AND
RJ1102'THE AZIMUTH MARK ON THE RIGHT.  CONTINUE EAST ON HIGHWAY 48 FOR 0.45
RJ1102'MILE TO THE
RJ1102'STATION ON THE LEFT NEAR THE NORTHWEST CORNER OF THE BRIDGE.
RJ1102'
RJ1102'STATION MARKS ARE STANDARD DISKS STAMPED OVERPASS 1965.  THE
RJ1102'SURFACE DISK IS
RJ1102'SET IN A ROUND CONCRETE MONUMENT WHICH IS FLUSH WITH
RJ1102'WITH THE SURFACE OF THE GROUND.
RJ1102'IT IS 213 FEET WEST OF THE CENTER OF
RJ1102'THE SOUTH BOUND LANE OF INTERSTATE 75, 173 FEET
RJ1102'SOUTHWEST OF A FENCE
RJ1102'CORNER, 133 FEET SOUTH OF A WIRE FENCE, AND 91 FEET NORTHEAST OF
RJ1102'THE NORTHWEST
RJ1102'CORNER OF THE BRIDGE.  THE UNDERGROUND DISK IS SET IN AN
RJ1102'IRREGULAR MASS OF CONCRETE
RJ1102'44 INCHES BELOW THE SURFACE OF THE GROUND.
RJ1102'
RJ1102'REFERENCE MARK NO. 1, A STANDARD DISK STAMPED OVERPASS NO 1 1965,
RJ1102'CEMENTED IN A
RJ1102'DRILLED HOLE IN THE NORTH END OF THE 3RD CONCRETE FOOTING
RJ1102'EAST OF THE WEST END OF THE
RJ1102'BRIDGE.  THE FOOTING PROJECTS 30 INCHES.
RJ1102'
RJ1102'REFERENCE MARK NO. 2, A STANDARD DISK STAMPED OVERPASS NO 2 1965,
RJ1102'CEMENTED IN A
RJ1102'DRILLED HOLE IN THE NORTH END OF THE 1ST CONCRETE FOOTING
RJ1102'EAST OF THE WEST END OF THE
RJ1102'BRIDGE.  THE FOOTING PROJECTS 14 INCHES.
RJ1102'
RJ1102'AZIMUTH MARK, A STANDARD DISK STAMPED OVERPASS 1965, IS SET IN A
RJ1102'ROUND CONCRETE
RJ1102'MONUMENT WHICH PROJECTS 4 INCHES.  IT IS 57 FEET SOUTH
RJ1102'OF THE CENTER OF STATE HIGHWAY
RJ1102'48, 32 FEET WEST OF THE CENTER OF A
RJ1102'GRAVELED ROAD, 3 FEET NORTH OF A TELEPHONE POLE,
RJ1102'AND 2 FEET SOUTH OF A
RJ1102'METAL WITNESS POST.

*** retrieval complete.
Elapsed Time = 00:00:02
```

The NGS Data Sheet

```
DATABASE = Sybase ,PROGRAM = datasheet, VERSION = 5.21
      Retrieval Date = MAY  5, 1997          Version = 5.21
Starting Datasheet Retrieval...
1       National Geodetic Survey,   Retrieval Date = MAY  5, 1997
 RJ0241 ***********************************************************************
 RJ0241  DESIGNATION -  T 44
 RJ0241  PID         -  RJ0241
 RJ0241  STATE/COUNTY-  MI/CHIPPEWA
 RJ0241  USGS QUAD   -  SULLIVAN CREEK (1978)
 RJ0241
 RJ0241                        *CURRENT SURVEY CONTROL
 RJ0241  ______________________________________________________________________
 RJ0241* NAD 83(1994)-  46 21 32.17537(N)    084 50 44.39915(W)      ADJUSTED
 RJ0241* NAVD 88     -       280.746  (meters)     921.08   (feet)  ADJUSTED
 RJ0241  ______________________________________________________________________
 RJ0241  X           -    396,162.391 (meters)                      COMP
 RJ0241  Y           -  -4,391,871.074 (meters)                     COMP
 RJ0241  Z           -   4,593,049.896 (meters)                     COMP
 RJ0241  LAPLACE CORR-          -5.88  (seconds)                    DEFLEC96
 RJ0241  ELLIP HEIGHT-         244.86  (meters)                     GPS OBS
 RJ0241  GEOID HEIGHT-         -35.89  (meters)                     GEOID96
 RJ0241  DYNAMIC HT  -         280.758 (meters)     921.12  (feet)  COMP
 RJ0241  MODELED GRAV-     980,650.3   (mgal)                       NAVD 88
 RJ0241
 RJ0241  HORZ ORDER  -  FIRST
 RJ0241  VERT ORDER  -  FIRST      CLASS II
 RJ0241  ELLP ORDER  -  FOURTH     CLASS I
 RJ0241
 RJ0241
 RJ0241
 RJ0241.The horizontal coordinates were established by GPS observations
 RJ0241.and adjusted by the National Geodetic Survey in February 1997.
 RJ0241
 RJ0241.The orthometric height was determined by differential leveling
 RJ0241.and adjusted by the National Geodetic Survey in June 1991.
 RJ0241
 RJ0241.The X, Y, and Z were computed from the position and the ellipsoidal ht.
 RJ0241
 RJ0241.The Laplace correction was computed from DEFLEC96 derived deflections.
 RJ0241
 RJ0241.The ellipsoidal height was determined by GPS observations
 RJ0241.and is referenced to NAD 83.
 RJ0241
 RJ0241.The geoid height was determined by GEOID96.
 RJ0241
 RJ0241.The dynamic height is computed by dividing the NAVD 88
 RJ0241.geopotential number by the normal gravity value computed on the
 RJ0241.Geodetic Reference System of 1980 (GRS 80) ellipsoid at 45
 RJ0241.degrees latitude (G = 980.6199 gals.).
 RJ0241
 RJ0241.The modeled gravity was interpolated from observed gravity values.
 RJ0241
 RJ0241;                    North         East      Units   Scale      Converg.
 RJ0241;SPC MI N     -   177,371.816 8,165,763.023   MT  0.99990366 +1 33 25.7
 RJ0241;UTM  16      - 5,136,184.510   665,731.283   MT  0.99993764 +1 33 33.8
 RJ0241
 RJ0241                          SUPERSEDED SURVEY CONTROL
 RJ0241
```

```
RJ0241  NAD 83(1986)-  46 21 32.16828(N)     084 50 44.39628(W)      ADJUSTED
RJ0241  NGVD 29      -       280.702  (meters)      920.94    (feet)  ADJ UNCH
RJ0241
RJ0241.Superseded values are not recommended for survey control.
RJ0241.NGS no longer adjusts projects to the NAD 27 or NGVD 29 datums.
RJ0241.See file format.dat to determine how the superseded data were derived.
RJ0241
RJ0241_MARKER: DB = BENCH MARK DISK
RJ0241_SETTING: 7 = SET IN TOP OF CONCRETE MONUMENT (ROUND)
RJ0241_STAMPING: T 44 1934
RJ0241_STABILITY: C = MAY HOLD, BUT OF TYPE COMMONLY SUBJECT TO
RJ0241+STABILITY: SURFACE MOTION
RJ0241_SATELLITE: THE SITE LOCATION WAS REPORTED AS SUITABLE FOR
RJ0241+SATELLITE: SATELLITE OBSERVATIONS - May 01, 1991
RJ0241
RJ0241  HISTORY      - Date      Condition        Recov. By
RJ0241  HISTORY      - 1934      MONUMENTED       CGS
RJ0241  HISTORY      - 1935      GOOD             NGS
RJ0241  HISTORY      - 1988      GOOD             USE
RJ0241  HISTORY      - 19910501  GOOD             NOS
RJ0241
RJ0241                           STATION DESCRIPTION
RJ0241
RJ0241'DESCRIBED BY NATIONAL GEODETIC SURVEY 1935
RJ0241'5.9 MI E FROM STRONGS.
RJ0241'5.9 MILES EAST ALONG THE DULUTH, SOUTH SHORE AND ATLANTIC
RJ0241'RAILWAY FROM STRONGS, CHIPPEWA COUNTY, 5 FEET SOUTH OF MILEPOST
RJ0241'26, AND 20 FEET NORTH OF THE TRACK.  A STANDARD DISK, STAMPED
RJ0241'T 44 1934 AND SET IN THE TOP OF A CONCRETE POST.
RJ0241
RJ0241                           STATION RECOVERY (1988)
RJ0241
RJ0241'RECOVERY NOTE BY US ENGINEERS 1988 (RAB)
RJ0241'THE STATION IS LOCATED ABOUT 5.9 MILE EAST OF STRONGS MICHIGAN.
RJ0241'
RJ0241'TO REACH THE STATION FROM STRONGS MICHIGAN, GO EAST FOR 9.5 KM
RJ0241'(5.9 MI) ALONG M-28 TO STATION LOCATED 6 METERS (20 FEET) NORTH OF
RJ0241'ABANDONED RAILROAD GRADE WHICH IS ALONG NORTH SIDE OF HIGHWAY M-28.
RJ0241
RJ0241                           STATION RECOVERY (1991)
RJ0241
RJ0241'RECOVERY NOTE BY NATIONAL OCEAN SURVEY 1991
RJ0241'RECOVERED IN GOOD CONDITION.

*** retrieval complete.
Elapsed Time = 00:00:02
```